Italian National Agency for New Technologies,
Energy and Sustainable Economic Development

High Performance Computing on CRESCO Infrastructure: research activities and results 2012

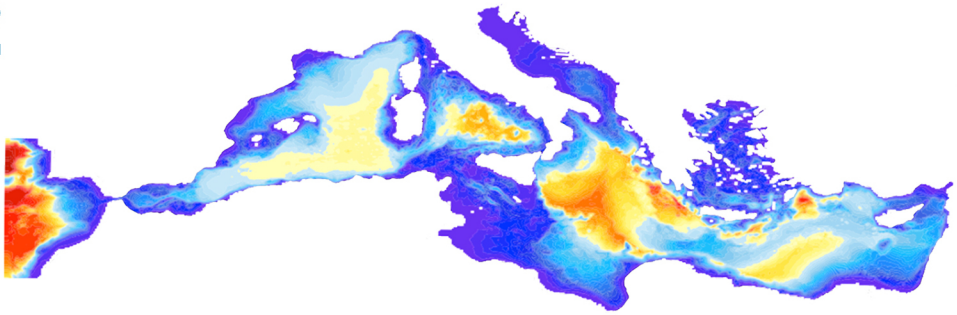

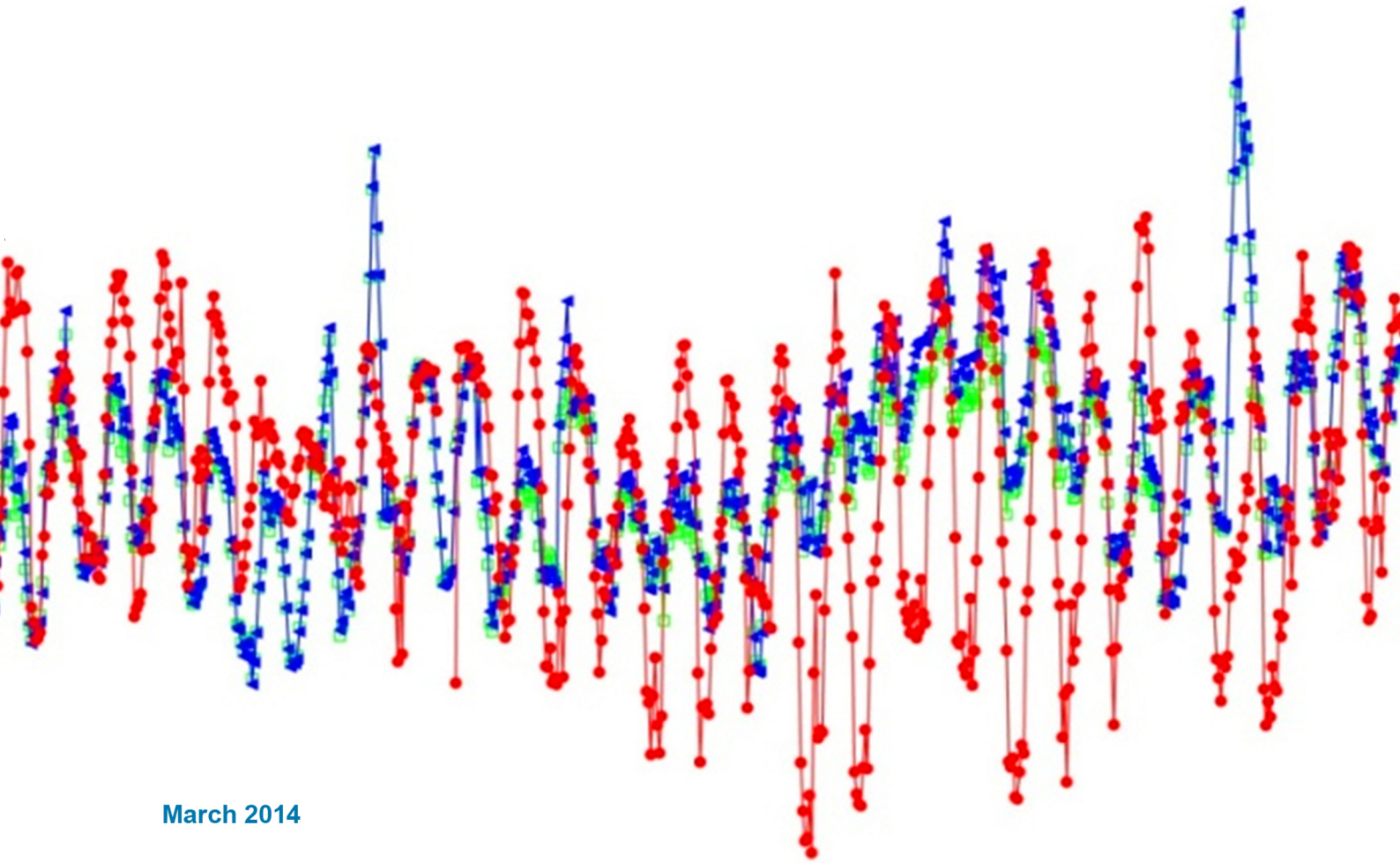

March 2014

High Performance Computing on CRESCO Infrastructures: research activities and results 2012

Contributions provided by a selection of users of the CRESCO infrastructure

Edited by: Filippo Palombi, Delinda Piccinelli

2014 ENEA
Agenzia per le Nuove tecnologie
l'Energia e lo sviluppo economico sostenibile

Lungotevere Thaon di Revel, 76
00196 Rome

ISBN 978-88-8286-302-9

INDEX **Pages**

Foreword

During the year 2012 CRESCO high performance computing clusters have provided about 20 million hours of computing time, at a high availability rate, to more than one hundred users, supporting ENEA research and development activities in many relevant scientific and technological domains. In the framework of joint programs with ENEA researchers and technologists, computational services have been provided also to academic and industrial communities.

This report, the fourth of a series started in 2008, is a collection of papers illustrating the main results obtained during 2012 using CRESCO HPC facilities in the fields of material science, computational fluid dynamics, climate research, nuclear physics and biophysics. The report shows the variety of the applications of high performance computing, which has become an enabling technology for science and engineering.

ENEA Portici Research Centre near Naples is the location hosting the main ENEA computational resources. This is a result of the Project CRESCO (Computational Centre for Research on Complex Systems), co-funded, in the framework of the 2001-2006 European Regional Development Funds Program by the Italian Ministry of Education, University and Research (MIUR).

The CRESCO Project provided the resources to set up the first large HPC x86_64 Linux cluster in ENEA, achieving a computing power relevant on Italian national scale (it ranked 126 in the HPC Top 500 June 2008 world list, with 17.1 TFlops and 2504 cpu cores). It was later decided to keep CRESCO as the signature name for all the clusters in the ENEAGRID infrastructure which integrates all ENEA scientific computing systems, and is currently distributed in six Italian sites.

In 2012 the ENEAGRID computational resources consisted of 3500 computing cores and about 300 TB of raw data storage.During the year a number of new projects - namely LAMRECOR, ITACHA, TEDAT and VIS4FACTORY - funded by MIUR in the framework of the 2007-2013 European Regional Development Funds Program, made it possible to carry out a substantial upgrading. In 2013 two new x86_64 clusters (named CRESCO3, 2016 AMD cores, and CRESCO4, 4864 Intel cores, ~120 TFlops peak) and new storage (600 TB raw) have been acquired and will enter in operation by the end of year.

The success and the quality of the results produced by CRESCO stress the role that HPC facilities can play in supporting science and technology for all ENEA activities, national and international collaborations, and the ongoing renewal of the infrastructure provides the basis for a similar role in the forthcoming years.

Peptide-TiO_2 surface interaction in solution by molecular dynamics simulation

Caterina Arcangeli*, Massimo Celino

ENEA, UTTMAT-DIAG, C. R. Casaccia

Keywords: Molecular dynamics, adhesion, titanium dioxide, surface, amino acids
*Corresponding Author: E-mail: caterina.arcangeli@enea.it, Tel: +39-0630486898, Fax: +39-0630483176

Classical Molecular Dynamics (MD) simulations were carried out to investigate both the structure and the stability of a full peptide on the (101) surface of TiO_2 in the anatase crystalline structure. The strength of the adhesion was estimated by pulling the peptide away from the surface. Our results shed light on the role played by some amino acids that are known to be essential in selective adsorption on TiO_2, as well as on the peptide structural conformation upon the surface. The simulations were carried on CRESCO HPC cluster by using the highly optimized parallel version of GROMACS (version 4.5.4).

Introduction

Investigation of the structure and properties of the interface between biological matter and titania surfaces have attracted a great deal of attention. Indeed titania-biomolecule interfaces are of fundamental importance not only for the development of biocompatible materials for surgical implants, but also for the bioinspired fabrication of nanostructured materials [1]. Experimental characterization of the peptide-titania interface [2] has revealed that electrostatic interactions play a key role and that peptide flexibility may also be important [3]. Moreover experiments point out that some aminoacids among the others, like for example Arg and Asp, have a peculiar role in the adhesion mechanism [2, 3]. In order to shed some light on this interaction, we investigated computationally the binding of a peptide on the (101) surface of TiO_2 anatase with the aim to define a model of interaction between selective-binding peptides and titania oxides. Even if a number of modeling and simulation studies have recently appeared for peptide-titania adsorption [4-11], these are limited to systems composed by only dipeptide, tripeptide or hexapeptide. In this study, MD simulations of the entire peptide composed of 13 amino acids and titania surface in the presence of the solvent is performed to investigate the role of the peptide flexibility and of the solvent on the interactions with the titania oxides.

Computational details

The MD simulation of the system (ca. 4400 atoms), composed by the folded peptide, the TiO_2 anatase (101) surface and the water solvent, was performed following the simulation protocol of Kang *et al.* [12]. The OPLSAA force field [13] was used to describe the protein and the TiO_2 parameters were supplemented. The Lennard-Jones parameters of Ti and O atoms were obtained from the literature [12, 14, 15]. For the water molecule the SPC water model was used [30]. During the simulation the inorganic surface was kept frozen. The simulation, for a total duration of 15 ns, was carried out in the canonical (NVT) ensemble. The peptide was placed close (at an average distance of 1 nm) to the TiO_2 surface oriented with the lateral chains of the arginine (Arg) and aspartic acid (Asp) perpendicular to the surface. The system was immersed in a rectangular box of $3.14 \bullet 3.03 \bullet z$ nm^3, where z is the box length along the direction perpendicular to the TiO_2 surface. In this study z is set to 5.0 nm to fit the starting orientation of the peptide. The box lengths, in the x and y directions, fit the crystal parameters of the surface, creating infinite slabs in the x-y plane.

Results and Discussions

MD simulations of the adsorption of the full peptide on the surface were performed by placing the peptide at about 1.0 nm distant from the TiO_2 surface. The peptide was oriented with the lateral chains of the Arg and Asp residues perpendicular to the surface. In Fig. 1 the configuration of the adsorbed folded peptide on the surface and the surrounding water molecules, after 5 ns of simulation is shown. The interfacial water molecules are quite stable and oriented on the TiO_2 surface to form a

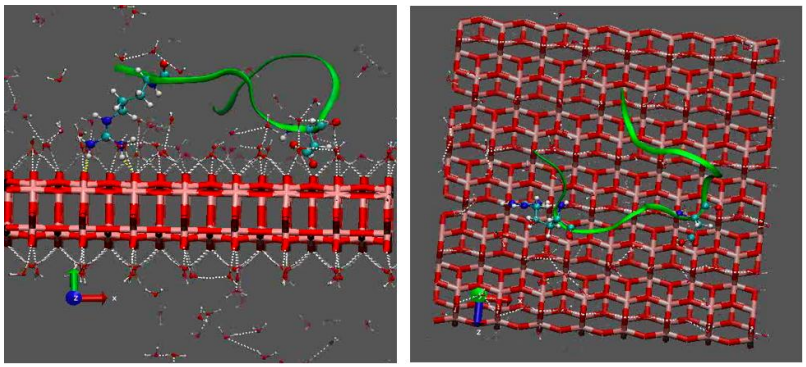

Fig 1: Snapshots of side view (left) and top view (right) of the adsorbed peptide onto TiO_2 (101) anatase surface taken at 5 ns. The peptide backbone is shown as a green ribbon while Arg3 and Asp7 are represented through CPK model. Only the interfacial water molecules are shown for clarity. The hydrogen bonding network among them is displayed as white dashed lines. The hydrogen bonding network among the atoms of the peptide and those of the surface is also shown, in yellow dashed lines. Movies of the simulation are at http://www.afs.enea.it/project/cmast.

hydrogen bond network induced by the surface. The side chain of the Asp7 residue adsorbs on the surface mediated by the interfacial water layer whereas the side chain of the Arg3 residue forms H-bonds with the oxygen atoms of the surface. Fig. 2 shows the effect of the adsorbed peptide on the structure of the interfacial water. The density profiles for both exposed surfaces have distinct peaks corresponding to different hydratation layers (Fig. 2a).

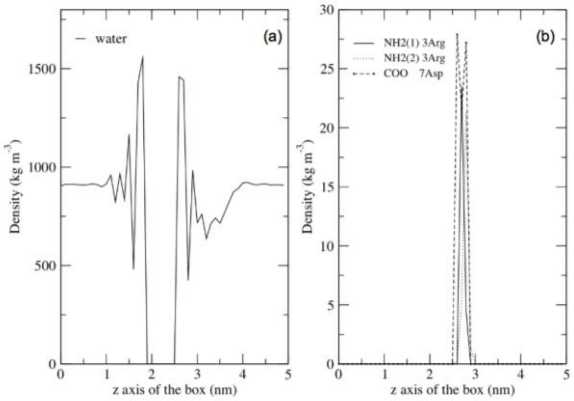

Fig 2: Density profile as function of the z axis for water (a) and peptide atoms (b). The plane containing the TiO_2 (101) anatase surface ranges from 1.9 to 2.5 nm and defines two interfaces. The left water-surface interface is free from the peptide; the right water-surface interface is affected from the presence of the peptide.

The presence of the peptide causes a decrease of the local water density. Similar results are observed for the adsorbed tripeptide (KEK) on negatively charged partially hydroxylated rutile (110) TiO_2 surface [6], in which the tripeptide affects only the first water layer that corresponds to molecularly adsorbed water molecules. The atoms of the lateral chains of the Arg3 and Asp7 are located in the first and second adsorbed water layer (Fig 2b). As shown in Fig. 3, in which the trend of the residue-surface minimum distance as a function of the simulation time is plotted, the acidic and basic residues show great affinity to the surface and, as extensively reported in previous simulations [7, 8,

10-12], the carboxyilic and guanidine groups ofthe residues are the main adsorbed groups that interact with the surface. In addition to the electrostatic interactions that seem to play the dominant role, Van der Waals interactions are also observed to occur between the peptide and the surface.

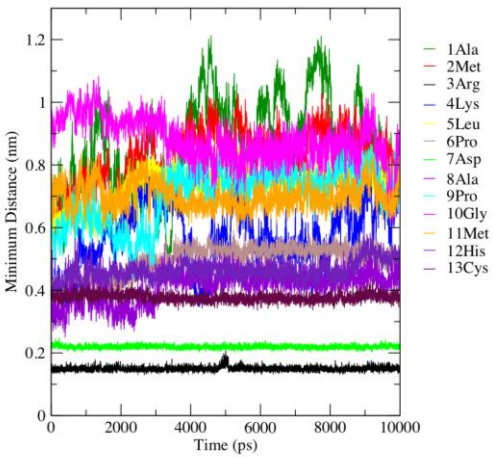

Fig 3: Residue-surface minimum distance as a function of the simulation time.

The non-polar Ala8 and Pro6 close to the surface (< 0.6 nm) due to the Van der Waals attractions, even if their interaction with the surface due to their connection with the adsorbed Asp7 can not be excluded. To better investigate the force of the interaction between the peptide and the surface, the peptide was pulled away from the surface along the z-direction, i.e. the direction perpendicular to the surface, over 10 ns of simulation using a spring constant of 5000 kJ/mol/nm^2 and a pull rate of 0.0005 nm/ps.

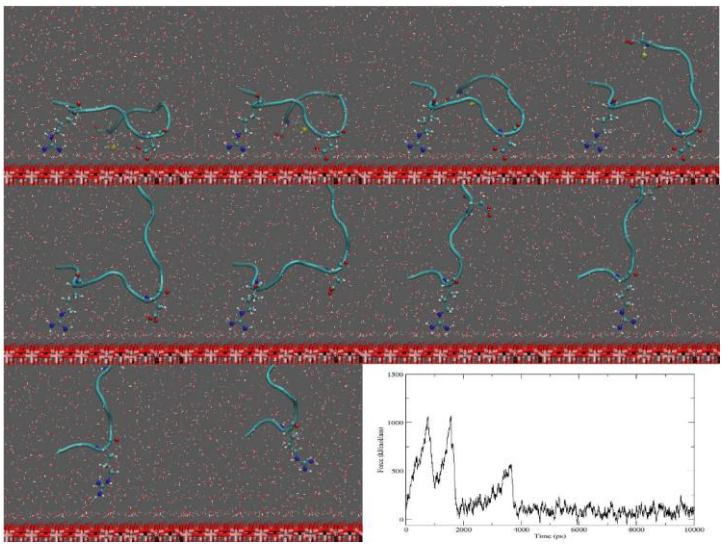

Fig 4: Snapshots of the dissociation pathway (from top left to bottom right) of the peptide from the surface. The peptide backbone is shown as a cyan ribbon while the Arg3, Asp 7 and Cys13, relevant for the adhesion mechanism, are represented though CPK model. The plot shows the pulling force applied as a function of the simulation time. Movie of the pulling simulation is at http://www.afs.enea.it/project/cmast.

Such a method can be used to bias the behaviour of a system toward a particular phenomenon that might otherwise be inaccessible on the time scale of a conventional MD simulation [17] and has been successfully applied to the study of many process, such as protein-protein and protein-ligand interactions [18]. The dissociation pathway of the peptide from the surface with the corresponding

plot of the force as a function of the time is shown in Fig. 4. By pulling on the center of mass of the peptide, force builds up until three breaking points are reached, at which the interactions between the Cys13, Asp7 and Arg3 with the surface are disrupted, allowing the peptide to dissociate from the surface. A similar behaviour has been observed for the desorption of the hexapeptide RKLPDA from a natively oxidized TiO_2 surface [10].

Conclusions

Atomic scale modeling is able to provide interesting insights in the design of novel materials. In the case of organic molecules interacting with inorganic surfaces, modeling can compute the adhesion properties and how these influence the physical and chemical properties. MD simulations of the peptide-surface interface enlight the cooperative behavior of amino acids.

Acknowledgment

This work was supported by META- Materials Enhancement for Technological Application- Project (FP7-PEOPLE-2010-IRSES-Marie Curie Actions, PIRSES-GA-2010-269182). We acknowledge the technical support of the ENEA-ICT team who provided the access to the ENEA-CRESCO high-performance computing facility (www.cresco.enea.it). We thank Drs. G. Aprea and S. Giusepponi for helpful discussions and suggestions.

References

1. M. B. Dickerson, K. H. Sandhage, R. R. Naik, Chem. Rev. 108, 4935-4978 **(2008)**.
2. K. I. Sano, K. Shiba, J. Am. Chem. Soc. 125, 14234-14235 **(2003)**.
3. H. B. Chen, X. D. Su, K. G. Neoh, W. S. Choe, Langmuir 25, 1588-1593 **(2009).**
4. V. Carravetta, S. Monti. J. Phys. Chem. B 110(12), 6160–9 (**2006**).
5. S. Monti, V. Carravetta, C. Battocchio, G. Iucci, G. Polzonetti. Langmuir, 24(7), 3205–14 (**2008**).
6. S. Monti, M. Alderighi, C. Duce, R. Solaro, M. R. Tine. J Phys Chem C 113, 2433–2442 (**2009**).
7. A. A. Skelton, T. Liang, T. R. Walsh, ACS Applied Materials & Interfaces 1(7), 1482–91 (**2009**).
8. C. Wu, A. A. Skelton, M. Chen, L. Vlček, P. T. Cummings. J Phys Chem C 115, 22375–22386 (**2011**).
9. S. Monti, A. C. T. Van Duin, S. Kim, V. Barone. J Phys Chem C 116, 5141–5150 (**2012**).
10. J. Schneider, L. Colombi Ciacchi. J Am Chem Soc 134(4), 2407–13 (**2012**).
11. C. Wu, A.A. Skelton, M. Chen, L. Vlček, and P.T. Cummings. Langmuir 28(5): 2799–811 (**2012**).
12. Y. Kang, X. Li, Y. Tu, Q. Wang, J. Phys. Chem. C 114 14496-14502 **(2010)**.
13. W. Jorgensen, D. Maxwell, J. TiradoRives, J. Am. Chem. Soc. 118 11225-11236 **(1996)**.
14. A. V. Bandura, J. D. Kubicki, J. Phys. Chem. B 107, 11072-11081 **(2003)**.
15. M. Predota, A. V. Bandura, P. T. Cummings, J. D. Kubicki, D. J. Wesolowski, A. A. Chialvo, M. L.Machesky, J. Phys. Chem. B 108, 12049-12060 **(2004)**.
16. J.A. Lemkul, D.R. Bevan, J. Phys. Chem. B. 114, 1652-1660 (**2010**).
17. S. Izrailev, S. Stepaniants, B. Isralewitz, .D Kosztin, H. Lu, F. Molnar, W. Wriggers, K. Shulten, Steered Molecular Dynamics, Vol. 4, Springer-Verlag, Berlin (1**998**).

Characterizing the energy landscape of biomolecules

Lorenzo Bongini

Abstract
The issue of characterizing the energy landscape is of great importance in the field of molecular dynamics simulation of bimolecules. Simulated trajectories often only provide a few examples of the many possible pathways of conformational change that characterize such large molecules and it is often difficult to assess how representative they are of the transition under study. Moreover, not infrequently the corresponding energetic information correlates with the kinetic features of the real system only qualitatively. An extensive of the energy landscape is, therefore, often necessary to understand at a reasonable level of detail conformational transition in biomolecules. Parallel computing is, therefore, necessary in tackling such a computationally expensive task.

DNA overstretching
The overstretching free energy landscape of a random DNA 23-mer containing 9 AT and 14 CG pairs was sampled via atomistic molecular dynamics simulations coupled with umbrella sampling. The conformational space of the chosen oligomer was investigated by simulating the effect of a heat bath trough a Langevin dynamics on 24 different copies of the system. Each copy was subjected to a restraining harmonic potential on its end-to-end distance in order to fix the average rise between consecutive base pairs during a simulation. The explored interval of base pair rise ranges from 0.34 to 0.58 nm. Simulations were performed with AMBER with the FF99SB force field. The different system copies were first heated at 400 K for 3 ns and then thermalized at 300 k for other 6 ns, until stabilization of the average enthalpy over a 1 ns window. After a preliminary analysis using an implicit solvent - employing the generalized Born solvation model and a rescaled Born radius (igb=5)- the simulation was repeated in explicit solvent, first with TIP3P and then with the SPC polarizable water model. In the implicit solvent simulation the ionic strength was set to 100 mM and the number of Na+ and Cl- ions in the explicit solvent simulations was chosen accordingly. In fig. 1 the radial distribution of the ionic cloud is investigated after 1 ns equilibration.

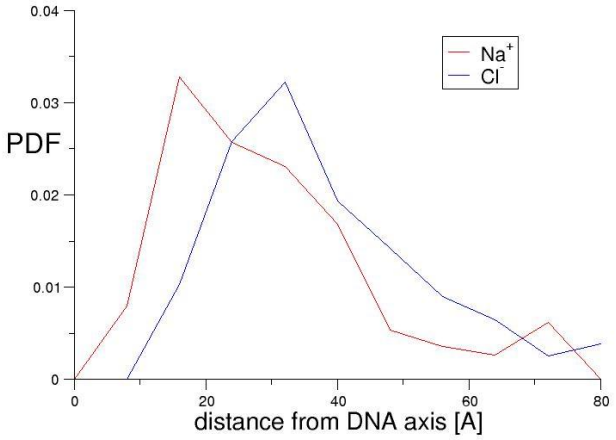

Fig. 1. Radial distribution function of the counter-ion cloud after 1 ns equilibration in SPC solvent.

Fig. 2 reports the free energy profile versus the average base pair rise. Free energy was computed by analyzing the end-to-end fluctuations of each constrained trajectory with the weighted histogram method, in the implementation of the freely available WHAM program by Alan Grossfield. Free energy grows monotonically with the base pair rise and no barrier is evident. The free energy difference between the maximally extended and compact conformations (0.58 and 0.34 nm rise) amounts to 4.8 k_BT per base pair, in reasonable agreement with the value of 3.7 k_BT per base pair coming from experiments [1].

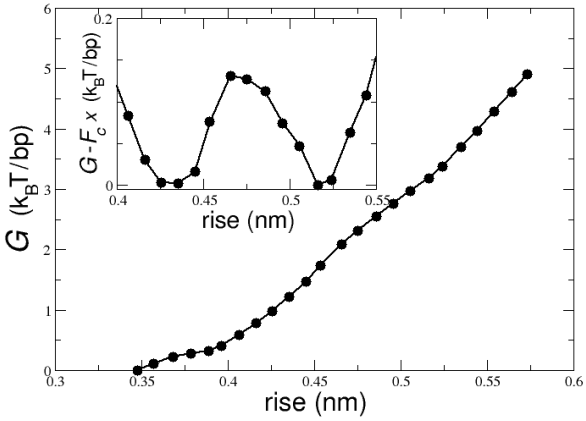

Fig. 2. Free energy profile for the overstretching of a DNA 23-mer. Free energy is computed by means of an umbrella sampling analysis over 2 ns trajectories. In the inset: free energy profile at the coexistence force between the compact and the extended state.

The knowledge of the free energy profile allows to compute the force of coexistence $\boldsymbol{F_c}$ as the force that best "flattens" the profile following the transformation $\boldsymbol{\Phi(x) \rightarrow \Phi(x) - F_c\, x}$. The result of this graphical procedure is illustrated in the inset of Fig. 2 were we report the free energy profile at the coexistence force F_C = 102 pN, which is high but reasonably near to the experimental value. Moreover at the coexistence force the free energy displays a nonzero barrier, 0.1 k_BT per base pair, separating the compact and extended state at the plateau. The compact state at the coexistence force corresponds the left most minimum in the curve reported in the inset of fig. 2 and it is now significantly shifted with respect to its zero force collocation (0.34 nm rise), now being characterized by an average base pair rise slightly higher than 0.43 nm. This shift corresponds to a stretch modulus of 600 pN, which is in resonable agreement with the values reported in literature (see the introduction of Gore et al for a short review on the subject).

However, Fig. 2 also marks a difference from experimental data. The extended state is shorter than expected, measuring just 0.52 nm in rise instead than 0.58 nm. It is difficult to speculate on the origin of these differences and a more extensive analysis with different force fields is in order.

The lack of a free energy barrier at 0 force and its presence at a given tension is a hallmark of enthalpy stabilized structures which, under tension, might undergo bond breaking events leading to higher energy, entropy stabilized structures. In this case, however, (see Fig. 3 where we report both the enthalpic and entropic profile of the transition) no clear signature of abrupt transitions can be seen in either the enthalpy of the process or in the vibrational entropy, which was estimated for each constrained trajectory by diagonalizing the mass weighted covariance matrix trough the PTRAJ tool of AMBER.

Only the Van der Waals contribution to the system enthalpy (inset of Fig. 3) shows a small discontinuity of approximately 2 k_BT per base pair above 0.46 nm base pair rise. The most significant conformational change taking place at that molecular extension is the unstacking of the AT base pairs. The observed energetic increase is however significantly smaller than expected for full unstacking (approximately 6

$k_B T$ per base pair), suggesting that unstacking is readily compensated by the appearance of non-native stacking contributions.

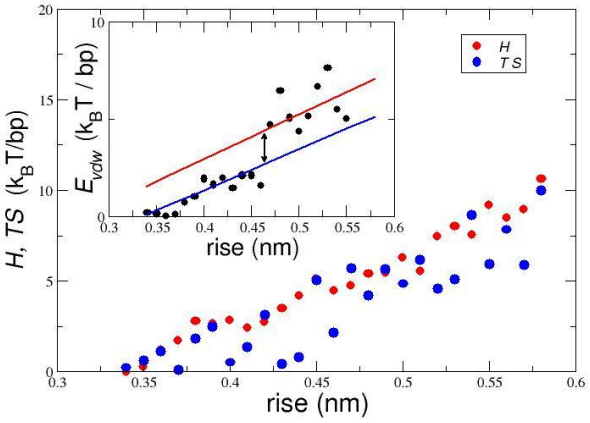

Fig. 3. Enthalpic and entropic contributions to the free energy. In the inset the Van der Waals contribution to free energy.

The lack of an enthalpy barrier observable in Fig. 3, is in full agreement with the findings recently reported in [1] and also the actual numerical vale for the $\Delta E_{+}^{\ddagger}$-the enthalpy difference between the transition and the compact state- is approximately 10 $k_B T$ per base pair, not too far off from the expected 8.2 $k_B T$ per base pair [1].

The values here reported correspond to the SPC simulations. The TIP3P results are qualitatively very similar but the coexistence force turns out significantly higher (160 pN) suggesting that the choice of the correct water model is of paramount importance when performing simulations of systems which undergo significant changes in their hydration properties.

A multiscale approach to the study of a molecular motor

Molecular motors are biomolecules that transform chemical energy in mechanical work. In the cell they are responsible not only for motility but also for trafficking between the various cellular compartments and they constitute a large part of the DNA repair and replication machinery.

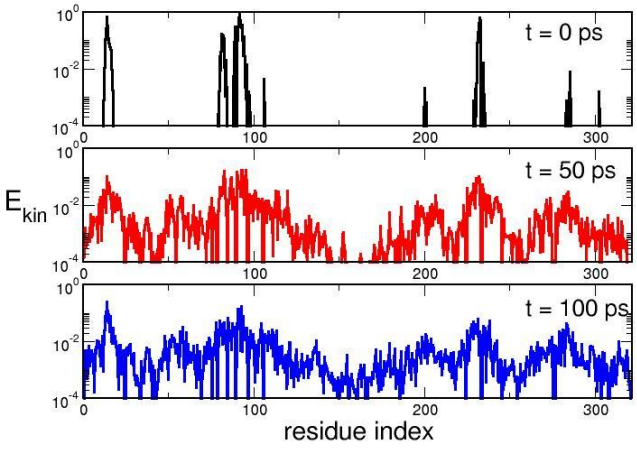

Fig. 5. Temporal evolution of the B-factors of a kinesin head after impulsive stimulation of the ENM with highest overlap with the ATP binding site.

The ratchet paradigm appears insufficient in explaining the behavior of biological molecular motors when the physiological data are taken in to account. Their typical force-velocity relation of a molecular motor (see [2] for the force velocity relation of the actin-myosin motor) is more immediately explained by a barrier limited diffusion between consecutive metastable states on a tilted landscape. The amount of time needed to sample with reasonable detail the huge configuration space accessible by such a large molecule is, nonetheless, too large. In order to devise strategies for the efficient sampling of the energy landscape we chose to compare the full atomistic landscape with that of a simplified model. We choose the Elastic Network Model because of its ability to capture with reasonable precision the low frequency eigenmodes of the system which are dictated solely by topology. Since ATP release is the force generating step in kinesin we are interested in detailing the propagation of information along the protein. In figure 4 we show that an impulsive stimulation along the ENM eigenmode with greater overlap with the ATP binding site is preserved for a significantly long time also when simulating the system with AMBER (in vacuo). The microtublule binding residues were held fixed with stiff harmonic constraints.

Bibliography

[1] Bongini L., Melli L, Lombardi V., Bianco P., "*Transient kinetics measured with force steps discriminate between double stranded DNA elongation and melting and define the reaction energetics"*, submitted to NAR

[2] Piazzesi G., Reconditi M., Linari M., Lucii L., Bianco P., Brunello E., Decostre V., Stewart A., Gore D. B., Irving T. C., Irving M., Lombardi V., "*Skeletal Muscle Performance Determined by Modulation of Number of Myosin Motors Rather Than Motor Force or Stroke Size"*, Cell **131**, (2007) pp.784–795.

VALIDATION OF THE MINNI ATMOSPHERIC MODEL SYSTEM (AMS) WITH THE TRISAIA FIELD CAMPAIGN DATA

Gino Briganti[1*], Andrea Cappelletti[1], Massimo D'Isidoro[2], Mihaela Mircea[2], Lina Vitali[2]

[1] ENEA-UTVALAMB-AIR. Territorial Office of Pisa
[2] ENEA-UTVALAMB-AIR. Bologna Research Centre
* e-mail: gino.briganti@enea.it

Introduction

MINNI [1] is the Italian Integrated Assessment Modelling System for supporting the International Negotiation Process on Air Pollution and assessing Air Quality Policies at national/local level sponsored by the Italian Ministry of the Environment. The MINNI system is composed of an Atmospheric Modelling System (AMS) and the Greenhouse Gas and Air Pollution Interactions and Synergies model over Italy (GAINS-Italy), connected to one another through the Atmospheric Transfer Matrices and RAINS Atmospheric Inventory Link. The main components of AMS are the meteorological model (RAMS [2]) and the air quality model (FARM [3], [4]), for simulating the atmospheric chemistry.
The standard air quality simulations of the reference scenarios have been carried out over the whole Italy with horizontal 20 km spatial resolution and over five sub-domains, including respectively north, centre and south of Italy, Sardinia and Sicily islands, with 4 km horizontal spatial resolution.
During the course of the Project, the whole AMS has been deeply upgraded to the present state of the art of the research, by introducing a new chemical mechanism SAPRC99 [5], a specific model for simulating biogenic emissions from vegetation (MEGAN [6]), the TUV (Tropospheric Ultraviolet and Visible Radiation Model) module [7]; moreover, the simulations have been performed for the first time at 1 km resolution. An *ad hoc* field campaign, supported by the Italian Ministry of the Environment and carried out at the ENEA Trisaia Research Center of Rotondella (Matera – Basilicata, May-June 2010), allowed us to test the performances of the AMS. This report shows some preliminary results of the application of AMS to the Trisaia campaign. The availability of ENEA-GRID computational resources has been crucial for achieving our purposes, because of the higher computational demand associated with the model upgrades such as the SAPRC99 mechanism, TUV module and, specially, the spatial resolution increase.

Air Quality fields production and evaluation

Computational Domains and Spatial Resolution

In the frame of this validation exercise, AMS has been applied to simulate the state of the atmosphere for all the period of the Trisaia field campaign (May – June 2010). As it is usually done for AMS-MINNI simulations, meteorological and concentration fields have been both produced with hourly time step and a spatial resolution of both 20 km, at national scale, and 4 km over a sub-domain covering the south of Italy (Fig. 1, on the left). Vertically, the computing domain consists of 16 terrain following vertical levels from 20 m to 10000 m above the ground. The availability of a comprehensive database to be used for model validation provided an opportunity for a first test of the MINNI modelling system downscaled at an higher resolution (1 km). The domain used for the high resolution simulations is illustrated on the right in Fig. 1, where the star identifies the site of Trisaia.

This domain was chosen to include Taranto urban area and the main industrial point sources of the area (green circles in the Figure).

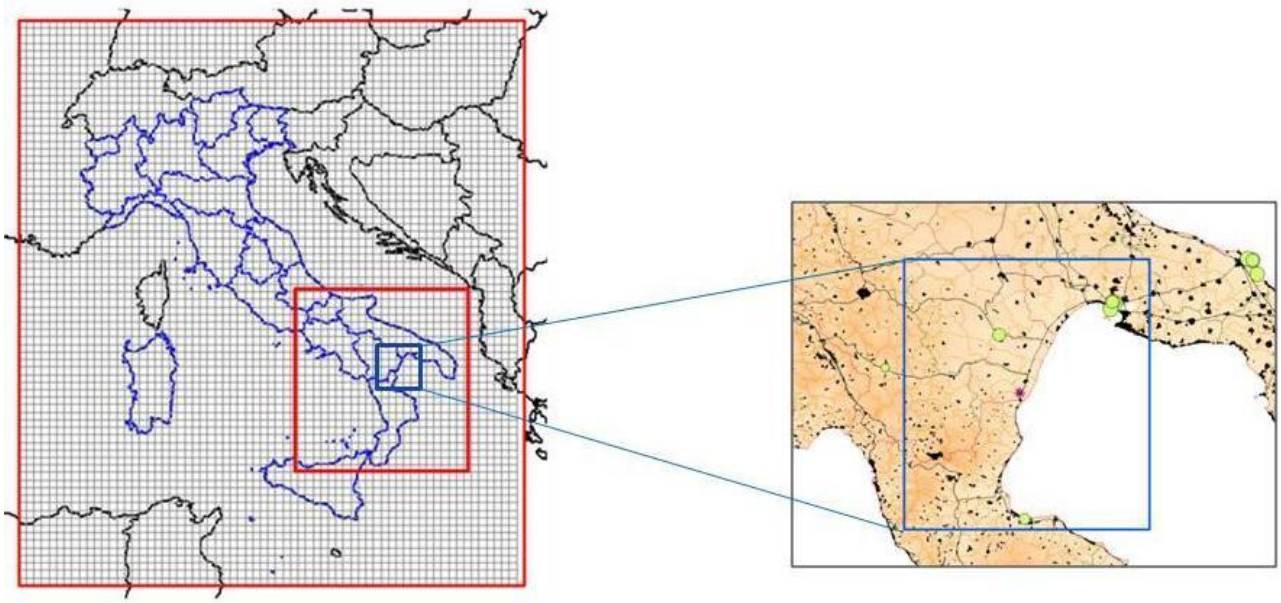

Figure 1. National domain and south of Italy sub-domain commonly used for AMS-MINNI simulations (left) and high resolution domain for Trisaia simulation (right).

The number of grid points needed for each of the three simulations at different spatial resolution is shown in Tab.1.

	20 km	**4 km**	**1 km**
Nx	67	116	119
Ny	75	121	131
Nz	16	16	16
Nx · Ny· Nz	80400	224576	249424

Table 1. Grid points number for simulations at different spatial resolution.

METEOROLOGICAL FIELDS INPUT

The meteorological fields have been reconstructed by means of the prognostic non-hydrostatic Regional Atmospheric Modeling System (RAMS) Version 6.0, developed at Colorado State University [2]. With regard to run settings, the same approach commonly used in the frame of the MINNI project has been largely retained. Initial, boundary conditions and data assimilation have been based on mesoscale analyses produced by means of a RAMS pre-processor which implements an optimal interpolation method. European Centre For Medium-Range Weather Forecast (ECMWF) analyses have been used as background fields and World Meteorological Organisation (WMO) surface observations as measured data. A nudging technique has been employed by RAMS to assimilate data analyses during the whole model simulation. In order to remove any possible drift of the calculated fields with respect to the large-scale analysis and local observations, the simulations have been re-initialized every ten days. RAMS implements a multilayer soil model [8] coupled to the atmospheric model to allow the evaluation of heat and moisture fluxes. For each decadal run, soil temperature and moisture profiles have been initialized using the data relating to the previous run,

allowing continuity of soil status during the whole 2 months simulation. To get a good initialization of the first ten days of May 2010, model simulation has been extended to the whole April 2010.
As an example of how the increasing resolution allows to describe more accurately atmospheric phenomena, Fig. 2 presents the monthly mean temperature for June 2010, modelled at the three different resolutions. To allow a qualitative comparison of the fields, the results, even at the resolution of 20 km and 4 km, are presented on the smaller domain for which high resolution fields are available too. In order to evaluate model performances, available observations from the ISPRA-SCIA database [9] are superimposed on each map (coloured symbols, provided in the same colour scale).

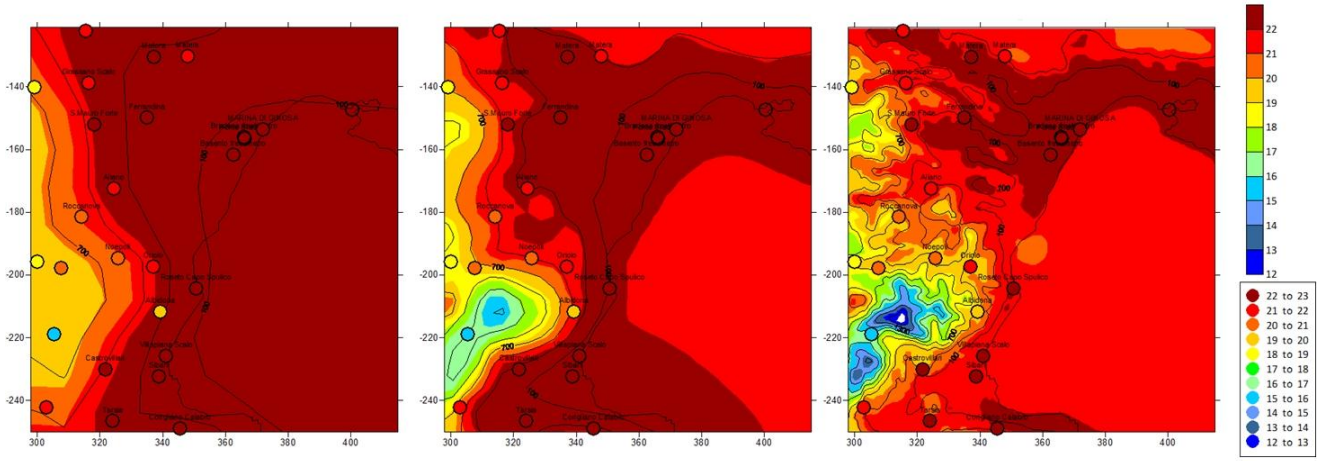

Figure 2. Monthly mean temperature (°C) fields for June 2010 produced by RAMS at different spatial resolutions: 20 km (left), 4 km (center) and 1 km (right). Comparison between simulated fields and observations from the ISPRA-SCIA database (colored symbols).

AIR QUALITY RESULTS AND EVALUATION

The chemical-diffusive simulations were conducted by using the FARM code (Flexible Regional Atmospheric Model) [3] [4], developed by ARIANET s.r.l. (http://www.aria-net.it/). FARM is a three-dimensional Eulerian grid model with K-type turbulence closure, that accounts for the transport, chemical reactions and ground deposition of atmospheric pollutants. The versions used are the 2.13 with SAPRC90 chemical mechanism [10] and 3.1, with SAPRC99 chemical mechanism [5] and the TUV module [7].
Grids specifications for FARM simulations are shown in Tab. 1. As initial and boundary conditions at 20 km resolution (Fig. 1) the EMEP (Meteorological Synthesizing Centre – West, MSC-W, http://www.emep.int/mscw/index.html) fields, suitably regridded and remapped to SAPRC90 and SAPRC99 mechanisms, were used. Higher resolution simulations were performed by employing an off-line one-way nesting.

Fig. 3 shows an example of the effects induced by the increase of the resolution on 2-month averaged ozone concentration at ground level. It is worth noting how spatial details are enhanced as the resolution increases. At 1 km we may appreciate even low values of ozone in the Basento valley, due to ozone titration resulting both from local industrial emissions and traffic; also in the Taranto area we observe an ozone consumption because of emissions from both the urban texture and the big industrial settlement.

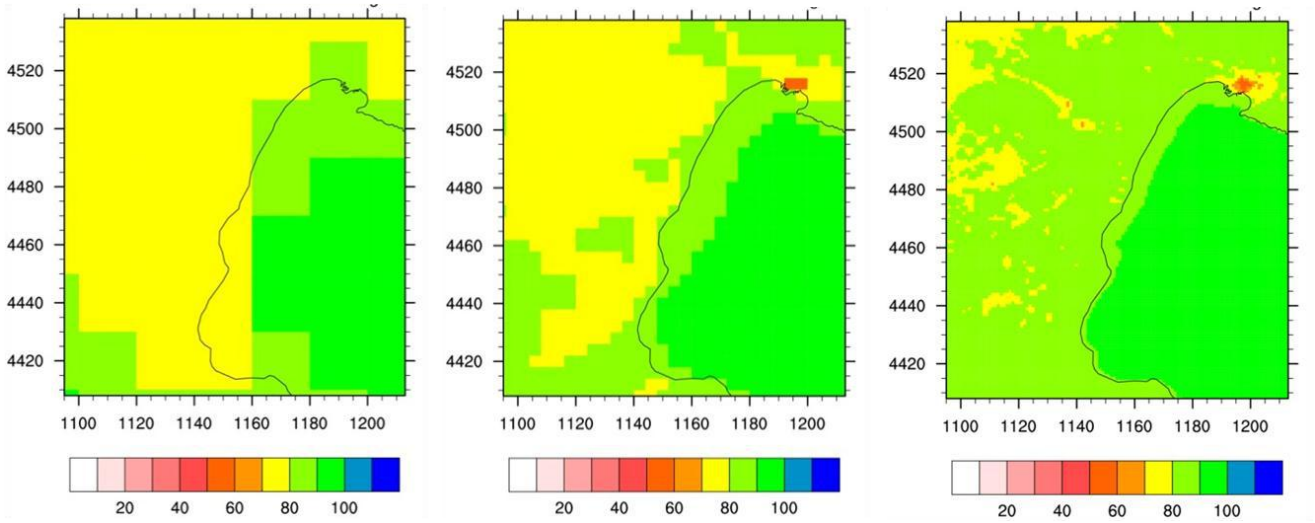

Figure 3. Effect of increased resolution on period-averaged ozone concentration pattern: 20 km (left), 4 km (center) and 1 km (right).

In Fig. 4 the hourly series of the experimental data (in red) compared to simulated ones for the Trisaia site are plotted. An improvement is obtained by using the biogenic emissions calculated by means of the MEGAN model [6] (in blue) rather than those derived from the ISPRA inventory (in green) (http://www.isprambiente.gov.it/it/banche-dati/aria-ed-emissioni-in-atmosfera). This improvement is more evident regarding the highest and maximum daily values, which are involved in the regulation compliance.

Another remarkable result obtained by using the MEGAN model is the good performance in reproducing the particulate matter speciation: Fig. 5 shows as the modelled speciation data are very close to measures; only the sulphates are slightly overestimated by the model compared to observations, possibly due to the incomplete modelling of the thermodynamics of Sicilian volcanic plumes. In particular the use of MEGAN model produced a significant increase of organic carbon amount. This is related to the enhanced production of secondary organic aerosols due to the oxidation of isoprene, whose MEGAN emissions result higher than the ones derived from ISPRA.

These are really the expected result, because the Basilicata region is populated by lots of greenery, whose emissions are obviously estimated with more accuracy by means of a specific biogenic model like MEGAN.

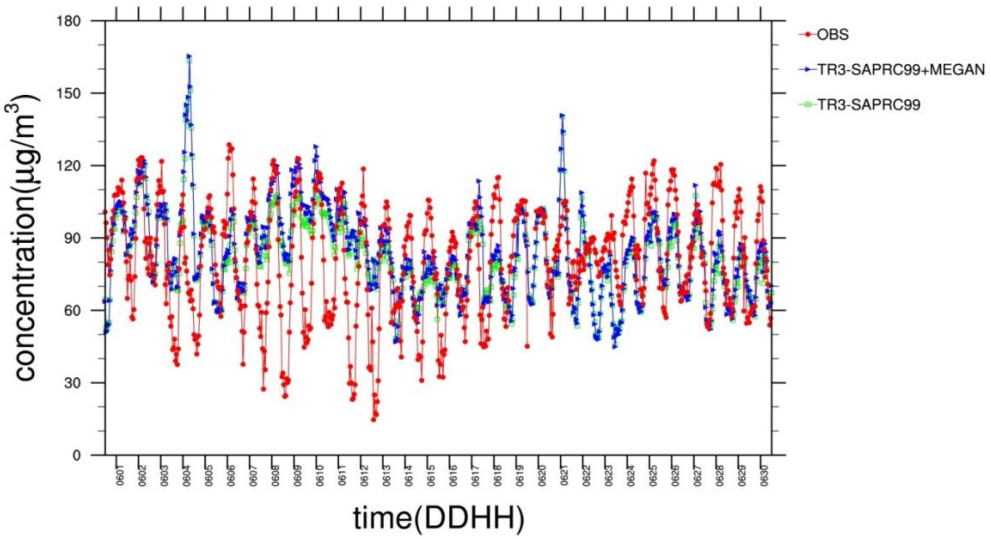

Figure 4. Time series of observed (red) vs simulated concentrations, using both the ISPRA inventory biogenic emission (green) and the MEGAN model (blue), at Trisaia site.

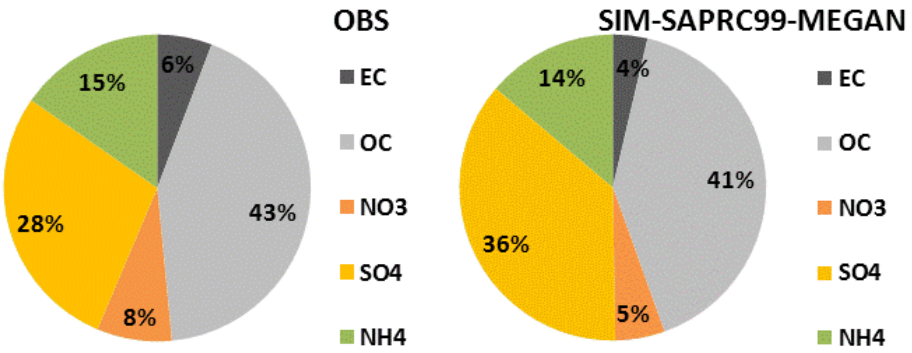

Figure 5. Particulate matter speciation observed (left) and modeled (right). EC=elemental carbon, OC=organic carbon, NO3=nitrates, SO4=sulfates, NH4=ammonia.

Information about Codes, Storage and CPU time

RAMS is an open source code (http://www.atmet.com/index.shtml) written in Fortran language. It was compiled in its parallel version and implemented in MVAPICH environment. In order to identify the optimal processor number minimizing execution times, some different processor numbers were tested and 64 was chosen as optimal one. Parallel jobs were dispatched on cresco2 machines.

The FARM finite-elements code is written in Fortran90 language and compiled with the Intel® Fortran Compiler, by employing the OpenMP parallelization paradigm. We already found that the optimal number of processors to be used in CRESCO environment is 8 [11]. In order to take advantage of the dedicate 24-hour queue "minni_128h24", the batch runs were arranged through the dependency option available with the LSF "bsub" command, by splitting then each job as follows: i) eight concatenated sub-jobs simulating 10 days at 20 km resolution; ii) fifteen concatenated sub-jobs simulating 4 days at both 4 and 1 km resolution.

CPU time and storage requirements for meteorological (Fig. 6 and Tab. 2) and air quality (Fig. 7 and Tab. 3) simulations are shown at the three different resolutions. About the air quality storage, both input (emissions) and output files are accounted.
It is worth noting that the amount of memory space for meteorology and air quality outputs depends almost linearly on the number of grid points (Tab. 1). Both meteorological and air quality inputs/outputs are stored in netCDF format, by means of 2D and 3D variables, with a own different amount of specific memory per variable. This is precisely the reason why air quality storages do not exactly scale with the grid spacing.
CPU times also grow almost linearly with the number of grid points for 20 and 4 km resolution; despite the number of grid points changes little passing from 4 to 1 km resolution, the considerable growth of CPU time, with respect to the 4 km run, is due to a smaller integration time, needed for guaranteeing reliable and convergent solutions. Even the appearance of new small-scale meteorological structures, arising as the grid space is reduced, may contribute to rise the CPU time.

Conclusions

The verification of AMS-MINNI with data from the Trisaia field campaign showed good performances and confirmed that both the introduction of new modules and the increasing spatial resolution substantially improved the model performances.
Future verifications of AMS-MINNI in polluted areas, such as the Po Valley, will provide further indications on the strengths and shortcomings of the modelling system.

	20 km	4 km	1 km
CPU time (hours x cores)	2207.10	5967.94	14321.46
Space (GB)	6.37	17.79	19.75

Table 2. CPU times and space requirement for meteorological simulations.

	20 km	4 km	1 km
CPU time (hours x cores)	807	2444	6198
Space (GB)	235	655	694

Table 3. CPU times and space requirement for air quality simulations.

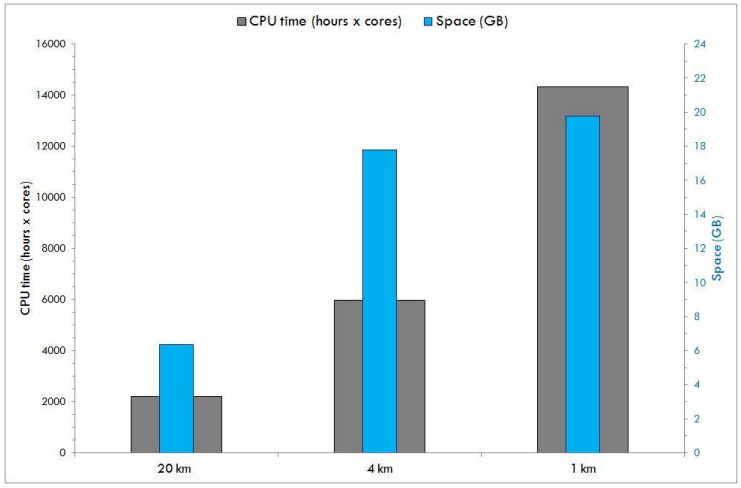

Figure 6. CPU time (left axis) and space requirement (right axis) for meteorological simulations.

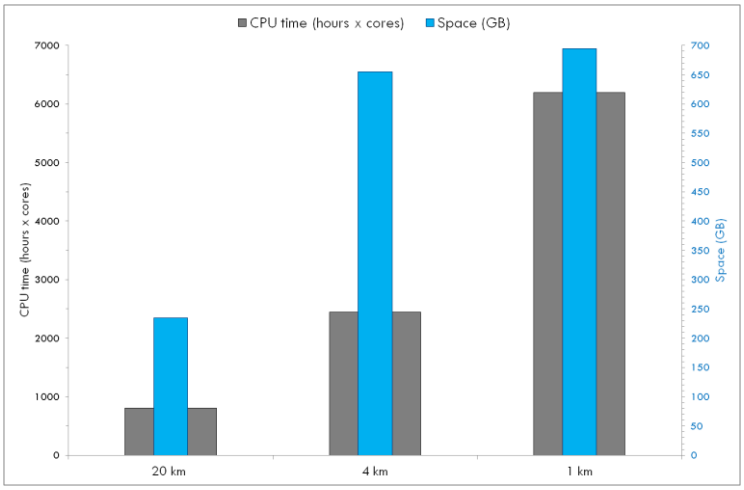

Figure 7. CPU time (left axis) and space requirement (right axis) for air quality simulations.

References

[1] ZANINI G., MIRCEA M., BRIGANTI G., CAPPELLETTI A., PEDERZOLI A., VITALI L., PACE G., MARRI P., SILIBELLO C., FINARDI S., CALORI G. *The MINNI project: an integrated assessment modeling system for policy making*. International Congress on Modelling and Simulation. Zealand, Melbourne, Australia, 12-15 December 2005, pp. 2005-2011. ISBN: 0-9758400-2-9.

[2] COTTON W.R., PIELKE R. A., WALKO R. L. , LISTON G. E., TREMBACK C. J., JIANG H., MC ANELLY R. L., HARRINGTON J. Y., NICHOLLS M. E., CARRIO G. G. AND MCFADDEN, J. P. *RAMS 2001: Current status and future directions*. Meteorology and Atmospheric Physics, 82, (2003) 5-29.

[3] SILIBELLO C., CALORI G., BRUSASCA G., CATENACCI G., FINZI G. *Application of a photochemical grid model to Milan metropolitan area*. Atmospheric Environment 32 (11), (1998) 2025-2038.

[4] GARIAZZO C., SILIBELLO C., FINARDI S., RADICE P., PIERSANTI A., CALORI G., CECINATO A., PERRINO C., NUSIO F., CAGNOLI M., PELLICCIONI A., GOBBI,G.P., DI FILIPPO P. *A gas/aerosol air pollutants study over the urban area of Rome using a comprehensive chemical transport model.* Atmospheric Environment 41, (2007) 7286-7303 .

[5] CARTER W.P.L.. *Documentation of the SAPRC-99 chemical mechanism for VOC reactivity assessment*. Final report to California Air Resources Board, Contract no. 92-329, and (in part) 95-308, (2000).

[6] GUENTHER A., KARL T., HARLEY P., WIEDINMYER C., PALMER P. I., AND GERON C. *Estimates of global terrestrial isoprene emissions using MEGAN (Model of Emissions of Gases and Aerosols from Nature)*. atmos. chem. phys., 6, (2006) 3181-3210.

[7] MADRONICH S. *Photodissociation in the atmosphere 1. Actinic flux and the effects of ground reflections and clouds*. J. Geophysical Research, 92, (1987) 9740–9752.

[8] WALKO R.L., BAND L.E., BARON J., KITTEL T.G.F., LAMMERS R., LEE T.J., OJIMA D., PIELKE R.A., TAYLOR C., TAGUE C., TREMBACK C.J., VIDALE P.J. *Coupled atmosphere-biophysicshydrology models for environmental modeling*. Journal of Applied Meteorology, 39, (2000) 931–944.

[9] DESIATO F., LENA F., TORETI A. *SCIA: a system for a better knowledge of the Italian climate*. Bollettino di geofisica teorica e applicata. Vol. 48, n.3, (2007) 351-358.

[10] CARTER W.P.L. A *detailed mechanism for the gas-phase atmospheric reactions of organic compounds*. Atmospheric Environment, 24 A (3), (1990) 481-518.

[11] BRIGANTI G., CALORI G:, CAPPELLETTI A., CIANCARELLA L., D'ISIDORO M., FINARDI S., VITALI L. *Determination of multi-year atmospheric transfer matrices for GAINS-Italy model. High Performance Computing on Cresco Infrastructure: research activities and results 2009-2010*, (2011), ENEA, ISBN: 978-88-8286-242-8.

THERMO-ACOUSTIC INSTABILITIES IN A LAB-SCALE BURNER

A. Di Nardo*, G. Calchetti*, S. Chiocchini **, E. Giacomazzi *, E. Giulietti*
antonio.dinardo@enea.it
*ENEA via Anguillarese 301 – 00123 ROMA ITALY
**Università ROMA TRE

Introduction

Lean premixed combustion in gas turbines (GT) is widely used in order to meet stringent low NO_x emissions demands. If this technique allows the achievement of a quite homogeneous temperature distribution, thermo-acoustic instabilities are a common problem in gas turbine combustors operating in lean premixed mode. Pulsations, caused by a resonant feedback mechanism coupling pressure and heat release [1–7], can lead to strong perturbations in the gas turbine and even to the destruction of system components. Equivalence ratio fluctuations is one of the major cause of flame instability [8, 9]: for example changes in air inlet velocity cause variations of the flow rate but may also produce mixing fluctuations and the introduction into the combustion zone of pockets with different equivalence ratio that can generate instabilities. The instabilities of turbulent premixed flames have been the subject of intense research in the last ten years. Numerical simulation tools at this moment are still not completely reliable in the studies of combustion instabilities and Large Eddy Simulation (LES) offers great possibilities for what concerns the self-excited combustion oscillations prediction [1–3, 10–14].

The burner

In this study the experimental campaign conducted at the German Aerospace Center (DLR) [15] was chosen as test case. The burner nozzle was designed by Turbomeca S.A. and was operated with premixed CH4/air, which for an equivalence ratio of Φ = 0.7 (25 kW) exhibited a strong self-excited thermoacoustic oscillation at a frequency of about 290 Hz. In Fig. 1 is shown a schematic of the entire system. Air at ambient temperature flows through a radial swirler to the burner nozzle. The fuel gas (CH_4) is supplied through small holes within the radial swirler with high momentum to ensure good mixing before entering the 85x85 mm combustion chamber. The burner is

operated at 25 kW with an equivalence ratio of 0.70. Reynolds number at the nozzle is about 35000 and the swirl number is approximately 0.6.

Numerical methods

The simulations were conducted using the commercial CFD code ANSYS-FLUENT. The computational grid consists of about 4.000.000 computational cells. For the combustion chamber a hexahedral grid properly refined at the chamber inlet was adopted, while, given the geometric complexity, a tetrahedral grid was used for the plenum. The dynamic Smagorinsky-Lilly LES approach was used for turbulence. The turbulence-chemistry interaction was modeled using the Eddy-Dissipation-Concept model [16], in conjunction with a simple 2-steps and 5 species mechanism [17] and a more complex 46-steps and 17 species chemical mechanism [18]. Simulations were run in parallel on a about 128 cores of the high-parallel ENEA-CRESCO cluster section 2, for a month.

Comments

Pressure signals coming from microphones placed in the chamber and the plenum oscillate at a frequency of about 290Hz and the two signals are not in phase. The two signals recorded at the same positions during the simulation are reported in figure 2. The dominating frequency of both is about 250Hz. The figure also shows that the trace of the signal from the plenum is smoother than that from the combustion chamber. This was confirmed experimentally. Mean temperature field is similar for the two mechanisms used, but the simple one exhibits general higher values. On the other hand instantaneous fields reveal very high and unrealistic temperature peaks in this case, with respect experimental data. The flame is anchored at the nozzle exit, where the swirl effect generates an inner recirculation zone. Here the recirculation of hot products ignites the incoming fresh mixture, stabilizing the flame, which assumes the shape of a cone (fig. 1). Chemical reactions however extend until up to chamber walls. An outer recirculation zone it is also present at the chamber corners. Temperature profiles are reported in figure 3. If the external part of the profiles matches satisfactorily with the experimental data, there is a certain mismatch for the internal part. It seems that the inner recirculation zone predicted by the simulations is less wide in terms of reaction, even if it is well captured in terms of flow field (fig. 4). Mixing of fuel and air within the swirler it is not perfect, as results from CH_4

profile at nozzle exit and the pulsating behavior of the flame is mainly due to changes in equivalence ratio of the fuel air mixture entering the combustion chamber. When pressure in the chamber is low, air flow velocities increase and the fresh mixture is not able to burn, also due to ignition delay.

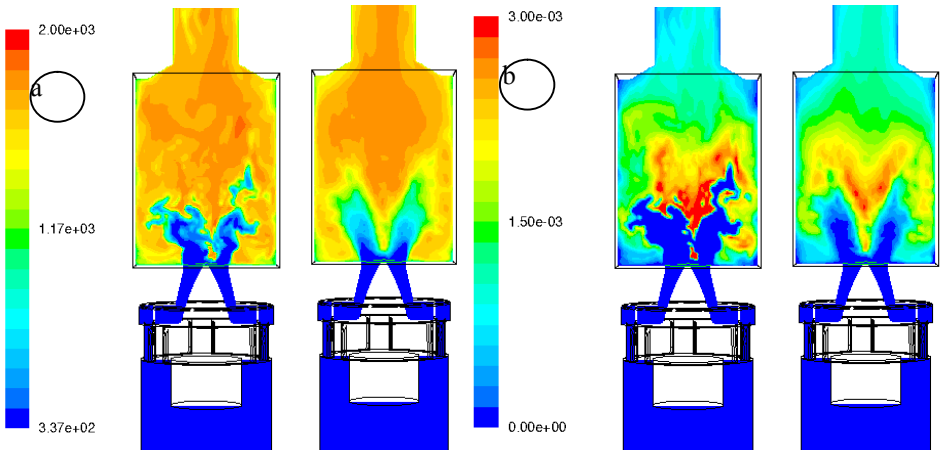

Figure 1. Mean (right) and instantaneous (left) temperature (a) (K) and OH mass fraction (b).

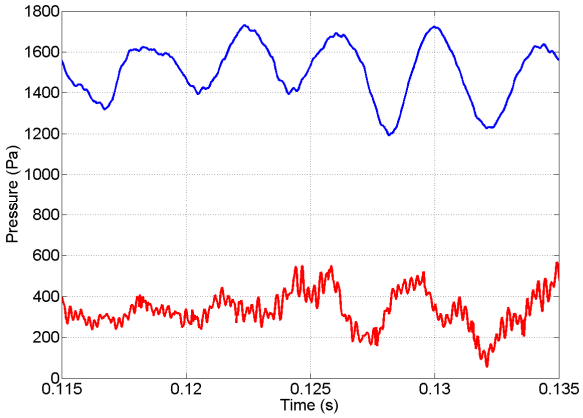

Figure 2. Pressure signal in the plenum and in the chamber.

Pockets of combustible mixture rise even very far from nozzle exit and burn at chamber walls, where velocities lower and the elapsed time is sufficient for mixing and ignition delay. This causes an increase in pressure and a

subsequent reduction in air flow, that again generates a fuel-rich mixture. It is then possible to conclude that pressure fluctuations and heat release sustain each other, fulfilling the criterion for self sustained oscillations in flames of Rayleigh.

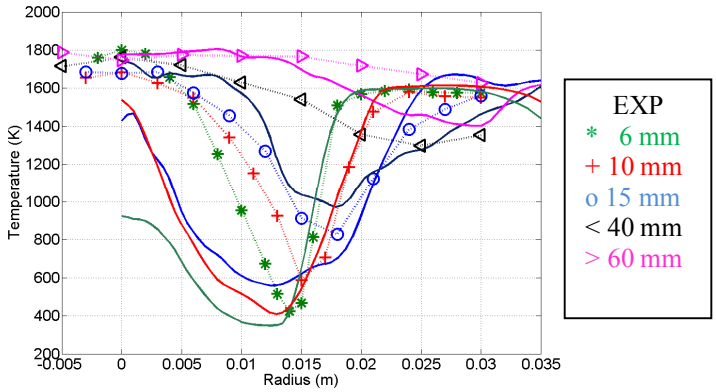

Figure 3. Temperature (top) and O_2 mole fraction (bottom) radial profiles.

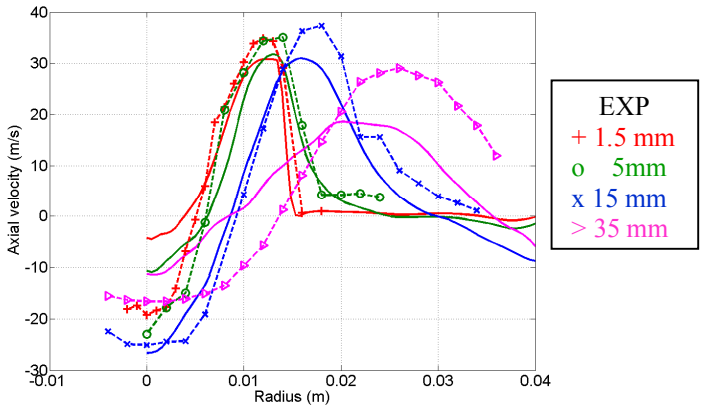

Figure 4. Axial velocity profiles.

References

[1] Keller J.J., AIAA J. 33: 2280–2287 (1995).
[2] Fernandes E.C., Heitor M.V. , in: F. Culick, M.V. Heitor, J.H. Whitelaw (Eds.), Unsteady Combustion, Kluwer Academic, Dordrecht, 1996, p. 1.
[3] Paschereit C.O., Gutmark E., Weisenstei, W., Combust. Sci. Technol. 138: 213–232 (1998).

[4] Lefebvre A.H., Gas Turbine Combustion, Taylor & Francis, (1999).
[5] Candel S., Proc. Combust. Inst., 29: 1–28 (2002).
[6] Lee J.G., Santavicca D.A., J. Propulsion Power 19:735–750 (2003).
[7] Syred N., Prog. Energy Combust. Sci., 32 93–161 (2006).
[8] Lieuwen T., Torres H., Johnson C., Zinn B., J. Eng. Gas Turb. Power 123 (1) 182–189 (2001).
[9] Shreekrishna S., Hemchandra S., Lieuwen T., Combust. Theory Model. 14 (5) 681–714 (2010).
[10] Dowling A.P., Hubbard S., Proc. Inst.Mech. Engrs. 214: 317–332 (2000).
[11] Stone C., Menon S., Proc. Combust. Inst. 29: 155–160 (2002).
[12] Cook D.J., Pitsch H., Peters N., Proceedings ASME Turbo Expo, GT2003-38558 (2003).
[13] Lieuwen T., J. Propulsion Power 19: 765–781 (2003).
[14] Roux S., Latigue G., Poinsot T., Meier U., Berat C., Combust. Flame 141: 40–54 (2005).
[15] Meier W., Weigand P., Duan X.R., Giezendanner-Thoben R., Combustion and Flame 150: 2–26 (2007).
[16] Magnussen B. F., Nineteeth AIAA Meeting, St. Louis (1981).
[17] Westbrook C. K., Dryer F. L., Combust. Sci. Technol., 27: 31–44 (1981).
[18] Smooke M.D., Puri I.K., Seshadri K., Proc. Combust. Inst. 21: 1783–1792 (1986).
[19] Van Leer B., Jounal of Computational Physics, 32: 101-136 (1979).

OXY-COAL COMBUSTION SIMULATIONS IN AN EXPERIMENTAL FURNACE

A. Di Nardo, G. Calchetti
antonio.dinardo@enea.it
*ENEA via Anguillarese 301 – 00123 ROMA ITALY

Abstract

One of the most promising techniques for CO_2 separation and capture is combustion in pure oxygen and recirculated exhaust gas atmosphere, named oxy-combustion. The use of exhaust gas is necessary for temperature containment, which otherwise would be too high. Theoretically, in this way it is possible to obtain CO_2 concentrations of about 95%, after water vapor condensation. In order to delve into this technology and make available experimental data to validate numerical models, IFRF has realized an experimental furnace called Fo.Sper. [1], installed at ENEL-Livorno, able to operate in oxy+flue_gas and air mode. In the first case exhaust gases are extracted, cooled, condensed and partly returned to the combustion chamber, after being enriched in oxygen.

Furnace description

The furnace is a 2x2x6.25m parallelepiped. It consists of 11 refractory water-cooled sections, in order to simulate the energy extraction and heat exchange that takes place in a full-scale plant. Measuring probes are inserted through 14 ports, arranged along the furnace. The burner is essentially constituted by three concentric ducts (primary, secondary and tertiary). The inner pipe (primary) is used for pulverized coal feeding. The combustion air is fed through the secondary and tertiary ducts, provided of adjustable swirler.

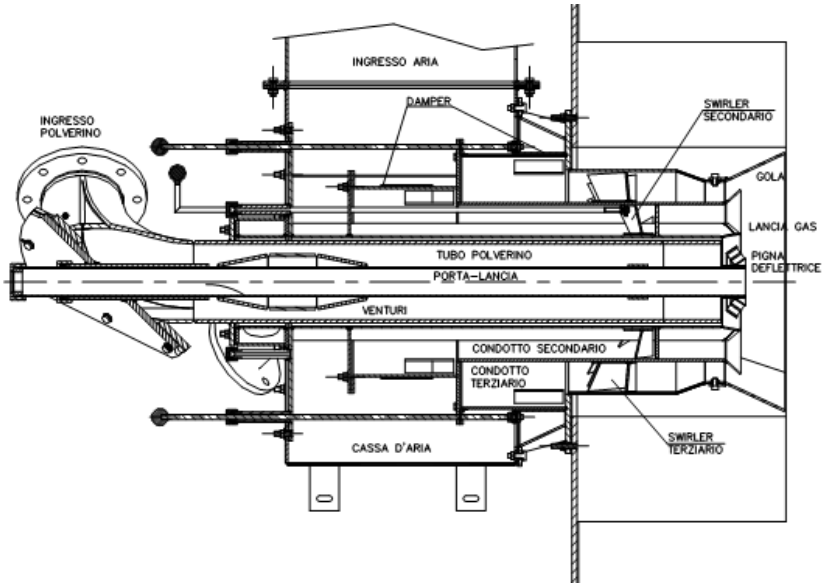

Figure 1. The burner section.

Simulation set-up and discussion

The simulation of the reactor Fo.Sper. was conducted using the ANYS-FLUENT software. The mesh is a hybrid mesh, tetrahedral in the inner of the burner and prismatic (triangular and quadrilateral base) in the combustion chamber and consists of about 500000 cells. Given the

periodicity of the problem, the study was limited to one quarter of the entire apparatus. The simulation uses for turbulence the k-ε model [2]. The EDC model (Eddy Dissipation Concept) [3] was adopted for chemical phenomena in gas phase and the P1 model for radiative heat transfer [4]. Temperature distribution on the walls was extrapolated from the available data. The trajectory and the exchange of energy and mass of the particles was evaluated according to a Lagrangian approach. Table 1 shows the boundary conditions used in the simulation. Pyrolysis was modeled as a two stage process. During primary pyrolysis coal particles decompose releasing volatile, composed of TAR, light hydrocarbons and gas. In the second stage, the TAR decomposes producing soot, hydrocarbons and light gases (mainly CO and H_2). Coal burned in the experimental campaign is the Sebuku Indonesian. Volatile release was modeled with the CPD [5, 6, 7] model. The volatile species were represented with a single pseudo molecule like $C_xH_yO_z$, which decomposes in the gas phase through an infinitely fast reaction according to:

$$C_xH_yO_z \rightarrow TAR + CH_4 + CO + CO_2 \quad (1)$$

Tab. 1. Operating conditions and reactions contsants.

Coal flowrate	360 kg/h
Primary air	-
Primary air temperature	-
Sec/tert air	-
Sec/tert air temperature	-
Measured internal camera cooling air	64 Nm^3/h
Oxygen	718 kg/h
Oxygen temperature	11°C
Primary RFG	700 kg/h
Primary RFG temperature	76°C
Sec/tert RFG	1063 kg/h
Sec/tert RFG temperature	255°C
Swirler setting	100 – 100%
Dumper setting	100 – 100%
Recycle ratio	0.61
Fuel thermal input	2.5 MW_t
Flue gas temperature	1250°C
Total heat extracted	0.93 MW
O_2	2.76 %
CO	19 ppm
CO_2	76.22 %
NO_x	238 ppm
SO_2	646 ppm
	330.7 mg/MJ

	Reaction, $\mathrm{kmol/s \cdot m^3}$	A_{rj}	E_{rj}/R, K
1	$\frac{d[C_nH_m]}{dt} = A_{r1} \cdot \exp(-E_{r1}/RT_g)[C_nH_m][O_2]$	$3.8 \cdot 10^7$	6670
2	$\frac{d[CH_4]}{dt} = A_{r2} \cdot \exp(-E_{r2}/RT_g)[CH_4]^{0.5}[O_2]^{1.25}$	$4.4 \cdot 10^{11}$	15098
3	$\frac{d[CH_4]}{dt} = A_{r3} \cdot \exp(-E_{r3}/RT_g)[CH_4][H_2O]$	$3.1 \cdot 10^8$	15098
4	$\frac{d[CO]}{dt} = A_{r4} \cdot \exp(-E_{r4}/RT_g)[CO][O_2]^{0.3}[H_2O]^{0.5}$	$2.5 \cdot 10^8$	8052
5	$\frac{d[H_2O]}{dt} = A_{r5} \cdot \exp(-E_{r5}/RT_g)[H_2][O_2]^{0.5}$	$7.9 \cdot 10^{10}$	17614

Reaction	A_{rj}, $\mathrm{kg/s \cdot m^2 \cdot Pa}$	E_{rj}, J/kmol	Order n	Reference
6	0.005	$74 \cdot 10^6$	1	Field (1969)
7	6.3510^{-3}	$162 \cdot 10^6$	1	Smoot (1997)
8	1.9210^{-3}	$147 \cdot 10^6$	1	Smoot (1997)

TAR is appoximated as C_nH_m, with a ratio C/H=1.1 and is oxidated via the following first order reaction while the formation of soot was neglected:

$$C_nH_m + m/2O_2 \rightarrow mCO + n/2H_2 \quad (2)$$

The light gases released during primary pyrolysis react according to the simplified mechanism of Jones and Lindstedt [8], whose constants are given in table 1.
Once the volatile species are issued during primary pyrolysis, the remaining char in the coal particles reacts with the surrounding gas. The mechanism adopted in this case is the following:

$C_{(s)}+1/2O_2 \rightarrow CO$ (7)
$C_{(s)}+CO_2 \rightarrow 2CO$ (8)
$C_{(s)}+H_2O \rightarrow CO+H_2$ (9)

Reaction (7) is important for combustion in air, while reaction (8) becomes important in the case of oxy-combustion, due to the high partial pressures of CO_2. Reaction (9) is relevant only under conditions typical of gasification. The rate of surface reactions is determined by the intrinsic kinetics of reactions (7) - (9) (whose constants are reported in Table 1) and the rate of gaseous species reagents diffusion within the particle [9-12].
Simulations were run in parallel on about 64 cores of the high-parallel ENEA-CRESCO cluster section 2, for a week.
In figure 2 particle trajectories are shown. The swirl ensures that the particles have, at least in the first part of their path, a helical motion within the combustion chamber and determines an increase in residence time and mixing. This, together with the fact that particles are relatively small (60 micrometers on average), makes the devolatilization process begin and run out very close to the burner. The same thing applies to char combustion.
The results were compared with experimental data measured through some of the ports located along the combustion chamber.
Species concentrations show a qualitative agreement, while temperature matches very well experimental data (figure 4).

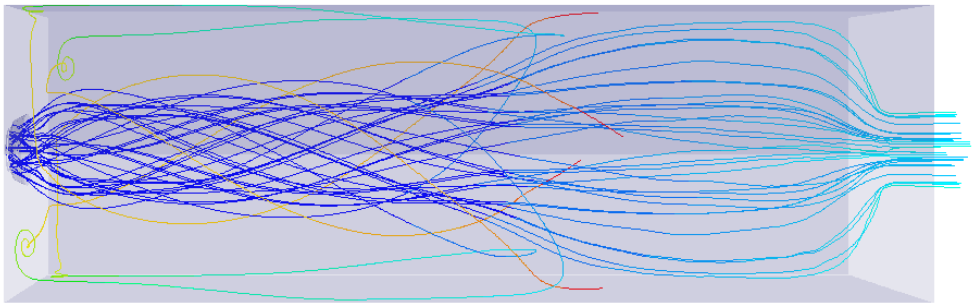

Figure 2. Particles trajectories colored by residence time (s).

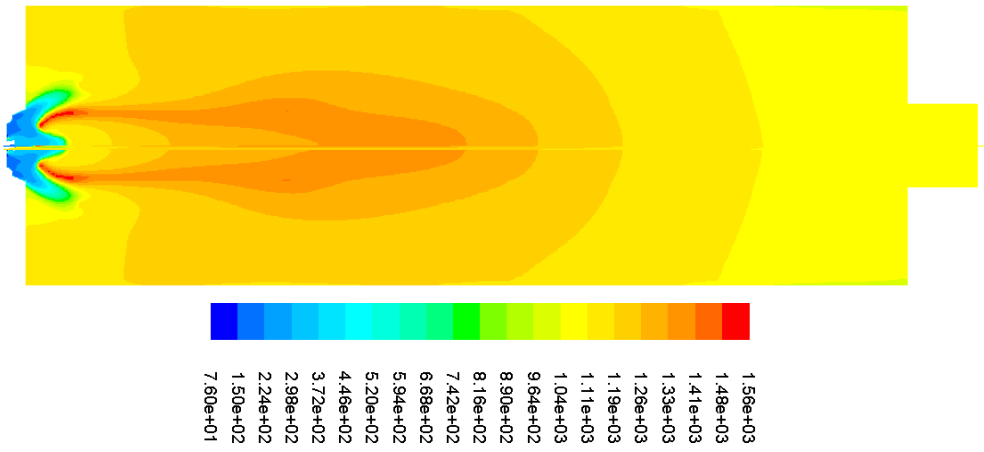

Figure 3. Temperature (°C).

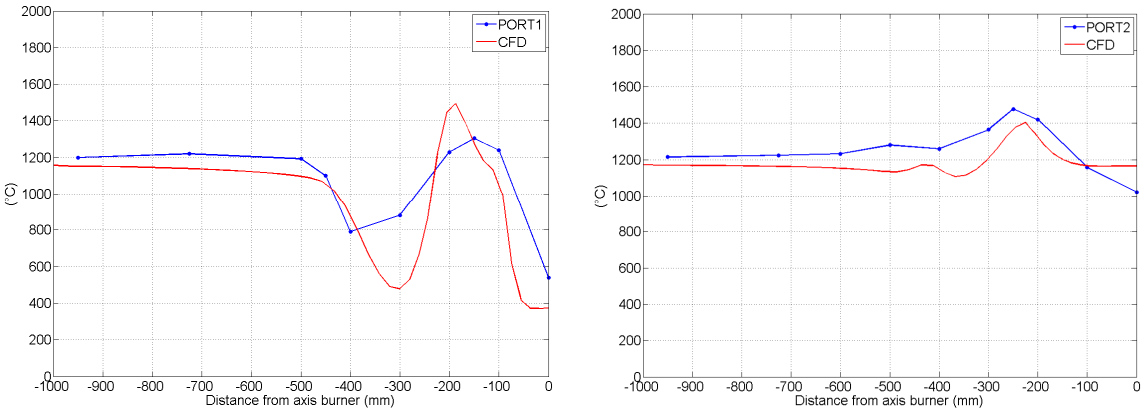

Figure 4. Temperature radial profiles.

References

[1]Coraggio G., Laiola M. "*Combustion of NG and pulverized coal in a mixture of oxygen and RFG"*. IFRF Doc NoF110/y/01 (2009).

[2]Launder B., Sharma B. "*Application of the energy-dissipation model of turbulence to the calculation of flow near a spinning disc*". Letters in Heat and Mass Transfer, 1:131–137 (1974).

[3]B. Magnussen. Modeling of NO x and soot formation by the Eddy Dissipation Concept. Int. Flame Research Foundation, Jan 1989.

[4]Cheng P. "*Two-dimensional radiating gas flow by a moment method"*. AIAA Journal, 2(9):1662–1664 (1964).

[5]Grant D., Pugmire R., Fletcher T., Kerstein A. "*Chemical model of coal devolatilization using percolation lattice statistics"*. Energy & Fuels, 3(2):175–186 (1989).

[6]Fletcher T. H., Kerstein A. R., Pugmire R. J., Grant D. M. "*Chemical percolation model for devolatilization. 2. Temperature and heating rate effects on product yields"*. Energy & Fuels, 4(1):54–60 (1990).

[7]Fletcher T. H., Kerstein A. R., Pugmire R. J., Solum M. S., Grant D. M. "*Chemical percolation model for devolatilization. 3. Direct use of carbon-13 NMR data to predict effects of coal type"*. Energy & Fuels , 6(4):414–43 (1992).

[8]Jones W. P., Lindstedt R. P. "*Global reaction schemes for hydrocarbon combustion"*. Combustion and Flame, 73(3):233–250 (1988).

[9]Smith I. W. "*The combustion rates of coal chars: A review"*. Symposium (International) on Combustion, 19(1):1045–1065 (1982).

[10]Baum M., Street P. "*Predicting the Combustion Behavior of Coal Particles"*. Combustion Science and Technology, 3(5):231–243 (1971).

[11]Smoot L. "*A decade of combustion research"*. Progress in Energy and Combustion Science (1997).

[12]Field M. "*Rate of combustion of size-graded fractions of char from a low-rank coal between1200K and 1200K"*. Combustion and Flame, 13(3):237–252 (1969).

TEMPERATURE EFFECT ON THE ELECTRONIC PROPERTIES OF SMALL CADMIUM SULFIDE NANOCLUSTER

E Burresi[1,*] **M Celino**[2]
[1]ENEA, Faenza Research Laboratories, Technical Unit for Faenza Material Technologies (UTTMATF) via Ravegnana, 186, Faenza, 48018, Italy;
[2]ENEA, C. R. Casaccia, via Anguillarese 301, 00123 Rome, Italy

*Corresponding Author: E-mail: emiliano.burresi@enea.it.
Tel: 0039-0546678546. Fax: 0039-0546678575

Keywords: Ab-initio molecular dynamics, nanomaterials, cadmium sulfide, quantum dots

Abstract
In this work the total and partial density of states were calculated for small single wurtzite CdS nanoparticle, quantum dots, with diameter below 2 nm, by performing DFT pseudopotentials calculations with generalized gradient approximation. The cluster was previously heated at different temperatures ranging from 100 to 600 K, by means of Car-Parrinello ab-initio molecular dynamics, finding a stable phase after 340 K. The density of states was obtained for the structures heated at 100K, 280K, 330K, 340K, 480K and 570K and substantial modifications were found after 340K, where the superficial effects cause some alterations of the intermediate electronic states around the band gap. This effect is meaningful for small particles, where the fraction of the surface atoms is larger than the fraction of the core atoms.

1) Introduction

In our previous work we focused on the behavior of the structure of small CdS nanocluster with size around 13 Å under the effect of the temperature, in the range from 100K to 600K [1]. In that context, we reported formation energy and an accurate analysis of the atomic structures after each simulation by means of distance distributions and coordination numbers. We observed that the initial hexagonal crystallographic structure bends towards an increase of bulk layer from 340 K, which involves surface structural modifications; the new structure is an equilibrated and more stable configuration at temperature T = 340K than the starting ideal atomic configuration.
The purpose of this work is to determine the density of states (total and partial DOS) for CdS quantum dots previously heated at different temperatures, in order to understand its influence on the electronic states of these nanostructures. The electronic DOS is correlated to the structural and surface modifications and the partial density of states is determined to establish the contribution of each atom.

2) Computational details

We used the generalized gradient approximation (GGA) in the DFT framework and pseudopotential approach, as implemented in the Quantum Espresso suite [2]. A plane wave cutoff energy of 30 Ry was used, and a box size of 16 Å. The ions positions have been taken from previous calculations, for different temperatures; in particular for geometry at 100K, 280K, 330K, 340K, 480K and 570K. The 100K, 280K, 330K, 340K, 480K and 570K clusters were labeled: CdS100, CdS280, CdS330, CdS340, CdS480 and CdS570, respectively. In order to perform Self Consistent Field plane-wave calculations, just gamma point was used. Martins-Trouiller type pseudopotentials for S and Cd were employed. All the simulation was performed by using 32 processors on the CRESCO infrastructure.

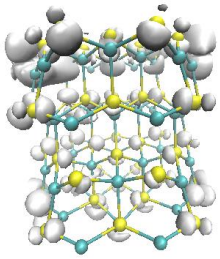

Figure 1: Views of CdS wurtzite cluster. In yellow sulphur atoms and blue cadmium atoms.

3) Results and Discussions

Figure 1 shows the CdS wurtzite structure cluster built with 96 atoms (Cluster96). The total DOS has been calculated for CdS cluster for CdS100, CdS280, CdS330, CdS340, CdS480 and CdS570 sample and for the first three structures the total DOS are reported in Figure 2.

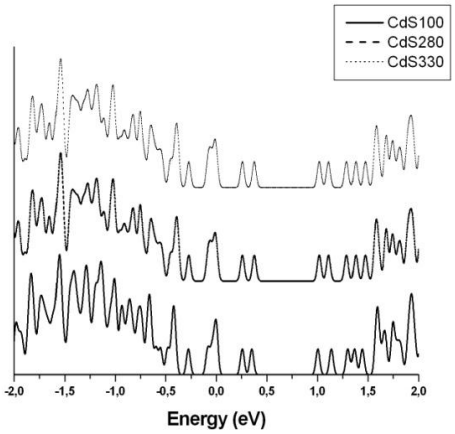

Figure 2 Total density of states for CdS100, CdS280 and CdS330.

These types of systems have large applications like luminescent material. For this reason, we are interested in modifications of the electronic structure near the band gap. Figure 2 shows a clear band gap of size around 1eV with presence of surface states around 0.3eV, probably due to the large fraction of surface atoms. In fact for small cluster, in our case with size below 2 nm, the surface atoms prevail with respect to core atoms and either electronic structure and stability are mainly influenced by surface effects. In addition from a qualitative point of view, for energy below -0.5eV and also for energy higher than 1.5eV the density of states is structured in bands, indicating an ordered atomic structure.

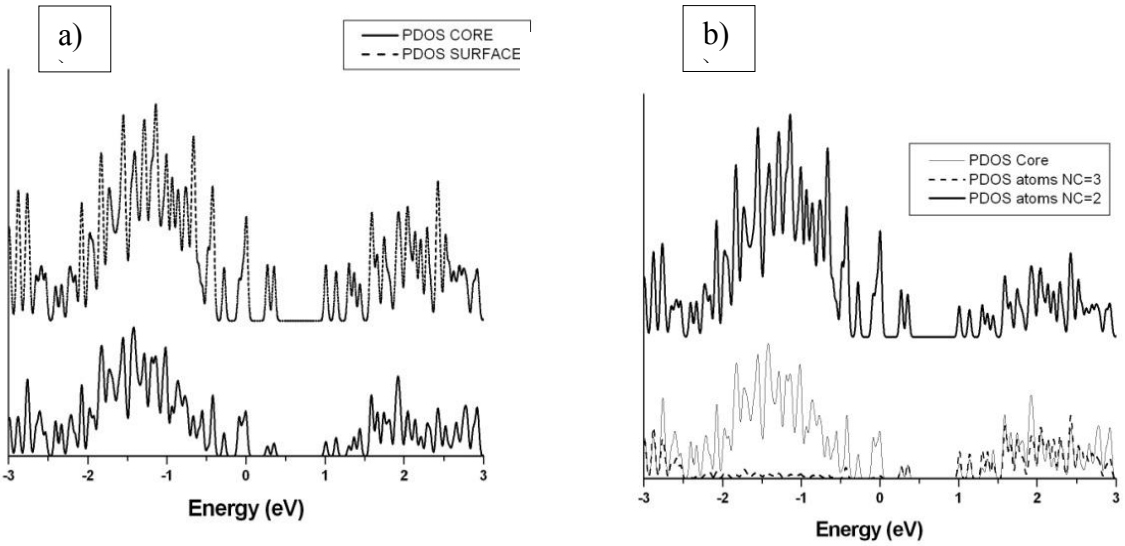

Figure 3: Partial density of states (PDOS) for CdS100; in figure 3a the contributions to the electronic states of the core atoms (solid line) and surface atoms (dashed line) have been reported. In figure 3b that of the surface contribution has been decomposed in two: dashed line for atoms with coordination NC = 3 and solid black line for atoms with coordination NC = 2.

Figure 3a reports the contribution of all the core atoms and surface atoms, summing over all orbitals (s and p-orbitals) and all atoms, core and surface. We can see that near the band gap the surface states give a bigger contribution to the electronic states, more than core atoms, also for intermediate states around 0.3eV. In Figure 3b the surface state contribution has been split in two other sub-contributions, for atoms with NC = 3 and for atoms with NC = 2. From the figure it seems that the electronic states in this energy range suffer bigger influence by the outer atoms with low number coordination.
Above 340K a modification of the cluster structure involves the surface, and diffusion of these atoms was detected. Due to the large number of atoms localized on the surface, the cluster suffers strong modifications at the temperature T = 340K. The total density of states of CdS340, CdS480 and CdS570 has been reported in Figure 4.

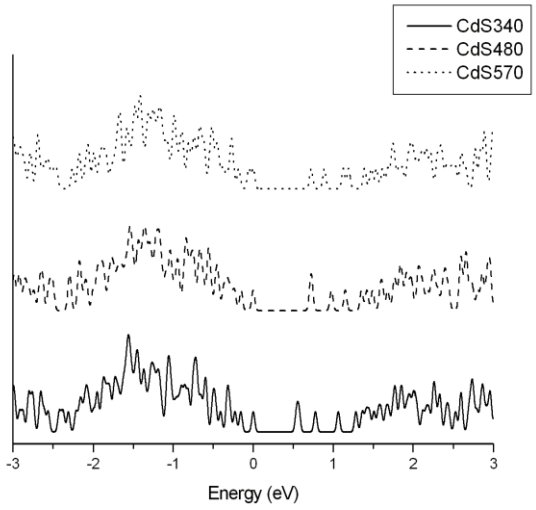

Figure 4: Total density of states for CdS340, CdS480 and CdS570.

Regarding the formation energy, these two surface modifications make the cluster more stable (in particular at 340K) with a substantial energy gain. A first data interpretation is that the atomic diffusion on the surface removes the electronic intermediate states at 0.3eV obtaining higher structural stability, probably corresponding to a better optics efficiency; in practice some surface defects of the nanoparticle are removed. In addition to this favourable effect, the increase of the temperature produces new defects corresponding to the novel electronic surface states after 0.5eV.
Finally, the temperature at 480K induces again a novel reconstruction of the surface and in particular the mean coordination number of surface atoms increases but in this case the shifts of the peaks have a low intensity.

4) Acknowledgments

We acknowledge the ENEA-HPC team for supporting our computational activities in the ENEA-GRID infrastructure and on the CRESCO high performance platform.

References

[1] E.Burresi, M. Celino, Solid State Science 14, 567 **(2012)**
[2] P. Giannozzi, S. Baroni, N. Bonini, M. Calandra, R. Car, C. Cavazzoni, D. Ceresoli, G. L. Chiarotti, M. Cococcioni, I. Dabo, A. Dal Corso, S. Fabris, G. Fratesi, S. de Gironcoli, R. Gebauer, U. Gerstmann, C. Gougoussis, A. Kokalj, M. Lazzeri, L. Martin-Samos, N. Marzari, F. Mauri, R. Mazzarello, S. Paolini, A. Pasquarello, L. Paulatto, C. Sbraccia, S. Scandolo, G. Sclauzero, A. P. Seitsonen, A. Smogunov, P.Umari, R. M. Wentzcovitch, J. Phys.: Condens. Matter 21, 395502 **(2009)**, http://arxiv.org/abs/0906.2569.

High-resolution regional climate modeling for impact studies in Africa

Sandro Calmanti, Emanuele Lombardi, Giovanna Pisacane, Maria Vittoria Struglia

ENEA UTMEA-CLIM, Casaccia

Corresponding author: sandro.calmanti@enea.it

Introduction

A global temperature increase of 2°C above the pre-industrial level is considered to be at a threshold between *dangerous* and *extremely dangerous* for its implied impacts on ecosystems and society [1]. The EU FP7 project IMPACT2C aims to identify and quantify the impacts and most appropriate response strategies of a 2°C global warming for Europe and three selected vulnerable regions in other parts of the world. The unit UTMEA-CLIM, ENEA Casaccia, contributes to the project with several activities including the coordination of a working group focussing on the impact of climate change in the Niger and Nile basin in Africa, and the production of dedicated high-resolution climate scenarios to be used for impact studies.

In the past, the African continent has been the target of less systematic and comprehensive studies on climate variability and change compared to other regions. To address this lack of climate information an initiative of the World Climate Research Programme (WCRP) aiming at COordinating Regional Downscaling EXperiments (the CORDEX framework) - has therefore selected Africa as the a priority target area for producing high resolution climate change scenarios [2].

The climate modeling activities conducted at ENEA within IMPACT2C have been therefore planned by following the CORDEX guidelines[1] in order to contribute to investigate the hyper-matrix of uncertainties in climate projections [3]. We have produced a climate scenario simulation for the African continent by using the regional climate model RegCM4 [4], which is an update to the modeling system already adopted by UTMEA-CLIM to develop the coupled ocean-atmosphere climate model for the Mediterranean region (the PROTHEUS system) [5] and to conduct climate studies over the Euro-Mediterranean area [6][7].

Tests and performances

RegCM4 is an open source software developed and maintained by the Earth System Physics Department of ICTP[2]. It integrates the 3-dimensional, hydrostatic, primitive equations for the atmosphere using a rectangular grid with uniform horizontal resolution and sigma-coordinates in the vertical (i.e. the vertical coordinate is the atmospheric pressure normalized with the surface pressure). From the point of view of the code architecture the main improvement in RegCM4 with respect to previous versions is a complete re-writing of the entire code from Fortran77 to Fortran90 and a more efficient strategy for domain decomposition, plus the addition of new modules such as an advanced description of the soil and

1 CORDEX specifications can be found at http://cordex.dmi.dk

2 The repository of the source code for RegCM con be found at http://gforge.ictp.it/gf/project/regcm/

vegetation layer. Overall, RegCM4 counts about $4x10^5$ lines of code, compared to the $4x10^4$ lines of RegCM3.

Previous versions of RegCM adopted a one dimensional domain decomposition whereby the model grid was divided into equal bands spanning the entire model domain in the north-south direction. With this domain decomposition strategy the maximum number of CPUs requested for the production of climate scenarios was typically less than 50. Instead, RegCM4 uses a two-dimensional domain decomposition with the model horizontal grid divided into rectangular subdomains, whose dimension depends on the number of assigned CPUs and whose shape is determined in order to be as close as possible to a square with an equal number of grid-points in both directions.

We started testing the performances of the version 4.3.0 of RegCM on CRESCO as soon as it has been released in the summer of 2012. The configuration adopted for the scalability test follows the Africa-CORDEX specifications: the horizontal grid has 256x256 grid-points and a unform resolution of 50km x 50km; in the vertical, the model uses 18 levels. The boundary conditions for the simulation consist of 6-hourly, three-dimensional data of atmospheric temperature, humidity and wind speed components for all vertical model level, plus the seas surface temperature and surface atmospheric pressure. The model output consists of 6-hourly data of three dimensional dynamic and radiative model variables, plus several two dimensional 3-hourly data of surface fields. Overall the simulation of one model year requires disk space for the input and output files for a total of about 120Gb. The code was compiled using the version 11.0 of INTEL Fortran and Open MPI version 1.2.8. Additional libraries are used for handling large geo-referenced datasets (NetCDF) and data compression (HDF5).

The core computation in RegCM consists of finite difference discretization of the partial differential equations for atmospheric dynamics. Therefore, the computational time depends not only on the number of CPUs over which the computation is distributed but also on the time required for the communication of data between adjacent subdomains and the corresponding CPUs. Furthermore, since all sub-domains must be synchronized at all times during the computation, the performance of the entire system is constrained by the speed of the slowest CPUs in a multi-architecture cluster such as CRESCO. When we started testing the performances of RegCM4 CRESCO was composed of 2048 Intel-Xeon_5345 (Clovertown) cores, 448 Intel-Xeon_5530 (Nehalem) and 224 Intel-Xeon_5620 (Westmere). In general, depending on the specific application, Westmere and Nehalem architectures have better performances than the Clovertown. However, tests have been performed first by submitting jobs to the standard queuing system without requesting the use of any specific resource. Afterwards, a specific case of interest has been considered.

The graph in Figure 1 shows two important issues that need to be addressed for an optimal use of the computational resources. First, given the multi-architecture composition of CRESCO, the overall performances is severely penalized when the queuing system allocates significant fractions of the workload to slower CPUs, specially when the total number of requested CPUs is small. As a consequence, the total elapsed time for a one-year simulation shows a large variability when the number of CPUs is small. Fluctuations in the total elapsed time decrease (as well as the total elapsed time itself) by increasing the number of CPUs, thereby indicating that by employing a sufficiently large number of CPUs the computation time becomes more predictable. A second aspect to be considered is that, with a very large number of CPUs ($N > 512$) the overhead for the parallelization becomes significant and the

total computation time increases. We have estimated the optimal size of the sub-domain to be assigned to each CPU (granularity) to be between 12x12 and 16x16 grid points.

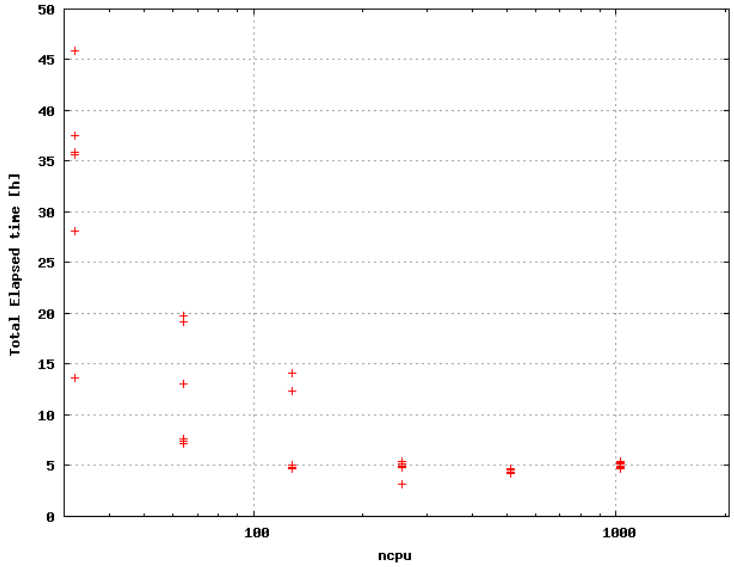

Figure 1. Total estimated elapsed time for one model year simulation as a function of the number of CPUs. We have conducted simulations of one model month and then extrapolated by simple linear scaling the length of the simulation of one model year.

The case of 256 CPUs is of particular interest. In this case, several simulations have been performed with a total elapsed time of about 24 min for a one-month simulation (equivalent to about 4.8 hours for a one-year one). However, one single outlier has been completed in about 15 min (2.4 hours for one year) when the queuing system was able to allocate 256 Nehalem CPUs. Based on these results and on a more detailed analysis of the idle time spent in the queues, we have chosen to enforce the use of the fastest components of CRESCO (allowed by the queuing system by requesting specific resources during the submission of a job) in order to safely complete chunks of 5-year simulation during each 24h cycle, which is the longest total elapsed time allowed by the queuing system in CRESCO. With this model configuration and an optimized use of the requested CPUs (256) we have then completed a 130-years long climate scenario in about 26 days, not including the time required for data transfer and the idle time in the queue.

The climate scenario

The RegCM4 configuration adopted for producing the climate scenario resembles the one adopted in previous studies where key aspects of the parameterization of sub-grid atmospheric physics in the tropics have been tested [8] and the model output has been validated against observations [9]. In particular, although RegCM4 may optionally use an advanced soil and vegetation layer modeling component (the Community Land Model, CLM), we have preferred to continue using the Biopshere-Atmosphere Transfer Scheme (BATS), which has been more thoroughly tested and validated. The model domain adopted for this study follows the indications provided within the CORDEX framework. The model grid is the same as for the tests discussed in the previous section (256x256x18). The model domain is centered at (2°S, 12°W) in order to include the entire African continent and most of the tropical and southern Atlantic Ocean. The boundary conditions for the model are extracted from the

scenario simulation produced with global climate model CNRM-CM5 [10]. In particular, we have used the RCP4.5 scenario, which has an intermediate CO_2 stabilization level at 450ppm. A key requisite for the mandatory simulations agreed between the partners of IMPACT2C was to cover the entire time interval between the reference period (1970-2000) and a window of ±15 years around the occurrence of a 1.5°C global surface temperature increase with respect to the reference, which corresponds to 2°C global warming compared to the pre-industrial level. For the RCP4.5 scenario of CNRM-CM5 adopted as a driver, the 1.5° threshold is reached approximately during the year 2070, thereby implying a minimum time interval 1970-2085 to comply with the IMPACT2C requests. Since the computational effort has been evaluated affordable for CRESCO, we have extended the model simulation to the time frame 1970-2100 which is also meeting the minimum requirements for the Africa-CORDEX uncertainty hyper-matrix.

The main results for the scenario simulation are summarized in Figure 2 by showing the changes in total cumulated rainfall for the main cropping seasons in Africa. Cumulated rainfall impacts directly on the food-security conditions in the continent, which depends to a large extent on local, rain-fed agricultural activities. The first season covers the period from February to mid-July and is a minor crop season in Eastern Africa. During this season, RegCM4 simulates a decrease in cumulated rainfall over the Ethiopian highlands. During the second season (main cropping season in western and eastern sub-Saharan Africa) the cumulated rainfall shows an overall increase although patches of decreasing rainfall occur in the area of the Greater Horn of Africa. The third season (September to March) is a crop season for the tropical eastern Africa, and no significant changes in the cumulated rainfall can be detected in this case. Finally, during the crop season in southern Africa (October to May) spots of limited decrease in cumulated rainfall are projected in Mozambique and in the southern Zambia whereas increasing rainfall is produced over northern Zambia and Malawi.

Figure 2. Total cumulated rainfall difference between the periods 2055-2085 and 1970-2000 for the main cropping season in Africa. From left to right: February-July, April-October, September-March, October-May.

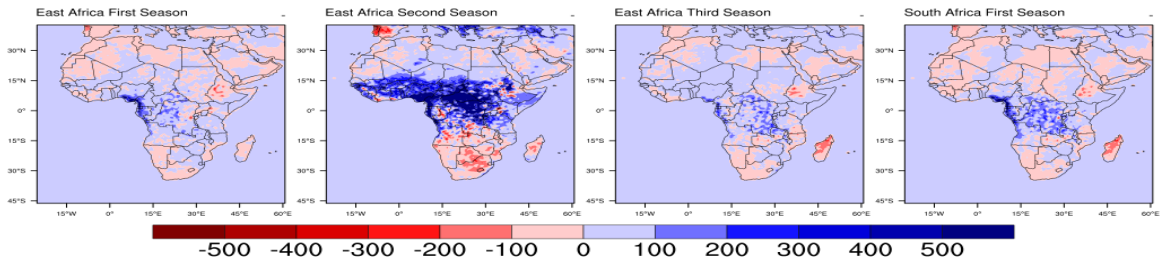

Conclusions

We have tested the performances of a state-of-the-art regional climate model, using massive parallelism to distribute the computation over small adjacent portions of the full model grid. The scalability of the code has been tested in order to optimize the use of available resources. With the access to CRESCO, the laboratory UTMEA-CLIM, ENEA Casaccia, has contributed to the mandatory simulations for the EU FP7 project IMPACT2C. The daily data of rainfall, temperature and other environmental parameters produced with this simulation will be used, to drive impact models focusing on food production and hydrology, to help design strategies for adaptation to climate change. Furthermore a climate scenario simulation has been produced which meets the requirements for contributing to the climate projection uncertainty hyper-matrix which is being explored within the CORDEX framework.

Acknowledgments

We wish to thank Guido Guarnieri (ENEA, Portici), Laura Mariotti and Graziano Giuliani (ICTP, Trieste) for technical assistance during the model setup and configuration. Tinebeb Yohannes Gelassie has helped for the analysis of the climate scenario.

References:

[1] ANDERSON K., BOWS A. *Beyond 'dangerous' climate change: emission scenarios for a new world.* Philosophical Transactions of the Royal Society A: Mathematical, Physical and Engineering Sciences, **369**, (2011), pp. 20-44.

[2] GIORGI F., JONES C., ASRAR G. R. *Addressing climate information needs at the regional level: the CORDEX framework*. World Meteorological Organization (WMO) Bulletin (2009), **58**, pp. 175.

[3] GIORGI F., et al. "*The regional climate change hyper-matrix framework*". Eos, Transactions American Geophysical Union, (2008), 89(45), 445-446.

[4] GIORGI F., et al. "*RegCM4: model description and preliminary tests over multiple CORDEX domains.*" Climate Research, (2012) **2**, 7.

[5] ARTALE V., et al. "*An atmosphere–ocean regional climate model for the Mediterranean area: assessment of a present climate simulation.*" Climate dynamics, **35**, (2010), pp. 721-740.

[6] DELL'AQUILA, et al. "*Effects of seasonal cycle fluctuations in an A1B scenario over the Euro-Mediterranean region.*" Climate Research, **2** (2012).

[7] CARILLO A., et al. "*Steric sea level rise over the Mediterranean Sea: present climate and scenario simulations.*" Climate Dynamics, **39**, (2012), pp. 2167-2184.

[8] SYLLA, M. B., et al. "*The impact of deep convection on the West African summer monsoon climate: a regional climate model sensitivity study.*" Quarterly Journal of the Royal Meteorological Society **137** (2011): pp. 1417-1430.

[9] SYLLA M. B., et al. "*Multiyear simulation of the African climate using a regional climate model (RegCM3) with the high resolution ERA-interim reanalysis.*" Climate Dynamics **35** (2010) pp. 231-247.

[10] VOLODOIRE A., et al. "*The CNRM-CM5. 1 global climate model: description and basic evaluation.*" Climate Dynamics (2012) pp. 1-31.

Simulation of chemical reactions catalyzed by transition metals complexes - I.

Laura Falivene, Luigi Cavallo*
Dipartimento di Chimica e Biologia, Università degli Studi di Salerno.
* e-mail: lcavallo@unisa.it.

1. Static DFT study of the mechanism of the Alkyne−Azide Cycloaddition catalyzed by Ruthenium Complexes

Within a collaboration with Prof. Nolan (St. Andrews University) on the azide−alkyne cycloaddition, DFT calculations have been performed to clarify the mechanism of the reaction.[1] Experimental results obtained by Nolan and co-workers showed that 16-electron ruthenium complexes with the general formula Cp*Ru(L)X [2] (in which L = phosphine or N-heterocyclic carbene ligand; X = Cl or OCH_2CF_3) are active in the azide−alkyne cycloaddition reactions leading to 1,2,3-triazole products.
Different ligands, L, and different groups, X, have been tested. These preliminary studies have showed that among the different ligands, the phosphines result in more efficient catalysts over the corresponding NHC complexes, and among the different X groups, Cl, was found to be the best one. As consequence, the 16-electron Cp*Ru($PiPr_3$)Cl complex has been classified as the optimal one and it was used for all the experimentals within this study.
As second step different alkynes have been tested: alkynes with electron-donating groups on the carbon at the α position to the triple bond of the alkyne substrate promote the highest reactivity. As a matter of fact, these properly substituted alkynes were found to be extremely active in the reaction with benzyl- and phenylazide, producing a number of new 1,5-disubstitued 1,2,3-triazoles with high yields under milder conditions and with shorter reaction times.
A DFT mechanistic study, which has been possible due to the CRESCO computational power, has been done to highlight the hole pathway, with the different steps and intermediates.
Computational studies have been focused on the reaction of complex Cp*Ru($PiPr_3$)Cl with phenylacetylene and benzylazide.
DFT results have shown that acetylene binding precedes azide coordination. Catalyst initiation was proposed to occur through the formation of Cp*Ru(η_2-HCCPh)($PiPr_3$)Cl followed by phosphine loss. The following coordination of a molecule of N_3Bn to Cp*Ru(η_2-HCCPh)Cl through the internal nitrogen is favored over coordination of a second molecule of HCCPh by 7.7 kcal/mol.
Figure 1 shows calculated free energies of the species involved in the triazole formation once both azide and acetylene substrates have been coordinated to the Ru metal center.

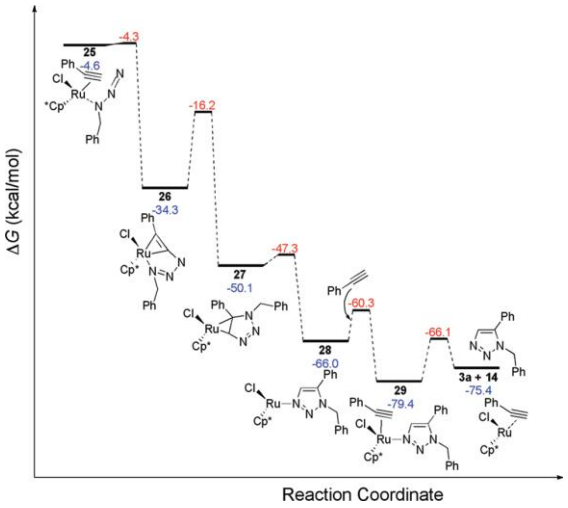

Figure 1. Free energies (kcal/mol) of triazole formation beginning from complex with both azide and acetylene substrates coordinated to the Ru metal center. All free energies in kcal/mol are relative to Cp*RuCl(PiPr3) + HCCPh + N3CH2Ph = 0.0 kcal/mol. Values in red above the arrows correspond to the energy of the transition states connecting the structures left and right of the arrow.

DFT calculations also resulted in locating the previously unidentified intermediate 27,
in which the formed triazole is bound to the Ru metal center in a C−Ru−C metallacyclopropane fashion, which ultimately isomerizes to the N-bound triazole Ru.

2. Static DFT study of the possible transformation of an olefin Metathesis Catalyst.

One of the most important challenges is to increase the stability of the catalysts under the reaction conditions without loss of activity.
Within an FP7 project (Eumet project, grant agreement n° CP-FP 211468-2) on the ruthenium-catalyzed olefin metathesis, we have tried to understand the decomposition routes of catalysts as extremely important tool for a more efficient catalyst design.
Although most ruthenium-based olefin metathesis catalysts, in the solid state, are stable to oxygen and moisture, they usually readily undergo decomposition in solution.
The well-defined and easily accessed [$RuCl_2(PPh_3)_2$(3-phenylindenylidene)] (M10) complex is not efficient in olefin metathesis itself because it often exhibits rapid decomposition.
An analysis of the progress of this decomposition in alcohol solution has been done.[3] The $^{31}P\{^1H\}$ NMR spectroscopy has revealed the appearance of two doublets at δ=42.3 and 48.7 ppm with a coupling of J_{PP}=46.1 Hz, all of which support the formation of a new complex bearing two spectroscopically non-equivalent phosphorus centers.
X-ray analysis has confirmed an unusual and unexpected transformation in which the complex is involved in alcohol oxidation and subsequent formation of a new ruthenium complex, wherein the indenylidene moiety rearranges into a h_5-coordinated indenyl in [$RuCl(PPh_3)(h_5$-3-phenylindenyl)].
To the best of our knowledge, this represents the first example of an indenylidene to indenyl rearrangement.
DFT calculations, done with CRESCO machines, permitted assembling all the experimental informations into the energy profile shown in Figure 1.

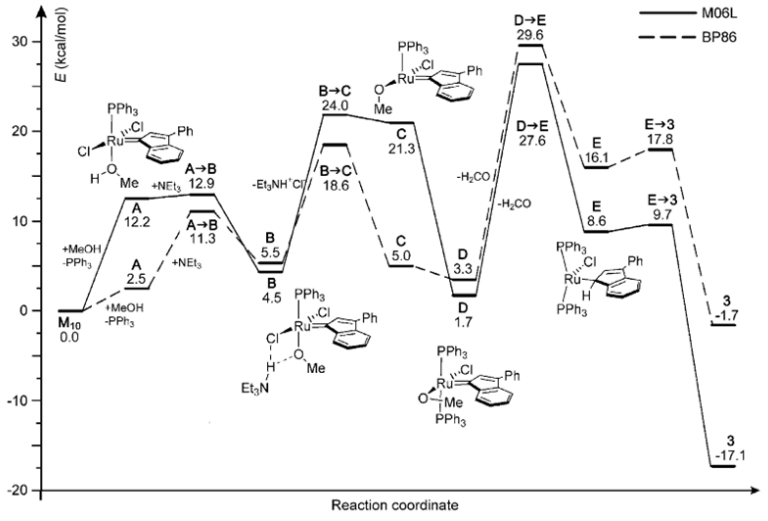

Figura 1 DFT Energy profile for the transformation of M_{10} into 3.

To facilitate the computational effort, MeOH was used as the model alcohol. The discussed energies have been calculated with the M06 L functional.
The first step corresponds to substitution of one PPh_3 ligand of the starting material by a MeOH molecule, a process that is endothermic by 12.2 kcal/mol. The next step corresponds to proton transfer from the coordinated MeOH to a NEt_3 molecule. This transfer requires overcoming the transition state A-B at 12.9 kcal/mol above the starting material, and collapsing into intermediate B,

which is 4.5 kcal/mol above the starting material. The formally anionic intermediate B is characterized by a methoxy ligand that is trans to the phosphine ligand, with the formally cationic NEt_3H^+ molecule hydrogen bonded to both the MeO and the nearby Cl ligand (H···O and H···Cl distances of 2.62 and 2.00 A, respectively). The Ru_Cl bond involved in the hydrogen bond is 0.1 A longer than the other Ru_Cl bond.

Dissociation of NEt_3H+Cl from the ruthenium center occurs through transition-state B-C, which sits 24.0 kcal/mol above the starting material. During this step the MeO ligand moves to the coordination position vacated by the leaving Cl ligand, and the ruthenium complex collapses into intermediate C, which presents a vacant coordination position trans to the phosphine ligand. This vacant coordination position can be occupied by the previously dissociated PPh_3 molecule, thus leading to the intermediate D, which sits at 1.7 kcal/mol above the starting material. The energy gain associated with PPh_3 coordination is 19.6 kcal/mol. The final steps of the transformation involve first a hydrogen atom transfer from the Me group of the MeO ligand to the ylidene carbon atom of the indenylidene ligand via the transition-state D-E at 27.6 kcal/mol, thus leading to intermediate E, which has an h_1-coordinated indenyl ligand, and liberates a H_2CO molecule.

The last step of the reaction corresponds to the almost barrierless isomerization of the h_1-coordinated indenyl ligand of E into a h_5-coordination mode, with formation of the classical piano-stool tetracoordinated ruthenium complex.

The overall reaction profile of Figure 1 indicates that the limiting step is the transfer of a hydrogen atom of the MeO ligand to the ylidene carbon atom via the transition-state D-E. This transition state is calculated to lay 27.6 kcal/mol above the starting material, which is in good agreement with the experimental E_a=25.7 kcal/mol, and it is in qualitative agreement with the experimental evidence that NEt_3 does not participate to the rate-determining step. However, the initial proton transfer from MeOH to the Cl ligand, assisted by NEt_3 via transition-state B-C at 24.0 kcal/mol, is not much lower in energy. The direct transfer from A to C, in the absence of a nearby NEt_3 molecule, is calculated to cost 39.9 kcal/mol, which clearly indicates the role of NEt_3 in promoting the transformation.

In an optimized protocol, 3 can be obtained quantitatively (92%yield of isolated compound) by refluxing M10 in ethanol for 2 hours in the presence of a stoichiometric amount of triethylamine.

The new complex obtained, formally a decomposition product from an olefin metathesis catalyst, displays exceptional activity in numerous catalytic transformations: alcohol racemization,[4] rearrangement of propargylic alcohols,[5] cyclization,[6] and polymerization, to name a few. We have identified here an opportunity to make use of a decomposition product as an active catalyst in other kinds of transformation.

References

[1] M. LAMBERTI, G. C. FORTMAN, A. POATER, J. BROGGI, A. M. Z. SLAWIN, L. CAVALLO, S. P. NOLAN**, "**Coordinatively Unsaturated Ruthenium Complexes As Efficient Alkyne–Azide Cycloaddition Catalysts", *Organometallics***, 2012,** 31, 756−767

[2] (a) HUANG, J.; SCHANZ, H.-J.; STEVENS, E. D.; NOLAN, S. P. "Stereoelectronic Effects Characterizing Nucleophilic Carbene Ligands Bound to the Cp*RuCl (Cp* = η^5-C_5Me_5) Moiety: A Structural and Thermochemical Investigation", *Organometallics* **1999**, 18, 2370−2375. (b) JOHNSON, T. J.; FOLTING, K.; STREIB, W. E.; MARTIN, J. D.; HUFFMAN, J. C.; JACKSON, S. A.; EISENSTEIN, O.; CAULTON, K. G. ".pi.-Stabilized, yet Reactive, Half-Sandwich Cp*Ru(PR3)X Compounds: Synthesis, Structure, and Bonding" *Inorg. Chem.* **1995**, 34, 488−499.

[3] S. MANZINI, C. A. URBINA-BLANCO, A. POATER, A. M. Z. SLAWIN, L. CAVALLO, S. P. NOLAN, "From Olefin Metathesis Catalyst to Alcohol Racemization Catalyst in One Step" *Angew. Chem. Int. Ed*. **2012**, 51, 1042 –1045

[4] a) D. LEE, E. A. HUH, M.-J. KIM, H. M. JUNG, J. H. KOH, J. PARK, "Dynamic Kinetic Resolution of Allylic Alcohols Mediated by Ruthenium- and Lipase-Based Catalysts"**,** *Org. Lett*. **2000**, 2, 2377 – 2379; b) J. H. KOH, H. M. JUNG, M.-J. KIM, J. PARK, "Enzymatic resolution of secondary alcohols coupled with ruthenium-catalyzed racemization without hydrogen mediator", *Tetrahedron Lett.* **1999**, 40, 6281 – 6284

[5] a) B. M. TROST, J. XIE, N. MAULIDE**, "**Stereoselective, Dual-Mode Ruthenium-Catalyzed Ring Expansion of Alkynylcyclopropanols" *J. Am. Chem. Soc.* **2008**, 130, 17258 – 17259; b) B. M. TROST, N. MAULIDE, R. C. LIVINGSTON, "A Ruthenium-Catalyzed, Atom-Economical Synthesis of Nitrogen Heterocycles", *J.Am. Chem. Soc.* **2008**, 130, 16502 – 16503; c) B. M. TROST, R. C. LIVINGSTON, *"*Two-metal catalyst system for redox isomerization of propargyl alcohols to enals and enones.**"***J. Am. Chem. Soc.*
1995, 117, 9586 – 9587

[6] a) Y. YAMAMOTO, H. KITAHARA, R. OGAWA, H. KAWAGUCHI, K. TATSUMI, K. ITOH, **"**Ru(II)-Catalyzed Cycloadditions of 1,6-Heptadiynes with Alkenes: New Synthetic Potential of Ruthenacyclopentatrienes as Biscarbenoids in Tandem Cyclopropanation of Bicycloalkenes and Heteroatom-Assisted Cyclocotrimerization of 1,6-Heptadiynes with Heterocyclic Alkenes", J. *Am. Chem. Soc.* **2000**, 122, 4310 – 4319; b) Y. YAMAMOTO, T. ARAKAWA, R. OGAWA, K. ITOH, "Ruthenium(II)-Catalyzed Selective Intramolecular [2 + 2 + 2] Alkyne Cyclotrimerizations"**,** *J. Am. Chem. Soc.* **2003**, 125, 12143 – 12160

Simulation of chemical reactions catalyzed by transition metals complexes - II.

Albert Poater, Luigi Cavallo*
Dipartimento di Chimica, Università degli Studi di Salerno.
*e-mail: lcavallo@unisa.it.

3. Deactivation of Ru-benzylidene Grubbs catalysts active in olefin metathesis

In this work, bearing in mind the effect of carbon monoxide (CO) on olefin metathesis Grubbs catalysts, we explore the reactivity induced by coordination of a CO molecule trans to the Ru-benzylidene bond of a prototype Ru-olefin metathesis catalyst bearing a N-heterocyclic carbene (NHC) ligand. DFT calculations, carried out with CRESCO computing facilities, indicate that CO binding to the Ru center promotes a cascade of reactions with very low-energy barriers that lead to the final crystallographically characterized product (see Figure 1), in which the original benzylidene group has attacked the proximal aromatic ring of the ligand leading to a cycloheptatriene ring through a Buchner ring expansion.

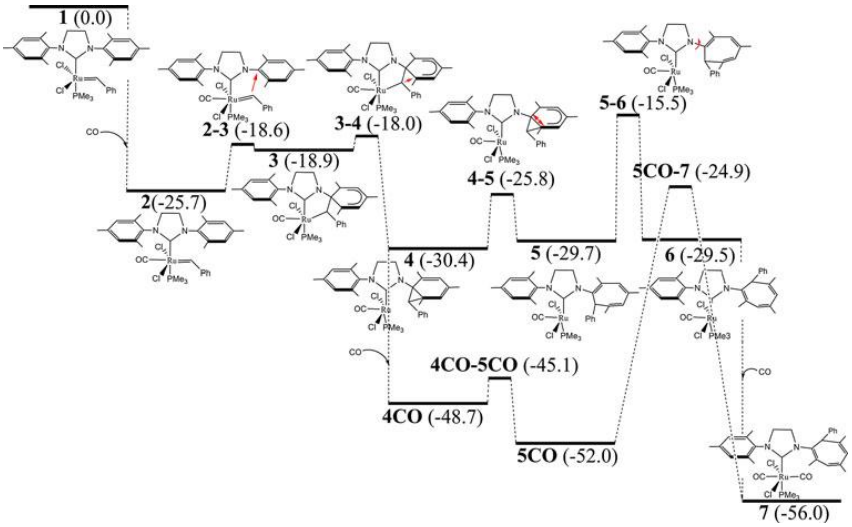

Figure 1. Energy diagram of the complete **1**–**7** deactivation pathway. In parentheses is the energy of the various species, in kcal/mol, relative to the (pre)catalyst **1**.

In this contribution, we evaluated the complete energy profile corresponding to the deactivation, promoted by coordination of a CO molecule, of a NHC-Ru catalyst for olefins metathesis presenting a Ru-benzylidene bond. Consistent with our previous work on the deactivation of a similar NHC-Ru precatalyst presenting a Ru-methylidene bond, after CO coordination trans to the Ru-ylidene bond, the overall decomposition energy profile is characterized by very low-energy barriers. These results indicate that the nature of the Ru-ylidene bond has a minor impact on the energetics of this deactivation pathway. The main difference between the two decomposition mechanisms is that in case of the Ru-benzylidene system, an additional step, corresponding to rotation around the N-cycloheptatriene bond is needed in order to orientate the Ph substituent on the cycloheptatriene ring away from the metal atom.

In conclusion, the overall mechanism is best described as a carbene insertion into a C–C bond of the aromatic N-substituent of the NHC ligand, forming a cyclopropane ring. This cyclopropanation step is followed by a Buchner ring expansion reaction, leading to the experimentally observed product presenting a cycloheptatriene ring.

References

[1] A POATER, L. CAVALLO**, "**Carbon Monoxide-Promoted Carbene Insertion into the Aryl Substituent of an N-Heterocyclic Carbene Ligand: Buchner Reaction in a Ruthenium Carbene Complex", *Theor. Chem. Acc.* **2012**, 131, 1155-1160. B. R. GALAN, M. GEMBICKY, P. M. DOMINIAK, J. B. KEISTER, S. T. DIVER, J. Am. Chem. Soc., **2005**, 127, 15702-15703.
[2] A POATER, F. RAGONE, A. CORREA, L. CAVALLO, "Exploring the Reactivity of Ru-Based Metathesis Catalysts with a π-Acid Ligand Trans to the Ru-Ylidene Bond", *J. Am. Chem. Soc.*, **2009**, 131, 9000-9006.
[3] A POATER, L. CAVALLO**, "**Deactivation of Ru-benzylidene Grubbs catalysts active in olefin metathesis", *Theor. Chem. Acc.* **2012**, 131, 1155-1160.

A Hybrid Particle-Field Coarse-Grained Molecular Model for Pluronics Water Mixtures

Antonio De Nicola, Giuseppe Milano*
Dipartimento di Chimica e Biologia, Università degli Studi di Salerno
*e-mail: gmilano@unisa.it

Introduction

The triblock-copolymers of poly(ethylene oxide)$_m$-poly(propylene oxide)$_n$-poly(ethylene oxide)$_m$ (PEO$_m$-PPO$_n$-PEO$_m$), are an important family of amphiphilic polymers. They are commercially known and available as Pluronic®. The hydrophilic-lipophilic character of these block-copolymers can be tuned varying the blocks length and the molecular weight of both, PEO and PPO blocks. Such adaptability allowed to employ such copolymers in many fields, like foaming, detergency, dispersion stabilization, emulsification, lubrication, cosmetic formulation[1], modification of surface for biocompatibility[2] for medical applications [3]. Extensive experimental studies of Pluronic phase behavior in water has been reported by Alexandridis[4-7] and Zhou[8].

Atomistic simulations, due to their computational costs, usually are confined to systems on time and length scales of μs and few nm. To study the phase behavior of such systems we need to reach time and length scales on the order of magnitude of μs and nm. We present a computational study of the phase behavior of binary Pluronic-water mixtures (L62 and L64), based on the hybrid particle-field (PF) molecular dynamics method. [9,10]

Recently PF models of phospholipids[11,12] have been reported to study the phase behavior of phospholipid/water mixture. Such models have shown the possibility to reach large time and length scales. In figure 1 the mapping scheme used for the Pluronic model is reported.

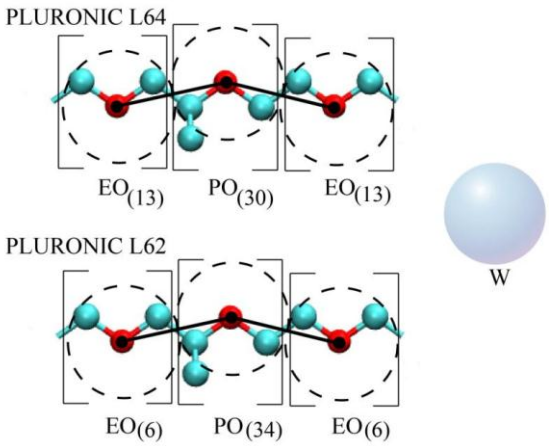

Figure 1. Mapping scheme used for the Pluronic model. Each EO bead corresponds to 3 heavy atoms. For PO, each bead correspond to 4 heavy atoms. The effective beads are centered on oxygen atoms (depicted in red) for both, EO and PO types. The bead type W corresponds to 4 real water molecules.

Results and Discussion

At low polymer concentrarion, in a water solution, a number of Pluronic self-assemblies in a micellar phase. The micelle is formed by a hydrophobic core, mainly composed by PPO blocks, and by a hydrophilic corona, formed by hydrated PEO blocks. Increasing the polymer wt% content the Pluronic chains self-assembly in different phases, passing through the lamellar phase to the isotropic solution at high polymer content[4,8,13,14].

We investigate a binary block-copolymer/water system of both, Pluronic L62 and L64, to observe the spontaneous formation of different morphologies as function of concentration and temperature. To

this aim, four different polymer concentrations have been considered (20, 52, 70, 90 wt% of polymer content).

In Figure 2 phase diagrams of Pluronic L62 (a) and L64 (b) are reported, together with snapshots of morphologies at chosen composition and temperature obtained from simulations.

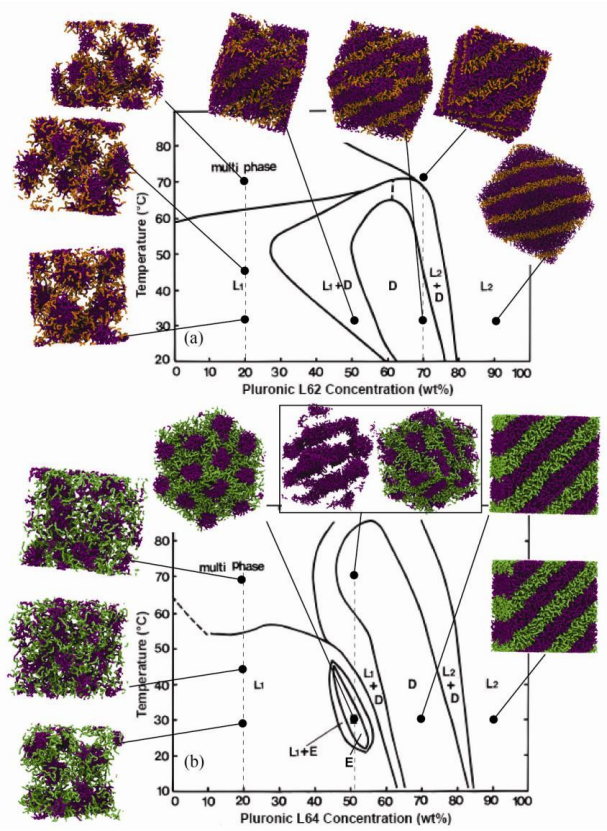

Figure 2. Phase diagrams for Pluronics L62 (a) and L64 (b). For any composition and temperature studied, a snapshot of the obtained morphology has been depicted on the diagram.

Conclusions

A hybrid PF coarse-grained model for Pluronics has been reported for Pluronic L62 and L64. The reproduction of morphologies depending on the concentration and temperature for water mixture solution of polymer has been tested. In particular the micellar and non micellar morphologies reproduced by the model has been found in agreement with the experimental phase diagram. Furthermore, the reproduction of the hexagonal morphology specific for the Pluronic L64 is a proof of the chemical specificity of the model. In fact, in a narrow range of composition, between 46~55 wt%, the hexagonal phase is stable for the Pluronic L64 and, at the same composition, is absent in the Pluronic L62 phase diagram.

To have an idea about simulations reported in this work, for the simulated systems formed by 70000 particles, it is possible to calculate about 0.5 μs/day using 32 processors (Intel E5530 – HPC ENEA-GRID CRESCO). The hybrid PF SCF scheme is particularly efficient in parallel simulations, especially for large systems when the use of a large number of CPUs is efficient[15], and the validation of the models presented in this paper will allow their application to large- scale systems.

References

1. I. R. Schmolka, *J Amer Oil Chem Soc* **1977**, *54*, 110.
2. M. Amiji, K. Park, *Journal of Biomaterials Science, Polymer Edition* **1993**, *4*, 217.
3. A. V. Kabanov, E. V. Batrakova, V. Y. Alakhov, *J Control Release* **2002**, *82*, 189.
4. P. Alexandridis, D. Zhou, A. Khan, *Langmuir* **1996**, *12*, 2690.
5. P. Alexandridis, V. Athanassiou, T. A. Hatton, *Langmuir* **1995**, *11*, 2442.
6. P. Alexandridis, J. F. Holzwarth, T. A. Hatton, *Macromolecules* **1994**, *27*, 2414.
7. S. Yang, S. Yuan, X. Zhang, Y. Yan, *Colloids and Surfaces A: Physicochemical and Engineering Aspects* **2008**, *322*, 87.
8. Z. Zhou, B. Chu, *Macromolecules* **1994**, *27*, 2025.
9. G. Milano, T. Kawakatsu, *The Journal of chemical physics* **2009**, *130*, 214106.
10. G. Milano, T. Kawakatsu, *Journal of Chemical Physics* **2010**, *133*, 214102.
11. A. De Nicola, Y. Zhao, T. Kawakatsu, D. Roccatano, G. Milano, *J. Chem. Theory Comput.* **2011**, *7*, 2947.
12. A. De Nicola, Y. Zhao, T. Kawakatsu, *Theoretical Chemistry ...* **2012**.
13. K. Mortensen, J. S. Pedersen, *Macromolecules* **1993**, *26*, 805.
14. A. Caragheorgheopol, S. Schlick, *J. Phys. Chem.* **1998**, *31*, 7736.
15. Y. Zhao, A. De Nicola, T. Kawakatsu, G. Milano, *J. Comput. Chem.* **2012**, *33*, 868.

Mg atomic diffusion in MgO grain boundary

[1]Fabio Landuzzi, [2*]Massimo Celino, [3]Fabrizio Cleri, [1]Luca Pasquini

[1] Department of Physics and Astronomy and CNISM, University of Bologna, v.le Berti-Pichat 6/2, I-40127 Bologna, Italy
[2] ENEA, C. R. Casaccia, via Anguillarese 301, 00123 Rome, Italy
[3] Institute of Electronics, Microelectronics and Nanotechnology (UMR CNRS 8520), 59652 Villeneuve d'Ascq, France.

Keywords: molecular dynamics, nanomaterials, diffusion, grain boundary
*Corresponding Author: E-mail: massimo.celino@enea.it. Tel: 0630483871. Fax: 0630483176

ABSTRACT
The study of magnesium and its oxide has a central importance in the development of new materials for solid state hydrogen storage. Self-diffusion of magnesium in porous materials, has been supposed to represent a serious drawback for future applications. In particular the diffusion through interfaces seems to be the main responsible for the deterioration of batteries. To better enlighten the atomic scale mechanism of Mg self-diffusion in oxide magnesium, a classical molecular dynamics model has been developed. Firstly we compare the properties exhibited by two different models of magnesium, the hard sphere and the shell model, with the experimental data available for a bulk system. Then we design a stable and reliable interface to compute and characterize the main features of Mg diffusion in MgO grain boundary.

INTRODUCTION
Magnesium oxide is a rock-salt crystal of great interest for several reasons. It is important in geophysical study, because it has a strong influence in rheological and chemical transport properties of the lower mantle. Moreover it is involved in the hydrogen absorption and desorption at relative low temperatures and pressures in magnesium-based compounds. In particular, for future applications in cars mobility or energy storage, many studies have been done on batteries constituted by porous magnesium covered by thin coating of nano-structured oxide to improve the hydrogen charging and discharging velocity. These experimental results reveal an obstacle in the deterioration of the porous compound due to the emptying of MgO shell. Self-diffusion of magnesium through the oxide, in a bulk system, is not sufficient to justify the production of allowed structures. On the contrary a mechanism of grain boundaries (GBs) diffusion is supposed [1].
No experimental data of the Mg diffusion in GBs is available. Thus a numerical model of GB for MgO could really help the understanding of the diffusion process. However the computation of the Mg diffusion in such systems is not an easy task because it requires a very large sample and accurate statistical analysis. Moreover long simulation times are required to detect the slow diffusivity of magnesium. For this reason a quantum description is not affordable and a classical molecular dynamics seems to be more suitable to catch the physical process.
The description of the atomic interaction in magnesium oxide is usually performed by using two different models: the hard sphere model, that does not describe the polarization of the anion, and the shell model that, by using a two body schema for the oxygen ion, allows the polarization of the atom [2,3,4].

In both models the long range attraction is described by the Coulomb interaction, the short range repulsion by Buckingham type potentials. Polarization of the cation is considered negligible. We compare the properties exhibited by these models using the Gale and Roll parametrization, to check if the shell model is necessary to obtain a correct description of diffusion. Experientally, MgO material is nano-crystalline and many different types of interface are found in the system. We design numerically a stable MgO interface characterized by high energy where the diffusion is favoured and could be compared with bulk values. This interface is based on the symmetric tilt [113] for the face centred cubic (FCC) sub-lattice of cation in the MgO crystal and shows a channel-type structure that could favour the diffusion.
Molecular dynamics simulations have been executed by using the software DLPOLY 4 [5] and the simulation has been performed on the high performance computing platforms: CRESCO (ENEA) and JADE (CNRS, France).

COMPUTATIONAL DETAILS

The magnesium charge is +2 and the oxygen is -2, but in the shell model this charge is divided in +0.15 to the oxygen core and -2.15 to the oxygen shell. The short range potentials (Buckingham type) act between both magnesium-oxygen and oxygen-oxygen. If the shell is used, these potentials are applied on the shell and no short range interaction is involved in the core:

$$V(r_{ij}) = Ae^{\frac{-r_{ij}}{\rho}} - \frac{C}{r_{ij}^6}$$

Hard sphere Model	**A**	ρ	**C**
Mg-O	821.60	0.3248	0.00
Mg-Mg	22764.0	0.1490	27.88
Shell Fractional Mass		**Core-Shell Spring Constant**	
0.200		15.740	

Table 1: Parameters for the short range potentials and spring harmonic constant k for the core-shell interaction in the shell models. The units of measure are expressed in native DlPoly unit.

Hard sphere Model	***A***	ρ	***C***
Mg-O	1295.55	0.3000	0.0
Mg-Mg	22764.0	0.1490	27.88

Table 2: Parameters for the Buckingham potentials in the hard sphere models. The units of measure are expressed in native DlPoly unit.

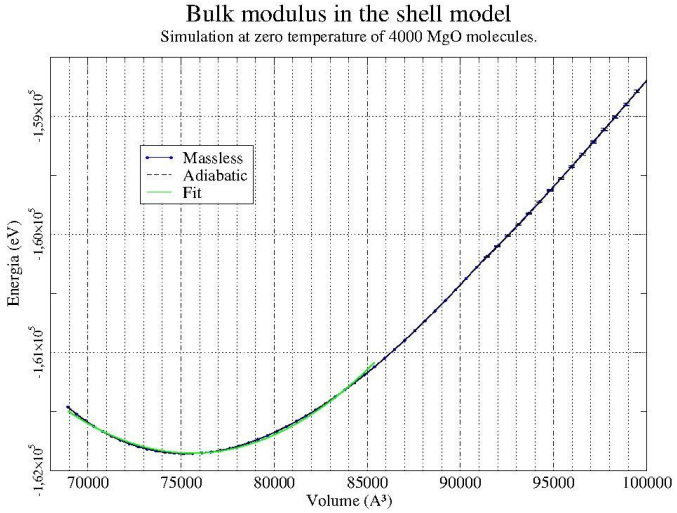

Figure 1: Potential energy versus volume.

Simulations of the bulk system, 8000 atoms, are performed in the NVT ensemble with periodic boundaries conditions. Lattice parameter and bulk modulus, at T= 0 K, are obtained by fitting the energy curves versus both the volume and the anion-cation distance. The thermal expansion coefficient is obtained by fitting the volume versus temperature after a simulation in the NPT ensemble at atmospheric pressure.

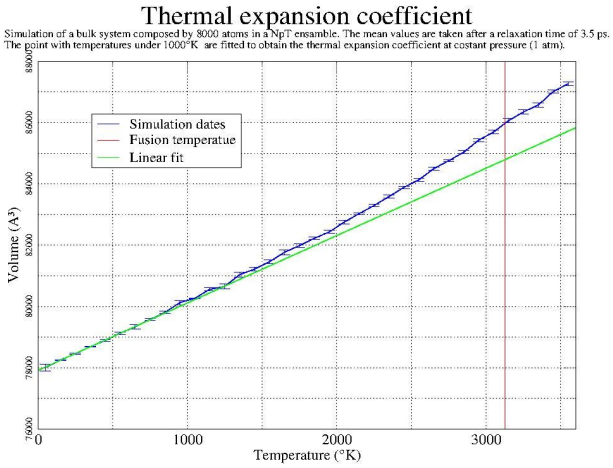

Figure 2: Thermal expansion coefficient versus temperature.

Name	**Lattice Parameter (Å)**	**Density (g/cm³)**	**Bulk Modulus (GPa)**	**Thermal Expansion Coeff (1/°K)**	**CPU Time (s)**
Experim.	4,21	3,51	160,3	1,340E-5	/
Hard Sphere	4,21	3,55	231,5	9,330E-6	400
Shell	4,22	3,52	194,4	9,497E-6	850

Table 3: Comparison of MgO models. Experimental values are taken from Ref. [6].

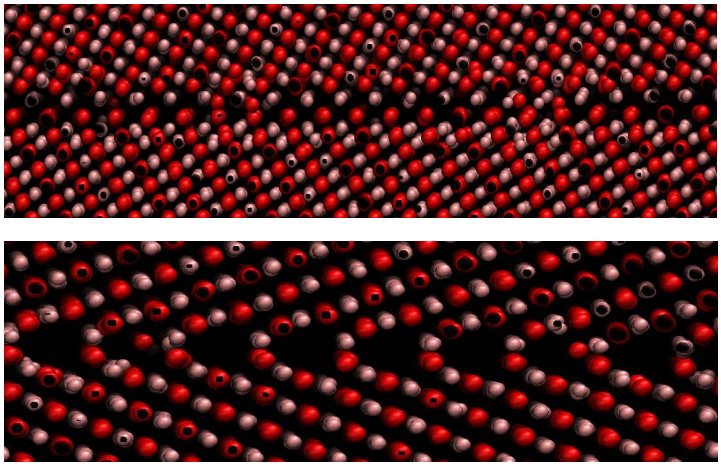

Figure 3: Plot of the interface in the XZ plane (up) and YZ plane (down) using VMD software, red spheres are oxygen anions, white ones are magnesium cations. In the YZ plane there is the channel structure of the interface along the X direction. In both figures there are atoms that diffuse along the interface.

MAGNESIUM SELF-DIFFUSION IN GRAIN BOUNDARIES

During the construction of the ground boundary, molecular dynamics simulations in the NPT ensemble have been performed to relax the system along the direction orthogonal to the interface. The stable configuration is characterized by a channel structure along the X direction were the motion of atoms is favoured.

Since the self-diffusion in the bulk system of magnesium in its oxide is small, we suppose that the diffusion occurs primarily at the interface and in a small region around it. Then we assume for the diffusion in the GBs, the type C in Harrison classification and we study the mobility of atoms in a range of 4.21 Å (a lattice parameter) around the interface plane. The entire crystal is composed by 154000 atoms and the numbers of atoms in the region of the interface is about 5500.

The calculation of the diffusion coefficient is obtained by a linear fit of the mean square displacement (MSD) as function of the inverse time. By using the Einstein formula:

$$D(T) = D_0 \exp(-\Delta E / k_B T)$$

we compute the activation energy in GB. The result for the magnesium is (0.43 ± 0.07) eV and for the oxygen (0.54 ±0.11) eV. Different types of diffusion are involved: oxygen has a low temperature behaviour, probably due to the extrinsic diffusion and a high temperature behaviour due to the intrinsic diffusion.

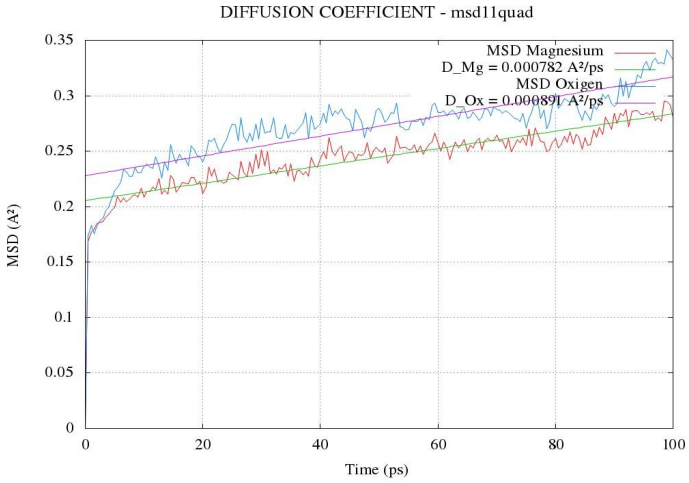

Figure 4: Graph of the mean square displacement versus time in the interface at 1750 K.

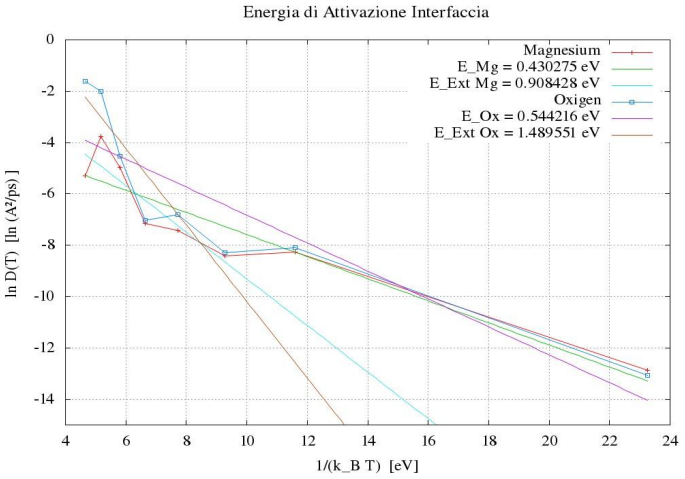

Figure 5: Graph of the logarithm of diffusion coefficient around the interface as function of the inverse of temperature, the purple and green line is the linear fit respectively of the cation and anion diffusion.

Fitting only the points with temperatures above 1000 K, the magnesium activation energy is (0.9 ± 0.2) eV and the oxygen activation energy is (1.4 ± 0.3) eV.
This value for magnesium is in the range that could be supposed to be, considering the activation energy of the GB as half of the activation energy for the bulk system 2.76 eV [7].

CONCLUSION

The shell model is in good agreement with the experimental data but long simulation times are necessary to overcome the hard sphere model, that is not able to describe accurately the bulk modulus and other experimental properties.
By using the hard sphere model we construct a GBs that models a channel structure along the X direction, where the motion of ions is favoured. Then we obtain values of diffusion coefficient for the magnesium cation and oxygen anion as a function of temperature to evaluate the activation energy for the self-diffusion in the oxide. These values show a different behaviour in the high temperature regime and low temperature regime, probably due to the different mechanism of diffusion (mainly extrinsic or intrinsic).

References

[1] Pasquini L, Montone A, Callini E, Antisari MV, "*Formation of hollow structures through diffusive phase transition across a membrane"*, App. Phys. Lett. **99**, 021911 (2011).

[2] Sangster MJL, Peckham G. and Saundersonz DH, *Lattice dynamics of magnesium oxide*, J. Phys. C: Solid State Phys. **3**, 1026 (1970).

[3] Catlow CRA, Faux ID, Nerget MJ, *"Shell and breathing shell model calculations for defect formation energies and volumes in magnesium oxide*" , J. Phys. C: Solid State Phys. **9**, pag …. (1976).

[4] Lewis GV, Catlow CRA, "*Potential models for ionic oxides"*, J. Phys. C: Solid State Phys. **18**, 1149-1161 (1985).

[5] Todorov IT, Smith W, Dl Poly 4, version 4.03.3 (2012).

[6] Speziale S, Zha CS, Duffy TS, Hemley RJ, Mao HK, "Quasi-hydrostatic compression of magnesium oxide to 52 GPa: Implications for the pressure-volume-temperature equation of state*",* J. Geophys. Res. **106** (2001) 515–528.

[7] Wuensch BJ, Steele WC, Vasilos T, "*Cation self‐diffusion in single‐crystal MgO"*, J. Chem. Phys. **58**, 5258 (1973).

The effects of vacancies in the mechanical properties of tungsten: an *ab-initio* study

Simone Giusepponi UTICT-HPC and **Massimo Celino** UTMAT-DIAG
ENEA, C. R. Casaccia, via Anguillarese 301, 00123 Rome, Italy
simone.giusepponi@enea.it; massimo.celino@enea.it.

Abstract
The ideal tensile strength of bcc crystal tungsten in presence of mono and divacancy has been investigated by using first-principles total energy method based on the density functional theory. Crystalline tungsten containing vacancies (concentration of vacancies about 2% and 4%) has been characterized in terms of structural and mechanical properties. The maximum tensile stress required to reach elastic instability under increasing load has been further computed.

Introduction
Tungsten (W) is presently considered as structural and shield material candidate in the future nuclear fusion reactors [1,2]. This is due to its thermal properties such as good thermal conductivity, high melting temperature and low sputtering erosion. The main requirement on tungsten materials for structural applications is to be ductile within the operation temperature range. An armor material needs high crack resistance under extreme thermal operation conditions and compatibility with plasma-wall interaction phenomena. Both material types have also to be stable with respect to high neutron irradiation doses and helium production rates. Thus, the mechanical properties are extremely important factors to be considered in developing W as a PFM (plasma facing materials). The ideal tensile strength of W can be a useful reference for the preparation and design of W as a PFM, because it sets an upper limit of the tensile strength. The ideal tensile strength of pure Tungsten in the [001] direction has been investigated by using first-principles pseudo-potential method [3-5]. Moreover, the same approach has been used to perform first-principles computational tensile tests to obtain the ideal tensile strength in [001] direction for W and W alloys [6].

However, these works do not provide details on the structural and mechanical properties of tungsten with different concentration of vacancy defects. For these reasons in the present work, we have investigated tungsten with monovacancy and divacancies point defects. For these systems lattice constants, bulk modulus, enthalpies of atomization, formation enthalpy of defects and ideal tensile strengths in [001] direction have been calculated. For 2NN divacancies case we have also calculated the binding energy and the ideal tensile strength in [100] direction. To address the study of W the first-principles Pwscf (Plane Wave self-consistent field) code of the Quantum ESPRESSO suite has been used [7,8]. This numerical code allows the accurate atomic-scale study of materials taking into account explicitly the contribution of the electronic structure. It is possible to perform both total energy-calculations on predefined atomic structures and to study the evolution of the material changing the external temperature. Firstly a reliable physical model for tungsten is developed, then total energy calculations are performed to check if the model can reproduce experimental structural properties. Then first-principles calculations are extensively performed to accurately compute lattice constants, bulk modulus, enthalpies of atomization, formation enthalpies of defects and ideal tensile strengths of tungsten with different concentrations of vacancies.

Computational details
Our calculations have been performed by using the PWscf code of the Quantum ESPRESSO suite. Quantum ESPRESSO is an integrated suite of Open-Source computer codes for electronic-structure

calculations and materials modeling at the nanoscale. It is based on density functional theory (DFT) [9,10], plane waves, and pseudopotentials. We compiled the codes of the Quantum ESPRESSO suite with Intel fortran compiler, MKL and OpenMPI, and we utilized the CRESCO clusters [11]. We used the W.pbe-nsp-van.UPF Vanderbilt ultrasoft pseudopotential [12] with Perdew-Burke-Ernzerhof (PBE) [13] approximant GGA (Generalized Gradient Approximations) exchange-correlation potential. All the calculations are performed in the supercell approximation with periodic boundary conditions (PBC) meant to mimic an infinitely extended system. We considered a cubic supercell composed by a 3×3×3 array of bcc conventional cells, and 54 W atoms. As shown in Fig.1, the role of vacancies in tungsten bulk is investigated by removing a W atom for the monovacancy case (concentration of defects about 2%), and by removing a couple of W atoms for divacancy cases (concentration of defects about 4%).

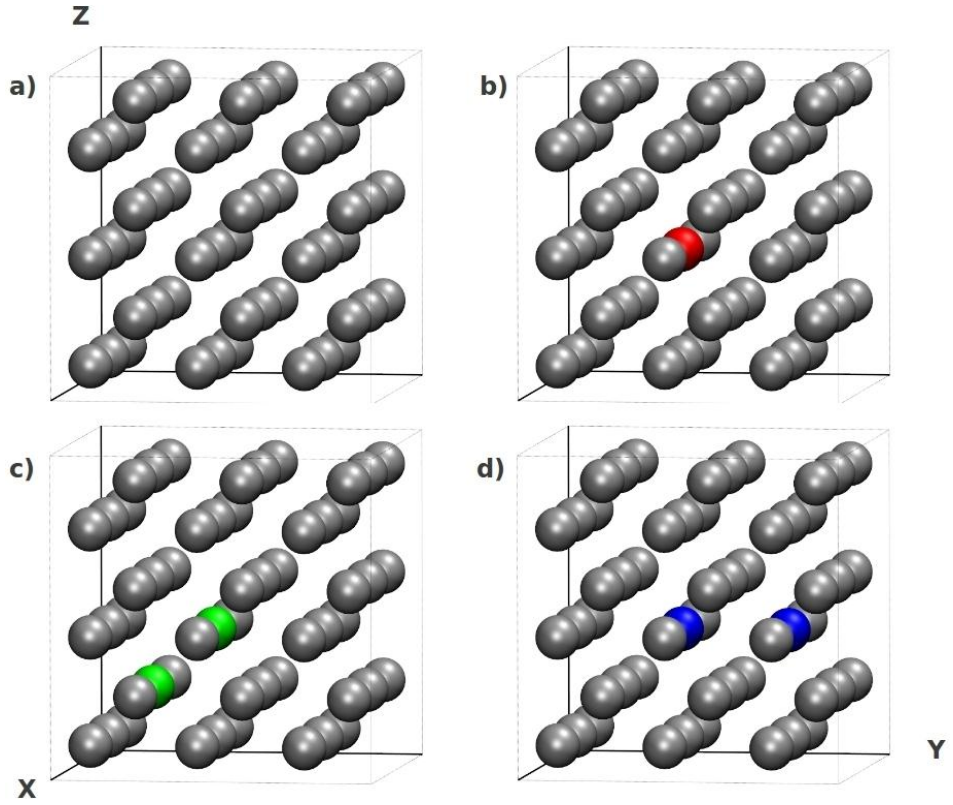

Figure 1: Simulation cell for the first-principles total energy calculations. Tungsten atoms are the gray spheres. b) monovacancy case; one tungsten atom is removed (red sphere). c) divacancy 1NN case; two tungsten atoms are removed in [111] direction (green spheres). d) divacancy 2NN case; two tungsten atoms are removed in [100] direction (blue spheres).

Thus we considered four cases:

i) tungsten without defects: a supercell of 54 W atoms (see Fig.1a);
ii) monovacancy case: a supercell of 53 W atoms in which we removed a W atom (see Fig.1b);
iii) divacancy 1NN case: a supercell of 52 W atoms in which we removed a couple of first-nearest-neighbor W atoms (see Fig.1c);
iv) divacancy 2NN case: a supercell of 52 W atoms in which we removed a couple of second-nearest-neighbor W atoms (see Fig.1d).

The electronic wave functions were expanded in a plane-wave basis set with a kinetic energy cutoff equal to 340 eV and a 4×4×4 Monkhorst-Pack mesh of **k** points [14]. We used Marzari-Vanderbilt smearing [15] with a width of 0.02 Ry. The kinetic energy cutoff, the **k** sampling and the smearing

width, were optimized by preliminary calculations on tungsten pseudopotential. The energy minimization is performed using conjugate gradient minimization method [16], with the convergence threshold for self consistency equal to 10^{-7} Ry. BFGS (Broyden-Fletcher-Goldfarb-Shanno) [17,18] quasi-newton algorithm is used to geometry optimization. Ionic relaxation is stopped when both the conditions are satisfied: energy changes less than 10^{-4} Ry between two consecutive scf steps; all components of all forces are smaller than 5×10^{-4} Ry/Bohr; For the variable cell relaxation we still used BFGS quasi-newton algorithm adding to satisfy the further condition: all components of the tensor stress are smaller than 0.05 GPa.

By first-principles total energy calculations we computed lattice parameter a, bulk modulus B, enthalpy of atomization H_a and the ideal tensile strength σ_m as described in Ref.[6]. Moreover we calculated formation energy of the vacancies ΔE_{xv} by the formula:

$$\Delta E_{xv} = E_{tot}^{xv} - \frac{N-x}{N} E_{tot}$$

where E_{tot}^{xv} is total energy of system with x vacancies and $N-x$ atoms of W, E_{tot} is total energy of bulk system with N atoms of W, x is the number of vacancies and $N = 54$. The binding energy of divacancy cluster $E_{bind.} = \Delta E_{1v} - \Delta E_{2v}$ can be computed by the difference between the formation energy of monovacancy and divacancy.

Results and discussion

The calculated equilibrium lattice constant for bcc W, a_0 =3.187 Å is in good agreement with the corresponding experimental value of 3.165 Å [19], with a difference within 0.7%, and with others first principles computations [4,5,20] where a_0 =3.17-3.19 Å. Our calculation for the bulk modulus gives B=322 GPa, the experimental value [19] is 316 GPa (error within 1.9%). The values of the ideal tensile strength in the [001] direction σ_m =27.3 GPa and the strain ε_m =13.6% are in agreement with other first principles calculations [3-6] σ_m =28.9-29.5 GPa and ε_m =12.3-14%. The full set of our results for tungsten is reported in Table 1.

	a_0 (Å)	$b_0 = c_0$ (Å)	B (GPa)	H_a (KJ/mol)	ΔE_{xv} (eV)	$E_{bind.}$ (eV)	σ_m (GPa)	ε_m (%)
Pure W	3.187	3.187	322	1052	-	-	27.3	13.6
Monovacancy	3.180	3.180	303	1046	3.25	-	26.8	13.5
Divacancy 1NN	3.173	3.173	284	1040	6.42	0.08	25.7	13.2
Divacancy 2NN	3.173	3.170	280	1039	6.84	-0.34	25.2	12.9
Divacancy 2NN(*)	-	-	-	-	-	-	25.9	13.2

Table 1: Calculated values of equilibrium cell size a_0 (b_0, c_0), bulk modulus B, enthalpy of atomization H_a, formation energy of vacancies ΔE_{xv}, binding energy of divacancy cluster $E_{bind.}$, ideal tensile strength σ_m and the related strain ε_m for pure bcc tungsten, monovacancy, divacancy 1NN and divacancy 2NN cases. The uniaxial deformation is along the [001] direction except for (*) where uniaxial deformation is in the [100] direction.

Having checked the reliability of our numerical model, we studied the structural and mechanical properties of tungsten with different concentration of vacancies to understand their effects on bulk properties. Calculated values of lattice parameter a_0, bulk modulus *B*, enthalpy of atomization H_a, ideal tensile strength σ_m and related strain ε_m for monovacancy and for 1NN and 2NN divacancy clusters are reported in Table 1. We reported also the formation energy of the vacancies ΔE_{xv} and the binding energy of divacancy cluster $E_{bind.}$. In all cases we observe small variations in the lattice parameter a_0. In the 2NN divacancy cluster we observe that there is no longer the cubic symmetry, now the supercell has tetragonal symmetry. On the contrary the bulk modulus *B* is reduced. A concentration of point defects of about 2% (4%) yields a decreasing in the bulk modulus of about 6% (12%). The calculated value for the formation energy of the vacancies and the value for the binding energy of divacancy clusters are in agreement with Refs. [21-23]. In Fig. 2 are shown the dependences of the total energy E vs. the strain ε. For the 1NN divacancy cluster we limit the stretching to ε=16%. At higher stretching the system does not reach a completely relaxed configuration. This is probably due to the interaction between the supercell replicas. For the 2NN divacancy cluster, to evaluate the effect of the loading direction, we consider a stretching along the [001] direction and a stretching along the [100] direction. The former is orthogonal to the direction of the two vacancies, the latter is parallel to the direction of the two vacancies. For all cases we observe a decreasing in the ideal tensile strength σ_m compared to the system without defects.

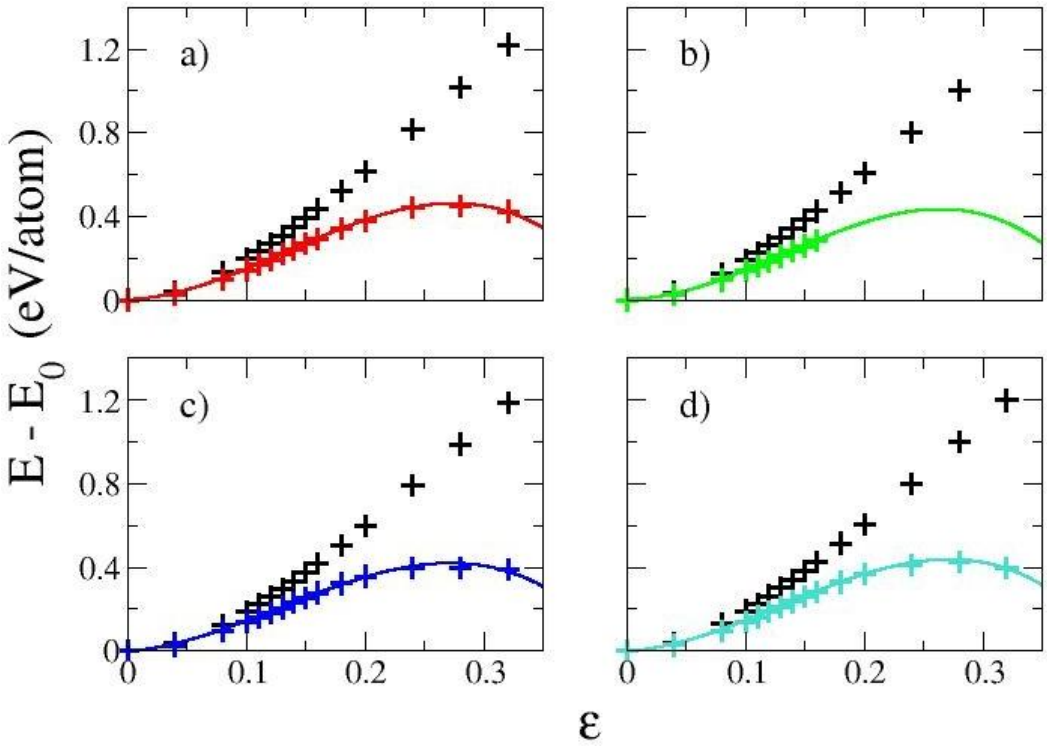

Figure 2: Total energy E per atom as a function of strain ε for uniaxial deformation. a) bcc W monovacancy case; b) bcc W divacancy 1NN case; c) and d) bcc W divacancy 2NN case. For a), b) and c) uniaxial deformation in [001] direction. For d) uniaxial deformation in [100] direction. E_0 is the ground-state energy of the systems. Energies for unrelaxed conditions are shown in black symbols, those for relaxed conditions are shown in red, green, blue, and light blue symbols respectively. Solid lines are cubic fitting functions.

Conclusion

The ideal tensile strengths in the [001] direction of bcc tungsten pure crystal and tungsten with different concentration of vacancies have been investigated by using DFT first-principles total energy method. The reliability of the numerical model has been extensively checked by computing several structural properties of W. We have calculated lattice parametrers, bulk modulus, enthalpies of atomization, formation enthalpy of vacancies and binding energy of divacancy cluster in very good agreement with both experimental and theoretical results. Despite the low concentration of defects (about 2% and 4%), results highlight that the presence of vacancy defects in W bulk is able to produce measurable variations with respect to pure tungsten crystal. The bulk modulus decreases are in the range of 6-13% whereas the ideal tensile strength decreases are in the range of 2-8% .

Acknowledgments

The computational resources and the related technical support for this work have been provided by CRESCO-ENEA GRID High Performance Computing infrastructure and its staff. The high performance computing infrastructure is funded by ENEA, the *"Italian National Agency for New Technologies, Energy and Sustainable Economic Development"* and by national and European research programs.

References

[1] RIETH M., *et al*. *"A brief summary of the progress on the EFDA tungsten materials program"* J. Nuc. Mater. in press.
[2] RIETH M., *et al*. *"Recent progress in research on tungsten materials for nuclear fusion applications in Europe"* J. Nuc. Mater. **432** (2013) p.482.
[3] ŠOB M., WANG L.G., VITEK V. *"Theoretical tensile stress in tungsten single crystals by full-potential first-principles calculations"* Mater. Sci. Eng. A **234-236** (1997) p.1075.
[4] ROUNDY D., KRENN C.R., COHEN M.L., MORRIS Jr. J.W. *"The ideal strength of tungsten"* Philos. Mag. A **81** (2001) p.1725.
[5] LIU Y.-L., ZHOU H.-B., ZHANG Y., JIN S., LU G.-H. *"The ideal tensile strength and deformation behavior of a tungsten single crystal"* Nucl. Instrum. Methods Phys. Res. B **267** (18) (2009) p.3282.
[6] GIUSEPPONI S., CELINO M. *"The ideal tensile strength of tungsten and tungsten alloys by first-principles calculations"* J. Nuc. Mater. **435** (2013) p.52.
[7] GIANNOZZI P., *et al*. *"QUANTUM ESPRESSO: a modular and open-source software project for quantum simulations of materials"* J. Phys.: Condens. Matter **21** (2009) 395502.
[8] www.quantum-espresso.org.
[9] HOHENBERG P., KOHN W. *"Inhomogeneous Electron Gas"* Phys. Rev. **136** (1964) p.B864.
[10] KOHN W., SHAM L.J. *"Self-Consistent Equations Including Exchange and Correlation Effects"* Phys. Rev. **140** (1965) p.A1133.
[11] www.cresco.enea.it
[12] VANDERBILT D. *"Soft self-consistent pseudopotentials in a generalized eigenvalue formalism"* Phys. Rev. B **41** (1990) p.7892.
[13] PERDEW J.P., BURKE K., ERNZERHOF M. *"Generalized Gradient Approximation Made Simple"* Phys. Rev. Lett. **77** (1996) p.3865.
[14] MONKHORST H.J., PACK J.D. *"Special points for Brillouin-zone integrations"* Phys. Rev. B **13** (1976) p.5188.
[15] MARZARI N., VANDERBILT D., DE VITA A., PAYNE M.C. *"Thermal Contraction and Disordering of the Al(110) Surface"* Phys. Rev. Lett. **82** (1999) p.3296.
[16] QTEISH A., *"Conjugate-gradient methods for metallic systems and band-structure calculations"* Phys. Rev. B **52** (1995) p.14497.
[17] FLETCHER R., *"Practical Methods of Optimization"* (1997) New York: Wiley.
[18] BILLETER S.R., TURNER A.J., THIEL W. *"Linear scaling geometry optimisation and transition state search in hybrid delocalised internal coordinates"* Phys. Chem. Chem. Phys. **2** (2000) p.2177.
[19] AYRES R.A., SHANETTE G., STAIN D. *"Elastic constants of tungsten-rhenium alloys from 77 to 298°K"* J. Appl. Phys. **46** (1975) p.1526.
[20] ROMANER L., AMBROSH-DRAXL C., PIPPAN R. *"Effect of Rhenium on the Dislocation Core Structure in Tungsten"* Phys. Rev. Lett. **104** (2010) 195503.
[21] BECQUART C.S., DOMAIN C. *"Ab initio calculations about intrinsic point defects and He in W"* Nucl. Instrum. Methods Phys. Res. B **255** (2007) p.23.
[22]MUZYK M., NGUYEN-MANH D., KUEZYDLOWSKI K.J., BALUC N.L., DUDAREV S.L. *"Phase stability, point defects, and elastic properties of W-V and W-Ta alloys"* Phys. Rev. B **84** (2011) 104115.
[23] KATO D., IWAKIRI H., MORISHITA K. *"Formation of vacancy clusters in tungsten crystals under hydrogen-rich condition"* J. Nucl. Mater. 417 (2011) p.1115.

Adhesion Chemistry and Work Function of (111) Silicon Surface Functionalized with Self-Assembled Alkylsilane Coatings: an *ab-initio* study.

Fabrizio Gala and Giuseppe Zollo

Dipartimento di Scienze di Base e Applicate per l'Ingegneria (Sezione di Fisica), Università "La Sapienza", Via A. Scarpa 14-16, 00161 Rome, Italy

I. Introduction

Self-assembled monolayers (SAMs) have been recently studied and reviewed in detail[1−4], because of their possible use in low cost devices for applications in many fields. Among the possible choices for the chemical species involved in the formation of SAM films, alkylsilanes exhibit appealing properties, such as low mechanical friction[3] or a high level of hydrophobicity[5,6], when employed in the functionalization of silicon surfaces. Moreover, octadecyltrichlorosilane films ($CH_3(CH_2)_{17}SiCl_3$, OTS) deposited on Si or SiO_2 exhibit high insulating properties, provided that a good control of film quality is achieved[7−9], making this system highly appealing for the fabrication of efficient field emitting transistors (FETs) or organic thin film transistors (OTFTs) at the nanoscale, where silicon dioxide (SiO_2) behaves as a poor insulator with high leakage currents. SAM coatings of semiconductor surfaces have been also employed in organic light-emitting diodes (OLED) as "adapting" dipolar thin films that may greatly improve the device performance by modifying the work function at the gate/substate interface[10]. The same is expected to occur also in the case of OTS−SAM on Si surfaces, affecting, as a consequence, the properties of devices based on this technology.

Self-assembled organic monolayers should be close-packed and highly ordered structures; however, defects may occur during the SAM formation[11,12] and the coating properties can be affected by the deposition parameters and methods used, resulting for instance, in multiple covalent attachments on the surface referred to as "poor self-assembly"[13, 14]. At present, the structural properties (i.e. coverage, surface, roughness, temperature, stability), its coarse-grained structure (i.e. self assembling properties, thickness, chain orientation, hydrophobic termination groups) and the stoichiometry of the OTS adsorption on Si surfaces (i.e., the number of bonds per molecule) obtained from ellipsometry, infrared spectroscopy, X-ray photoelectron spectroscopy (XPS), reflectivity, and absorption fine structure (NEXAFS)[13, 15-17], have not been clarified yet. Therefore only partial indications on atomistic structural properties, such as the tilt angle θ_{tilt} formed by the alkyl chain axis and the normal to the Si surface in the range $\theta_{tilt} \in [0°,10°]$, have been obtained that, however, should be considered as an average value calculated over neighboring self-assembled domains[11]. The adhesion geometries and energetics of both OTS and n-alkanes have been recently approached by density functional theory (DFT) calculations[18], showing that, in the case of perfect SAM adhering to the Si surface with one covalent bond per molecule, the self-assembly mechanism involves H-bonds between hydroxyl groups of neighboring of OTS molecules. Defects, discontinuities, or "poor self-assembly" features in the OTS SAM dramatically affect the system properties resulting in poor device performance, especially those exploiting the work function modification of the Si substrate induced by the deposited layer.

Thus we have focussed on the work function calculation of OTS−SAM coatings deposited on a (111) hydrogenated Si surface. In particular, the work function change, $\Delta\Phi$, with respect to the perfect hydrogenated surface is calculated for various adhesion configurations and coverage ratios, demonstrating the relationship between the work function and the local dipole of the coating that could provide deep insight into SAM film properties.

II. Theoretical Method

OTS adsorptions onto the (111) Si surface have been modeled by ab initio density functional theory (DFT), with a generalized gradient approximation (GGA), using the Perdew− Burke−Ernzerhof formula[19] (PBE) for the electron exchange and correlation energy, together with norm-conserving pseudopotentials, constructed using the Troullier−Martins scheme[20], and a plane wave basis set expansion scheme. First-principles calculations have been performed using the QUANTUM-ESPRESSO package[21], with an energy cutoff of 150 Ry for the wave functions.
The Si (111) surface has been chosen to lie in the *xy* plane and is represented by a three-layer slab (32 Si atoms per layer) and a vacuum region nearly 43 Å thick; all the dangling bonds at the surface have been passivated with H atoms. Periodic boundary conditions (PBCs) have been employed together with a dipole correction rectifying the artificial electric field across the slab induced by the PBCs[22]. A (2x2x1) Mokhorst-Pack k-point grid[23] for the Brillouin zone sampling has been employed, being sufficient for the total Energy convergence[18]. The ground-state configurations have been fully relaxed using the Broyden−Fletcher−Goldfarb−Shanno (BFGS) method[24] together with the Hellmann−Feynman forces acting on the ions, until the convergence threshold of 0.001 au of the total force was reached. In a previous article we have shown that the ground-state configurations of alkyl-based SAMs were not affected by the usage of the van der Waals empirical corrections[18, 25] and thus we have not used the long-range corrections. As a OTS precursor, its hydroxylated counterpart, OTS†, namely $CH_3(CH_2)_{17}Si(OH)_3$, has been considered. When the Cl atoms are replaced by OH groups, the alkylsilane is easily accessible in water solution. The adsorption reaction consisting of one or more covalent attachments (up to three) between the (OH) radicals of the OTS† molecule and the substrate is:

$$OTS\dagger + H{:}Si \rightleftharpoons CH_3(CH_2)_{17}Si(OH)_{3-n}O_n/H{:}Si + nH_2 \qquad (1 \leq n \leq 3) \qquad (1)$$

with an adsoprtion energy of

$$E_{ads} = E(CH_3(CH_2)_{17}Si(OH)_{3-n}O_n/H{:}Si) + nE(H_2) - E(OTS\dagger) - E(H{:}Si) \qquad (1 \leq n \leq 3) \qquad (2)$$

Work function changes have been computed for the different configurations through the "Z-potential" obtained by solving the Poisson equation (given the DFT charge density) and then by averaging the electrostatic potential $V_{el}(\mathbf{r})$ in the *xy* plane:

$$V_{el}(z) = (1/A)\int_A V_{el}(\mathbf{r})dxdy = (-e/2\varepsilon_0 A)\int |z'-z|\bar{\rho}(z')dz' \qquad (3)$$

resulting in

$$\Delta\Phi = \Phi^{OTS\dagger/H:Si} - \Phi^{H:Si} = (-eV_{el}{}^{OTS\dagger/H:Si}(\infty) - \mu_{bulk}{}^{Si}) - (-eV_{el}{}^{H:Si}(\infty) - \mu_{bulk}{}^{Si}) = -e\Delta V_{el} = -eV_{el}{}^{OTS\dagger/H:Si}(\infty) \qquad (4)$$

with A being the surface area, z the coordinate of an arbitrary plane parallel to the surface, and $\bar{\rho}(z)$ the *xy* average of the total charge. Moreover, in eq. 4, the "Z-potential" of the hydrogenated surface calculated deep in the vacuum (i.e., for $z \rightarrow \infty$) has been set as a reference value.
Lastly, the partial dipole moments[26] (referred to the vacuum region) along the z direction have been calculated through the formula

$$d(z) = \int_z (z' - z)\bar{\rho}(z')dz' \qquad (5)$$

with the aim to demonstrate their relationship with the work function differences $\Delta\Phi$ of the various structures studied. The Z-potential, calculated in terms of the partial dipole d(z), casts into:

$$V_{el}(z) = (e/2\varepsilon_0 A)(d(0) - 2d(z)) \quad (6)$$

where d(0) is the total dipole moment of the system that should be ideally calculated as the partial dipole at a reference z plane deep in the Si bulk, dividing it into two neutral subunits[26]. Equation 6, together with the assumption that $V_{el}^{H:Si}(\infty)= 0$, implies $d^{H:Si}(0) = 0$. Therefore, the work function difference with respect to the hydrogenated Si surface is:

$$\Delta\Phi = -eV_{el}^{OTS\dagger/H:Si}(\infty) = -(e^2/2\varepsilon_0 A)(d^{OTS\dagger/H:Si}(0) - 2d^{OTS\dagger/H:Si}(\infty)) = -(e^2/2\varepsilon_0 A)d^{OTS\dagger/H:Si}(0) \quad (7)$$

III. RESULTS AND DISCUSSION

The fully relaxed structures of the (1:1), (1:2), and (1:3) OTS† ground-state adsorption configurations on the (111) Si surface are drawn in Figure 1; the adsorption energy values calculated on the basis of the eq. 2 are listed, together with the relevant tilt angles, in Table 1 and reveal that all the adsorption reactions are exothermic with larger adsorption energy for multiple covalent bonds per molecule, ranging from 0.64 eV per bond for the (1:1) case to 0.43 eV per bond for (1:3).

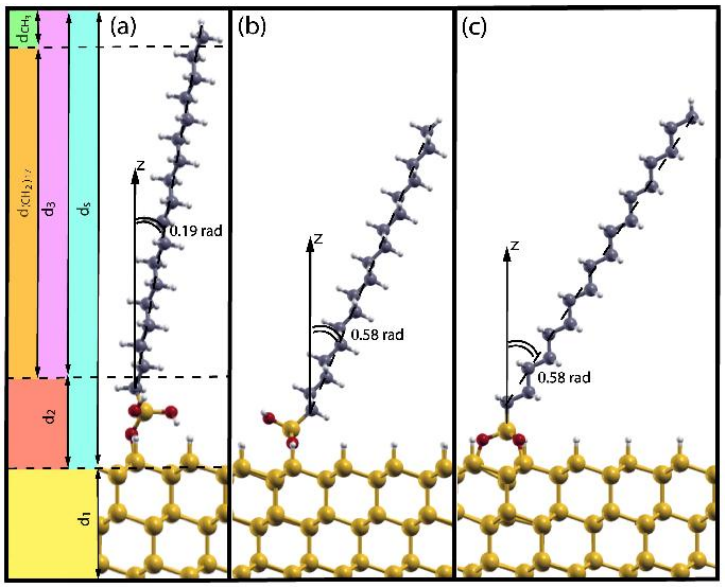

Fig. 1 Fully relaxed configurations of the (1:1) (a), (1:2) (b), and (1:3) (c) OTS adhesion on the hydrogenated (111) Si surface.

As for the (1:1) case[18], the ground-state structures are those preserving the tetrahedral coordination of the OTS Si atom involved in the bonding between the surface and the alkylsilane. Such a coordination is even more strictly preserved for both the (1:2) and the (1:3) configurations, with a maximum deviation from the tetrahedral angle of $\Delta\alpha_{max} \leq 0.5°$, compared to the value of $\Delta\alpha_{max} \leq 5.5°$ obtained in the (1:1) case. The (1:2) and (1:3) structures are apparently very similar, showing the same tilt angle and global geometry along the polymer chain; moreover, due to the elevated value of θ_{tilt}, both configurations tend to eclipse at least one adsorption site of the (111) surface honeycomb lattice. Besides the different number of covalent bonds per molecule involved with respect to (1:2), the (1:3) adsorption case also demonstrates a different rearrangement just below the topmost Si layer where the Si atom, located below the hydroxylated silane group of the OTS† molecule, is shifted downward by $\Delta z \sim 0.44$ Å with respect to the H:Si slab, thus leading to a non negligible charge rearrangement at the adhesion site. The work function differences $\Delta\Phi$ with respect to the bare H:Si surface have been calculated with eq. 7 where d(0) has been considered at the central Si layer of the three-layer slab. $\Delta\Phi$ values are listed in the third column of Table 1 and demonstrate that the

molecular dipole for all the ground-state configurations studied lowers the work function with respect to the hydrogenated (111) Si surface, thus reducing the energy needed to extract an electron from the bulk Si and increasing the hole isolation properties; indeed the negative partial dipole moment at the topmost Si layer for the functionalized surface is less then the hydrogenated one.

TABLE I. Adsoprtion Energies, Tilt Angles, Work Function Changes, and Surface Dipole Moment Changes with Respect to the Bulk Si:H Case for Single Molecule Adhesion Configurations Involving n Bonds with $1 \le n \le 3$

Configuration	**E_{ads}(eV)**	**θ_{tilt}(rad)**	**$\Delta\Phi$(meV)**	**Δd_s(D)**
(1:1)Si-O-Si	-0.64	0.19	-170	1.95
(1:2)Si-O-Si	-0.90	0.58	-87	1.17
(1:3)Si-O-Si	-1.30	0.58	-50	0.57

The different order of magnitude of the work functions for (1:1) with respect to (1:2) and (1:3) originates from the different geometric features of the SAM adhesion configuration (i.e., the tilt angle and the surface relaxation) but the (1:2) and (1:3) can still be distinguished from the work function thus indicating that the adhesion chemistry should be accessible through work function measurements.

Partial dipole moments at the z-coordinate z_s, corresponding to the midplane of the topmost Si−Si bond (see Figure 2), have been calculated for the various adsorption structures because the work function is mainly determined by the surface dipole that includes the contribution of the coating and of the surface charge rearrangement. The differences $\Delta d_s \equiv \Delta d(z_s)$ of such surface dipoles with respect to the ones of the H:Si structure are reported in the fourth column of Table 1. Δd_s is, as expected, positive, and its absolute value decreases with the number of adhesion Si−O bonds; the result for the (1:1) case reflects the smaller θ_{tilt} value of the configuration as compared to those of (1:2) and (1:3), and it is consistent with the fact that a small tilt angle implies a greater z component of the molecular dipole resulting in a larger $\Delta\Phi$. The Δd_s difference of (1:3) with respect to (1:2) reflects the different adhesion patterns involving one Si−O−Si bond more and one OH group less in the (1:3) case, which is also characterized sxby a more marked surface relaxation with one Si atom pusher downward. However the contribution of the alkyl chain to the surface dipole is not simply related to the tilt angle, as detailed next.

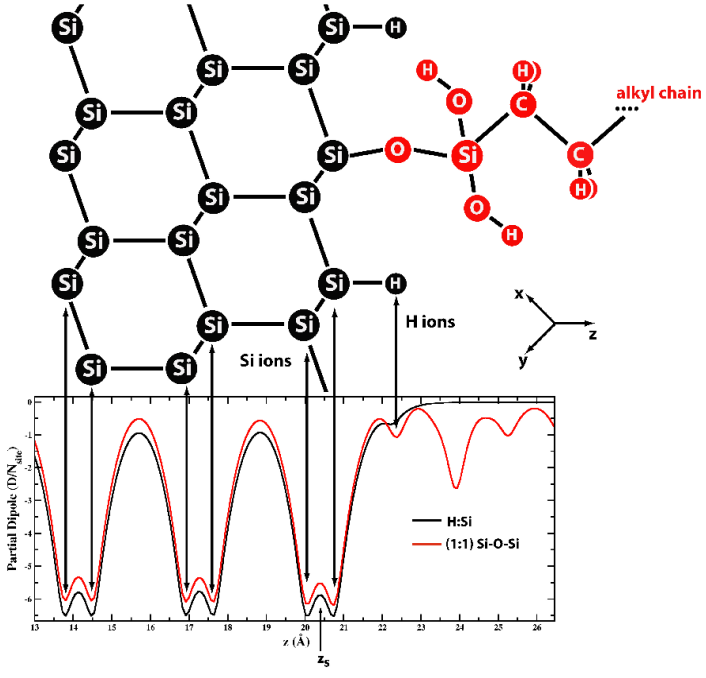

Fig. 2 Partial dipole as a function of z, for the H:Si slab (black line) and 1x(1:1) structure (red line). The surface dipoles have been evaluated at z_s, which is one of the special planes dividing the whole structure into two neutral subunits.

Due to the PBCs along the x, y directions of the supercell, the work functions and the partial dipoles calculated must be considered as the values of a (111) Si surface partially covered, the coverage ratio being 1/16, 1/8, and 3/16 for the (1:1), (1:2), and (1:3) cases, respectively; indeed, due to the different bonds per molecules in the three cases, only the (1:1) case makes a full coverage possible while, in the other two cases, the theoretical maximum coverage values (MCV), i.e., the maximum number of OTS molecules that can be arranged on the surface divided by the number of single adsorption sites (16 in our supercell), are respectively MCV(1:2) = 50% and MCV(1:3) = 33%. Therefore the cases described above correspond to MCV(1:2)/4 and MCV(1:3)/1.8 for (1:2) and (1:3), respectively. The work function difference with respect to the bare H:Si depends on the packing density of the adsorbent species, i.e., on the coverage ratio; hence, adsorption configurations including more than one OTS† molecule on the same portion of the Si surface have been studied. We have first considered two OTS† molecules attached with one bond per molecule at adjacent sites of the Si surface (2x (1:1) configuration).

Dipolar interactions between the adsorbed molecules act, in general, as depolarizing factors that decrease the overall dipole moment; furthermore, the self-assembling mechanism, which is promoted by the hydrogen bonds between the adjacent molecules, have an effect on both the partial dipole and the Z-potential because the orientation of the polar hydroxyl groups of OTS† may be different. Two configurations, both involving two OTS† molecules but differing by the number of hydrogen bonds between them, have been examined and compared (see Figure 3, where the two configurations are labeled as (a) and (b)).

Configuration (b) in Figure 3 is the most stable and exhibits a total energy that is lower by $\Delta E = 247$ meV with respect to configuration (a) of Figure 3. This is due to the stronger hydrogen bonding of configuration (a), resulting in a closer proximity of the two molecules that are highly packed (d_{OH} =1.67 Å with respect d_{OH} = 1.75 Å in (b)) and therefore repel each other. In the first configuration (a) (Figure 3), the SAM molecules interact, forming two H-bonds while in the second
configuration (b) (Figure 3), only one H-bond is formed between the molecules; hence, we can use these systems to estimate the contribution of a single OH group to the work function.

The work functions of the two configurations referring to the bare H:Si configuration are respectively $\Delta\Phi = -97$ meV and $\Delta\Phi = -230$ meV for the (a) and (b) configurations; this is consistent with the fact that the relative xy planar rearrangement of the hydroxyl groups is more marked in configuration (a) than in (b) due to the formation of an additional H-bond.

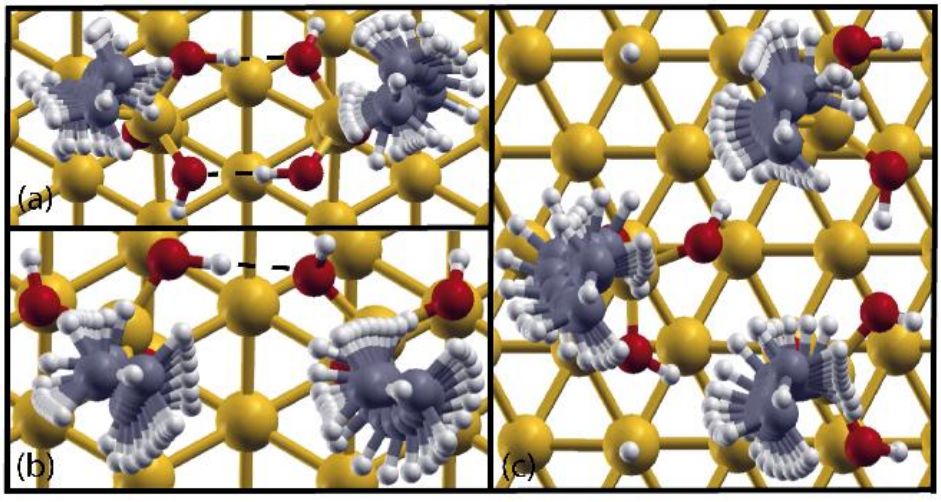

Fig. 3 (111) top view of various (1:1) adsorption configurations involving two or three OTS† molecules at adjacent sites: two molecules interacting through two H-bonds (a), two molecole forming only one H-bond (b), and three OTS† molecules adsorbed on adjacent sites (c).

Indeed the two configurations have nearly identical average charge densities in the *xy* plane except for one oxidryl group that, in (a), stays almost in the xy plane while, in (b), it forms an angle of θ_{up} = 40° with the surface normal. Therefore, the OH dipolar contribution can be evaluated as follows:

$$d_{OH}=[d^{(b)}(z_{C\text{-}C})- d^{(b)}(z_{Si\text{-}O})-(d^{(a)}(z_{C\text{-}C})- d^{(a)}(z_{Si\text{-}O}))]/\cos(\theta_{up}) \quad (8)$$

where z(C−C) and z(Si−O) are the z coordinates of the midbonds of, respectively, the C−C bond of the alkyl chain that is the closest to the surface and of the adhesion Si−O bond belonging to the hydroxylated silane group (see Figure 1), giving d_{OH} ~0.6 D.
The voltage between the vacuum and the bulk Si can be obtained from eq. 6 as:

$$\Delta V=V_{el}(\infty) - V_{el}(0)=(e/2\varepsilon_0 A)d(0)= (e/2\varepsilon_0 A)(d_1+d_s) \quad (9)$$

and can be simply interpreted as a multilayer capacitor [27] where d_1 is the dipole arising from the bulk Si atoms while d_s accounts for the various contribution of the dipoles associated with the alkyl chains, the hydroxylated silane group (including the Si−O−Si bridging bonds and H-bonds, if present), and last of the polarization and charge reordering at the topmost Si layers induced by the OTS† molecules. Due to the limited thickness of the Si slab, d_s has been chosen to include only the topmost (111) Si plane of the substrate, d(0) being calculated at the central Si layer as already discussed (see Figure 1).
Hence, if each SAM molecule is adsorbed on the Si surface with the same number of covalent bonds per molecule and if the Si slab rearrangement is negligible below the topmost Si layer in the minimum coverage ratio adsorption configuration, it can be assumed that d1 keeps the same value as that calculated in the minimum coverage case (i.e., MCV(1:1)/16); thus, from eq. 7, the work function referring to the hydrogenated Si surface casts into:

$$\Delta\Phi[n]\approx-(e^2/2\varepsilon_0 A)\, \Delta d_s[n] \quad (10)$$

where n is the number of SAM molecules adsorbed on the surface and $\Delta d_s[n]$ is the corresponding surface dipole change (projected on the surface normal) with respect to the H:Si case.

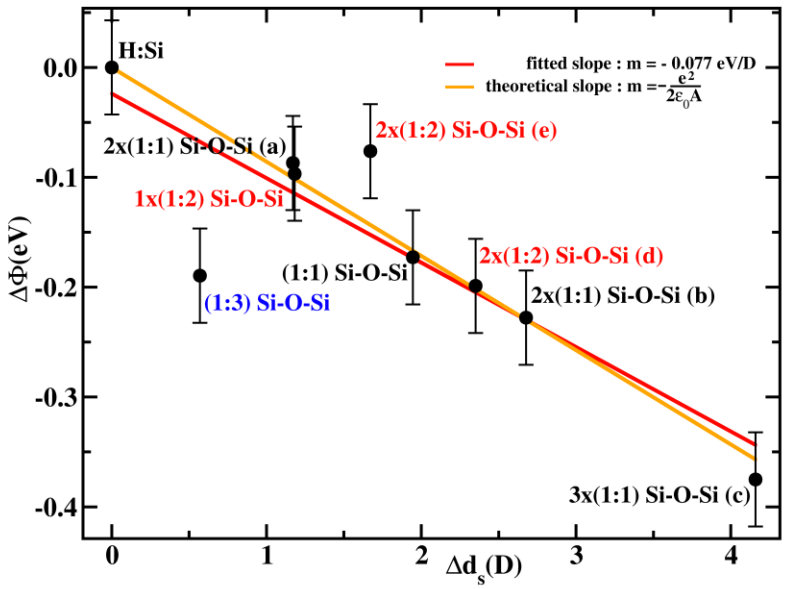

Fig. 4 Work function shifts ΔΦ with respect to the hydrogenated (111) Si surface as a function of Δd_s for the various configurations studied.

The relationship between the work function and the surface dipole is drawn in Figure 4, demonstrating a clear linear dependence of the work function on the surface dipole for the 1x(1:1) and 2x(1:1) configurations studied. The linear dependence is still valid also for the case n = 3 (corresponding to 3/16 MCV(1:1)), i.e., the ground-state configuration of three (1:1) OTS† molecules adsorbed on the Si surface, whose configuration (c) is shown in Figure 3.

Nearly the same linear relationship can be found if one considers the (1:2) adhesion stoichiometry: indeed, as shown in Figure 4, the calculated variations of the work function and surface dipole for different surface coverage ratios (MCV(1:2)/4 and MCV(1:2)/2 stay on the same linear fit found for the (1:1) adhesion, except for configuration (e) (see Figure 5) that, however, is not characterized by self-assembling features, being reported only for completeness. Concerning (1:3), on the contrary, the calculated work function and surface dipole deviate markedly from the linear fit discussed above. The reason for such a behavior is that the assumption of negligible relaxation of the Si bulk atoms does not hold anymore, as discussed above. Rigorously speaking, a small relaxation of the Si slab occurs in each case studied, and this is the reason why the slope of the linear fit deviates from the theoretical value of −0.0858 eV/D by about 10%, being −0.077 eV/D instead.

The linear relationship between the work function and the surface dipole values suggest a simple route to get a realistic estimate of the $\Delta\Phi^{full}$ at full coverage by computing the corresponding change of $\Delta d_{s,full}$ when a densely packed layer of OTS† molecules with (1:1) stoichiometry is adsorbed; partial dipole ds, in fact, can be further decomposed as $d_s = d_2 + d_3$, as schematically drawn in the left panel of Figure 1 (a): d_2 is the contribution of the dipoles in the upper region of the surface accounting for the stoichiometry of the covalent bonding and the interactions between OH groups, while d_3 includes the dipole moment of the OTS†'s alkyl chains.

However, from the relaxed geometry of the (1:1) configurations studied, it appears that the distortions of the CH_2 units lie mostly in the *xy* plane, and thus their dipole moments do not contribute to d_3; then it can safely be assumed that the value of d_3 comes almost entirely from the dipole moment of the terminal CH_3 groups. Moreover the d_2 contribution mainly depends on both the orientation of the OH groups with respect to the z direction and the dipole related to the Si−O−Si adhesion bonds. These considerations allow a reasonable prediction of the work function change,$\Delta\Phi^{full}$, at full coverage, provided good estimates of d_2 and dCH_3 are given.

The z component of the OH dipole has already been estimated above, and therefore we need to give reliable estimates of the dipole moments of the methyl group and of the Si−O−Si bridge bonds (referring to the hydrogenated Si surface). Concerning the methyl group, we simply take the partial dipole at the first C−C midbond below CH_3 that provides $d_{CH3} \simeq -1.67$ D, the contribution of $(CH_2)_{17}$ being quite small ($d_{(CH2)17} \simeq -0.19$ D and resulting in a work function change of ≈14 meV, which is close to the value recently found for a methylene group in alkylthiols on GaAs[28]). The contribution from the Si−O−Si structure can now be obtained directly from the configuration 1x (1:1) by noticing that the orientations of the two OH groups in this case cancel out, being equal but opposite in orientation with the angles with respect to the z axis of 38° and 128° for the one pointing up and the one pointing down, respectively (see Figure 1a); thus, the difference Δd_2 between the (1:1) Si−O−Si case and H:Si is due just to the dipole moment of the Si−O−Si bond and of a H:Si bond that must be removed from the adsorption site resulting in $d_{Si-O-Si} \cong 3.42$ D. Now, before extrapolating the results for full coverage of the (1:1) adhesion, we show that a simple superposition of the above contributions can be arranged to predict the above calculated surface dipoles that are reported in Figure 4. Let us first examine the configuration 3x(1:1): it is characterized by three Si−O−Si adhesion structures, three methyl groups, and six OH groups, four oriented downward, one upward, and one lying in the xy plane; therefore, using the above estimates, we get a partial dipole at the surface $\Delta d_s \simeq 4.08$ D that is quite close to the surface dipole calculated through the partial dipole. Concerning the most stable configuration 2x(1:1) (b), reported in Figure 3, the same analysis gives $\Delta d_s \simeq 3.04$ D, which is not far from the value obtained from the partial dipoles $\Delta d_s \simeq 2.68$ D.

The 2x(1:1) structure (a) reported in Figure 3 deviates from the linear behavior because of a marked distortion of the Si−O−Si structures with respect to the ground-state configuration but its surface dipole can be again obtained in the context of this simple model by using a revised value of the of the Si−O−Sidipolar contribution.

At full coverage, for each OTS† molecule adsorbed with the (1:1) stoichiometry, one of the two free hydroxyl groups binds the adjacent molecule through a planar H-bond carrying no dipole moment in the z direction, while the other is, in principle, free to point up or down with respect to the normal direction of the surface; however, the relative orientations of the hydroxyl groups of the 3x(1:1) configuration c in Figure 3 indicates that the O atoms of the Si−O−Si bridge bonds may also participate in the formation of an intermolecular H-bond by forcing the downward orientation of a neighboring OH group (with an angle between 114° and 128°) and, contextually, by stabilizing the whole configuration. The above considerations lead to an estimate of $\Delta d_2^{full} = |d_{Si-O-Si}| + |d_{OH}|\cos(\theta)$ per SAM molecule.

To consider the depolarization induced by the neighbors on a single alkyl chain in a full coverage condition, the d_{CH3} term has been revised in a system mimicking the full coverage of the Si surface; the resulting value reported in Table 2 shows a dipole moment of the methyl group per molecule slightly smaller than the one obtained in the 1x(1:1) configuration, due to a depolarization effect. Then we were able to estimate the surface dipole under full coverage conditions by simply superposing the various dipolar contributions giving $\Delta d_s^{full} = 26.56 \pm 0.50$ D which results in $\Delta\Phi^{full} \simeq -2.04 \pm 0.04$ eV.

TABLE 2. Partial Dipole Moments for Various Configurations with (1:1) Adsorption Stoichiometry

Configuration	d_2(D)	d_{CH3}(D)	d_{CH3}/n(D)
H:Si	-92.89	-	-
1x(1:1)Si-O-Si	-91.36	-1.67	-1.67
2x(1:1)Si-O-Si	-89.44	-2.80	-1.40
3x(1:1)Si-O-Si	-87.34	-3.95	-1.32
Full coverage	-	-20.80	-1.30

Concerning the (1:2) adhesion stoichiometry, we have to consider that the tilt angle of the alkyl chain is about $\theta_{tilt} = 33°$ and that the adsorbed molecule is rotated around the x axis by about $\theta_x \simeq 54°$ with respect to the 1(1:1) configuration (see Figure 1(a),(b)). Therefore, the *z* component of the methyl partial dipole becomes $d_{CH3} \simeq -2.52$ D, which is larger than the methyl contribution in the (1:1) adhesion configurations by about 60%; such a striking difference is a consequence of the different relative orientation of the CH_3 groups, resulting in a different xy average of the total charge $\bar{\rho}(z)$ that affects to a large extent the partial dipole calculated from eq 5. In addition, the CH_2 groups of the chain do not lie in the *xy* plane anymore and, consequently, add a non negligible dipolar contribution of $d_{(CH2)17} \simeq -1.13$ D. The dipole moment arising from the Si−O−Si structure, on the contrary, can be obtained similarly to the (1:1) case by noticing that the OH group is oriented upward with respect to the *z* axis of 67° (see Figure 1b); thus, the difference Δd_2 between the 1x(1:2) case and the hydrogenated Si is due to the dipole moment of the double Si−O−Si bonds structure and to that of the OH group pointing up; using the above estimate for the OH dipole, we obtain in this case $d_{Si-O-Si} \simeq 4.59$ D. The validity of such values has been checked on two different 2x(1:2) configurations corresponding to a coverage of MCV(1:2)/2 and represented in Figure 5: the first one is a pseudo-self-assembled configuration (d) made of two parallel OTS† molecules adsorbed on adjacent sites (Figure 5), while the second one (e) is made of two randomly oriented OTS† molecules (Figure 5) mimicking the first formation stage of a disordered SAM on the substrate. For such configurations,

our simple toy model predicts the surface dipoles values of $\Delta d_s^{(d)} \simeq 2.81$ D and $\Delta d_s^{(e)} \simeq 1.43$ D, not far from the corresponding values measured with the partial dipoles of respectively $\Delta d_s^{(d)} \simeq 2.35$ D and $\Delta d_s^{(d)} \simeq 1.67$ D (see Figure 4). The above considerations demonstrate that, as in the (1:1) case, the adopted simple toy model permits the prediction of the surface partial dipoles within an error of ≤20%; hence, the extrapolation of such a quantity to larger coverage values until MCV(1:2) is possible within an acceptable error bar. At MCV(1:2) we get an estimate of $\Delta d_s^{full} \simeq 1.17 \pm 0.50$ D per SAM molecule for the case where all the OH groups are oriented upward, resulting in $\Delta\Phi full \simeq -0.72 \pm 0.04$ eV for the (1:2) adhesion stoichiometry at full coverage that is well below the work function shift obtained in the (1:1) case.

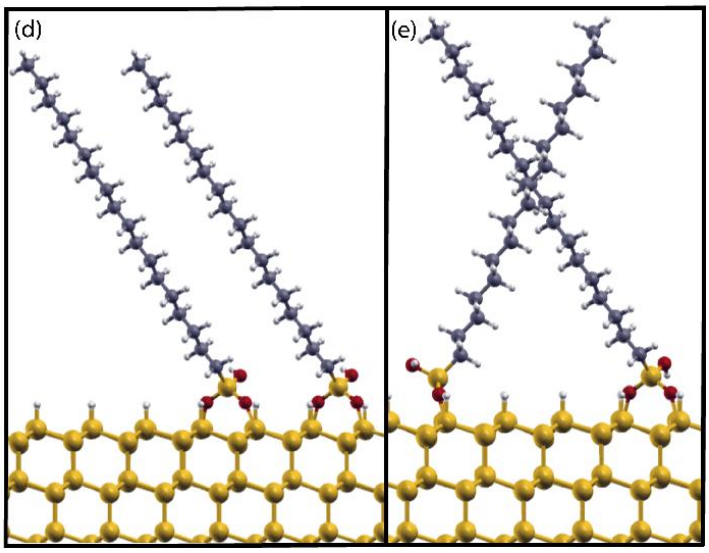

Fig. 5 Two possible configurations of the 2x(1:2) adhesion stoichiometry: self-assembling geometry (d) and disordered geometry (e).

The analysis of the (1:3) adhesion pattern and surface dipole was not possible in this context because the surface relaxation is pronounced in this case making the hypotheses on the base of the toy model invalid. Anyway, as mentioned in section 1, some experimental results seem to indicate that the (1:3) adsorption configuration is dubious during standard deposition conditions[14], and hence we are confident that the data reported and discussed here, without lack of generality, could be used for experimental comparison and predictions.

Acknowledgements

Computational resources have been provided the Italian National Agency for New technology, Energy and the Environment (ENEA) under the ENEA-GRID CRESCO project. We warmly acknowledge these institutions for contributing to the present article.

References

[1] KÄLBLEIN D., WEITZ T., BÖTTCHER H. et al. "*Top-Gate ZnO Nanowire Transistors and Integrated Circuits with Ultrathin Self-Assembled Monolayer Gate Dielectric*" Nano. Lett. **11** (2011) pp. 5309-5315

[2] HONG J., PARK A.Y., LEE S., KANG J. "*Tuning of Ag work functions by self-assembled monolayers of aromatic thiols for an efficient hole injection for solution processed triisopropylsilylethynyl pentacene organic thin film transistor*" Appl. Phys. Lett. **92** (2008) pp. 143311-1-143311-3.

[3] LANE J. M. D., CHANDROSS M., LORENZ C. D., STEVENS M. J., GREST G. S. "*Water Penetration of Damaged Self-Assembled Monolayers*" Langmuir **24** (2008) pp. 5734-5739.

[4] WANG M., LIECHTI K. M., SRINIVASAN V., WHITE J. M., ROSSKY P. J., STONE M. T. "*A Hybrid Continuum-Molecular Analysis of Interfacial Force Microscope Experiments on a Self-Assembled Monolayer*" J. Appl. Mech. **73** (2006) pp. 769-777

[5] CHINAPPI M., CASCIOLA C. M. "*Intrinsic slip on hydrophobic self-assembled monolayer coatings*" Phys. Fluids **22** (2010), pp. 042003-1-042003-8.

[6] CHINAPPI M., GALA F., ZOLLO G., CASCIOLA C. M. "*Tilting angle and water slippage over hydrophobic coatings*" Phil. Trans. R. Soc. A **369** (2011) pp. 2537-2545.

[7] BOULAS C., DAVIDOVITS J. V., RONDELEZ F., VUILLAUME D. "*Suppression of Charge Carrier Tunneling through Organic Self-Assembled Monolayers*" Phys. Rev. Lett. **76** (1996) pp. 4797-4800.

[8] VUILLAUME D., BOULAS C., COLLET J., DAVIDOVITS J. V., RONDELEZ F. "*Organic insulating films of nanometer thicknesses*" Appl. Phys. Lett. **69** (1996) pp. 1646-1648.

[9] COLLET J., VUILLAUME D. "*Nano-field effect transistor with an organic self-assembled monolayer as gate insulator*" Appl. Phys. Lett. **73** (1998) pp. 2681-2683.

[10] KHODABAKHSH S., POPLAVSKYY D., HEUTZ S., NELSON J., BRADLEY D. D. C., MURATA H., JONES T. S. "*Using Self-Assembling Dipole Molecules to Improve Hole Injection in Conjugated Polymers*" Adv. Func. Mater **14** (2004) pp. 1205-1210.

[11] YASSERI A. A., SHARMA S., KAMINIS T., XIA Q., CHOU S. Y., PEASE R. F. W. "*Alkylsiloxane self-assembled monolayer formation guided by nanoimprinted Si and SiO_2 templates*"Appl. Phys. Lett. **89** (2006) pp. 153121-1-153121-3.

[12] ULMAN A. "*Formation and Structure of Self-Assembled Monolayers*" Chem. Rev. **96** (1996) pp. 1533-1554.

[13] FADEEV A., McCARTHY T. "*Self-Assembly Is Not the Only Reaction Possible between Alkyltrichlorosilanes and Surfaces: Monomolecular and Oligomeric Covalently Attached Layers of Dichloro- and Trichloroalkylsilanes on Silicon*" Langmuir **16** (2000) pp. 7268-7274.

[14] ROUMELIOTIS P., UNGER K. K., "*Structure and Properties Of n-Alkyldimethylsilyl Bonded Silica Reversed-Phase Packings*" J. Chromatogr. **149** (1978) pp. 211-224.

[15] ALLARA D., PARIKH A., RONDELEZ F. "*Evidence for a Unique Chain Organization in Long Chain Silane Monolayers Deposited on Two Widely Different Solid Substrates*" Langmuir **11** (1995) pp. 2357-2360.

[16] BIERBAUM K., KINZLER M., WÖLL C., HÄNE G., HEID S., EFFENBERGER F. "*A Near Edge X-ray Absorption Fine Structure Spectroscopy and X-ray Photoelectron Spectroscopy Study of the Film Properties of Self-Assembled Monolayers of Organosilanes on Oxidized Si(100)*" Langmuir **11** (1995) pp. 512-518.

[17] JEON N., FINNIE K., BRANSHAW K., NUZZO R. "*Structure and Stability of Patterned Self-Assembled Films of Octadecyltrichlorosilane Formed by Contact Printing*" Langmuir **13** (1997) pp. 3382-3391.

[18] GALA F., ZOLLO G. "*Functionalization of hydrogenated (111) silicon surface with hydrophobic polymer chains*" Phys. Rev. B **84** (2011) pp. 195323-1-195323-10.

[19] PREDEW J., BURKE K., ERNZERHOF M. "*Generalized Gradient Approximation Made Simple*" Phys. Rev. Lett. **77** (1996) pp. 3865-3868.

[20] TROULLIER N., MARTINS J. "*Efficient pseudopotentials for plane-wave calculations*" Phys. Rev. B **43** (1991) pp. 1993-2006.

[21] GIANNOZZI P., BARONI S., BONINI N., CALANDRA M., CAR R., CAVAZZONI C., CERESOLI D., et al. *"QUANTUM ESPRESSO: a modular and open-source software project for quantum simulations of materials"* J. Phys.: Condens. Matter **21** (2009) pp. 395502/1-395502/19.
[22] BENGTSSON L., "*Dipole correction for surface supercell calculations*" Phys. Rev. B **59** (1999) pp. 12301-12304.
[23] MOKHORST H., PACK J. "*Special points for Brillouin-zone integrations*" Phys. Rev. B **13** (1976) pp. 5188-5192.
[24] FLETCHER R. "*A new approach to variable metric algorithms*" The Computer Journal **13** (1970) 317-322.
[25] GRIMME S. "*Semiempirical GGA-type density functional constructed with a long-range dispersion correction*" J. Comput. Chem. **27** (2006) pp. 1787-1799.
[26] NATAN A., KRONIK L., SHAPIRA Y. "*Computing surface dipoles and potentials of self-assembled monolayers from first principles*" Appl. Surf. Sci. **252** (2006) pp. 7608-7613.
[27] TAYLOR D., BAYES G. "*Calculating the surface potential of unionized monolayers*" Phys. Rev. E **49** (1994) pp. 1439-1449.
[28] AQUA T., COHEN H., SINAI O., FRYDMAN V., et al. "*Role of Backbone Charge Rearrangement in the Bond-Dipole and Work Function of Molecular Monolayers*" J. Phys. Chem. C **115** (2011) pp. 24888-24892.

LES INVESTIGATION OF TURBOMACHINERY FLOWS

Borello, D., Cardillo, L., Corsini, A., Delibra, F., Rispoli, F. and Salvagni, A.
Dipartimento di Ingegneria Meccanica e Aerospaziale
Università di Roma "La Sapienza"
Corresponding author: *domenico.borello@uniroma1.it*

Introduction

The present contribution aims to illustrate the research activities carried out in 2012 by the group working at Dipartimento di Ingegneria Meccanica e Aerospaziale, Sapienza Università di Roma, using the CRESCO computational resources.

The research group has a long record of publication in the field of Computational Fluid Dynamics and it is cooperating with ENEA groups since 2001. During 2012, the numerical investigations were focused on the LES-like investigations of the flow in turbomachinery relevant flows.

Two main research lines were pursued in this field: a) aerodynamic analysis of flow in the blade vane of an axial flow fan [1]; b) analysis of the flow in a rotating rib-roughened duct reproducing the internal cooling mechanism in a turbine blade [2].

Both of these activities led to a production of two papers presented to peer-reviewed International Conferences and now submitted for publication in journals or selection of papers.

In the following a brief description of the two simulations is carried out.

Aerodynamic analysis of an axial flow fan for motorway tunnels

For this application we used OpenFOAM 2.1.0 code that is available on the CRESCO machines. The blade vane of a 3D axial flow fan was previously analysed by some of the authors to investigate the presence of turbulent unsteadiness and its influence on aerodynamic noise. As a matter of fact, very strict regulations are now enforced in terms of noise in motorway tunnels and then, in recent years the efforts in design procedure were devoted not only on performance, but also in reduction of aerodynamic noise. Furthermore, the passage of trucks and cars under the fans induces pressure pulses on the fan inlet and this affects the aerodynamic performance of the machine. To perform a LES of such a case a very refined 9 Mo. cells grid was considered (see Fig.1.a).

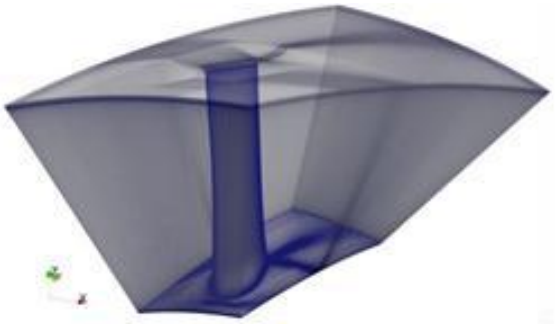

Fig.1.a Computational domain

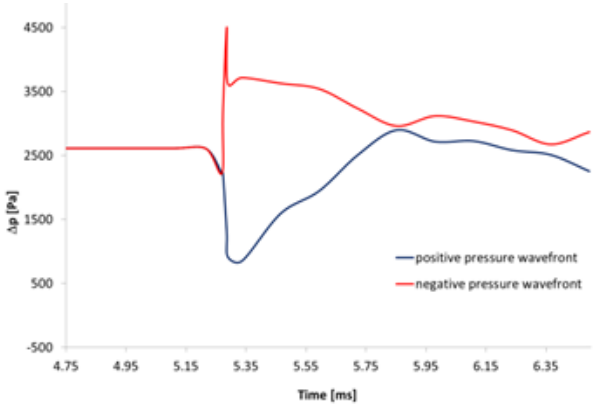

Fig.1.b Static pressure rise evolution after pressure pulses

A velocity profile was set in inflow. This profile was regularly perturbed imposing a constant rate of variation (5%) to the velocity profiles to simulate the passage of trucks in the tunnel. The pressure-rise of the rotor stage over time during the pressure pulses (considered both positive and negative) is shown in Fig.1.b. As the positive pressure wave-front hits the fan a sudden drop is recognizable due to choking. The rotor adapts to the increase of volume flow, the pressure rise is recovered and the operating point moves to reach the equilibrium point on the characteristic curve. The effect of a

negative wave-front is less drastic: a sudden pressure rise, that can be explained with the sudden increase of lift on the blade, is recognizable, after which the rotor adapts again to the new volume flow rate.

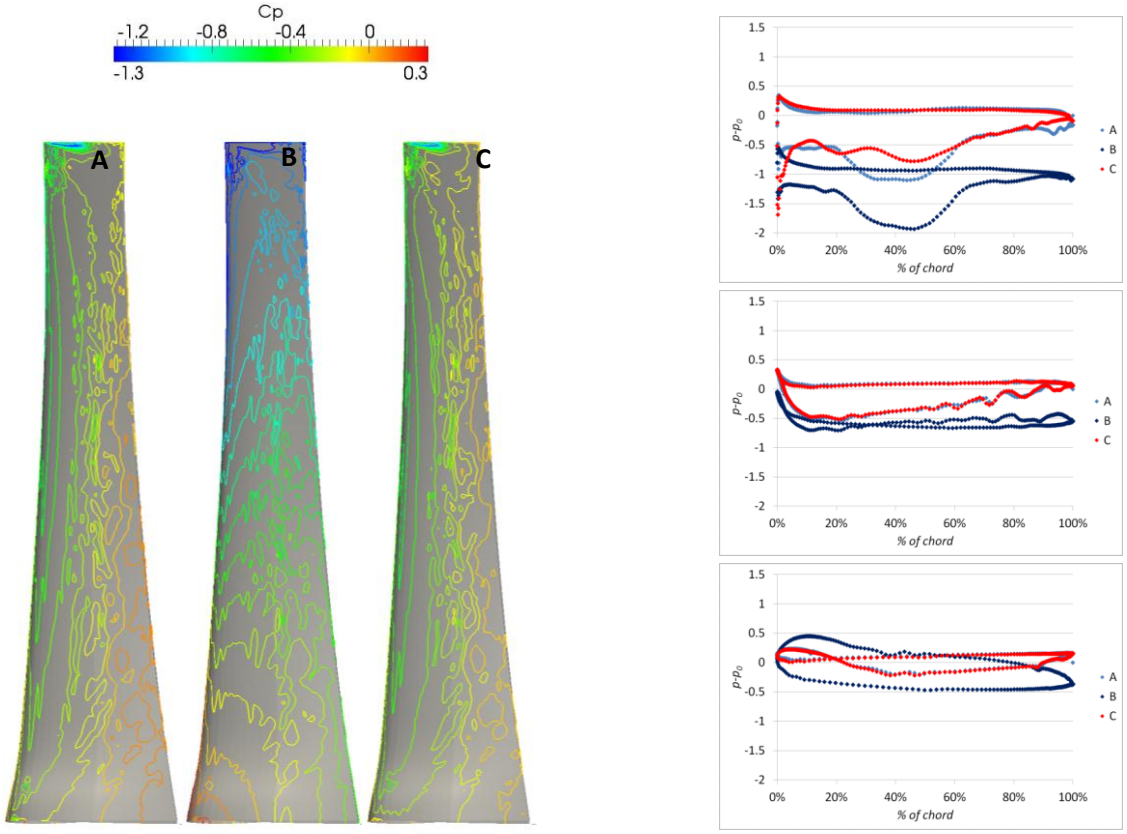

Figure 2 Left: pressure coefficient on the suction surface of the rotor for instants A, B, C. Right: pressure coefficient along the blade at tip (top), midspan (middle) and hub (bottom).

In Figure 2, the static pressure coefficient distribution over the suction surface of the blade is shown for the positive pressure wave case, together with plots at tip, mid-span and hub to give an insight of the sudden increase of mass flow. Iso-contours of pressure coefficient show the sudden change of the pressure distribution during the pulse (label B) confirmed by pressure iso-lines over the suction side of the surface of the blade that show a clear 90 deg turning.

Nevertheless the rotor adapts to the new volume flow rate (label C) quite quickly as shown from the evolution of C_p. As the rotor is working at operating point (A) or adjusting to the new volume flow rate (C) pressure-isolines are quasi-vertical and aligned with the blade span, whereas during pressure pulse (B) isolines are more radial and give evidence of a flow separation from the hub to 2/3 of the span, while the outer section, in proximity of the tip, is still capable of contributing to the rotor pressure developing capability. Distribution of the pressure coefficient show also that the blade is stalled during the pulse at mid-span while is still able to provide lift at the tip and the hub.

Conspicuous data for the sudden drop of flow rate are shown in Figure 8 that reveals a different behaviour. As the pulse hits the blade the rotor adjust to the drop of mass flow increasing the work and so the lift over the blade. In this case the distribution of pressure isolines remains “vertical”, yet an increase of load at mid-span is recognisable. Distributions of the pressure coefficient show that mid-span and tip sections are over-loaded. At the hub the effect of the pressure wave is to recover the work capability of the blade, that in normal operations is compromised. In fact the design of the blade at the hub is constrained by mechanical requirements that do not allow an aerodynamic optimisation.

Further details about the simulation are reported in the cited paper.

LES of flow in a rotating rib-roughened channel

For this application we used T-FlowS code that is a FV unstructured parallel research code developed by some of the authors. We implemented, checked and validated T-FlowS on the CRESCO machines since 2007.

The test case is particularly relevant for the analysis of internal cooling efficiency in the first stages of turbine blades. At the moment only the flow field is investigated while it is expected that the heat transfer simulation will start in the autumn 2013.

A refined LES analysis is required in this case due to the presence of very small structures generated by the interaction of the several walls and the influence of rotation. The grid used has 6 Mo. cells. Here we present the results of the case with anti-clockwise rotation corresponding to a destabilizing effect on the ribbed surface. The rotational number is equal to 0.3

The channel has an aspect ratio equal to 0.9 and the ribs generate a blockage factor of 0.1, h is the rib height. The Navier-Stokes equations system was solved in dimensionless variables. As reference values we used duct hydraulic diameter, bulk flow velocity and air properties at 20 °C. The ensuing Reynolds number is equal to 15,000.

A Crank-Nicolson/CDS scheme was adopted to obtain a second-order accurate solution. Fully coupled solution of the Navier-Stokes system was obtained using the SIMPLE scheme, while the Preconditioned BiCG solver is adopted for the solution of the algebraic linearized equation system. Periodic boundary conditions were imposed at the inlet and outlet surface in stream-wise conditions. On the solid walls no-slip conditions were set. The non-dimensional time step was selected equal to 5e-4. The maximum CFL number is smaller than 0.3. The computations were performed on the CRESCO SP5 cluster at Casaccia (ENEA) using 32 processors. On such a computer 25 seconds are required for performing 1 time step for both computations on the fine grid. Computations were performed for 2 flow through times (FTT) before starting to collect statistics.

To analyse the influence of Coriolis forces on the mean flow, streamlines are plotted for the rotating simulations in Figure 3.

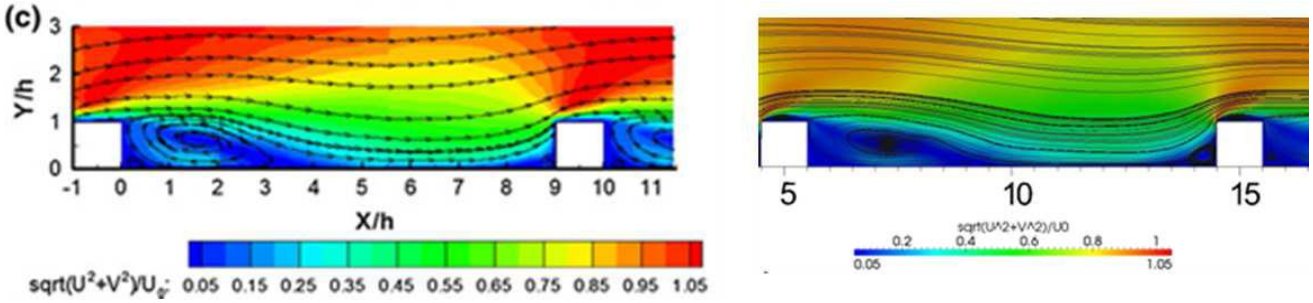

Fig. 3 Streamlines for the rotating case - left: exp; right: LES

The presence of the rib generates a large recirculation bubble. The anti-clockwise rotation enhance the entrainment of the separated region, leading to a pressure reduction in the separated region. This stronger pressure gradient induces a stronger streamlines deviation and to a reduction in the length of the separation bubble when compared with the results of the non-rotating case.

The influence of the lateral walls on the flow field were out of the scope of the PIV (referring only to the mid-plane). It is then interesting to investigate the influence of rotation in planes that are parallel to the rib-roughened wall.

In particular, we analysed the streamlines plot in two planes: at 0.05 h and 0.5 h far from the wall (Figure 4). On the first plane (0.05 h) it is possible to see the presence of the following vortical structures: upstream corner vortex (clockwise rotation), downstream corner vortex (anti-clockwise) and the recirculation bubble extending for about 0.3 of the space between two consecutive ribs. In the non-rotating case, when moving towards the lateral walls, the recirculation bubble length is strongly reduced and then its footprint of this plane has a bow shape. Notably, this effect is less

evident in the rotating case due to the cited shrinking of the recirculation bubble that is particularly relevant in the mid-plane.

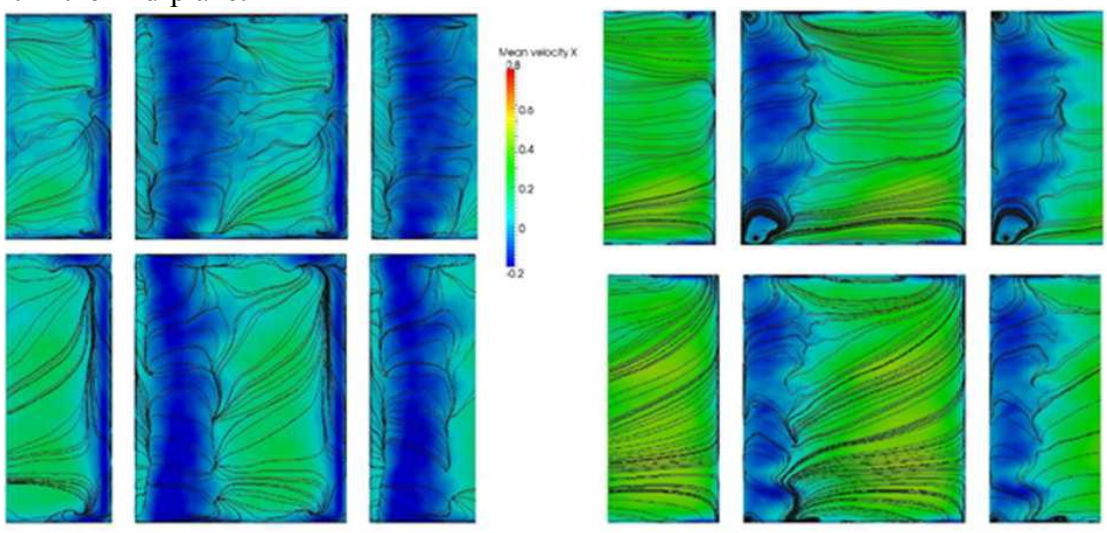

Fig. 4 Streamlines on the wall parallel plane; left: 0.05 h; right: 0.5 h; up: non rotating; down: anti-clockwise rotating

The section at y/h=0.5 shows some differences: first of all the two small vortices close to the rib are not existing at this distance from the wall. Furthermore, two pitch-wise vortical structures are present close to the lateral walls immediately downstream from the rib. Again, the bow shape of the recirculation bubble is somewhat suppressed in the rotating case.

Further details can be found on the publication [2].

Summary & Conclusions

The authors used the CRESCO computational resources in 2012 for studying turbomachinery applications. The analysis allowed to obtain relevant details about the turbulence structures via a LES of flow in an axial flow fan and in a rib-roughened rotating channel.

The results of the simulations allowed to produce two papers presented in peer-reviewed International Conferences and that will be delivered to indexed publications (journals or edited books).

Used Clusters

- Sp-5 AIX clusters at Frascati
- CRESCO cluster at Portici

List of publications

1. Borello, D., Corsini, A., Delibra, G., Rispoli, F. and Sheard, A. G., *'Numerical Investigation on the Aerodynamics of a Tunnel Ventilation Fan during Pressure Pulses'*, 10th European Conference on Turbomachinery, 15-19 April 2013, Lappeenranta, Finland
2. Borello, D., Salvagni, A., Rispoli, F., and Hanjalic, K., 'LES of the Flow in a Rotating Rib-Roughened Duct', Direct and Large Eddy Simulation 9, 3-5 April 2013, Dresden, Germany

Effect of superficial water on the structure of a spherical cluster of ZrO_2

Roberto Grena
C.R. ENEA Casaccia, UTRINN-PCI
e-mail: roberto.grena@enea.it

keywords: ab-initio computations, DFT, structure optimization, nanoclusters. Zirconium oxide

Structural properties of a spherical Zirconium oxide cluster with water molecules on the surface are studied. The work was made as a complement to the experimental research conducted at SPCTS in Limoges (France), where Zirconium oxide nanoclusters of diameter less than 2 nm are produced and studied; the work was done in collaboration with Philippe Thomas, Olivier Masson, Laura Portal and other researchers of the SPCTS. The work is the continuation of a study already described in 2010-2011 Cresco report [1]. The difficulties in reproducing by computation the experimental pair distribution function of the cluster lead to the hypothesis that a surface stabilization occurs in the cluster, caused by impurities or other reasons; this motivates the study of the presence of superficial water on the cluster.

Introduction

Nanoclusters of small size (less than 5 nm) present features that are not reconducible to the properties of the bulk material, and cannot be explained by a simple bulk/surface model, since the overall structural organization of the cluster is altered. Interesting properties can arise, and transition to disordered structure can happen below a certain size. So, many studies are devoted to the characterization of small nanoclusters, with experiments (X-ray diffraction, neutron scattering, TEM microscopy) or simulations (classical or ab-initio molecular dynamics).

At SPCTS, very small clusters of ceramic materials are produced; at the moment, Zirconium oxide clusters with diameter less than 2 nm are under investigation. ENEA is interested in chemically inactive nanoclusters as additive to thermal fluids; ceramic oxide as TiO_2 or ZrO_2 are among the possibilities. For this reason, a simulation of the clusters with CRESCO computational facilities was undertaken; the first results were already described in [1]. Unfortunately, the attempt to reproduce the pair distribution function, obtained at SPCTS with X-ray diffraction, proved to be unsuccessful; the simulated clusters were too much disordered, while from the experimental PDF was clear that a crystalline structure was partially preserved. Among the hypotheses for the discrepancies, the possibility of impurities on the cluster surface was considered; so, a simulation with the most simple and probable impurity (water) was planned.

In the following, the simulation of clusters with different degrees of surface hydration will be described.

Computational details

Computations were made using the Density Functional Theory [2-3] and the Car-Parrinello methods [4]. The software used is CPMD [5], a plane wave - pseudopotential computational software which performs DFT wavefunction calculations, structural optimization, and Car-Parrinello molecular dynamics. The DFT functional chosen for the computation was PBE [6]. Norm-conserving pseudopotentials of Troullier-Martins type [7] were used.

The computations were started from an initial configuration of good sphericity (see Fig. 1) with different numbers of impurities on the surface. The impurities were modeled as OH groups or H atoms bound to atoms on the surface, in order to describe the contamination with H_2O molecules. A number of H_2O

molecules ranging from 0 (absence of impurities) to 24 (complete covering of the surface) was considered.

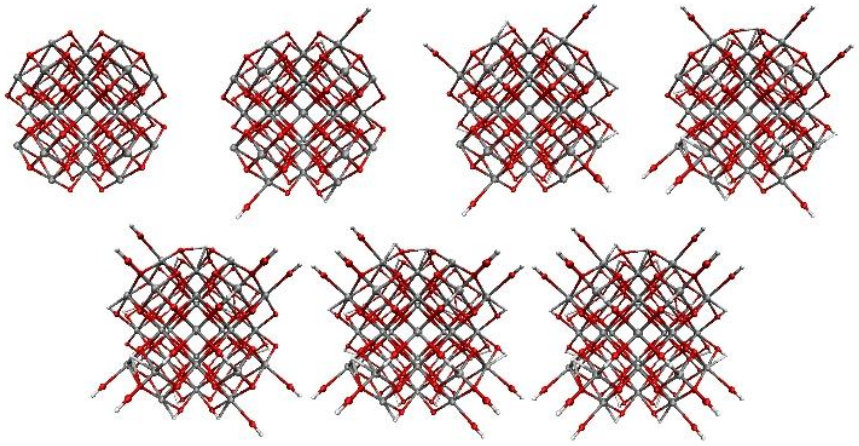

Figure 1: Starting configurations of the clusters. The clusters are ordered with an increasing number of water molecules on the surface, from 0 molecules (left, above) to 24 molecules (right, below), increasing the covering of 4 molecules from a figure to the subsequent.

The system was then relaxed in order to achieve a minimum of energy. Unfortunately, instabilities arise when applying ordinary minimum search; the instabilities are caused by the large number of degrees of freedom; so, an initial relaxation with a long run of low temperature Car-Parrinello molecular dynamics was required to obtain a configuration near a minimum. Then, the configuration was further optimized with ordinary minimization techniques.
The computational task is heavy, for the following reasons:

- The number of atoms to be simulated is high (from 129 to 201 atoms), and the atoms (except H) have a quite large number of valence electrons to consider in the computation (12 for Zr and 6 for O);
- The presence of small-core atoms as Oxygen and Hydrogen requires the use of a large number of plane waves as basis;
- A high degree of disorder arises in many of the clusters, making the geometrical optimization nontrivial.

Tests on parallelization showed significant advantages using up to 96 cores for the computation; for a larger number of cores the advantages were not strong and after 144 cores no gain at all was achieved. So, a number of 96 cores was chosen as a standard. The computational time required depends on the modification of the initial configuration; from about 10 days for the most ordered cluster, to about 1 month for the most disordered one.
Despite the difficulties, an equilibrium configuration was obtained for all the 7 clusters considered. In the case of no impurities, as already discussed in [1], the configuration is probably only a local minimum, and many other minima with similar energy can be found (likely more disordered); however, this is the least interesting case, being too much disordered with respect to the experimental results.

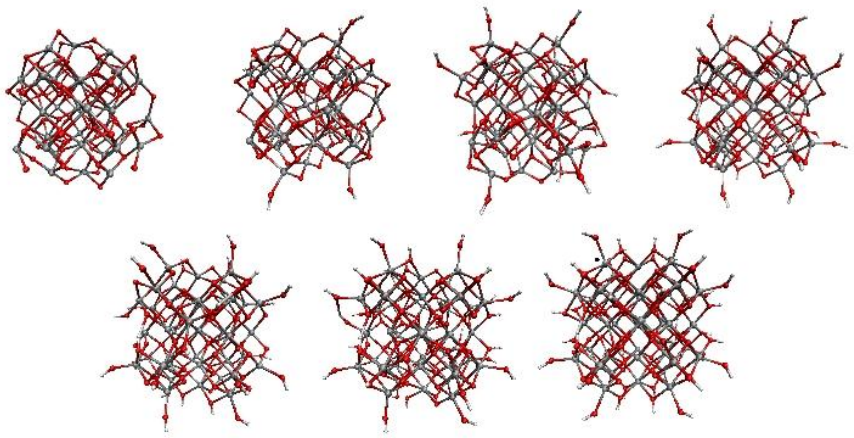

Figure 2: Configurations of the clusters that minimize the energy. The clusters are ordered with an increasing number of water molecules on the surface, from 0 molecules (left, above) to 24 molecules (right, below), increasing the covering of 4 molecules from a figure to the subsequent.

Results

The equilibrium configurations obtained are shown in Fig. 2. From the figure it can already be seen the trend toward more ordered structures with the increasing of water impurities. The cluster with no impurities is highly disordered (and probably not unique); however, even from the figure a much better ordered structure can be observed for 12 molecules and more. At the other extreme, one can see that the cluster entirely covered by water impurities is almost perfectly crystalline; the deviations from the initial configuration are few and concern especially the arrangement of the impurities at the surface. It is interesting to note that the degree of disorder of the clusters with a partial water covering from 12 to 20 molecules are not too different, while an extreme ordering occurs suddenly if the covering is fulfilled. Since the two extreme cases are the most unlikely in the presence of impurities, physical results are probably to be looked for in the intermediate region (12 - 20 molecules); these clusters also presents properties that at a first glance seems largely independent of the exact degree and nature of the covering.

Conclusions

The effect of the partial covering of a ZrO_2 cluster with water molecules is modeled and studied. The covering affects strongly the equilibrium structure of the cluster, increasing the order of the atoms. At the two extremes we found a highly disordered cluster with no water on the surface, and an almost perfect crystal structure with a complete water covering; between these two cases, partially ordered structures are found. The changes are strong near the most ordered case: few “vacancies” in the water covering produce a significant degree of disorder.

Future activities will concern the computation of the pair distribution function of the clusters and the comparison with experimental data. Since the main problem with non-hydrated cluster was the excess of disorder, the ordering induced by the water covering is likely to improve the comparison.

References

[1] R. Grena, Structure and molecular dynamics of a spherical cluster Zr43O86, in High Performance Computing on CRESCO infrastructure: research activities and results 2010-2011 (2012), 179-186.
[2] P. Hohenberg, W. Kohn, Inhomogeneous electron gas, Physical Review 136 (1964), B864 - B871.
[3] W. Kohn, L.J. Sham, Self-consistent equations including exchange and correlation effects. Physical Review 140 (1965), A1133 - A1138.
[4] R. Car, M. Parrinello, Unified Approach for Molecular Dynamics and Density Functional Theory, Physical Review Letters 55 (1985), 2471 - 2474.
[5] W. Andreoni, A. Curioni, New advances in chemistry and material science with CPMD and parallel computing. Parallel Computing 26 (2000), 819 - 842.
[6] J.P. Perdew, K. Burke, M. Ernzerhof, Generalized Gradient Approximation Made Simple, Physical Review Letters 77 (1996), 3865 - 3868.
[7] N. Troullier, J.L. Martins, Efficient pseudopotentials for plane-wave calculations, Physical Review B 43 (1996), 1993 - 2006.

Ab-initio study of amorphous germanium

[1]Giorgio Mancini, [2]Massimo Celino and [1]Andrea Di Cicco

[1]Università di Camerino, Via Madonna delle Carceri 62032, Camerino (MC), Italy
[2]ENEA, C. R. Casaccia, via Anguillarese 301, 00123 Rome, Italy
giorgio.mancini@unicam.it; massimo.celino@enea.it, andrea.dicicco@unicam.it
keywords: materials science, amorphous materials, molecular modeling, ab-initio, molecular dynamics, amorphous Ge

Abstract
We employ ab-initio molecular dynamics simulations to study the atomic structure of amorphous germanium. The preparation of an amorphous Ge numerical sample is performed by cooling down from the liquid phase. Calculated structural and thermal properties of the amorphous phase result in good agreement with experimental data. This is a necessary step for starting a complete characterization of the pressure effects on the amorphous germanium.

Introduction

Amorphous germanium (*a*-Ge) has been largely studied in the last decades using a variety of experimental and theoretical methods, being a material of outmost importance in basic science and applications in everyday life. Moreover the investigation of the structure of the condensed phases of germanium is of importance for fundamental science since it exhibits polymorfism in the solid state and pronounced changes in density and bonding upon melting and application of external pressure.
Germanium in its stable crystalline phase at ambient pressure, has a diamond structure (GeI) in which each atom is surrounded by four covalently bonded first neighbors in a tetrahedral formation. This phase of Ge has a very low density with respect to a close-packed structure and is semiconducting with an indirect gap of about 0.7 eV. Upon application of pressure, the tetrahedrally bonded network is broken and both the number of neighbors and the density increase. Around 11 GPa, a phase transition to the metallic β-Sn structure (GeII) occurs and even at higher pressures a hexagonal phase and a close-packed phase are found. Upon decompression, the crystalline stable structure is not always recovered, rather metastable crystalline phases are observed. The most common one is called ST12 (GeIII). It is based on tetrahedral structure with 12 atoms per unit cell arranged to form fivefold and sevenfold rings. Ge has higher density (about 10%) in this phase than in the underlying stable one Ref. [1]. It is based on tetrahedral structure with 12 atoms per unit cell arranged to form five-fold and seven-fold rings. As reported in Ref. [2], in case of rapid decompression, a cubic structure characterized by eight atoms per unit cell and called BC8 (or GeIV) is likely to occur [2,3]. This structure is not stable at room temperature but it transforms into the lonsdaleite structure (hexagonal with four atoms per unit cell) within a few hours.
At standard pressure the melting temperature of crystalline Ge is T_m= 1210 K. At the melting transition the tetrahedral network is disrupted and the average coordination number increases from 4 to about 7, which is still low compared to other liquid metals which typically have coordination numbers between 9 and 12. Liquid Ge is metallic and amorphous Ge is semi-conducting. Amorphous Ge is characterized by a continuous random network of distorted defective tetrahedra. Numerous experimental investigations of the density and bonding changes in different phases of germanium, using both x-ray [4] and neutron diffraction [5] techniques, are known in literature. Bond lengths do not differ more than 1% from the crystalline phase and bond angles show a modest spread of the order of 10 degrees about the ideal value of the crystalline counterpart.

Moreover *a*-Ge shows a complex behavior when an external pressure is applied, and scattered results are reported in literature. In particular, evidence for a sharp drop in resistivity and crystallization of thin *a*-Ge films was found at about 6 GPa [3,6].
The x-ray absorption spectroscopy (XAS) technique was used to study the evolution of the local structure at high pressures. Freund et al. [7] showed that *a*-Ge remains amorphous up to 8.9 GPa whereas more recent XAS measurements showed that *a*-Ge undergoes a phase transition at 8 Gpa, though remaining amorphous [8]. The glass transitions in Ge under pressure was also studied in recent works both experimentally [9,10] and through molecular dynamic simulations [11]. The combination of Raman and XAS spectroscopy measurements allowed to confirm that 8 GPa mark the onset of a polyamorphic transition in more homogeneous samples [12]. Moreover, Ref. [12] demonstrates that the actual transitions observed in a given sample depend on the initial morphology of the sample itself.
Polymorphism of amorphous Ge is reported to occur between the low-density amorphous (LDA) semiconductor and the high-density metallic amorphous (HDA) states. This intriguing phenomenon is linked to a proposed first-order density, entropy-driven phase transition in the supercooled liquid state. The LDA-HDA transition has been studied in details for thin film samples by x-ray absorption, extended x-ray-absorption fine structure (EXAFS), and Raman scattering methods [8,12,13]. Nevertheless, a detailed and unambiguous understanding of the complex phenomena taking place in *a*-Ge under pressure has been only recently published [13].
In the present paper, we report the study of the structural properties of *a*-Ge via ab-initio molecular dynamics in the framework of density functional theory. The atomic structure is characterized in terms of pair correlation functions, nearest neighbor analysis and neutron structure factor. The very good agreement with experimental results confirms that this amorphous system is a reliable starting point to study the pressure effects.

Computational details
Reliable amorphous structures of Ge are generated in the framework of first-principles molecular dynamics; the software employed is CPMD (Car-Parrinello Molecular Dynamics) [14,15]. The self consistent evolution of the electronic structure during the motion is described within density functional theory. A generalized gradient approximation (BLYP-GGA) is adopted for the exchange and correlation part of the total energy [16,17] and norm conserving pseudopotentials are used for the core-valence interactions. A Γ-point sampling for the supercell's Brillouin-zone integration, a reasonable choice for a 125-atom model, has been adopted. The electronic wave functions were expanded in plane waves up to a kinetic energy cutoff of 60 Ry and an integration time step of 3 a.u. (0.072 fs) was used.
During the equilibration of the liquid and solid structures a Nosé thermostat was used to control the ion temperature [18,19,20]. The characteristic frequency for the thermostat was 1000 cm^{-1}, which lies close to the peak at 37 THz in the diamond phonon density of states. A second Nosé thermostat was used to control the fictitious electronic kinetic energy [21]. This thermostat prevented the electronic wave functions from drifting away from the instantaneous ground state (the Born-Oppenheimer surface), by removing excess fictitious kinetic energy. This drift is particularly severe for metals. In our simulation the liquid Ge sample possesses no band gap and hence the energy transfer rate is high. The characteristic frequency for the thermostat and the target kinetic energy was chosen according to the prescription in Ref. [21]. The Nosé thermostat on the electrons was used throughout the simulation and proved to be an effective way of keeping the electrons on the Born-Oppenheimer surface. During the equilibration of the liquid, the cooling of the liquid, and the temporal averaging of the solid, the deviation from the Born-Oppenheimer surface was never more than 0.01 eV/ion, and was often much less.

This set of parameters yields accurate and converged properties for the dimer Ge_2 as well as for Ge crystalline lattices, both diamond and β-Sn. Further legitimacy of our computational approach comes from the characterization of the amorphous structure described in the next section.
The amorphous structure has been obtained for a system consisting of N= 125 atoms in periodically repeated cubic cells of size L= 14.14 Å. The density is equal to the experimental value for a-Ge at T= 300 K: ϱ= 5.3 gr/cm^3 [22,23]. To ensure that our results are independent of the initial atomic configurations, they are chosen to be drastically different from the crystalline counterpart. Since it is expected that the amorphous structures have a high percentage of four-fold coordinated Ge atoms, the starting configuration has been generated by randomly placing the atoms in the simulation cell. This procedure designs a starting configuration with many defects and many atoms with coordination different from four. We further disordered the configuration by constant temperature and constant pressure MD equilibration at high temperature (T= 4000 K).

Results and discussion

During the high temperature simulations, atoms covered a distance as long as about 2 nm ensuring the final configuration retains no memory of the initial geometry. Then we gradually lowered it to T= 1278 K in 10 ps and performed an additional equilibration for additional 5 ps. The liquid configuration at T= 1278 K, just above the melting temperature, has been used as starting point for the quenching procedure. The amorphous Ge is attained by cooling to 300 K the liquid sample over 8 ps. Then this system was equilibrated for additional 8 ps to gain temporal averages. Two complementary simulations were performed to check the effect of quench-rate on the atomic structure. One used a slower cooling rate whereas in the other one the liquid was cooled instantly to 300 K. In all systems the main features of the amorphous Ge were all reproduced with minimal differences among them. This procedure is an essential check to produce a reliable amorphous atomic structure.

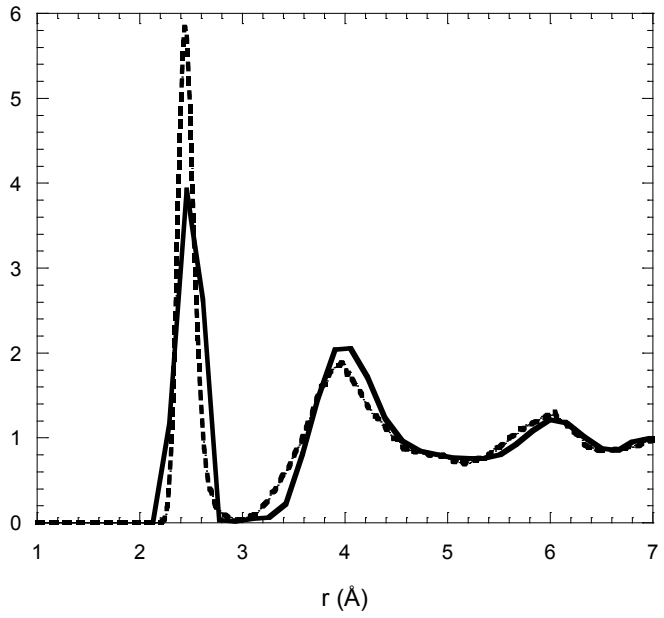

***Figure 1**: Comparison between experimental (continuous line) and ab-initio prediction of the radial distribution function of amorphous germanium.*

To analyze the short-range order of the obtained amorphous phase we have calculated the total radial distribution function, reported in **Fig. 1**. The comparison with the experimental one reported in [23] confirms the reliability of our numerical model. It is interesting to note that our model well

reproduces the position of the first peak at 2.44 Å even if more pronounced. The second peak is located at 3.97 in good agreement with experiments.
The calculation of the coordination, as the integral over the first peak of the radial function, confirms the picture of an amorphous system composed essentially by Ge atoms fourfold coordinated and a few threefold and fivefold coordinated. On the average each atom has 4.06 nearest neighbors: 90.5% of the atoms is four-fold coordinated, 1.8% is three-fold coordinated and 7.7% are five-fold coordinated.

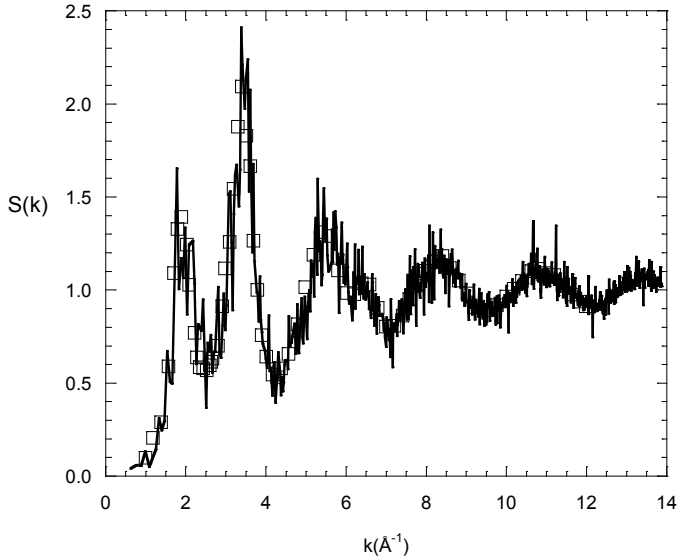

Figure 2: *Comparison between experimental (squares) and ab-initio prediction of the structure function S(k) of the amorphous germanium*

To verify the reliability of our approach also on longer length scales, we have computed the structure factor function. The calculated structure factor is shown in **Fig. 2** together with the neutron structure factor experimentally measured in Ref. [23]. The agreement is very good over the entire k range, the position of maxima and minima being accurately reproduced.

Conclusion

In this report our first goal has been to achieve a precise characterization of the atomic structure of amorphous Ge systems through a simulated sample. This amorphous sample, that we have demonstrated to be a reliable representation of a real amorphous phase, represents a good starting point for the study of pressure effects.
We have shown that our theoretical approach is able to accurately model all the main features of an amorphous system both in the short and long range scale. Moreover we are confident that this procedure can be successfully applied to produce and characterize the amorphous phase under pressure. This approach will allow to accurately study the relations between atomic scale intrinsic defects and the macroscopic structural and electronic properties.

Acknowledgments. The computing resources and the related technical support used for this work have been provided by CRESCO-ENEAGRID High Performance Computing infrastructure and its staff; see www.cresco.enea.it for information. CRESCO-ENEAGRID High Performance Computing infrastructure is funded by ENEA, the "Italian National Agency for New Technologies, Energy and Sustainable Economic Development" and by national and European research programs.

References

[1] F. Bundy and J. S. Kasper. *"A new dense form of solid germanium"*. Science **139** (1963) pp. 340-341.

[2] R. J. Nelmes, M. I. McMahon, N. G. Wright, D. R. Allan, and J. S. Loveday. *"Stability and crystal structure of BC8 germanium"*. Phys. Rev. B 48 (1993) pp. 9883.9886.

[3] O. Shimomura, S. Minomura, N. Sakai, K. Asaumi, K. Tamura, J. Fukushima and H. Endo, *"Pressure – induced semiconductor-metal transitions in amorphous Si and Ge"*. Philos. Mag. **29** (1974) pp. 547-558.

[4] A. Filipponi and A. Di Cicco. *"Short-range order incrystalline, amorphous, liquid, and supercooled germanium probed by x-ray-absorption spectroscopy"*. Phys. Rev. B **51** (1995) pp. 12322-12336.

[5] P. S. Salmon, J. Phys. F: Met. Phys. **18** (1988) pp. 2345.

[6] K. Tanaka. *"Amorphous Ge under pressure"*. Phys. Rev. B **43** (1991) pp. 4302-4307.

[7] J. Freund, R. Ingalls and E. D. Crozier, J. Phys. Chem. **94** (1990) pp. 1087.

[8] E. Principi, A. Di Cicco, F. Decremps, A. Polian, S. De Panfilis and A. Filipponi. *"Polymorphic transition of germanium under pressure"*. Phys. Rev. B **69** (2004) pp. 201201-1-201201-4.

[9] A. Hedler, S. L. Klaumunzer and W. Wesch, Nature Mater. **3** (2004) pp. 804.

[10] M. H. Bhat, V. Molinero, E. Soignard, V. C. Solomon, S. Sastry, J. L. Yarger and C. A. Angell, Nature (London) **448** (2007) pp. 787.

[11] J. Kōga, K. Nishio, T. Yamaguchi and F. Yonezawa, J. Phys. Soc. Jpn. **73** (2004) pp. 388.

[12] A. Di Cicco, A. Congeduti, F. Coppari, J. C. Chervin, F. Baudelet and A. Polian, *"Interplay between morphology and metallization in amorphous-amorphous transitions"*. Phys. Rev. B **78** (2008) pp. 033309.

[13] F. Coppari, J. C. Chervin, A. Congeduti, M. Lazzeri, A. Polian, E. Principi and A. Di Cicco, *"Pressure-induced phase transitions in amorphous and metastable crystalline germanium by Raman scattering, x-ray spectroscopy, and ab initio calculations"*. Phys. Rev. B 80 (2009) pp. 115213.

[14] CPMD V3.13.2 Copyright IBM Corp 1990-2008, Copyright MPI fùr Festkörperforschung Stuttgart 1997-2001.

[15] W. Andreoni, A. Curioni. "*New advances in chemistry and materials science with CPMD and parallel computing"*. Parallel Computing **26** (2000) pp. 819-842.

[16] D. Becke. *"Density-functional exchange-energy approximation with correct asymptotic behavior"*. Phys. Rev. A **38** (1988) pp. 3098-3100.

[17] C. L. Lee, W. Yang and R. G. Parr. *"Development of the Colle-Salvetti correlation-energy formula into a functional of the electron density"*. Phys. Rev. B **37** (1988) pp. 785-789..

[18] M. Parrinello, A. Rahman. *"Polymorphic transitions in single crystals: A new molecular dynamics method"*. J. Appl. Phys. **52** (1981) pp. 7182-7190.

[19] S. Nosé, Mol. Phys. **52** (1984) pp. 255.

[20] S. Nosé. *"A unified formulation of the constant temperature molecular dynamics methods"*. J. Chem. Phys. **81** (1984) pp. 511-519.

[21] P. E. Blöchl and M. Parrinello. *"Adiabaticity in first-principles molecular dynamics"*. Phys. Rev. B **45** (1992) pp. 9413-9416.

[22] G. Etherington, A. C. Wright, J. T. Wenzel, J. C. Dore, J. H. Clarke and R. N. Sinclair. "*A neutron diffraction study of the structure of evaporated amorphous germanium*". J. Non-Cryst. Solids **48** (1982) pp. 265-289.

[23] Y. Waseda, *The structure of non-crystalline materials - liquids and amorphous solids*, McGraw-Hill, New York, 1981.

AMD 6234 Interlagos *vs.* Intel E5-2680 Sandy Bridge. Benchmark of different computational codes.

Simone Giusepponi, Agostino Funel, Fiorenzo Ambrosino, Guido Guarnieri, Giovanni Bracco
ENEA UTICT-HPC

1 Introduction

In this paper we report results concerning the performances of the AMD 6234 Interlagos 2.4 GHz and Intel E5-2680 Sandy Bridge 2.7 GHz processors by running standard application benchmarks. The tests were conducted on an experimental node with 24 cores, 64 GB RAM and 16 cores, 32 GB RAM for AMD and Intel processors, respectively. The Sandy Bridge processor supports Hyper Threading (HT) [1] technology which makes a single physical processor appear as two logical processors. Thus by enabling HT the Sandy Bridge is seen by the OS as a node with 32 cores. With HT each logical processor maintains a complete set of the architecture state but share all other resources on the physical processors (caches, execution units, branch predictors, control logic and buses). Instead of using a single benchmark we have considered several applications which refer to actual usage cases as CFD (Computational Fluid Dynamics) and MD (Molecular Dynamics). We also tested the HPL (High Performance Linpack) code which is a standard benchmark used in the HPC (High Performance Computing) community. In the case of CFD the open source code OpenFOAM and the commercial code Ansys Fluent have been tested. For the MD simulation we used the CPMD code. We also tested both architectures with Intel MPI Alltoall benchmark. Usually this benchmark is used to provide a measure of network performances testing a set of MPI functions; in this case it was used to have a measure of shared memory access performances.

2 HPL benchmark

The HPL [2,3] is a benchmark widely used in the HPC community for ranking supercomputers according to their computing power in terms of floating point operations per second (flops). The flops rate is evaluated by solving in parallel a dense linear system of order n:

$$\mathrm{A}\cdot\mathrm{X}=\mathrm{B},\quad A\in\Re^{n\times n},\quad X,B\in\Re^{n}$$

using LU factorization [4-6] with row partial pivoting of the n by n+1 coefficient matrix:

$$P[A,B]=[[L,U],Y].$$

P is the permutation matrix representing the row pivoting and L is the lower triangular matrix. P and L are applied to B as the factorization progresses. The solution is obtained by solving the upper triangular system:

$$U\cdot\mathrm{X}=Y.$$

The factorization requires $2n^3/3 - n^2/2$ operations and the solving phase $2n^2$ thus if t_s is the time to solution, the theoretical peak performance p_{th} (in Gflops) is given by:

$$p_{th}=\frac{\frac{2n^3}{3}+\frac{3n^2}{2}}{t_s}\cdot 10^{-9}.$$

Under very general assumptions it can be shown that the HPL algorithm makes the leading term of time to solution t_s of order $O(n^3)$. The time spent for communication is of order $O(n^2)$. The HPL benchmark scales very well with the size n and the scaling does not depend strongly on the communication volume.

2.1 HPL results

The HPL benchmark was compiled with the Open64 (ver. 4.5.1) compiler and ACML 64 bit (ver. 5.0.0) libraries with fma4 support for AMD Interlagos, and with the Intel compiler suite (ver. 12.1.4) and MKL libraries for the Intel Sandy Bridge. We also made a compilation with the GCC compiler (ver. 4.6.3) for both AMD and Intel processors. In all cases the Open MPI 1.5.4 libraries were used for parallel runs. The compiler flags used for optimization are shown in Table 1.

Open64 (ver. 4.5.1)	-O3 -OPT:Ofast -fno-math-errno -ffast-math march=bdver2 -mfma4 -mavx
Intel mpicc (ver. 12.1.4)	-fomit-frame-pointer -unroll-aggressive -O3 -simd –msse3
GCC (ver. 4.6.3)	-fomit-frame-pointer -O3 -funroll-loops -mavx -mfma4

Table 1: Optimization flags used for the HPL benchmark.

In Table 2 are reported the best results for serial, 8 and 24 cores. We see that, considering the same clock frequency normalization, the Intel Sandy Bridge processor achieves in the serial (parallel) case a higher rate of about 30% (18%). Also the amount of used node RAM is higher for Intel Sandy Bridge. The same behavior has been observed by using the same compiler and libraries (GCC + ACML) for runs involving all node cores of both processors. Also for HPL with HT on (24 cores case) the performance of Sandy Bridge is 18% higher than Interlagos in spite of using 30% more memory with respect the total RAM of the node.

Best rate (Gflops) The percentage refers to the used node RAM		
Cores	**AMD 6234 Interlagos 2.4 GHz, 64 GB RAM (Open64+ACML)**	**Intel E5-2680 Sandy Bridge 2.7 GHz, 32 GB RAM (Intel +MKL)**
1	16.4 (13.4) 20%	26.3 (19.5) [23.4] 40%
8	59.4 (49.5) 61%	182.1 (134.9) [161.9] 90%
24	170.6 (142.5) 61%	234.6 (173.8) [208.5](*) 90%

Table 2: HPL best results obtained on AMD Interlagos and Intel Sandy Bridge processors. The results in round [square] brackets are normalized to 2.0 [2.4] GHz clock frequency. (*) means HT switched on.

3 OpenFOAM code

OpenFOAM [7,8] is a free, open source toolbox for CFD. The software has many features for solving anything from complex fluid flows, including chemical reactions, turbulence, and heat transfer to solid dynamics and electromagnetics. OpenFOAM supports parallel computations and is capable of running on very large HPC clusters. The code is written in C++ and can be extended by users who need to write their own solvers and libraries. The core technology includes numerical methods, linear and ODE (Ordinary Differential Equations) system solvers and dynamic mesh functionalities.

3.1 Benchmark description

We present a case test which has been performed to analyse the performances of OpenFOAM on Intel Sandy Bridge and AMD Interlagos processors. We made a 64 bit compilation for Linux on x86_64 systems with the GCC (ver. 4.6.3) compiler. The Open MPI 1.5.4 libraries were used for parallel runs. The case is well described in the OpenFOAM tutorial. We studied a 2 dimensional multiphase problem of simplified dam break. The feature of the problem is a transient flow of two fluids separated by a sharp interface. The OpenFOAM solver uses a specie transport equation to determine the relative volume fraction of the two phases. The geometry and the initial setup are shown in Fig. 1.

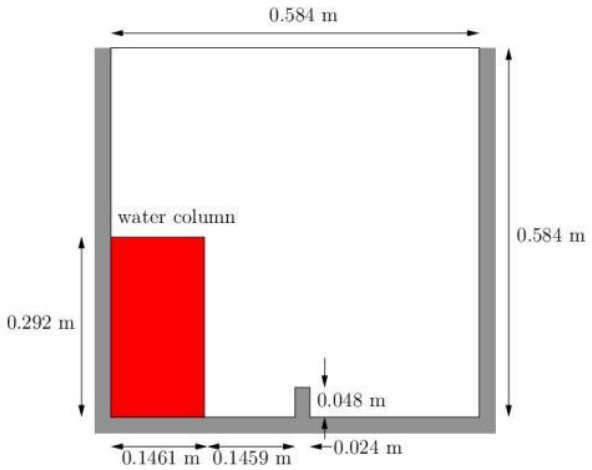

Figure 1: The geometry and initial set up of the OpenFOAM benchmark. The solver uses an incompressible transport Newtonian model and a laminar approximation for turbulence.

A column of water at rest is located behind a membrane on the left side of a tank. At time $t = 0$ the membrane is removed and the column of water collapses. During the collapse, the water impacts an obstacle at the bottom of the tank and creates a complicated flow structure, including several captured pockets of air. The computational domain consists of 123200 cells.

Execution Time (s)		
Cores	**AMD 6234 Interlagos 2.4 GHz, 64 GB RAM**	**Intel E5-2680 Sandy Bridge 2.7 GHz, 32 GB RAM**
1	45069.0 (54082.8)	19069.9 (25744.4) [21453.6]
24	2718.5 (3262.2)	1923.0 (2596.0) [2163.4](*)

Table 3: Execution time for the OpenFOAM case test on AMD Interlagos and Intel Sandy Bridge processors. The results in round [square] brackets are normalized to 2.0 [2.4] GHz clock frequency. (*) means HT switched on.

3.2 OpenFOAM results

The results are reported in Table 3. We see that in the case of a serial run the Intel Sandy Bridge is about twice faster than AMD Interlagos. This is due to the fact that two cores of the AMD Interlagos processor share the same FPU. The discrepancy, however, is less significant with parallel runs and with 24 cores. This may be due to the HT switched on. However, this effect does not impact too much and the Sandy Bridge still takes about 20% less time than AMD Interlagos for completing the run.

4 Ansys Fluent code

ANSYS Fluent software contains the broad physical modeling capabilities needed to model flow, turbulence, heat transfer, and reactions for industrial applications ranging from air flow over an aircraft wing to combustion in a furnace, from bubble columns to oil platforms, from blood flow to semiconductor manufacturing, and from clean room design to wastewater treatment plants [9].

The code is commercial and to make the benchmarks, the academic research licenses are been used to made the simulations. The code, being not open source, is provided precompiled for a generic Linux x86_64 architecture therefore it was not possible to recompile it with optimization techniques as has been done with other codes discussed in this report. The software used for the benchmarks is Ansys Fluent version 12.1.

4.1 Ansys Fluent benchmark

Three different test cases of CFD problems have been simulated. These benchmarks are part of a pool of nine different CFD problems provided by Ansys in the version 6.3 of Fluent; these are arranged by computational demand that is mainly influenced by the size of the mesh and the complexity of the equations modeled. For sake of brevity we want to avoid the detailed description of the physical model of each benchmark; the main characteristics are:

- M2: about 250000 cells; turbulence modeling with k-ε, steady simulation;
- M3: about 350000 cells; turbulence modeling with k-ε, steady simulation, chemical species transport;
- L1: about 850000 cells; turbulence modeling, compressible fluid.

4.2 Ansys Fluent results

The temporal element that identifies the performance, t_n expressed in seconds, was obtained by measuring only the time required to perform 50 iterations of the solver and therefore does not include loading the software in memory, reading and writing data among the disk and any of the domain partitioning calculation.

For each of the three benchmarks several simulations have been conducted: the number of cores is varied from one to the maximum allowed on the single working node. In particular the simulations can be summarized in:

- AMD 6234 Interlagos: serial, 8 cores, 16 cores, 24 cores (full node);
- Intel E5-2680 Sandy Bridge: serial, 8 cores, 16 cores (full node), 24 cores with HT, 32 cores with HT (full node).

Results are showed in terms of *Rating*, *Speed-up* and *Efficiency* as proposed by Ansys in Ref. [10]. This is a short description of their meaning:

Rating: is an index that represent the "speed" or absolute performance of the simulation; it is the number of simulations that can run in a day:

$$\frac{24 \times 60 \times 60}{t_n}$$

it is inversely proportional to the time t_n.

Speed-up (S): for parallel simulations with n cores, is the ratio between the serial (t_s) and the parallel (t_n) execution time:

$$S = \frac{t_s}{t_n}.$$

Efficiency (E): is the speed-up normalized to the number of cores:

$$E = \frac{S}{n}.$$

Results of the benchmarks can be summarized as follows in the Tables 4, 5 and 6.

Execution time t_n (s) M2 case		
Cores	**AMD 6234 Interlagos 2.4 GHz, 64 GB RAM**	**Intel E5-2680 Sandy Bridge 2.7 GHz, 32 GB RAM**
1	123.3	62.1
8	22.2	9.80
16	12.7	5.75
24	9.6	7.14
32	-	5.73

Table 4: Execution time for M2 benchmark at different number of cores on the tested architectures.

Execution time t_n (s) M3 case		
Cores	**AMD 6234 Interlagos 2.4 GHz, 64 GB RAM**	**Intel E5-2680 Sandy Bridge 2.7 GHz, 32 GB RAM**
1	553.8	235.5
8	95.3	39.1
16	56.3	23.5
24	41.0	30.0
32	-	23.2

Table 5: Execution time for M3 benchmark at different number of cores on the tested architectures.

Execution time t_n (s) L1 case		
Cores	**AMD 6234 Interlagos 2.4 GHz, 64 GB RAM**	**Intel E5-2680 Sandy Bridge 2.7 GHz, 32 GB RAM**
1	1068.6	532.5
8	194.8	77.3
16	115.0	43.8
24	81.6	55.2
32	-	43.4

Table 6: Execution time for L1 benchmark at different number of cores on the tested architectures.

The Fig. 2 show the graphs of the comparisons of the three characteristics previously defined; the graphs are very similar for all the considered benchmarks so we show only the L1 benchmark in order to do not overload the reader.

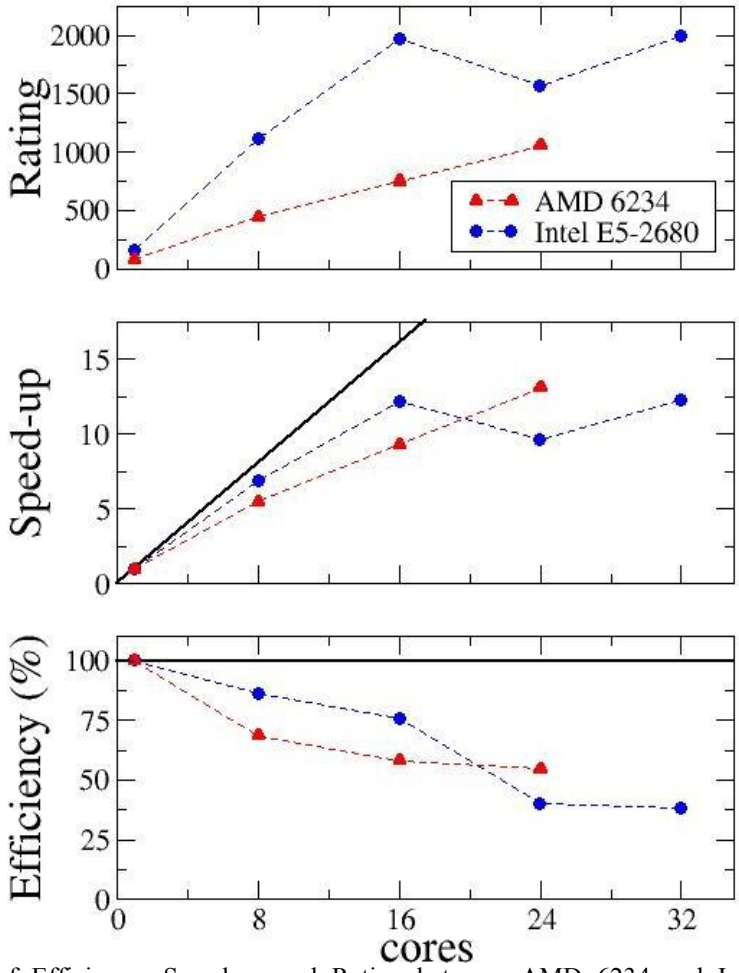

Figure 2: Comparison of Efficiency, Speed-up and Rating between AMD 6234 and Intel E5-2680 for the L1 benchmark.

5 CPMD code

Car-Parrinello Molecular Dynamics (CPMD) code [11,12], is an *ab-initio* electronic structure and MD program using a plane wave/pseudopotential implementation of density functional theory (DFT) [13,14]. It is mainly targeted at Car-Parrinello MD simulations, but also supports geometry optimizations, Born-Oppenheimer MD, path integral MD, response functions, excited states and calculation of some electronic properties. CPMD code runs on many different computer architectures and allows good scalability till a large number of processors depending on the system size [15-17]. We compiled the code on the AMD 6234 Interlagos with Intel Fortran Compiler ver. 12.1.3, ACML 5.1.0 with fma4 extension, and on the Intel E5-2680 Sandy Bridge with Intel Fortran Compiler ver. 12.1.4 and MKL library. The OpenMPI ver. 1.5.4 libraries were used for both the compilations.

5.1. Physical system

Solid-state metal hydrides are considered useful for storing hydrogen although materials suitable for practical use are still under development. Magnesium is an important candidate in this respect as it can reversibly store about 7.6 wt% hydrogen, is light weight and is a low-cost material. However, its thermodynamic parameters are not completely favorable and the reaction with hydrogen often shows sluggish kinetics. Different treatments in Mg based materials have been proposed to overcome these

drawbacks. One of these is tailoring Mg nanoparticles in view of an enhancement on the reaction kinetics and thermodynamics of the Mg-MgH2 phase transformation [18-20]. Because metallic nanoparticles often show size dependent behavior different from bulk matter, a better understanding of their physical-chemical properties is necessary. To approach numerical studying of Mg nanoparticles, starting from the magnesium bulk, we have considered the cluster built from the Mg atoms inside a 12 Å radius sphere centered on a Mg atom. To take in consideration the Kirkendall effect [21], we then have removed the inner Mg atoms inside a 5.6 Å radius sphere. The system is composed of a hollow nanoparticle of 266 magnesium atoms. In view of a better understanding of the Mg nanoparticles physical-chemical properties, we want to set up a numerical model to perform first principle calculations based on the density functional theory, using CPMD code.

5.2. Computational details

The Kohn-Sham method of DFT simplifies calculations of the electronic density and energy of a system of *Ne* electrons in an external field without solving the Schrödinger equations with *3Ne* degrees of freedom, but it takes into consideration the electronic density as the fundamental quantity (with only 3 degrees of freedom). The total ground-state energy of the system can be obtained as the minimum of the Kohn-Sham energy which is an explicit functional of the electronic density. This leads to a set of equations (Kohn-Sham equations) that has to be solved self-consistently in order to yield density and the total energy of the electronic ground-state. In the calculations, starting from an initial guess for the electronic density, the Kohn-Sham equations are solved iteratively until convergence is reached. We employed for all the calculations the CPMD code with Goedecker-Teter-Hutter pseudopotentials for magnesium, together with Pade approximant LDA exchange-correlation potentials [22-24]. The preconditioned conjugate gradient with line search method was used in order to yield density and the total energy of the electronic ground-state. We considered two cases: A) The electronic wave functions cutoff equal to 20 Ry, the density cutoff equal to 80 Ry, the number of plane waves for wavefunction equal to 218524, the number of plane waves for density equal to 1747687 and real space mesh 192x192x192. B) The electronic wave functions cutoff equal to 45 Ry, the density cutoff equal to 180 Ry, the number of plane waves for wavefunction equal to 737585, the number of plane waves for density equal to 5899402 and real space mesh 288x288x288.

Execution total time t_{tot} and average time for iteration t_{avg} (s) System A					
Cores	**PM (MB)**	**AMD 6234 Interlagos 2.4 GHz, 64 GB RAM**		**Intel E5-2680 Sandy Bridge 2.7 GHz, 32 GB RAM**	
		t_{tot}	t_{avg}	t_{tot}	t_{avg}
2	4037.1	10h57m32s	383.13	4h01m34s	142.39
4	2024.6	6h49m35s	238.21	2h10m32s	76.84
6	1353.8	5h32m14s	193.28	-	-
8	1018.5	4h08m33s	144.69	1h19m44s	46.77
12	683.3	2h46m30s	96.97	1h03m40s	37.17
16	515.4	2h06m18s	73.57	1h00m38s	35.28
24	347.7	1h27m22s	50.89	1h02m41s	36.46
32	263.7	-	-	1h10m42s	41.25

Table 11: Execution total time t_{tot} and average time for iteration t_{avg} for system A in function of number of cores on the tested architectures. PM is the Peak Memory for core.

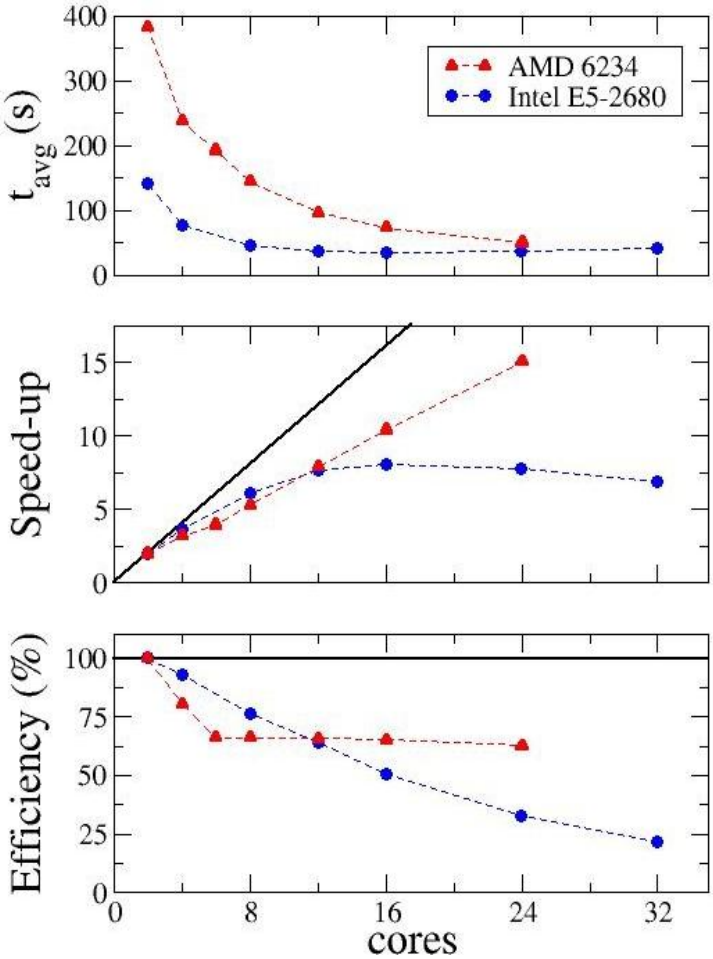

Figure 3: Average time for iteration t_{avg} for system A in function of number of cores for AMD 6234 and Intel E5-2680 processors. We also report the speed-up and the efficiency. Solid black lines are for ideal performance.

Execution total time t_{tot} and average time for iteration t_{avg} (s) System B					
Cores	**PM (MB)**	**AMD 6234 Interlagos 2.4 GHz, 64 GB RAM**		**Intel E5-2680 Sandy Bridge 2.7 GHz, 32 GB RAM**	
		t_{tot}	t_{avg}	t_{tot}	t_{avg}
2	13574.2	8h27m39s	1311.84	3h25m16s	561.04
4	6795.4	5h19m36s	806.35	1h37m32s	266.47
6	4535.6	4h23m50s	652.68	-	-
8	3406.0	3h19m13s	490.38	1h02m24s	166.65
12	2275.7	2h10m46s	330.05	50m01s	130.41
16	1711.3	1h36m26s	247.54	47m58s	122.36
24	1145.9	1h04m50s	167.91	47m11s	121.98
32	863.1	-	-	42m31s	107.61

Table 12: Execution total time t_{tot} and average time for iteration t_{avg} for system B in function of number of cores on the tested architectures. PM is the Peak Memory for core.

5.3 CPMD benchmark results

In Table 11 and 12 are shown the results for the CPMD benchmarks for system A and system B respectively. Because both the systems are very compute demanding, we limit our calculation to the first 100 iterations in the resolution of the Kohn-Sham equations for system A, and to the first 10 iterations for system B. We reported the total time required to complete the calculations and the average time for iteration. In Fig.3 and Fig.4 is shown t_{avg} in function of the number of cores. We also showed the speed-up and the efficiency for both systems. From the results we observe a better performance of the Intel Sandy Bridge processor compared to AMD Interlagos. The differences are more evident when little number of cores are used (about 50% less time).

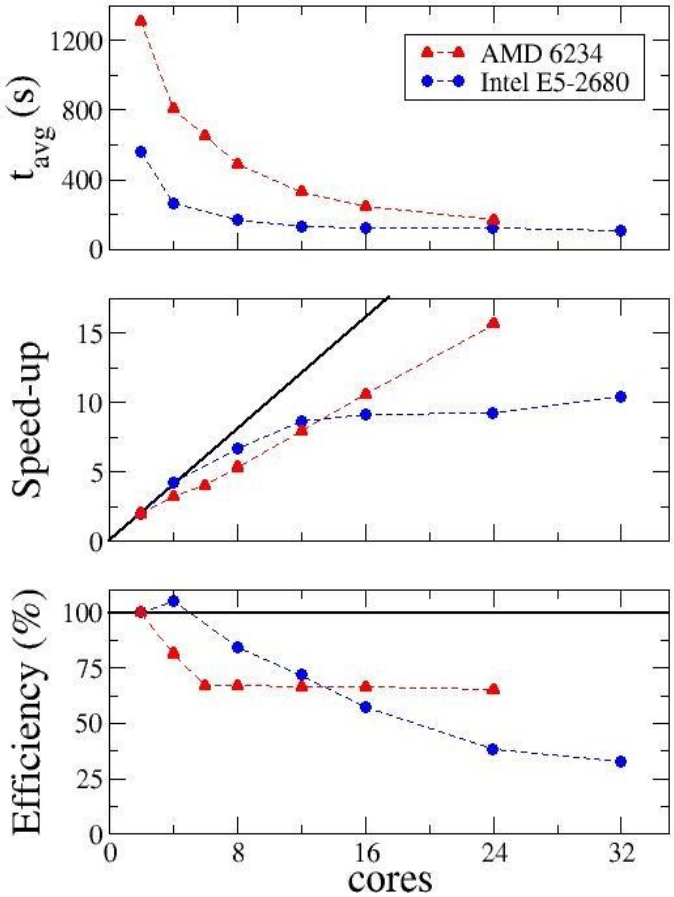

Figure 4: Average time for iteration t_{avg} for system B in function of number of cores for AMD 6234 and Intel Sandy E5-2680 processors. We also report the speed-up and the efficiency. Solid black lines are for ideal performance.

6 IMB-MPI1 Alltoall benchmark

The Alltoall is part of the Intel MPI Benchmarks family [25]. The Intel MPI Benchmarks is a concise, easy-to-use set of MPI benchmarks. It compares the performance of various computing platforms or MPI implementations and is very useful to test the interconnection network in HPC systems. In this work the test was used to compare the performances in terms of access to the shared memory between AMD 6234 Interlagos and Intel E5-2680 Sandy Bridge processors.

The Alltoall benchmark uses the MPI_Alltoall function and during the test each parallel process sends buffers of different lengths to all other processes in the same application. This procedure is iterated several times for each buffer length (from 0 to 4MB). The minimum, the maximum and the mean value of execution times are reported in the standard output for each step of the test. We performed the test on both architectures involving 24 processes, compiling both with GCC ver. 4.6.3, and Intel compiler ver 12.1.4 for Intel Sandy Bridge and Intel compiler ver 12.1.3 for AMD Interlagos.

6.1 IMB-MPI1 Alltoall benchmark results

We have observed that AMD Interlagos performs better than Intel Sandy Bridge Intel for buffers with length <= 32 bytes; instead Intel Sandy Bridge performs better than AMD Interlagos for buffers with length between 32 bytes and 4 MB. In order to compare the architectures, we computed for each step of the test the ratio between the mean value of the execution times on Intel Sandy Bridge and the mean value of the execution times on AMD Interlagos and then the mean value among these ratios, obtaining:

- test compiled with GCC: R=0.762;
- test compiled with Intel: R=0.768.

Whereas the clock frequency of Intel Sandy Bridge is 2.7 Ghz and the AMD Interlagos one is 2.4 Ghz we can normalize the results to 2.4 Ghz, obtaining:

- test compiled with GCC: R=0.857;
- test compiled with Intel: R=0.864.

The mean values of the execution times for the iteration on each buffer length are reported below in Table 13.

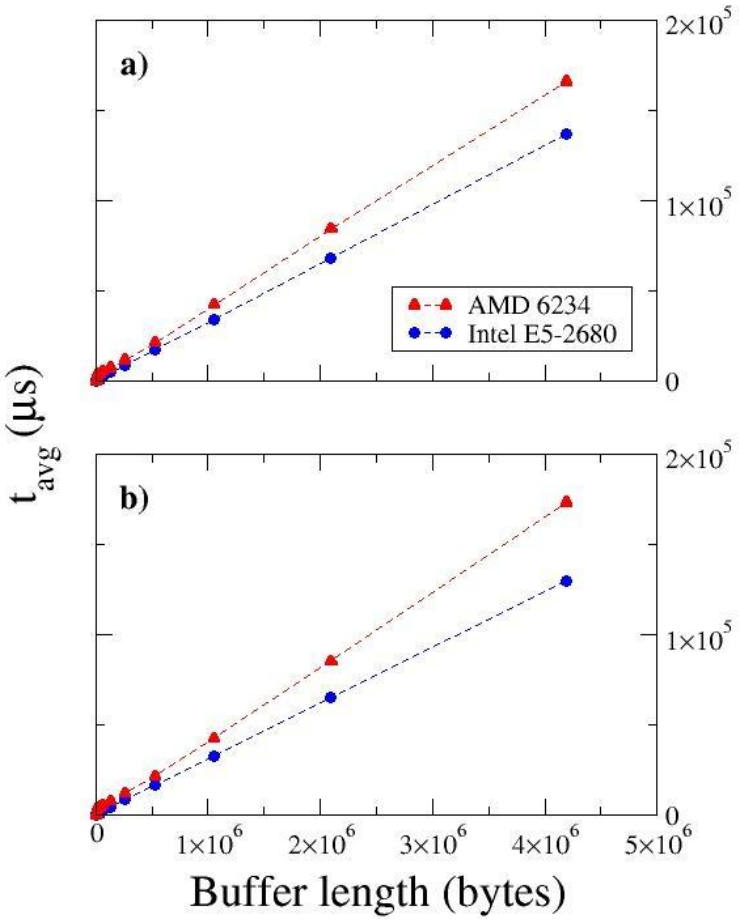

Figure 5: Intel MPI Alltoall benchmark. AMD 6234 vs. Intel E5-2680. a) Test compiled with . b) Test compiled with Intel.

Mean value of execution times t_{avg} (µs)				
Buffer Length (bytes)	**AMD 6234 Interlagos 2.4 GHz, 64 GB RAM**		**Intel E5-2680 Sandy Bridge 2.7 GHz, 32 GB RAM**	
		Intel		Intel
0	0.25	0.24	0.13	0.14
1	34.95	34.95	40.08	42.86
2	35.44	34.46	39.79	42.93
4	34.57	35.11	39.86	43.3
8	34.51	35.21	39.84	43.17
16	40.54	40.4	39.78	42.86
32	40.75	41.14	40.94	43.98
64	50.92	51.53	40.41	43.5
128	56.21	56.56	41.04	44.15
256	64.34	64.7	44.84	47.51
512	79.37	79.24	38.65	39.13
1024	110.47	109.72	44.48	45.93
2048	167.12	165.07	59.78	59.84
4096	314.9	313.57	153.14	153.34
8192	602.47	601.16	967.08	895.13
16384	3940.7	3864.2	1006.5	845.99
32768	4549.5	4504.6	1107.7	934.09
65536	5693.7	5637.4	2720.1	2517.6
131072	7633.2	7935.4	4943.4	4574.1
262144	11936	12232	9057.2	8537
524288	21541	21713	17463	16515
1048576	42399	42459	34252	32482
2097152	84406	85194	68542	65070
4194304	1.6603e+05	1.7315e+05	1.369e+05	1.297e+05

Table 13: Intel MPI Alltoall benchmark. AMD Interlagos vs. Intel Sandy Bridge. Mean values of execution time among the iterations on each buffer length.

7 Conclusions

In this report we have presented the results of different types of computational benchmarks realized to test the performance of the AMD 6234 Interlagos 2.4 GHz and Intel E5-2680 Sandy Bridge 2.7 GHz processors. The tests range from typical HPC benchmark to simulations of different physical systems. Moreover, we have used the Intel MPI benchmark to compare the performances in terms of access to the shared memory.

The HPL runs have made it possible to analyze the floating point performances under varying memory load. The Intel Sandy Bridge can achieve on average (from serial to 24 cores) 24% higher flops rate by using 24.5% more of the available node RAM. Also the results of OpenFOAM with 24 cores show that the Intel Sandy Bridge processor performs better than AMD Interlagos by taking about 20% less time to complete the run even with HT switched on. The results of Ansys Fluent show that Intel Sandy Bridge architecture appears to be faster for the proposed benchmarks in the serial simulation, and even without HT, Intel shows a parallel efficiency greater of the AMD. Intel performances are the same if the node is fully loaded without dependence of the HT. Instead, the efficiency decrease when HT is active (minimum is at 24 =16 + 8 cores) but absolute performance is greater of the corresponding Interlagos. The performances of Interlagos always grow at higher number of cores but the efficiency decreases and reaches the minimum at around 60% at full node loaded. The CPMD tests confirm the previous results. When little number of cores are used, for Intel Sandy Bridge the execution times are halved compared to those of AMD Interlagos. The differences are attenuated with increased number of cores. From the Intel MPI benchmark we have observed that AMD Interlagos performs better than Intel Sandy Bridge for buffers with length <= 32 bytes; instead, Intel Sandy Bridge performs better than AMD Interlagos for buffers with length between 32 bytes and 4 MB.

Bibliographic references:

[1] Binns F., et al. *"Hyper-Threading Technology Architecture and Microarchitecture"* Intel Technology Journal Q1 (2002).
[2] Petitet A., Whaley R.C., Dongarra J.J., Cleary A. *"Hpl: A portable implementation of the high-performance linpack benchmark for distributed-memory computers"* Innovative Computing Laboratory, Available online (2000). URL http://icl.cs.utk.edu/hpl/ and www.netlib.org/benchmark/hpl/.
[3] Dongarra J., Luszczek P., Petitet A. *"The linpack benchmark: past, present and future. Concurrency and Computation"* Practice and Experience **15**(9) (2003) pp. 803-820.
[4] Dongarra J., van de Geijn R.A., Walker D.W. *"Scalability issues affecting the design of a dense linear algebra library"* J. Parallel Distrib. Comput. **22**(3) (1994) pp. 523-537.
[5] Dongarra J., Eijkhout V., Luszczek P. *"Recursive approach in sparse matrix LU factorization"* Scientific Programming **9**(1) (2001) pp. 51-60.
[6] Petitet A.P., Dongarra J. *"Algorithmic redistribution methods for block-cyclic decompositions"* IEEE Transactions on Parallel and Distributed Systems **10**(12) (1999) pp.201-220.
[7] Weller H.G, Tabor G., Jasak H., Fureby C.*"A tensorial approach to computational continuum mechanics using object orientated techniques"* Computers in Physics **12**(6) (1998) pp.620-631.
[8] www.openfoam.com.
[9] www.ansys.com.
[10] www.ansys.com/Support/Platform+Support/Benchmarks+Overview/ANSYS+Fluent+Benchmarks.
[11] Car R., Parrinello M. *"Unified approach for molecular dynamics and Density-Functional Theory"* Phys. Rev. Lett. **55** (1985) p. 2471.
[12] www.cpmd.org.
[13] Hohenberg P., Kohn W. *"Inhomogeneous Electron Gas"* Phys. Rev. **136** (1964) p. B864.
[14] Kohn W., Sham L.J. *"Self-Consistent Equations Including Exchange and Correlation Effects"* Phys. Rev. **140** (1965) p. A1133.
[15] Andreoni W., Curioni A. *"New Advances in Chemistry and Material Science with CPMD and Parallel Computing"* Paral. Comp. **26** (2000) p. 819.
[16] Hutter J., Curioni A. *"Dual-level parallelism for ab initio molecular dynamics: Reaching teraflop performance with the CPMD code"* Paral. Comp. **31** (2005) p. 1.
[17] Giusepponi S., Celino M., Cleri F., Montone A. *"Hydrogen storage in MgH_2 matrices: a study of Mg-MgH_2 interface using CPMD code on ENEA-GRID"* Il Nuovo Cimento C **32** (2009) p. 139.
[18] Pasquini L., Callini E., Piscopiello E., Montone A., Vittori Antisari M. *"Hydrogen sorption in Pd-decorated Mg–MgO core-shell nanoparticle"* Appl. Phys. Lett. **94** (2009) 041918.
[19] Krishnan G., Kooi B.J., Palasantzas G., Pivak Y., Dam B. *"Thermal stability of gas phase magnesium nanoparticles"* J. Appl. Phys. **107** (2010) 053504.
[20] Pasquini L., Callini E., Brighi M., Boscherini F., Montone A., Jensen T.R., Maurizio C., Vittori Antisari M., Bonetti E. *"Magnesium nanoparticles with transition metal decoration for hydrogen storage"* J. Nanopart. Res. **13** (2011) p. 5727.
[21] Smigelskas A.D., Kirkendall E.O. Trans. AIME **171** (1947) p. 130.
[22] Perdew J.P., Burke K., Ernzerhof M. *"Generalized Gradient Approximation Made Simple"* Phys. Rev. Lett. **77** (1996) p. 3865.
[23] Goedecker S., Teter M., Hutter J. *"Separable dual-space Gaussian pseudopotentials"* Phys. Rev. B **54** (1996) p. 1703.
[24] Hartwigsen C., Goedecker S., Hutter J. *"Relativistic separable dual-space Gaussian pseudopotentials from H to Rn"* Phys. Rev. B **58** (1998) p. 3641.
[25] http://software.intel.com/en-us/articles/intel-mpi-benchmarks.

Atmospheric dispersion of Iodine-131 released after the Fukushima event

Giuseppe A. Marzo
ENEA, C. R. Casaccia, Roma
giuseppe.marzo@enea.it

Keywords: Atmospheric simulations, Fukushima, Iodine-131, Lagrangian models, Emergency preparedness

1. Introduction

On March 11, 2011, an earthquake off the Pacific coast of the Fukushima prefecture generated a tsunami that hit two Nuclear Power Plants (NPPs), named Fukushima Dai-ichi and Fukushima Da-ini operated by the Tokyo Electric Power Company Inc. (TEPCO), located along the coast.
Fukushima Dai-ichi consists of six Boiling Water Reactors (BWR) with a total generation capacity of 4696 MW. The six units commenced commercial operation in succession, starting with unit 1 in March 1971 through unit 6 in October 1979. Fukushima Da-ini is located approximately 12 km south of Fukushima Dai-ichi NPP and consists of four BWR units. Each unit has generator output capacity of 1100 MW for a total generation capacity of 4400 MW. Unit 1 began commercial operation in April 1982, unit 4 in August 1987, with the four units having commenced commercial operation successively [1].
On March 11, 2011, units 1 to 3 at Fukushima Dai-ichi and units 1 to 4 at Fukushima Da-ini were in operation. Units 4 to 6 at Fukushima Dai-ichi were in outage for periodic inspection. When the tsunami struck, 50 minutes after the earthquake, it was high enough to inundate several buildings at the Fukushima Dai-ichi NPP, including many power panels. As a consequence, most of the auxiliary power generators shut down causing loss of all cooling functions using electrical power and the function of transferring the decay heat inside the reactor to seawater was lost. In unit 1 almost all of the fuel assemblies melted and accumulated at the bottom of the pressure vessel. Partial melting of the fuel rods in units 2 and 3, damaging approximately one third of the fuel assemblies in each, occurred over the following days. Damaged fuel rods released radioactive materials into the vessels and reaction of the zirconium alloy fuel cladding with water at high temperatures generated hydrogen gas [2] that accumulated causing explosions that damaged the upped part of units 1 and 3 on March 12 and 14, respectively [3]. Due to hydrogen which is thought to be inflow from venting unit 3, another explosion, on March 15 [3], damaged the upper structure of the reactor building in unit 4.
From March 12, 2011, a significant amount of radioactive material was therefore discharged into the atmosphere and several efforts have been undertaken to estimate the amount of radioactivity released (e.g., [4-6]). Environmental measurements in the Fukushima area confirmed that the most abundant radioactive species released were ^{131}I, ^{133}Xe, and ^{137}Cs, although other minor species were also detected [5]. Total emission of ^{131}I has been estimated in 1.28×10^{17} Bq [5], while ^{133}Xe, and ^{137}Cs total emissions have been estimated in 1.53×10^{19} Bq and 3.66×10^{16} Bq, respectively [6].

In this work the global atmospheric dispersion of ^{131}I (half-life 8.02 days) released by the Fukushima accident is carried out, focusing on this specific radionuclide due to its radiological relevance in terms of consequences on the human health.

2. Model and data

Global atmospheric dispersion is performed by means of FLEXPART, a publicly available (http://transport.nilu.no/flexpart/) and extensively validated Lagrangian Particle Dispersion Model developed at the Norwegian Institute for Air Research in the Department of Atmospheric and Climate Research [7]. FLEXPART simulates the long-range and meso-scale transport, diffusion, dry and wet deposition, and radioactive decay of tracers released in the atmosphere [7]. The model can be used backward in time to determine potential source contribution for given receptors or forward in time, such as in the case illustrated in this work, to simulate the dispersion of tracers from their sources.
The Lagrangian model has been used with the six-hourly meteorological data from the National Centers for Environmental Prediction (NCEP) Climate Forecast System (CFS) Reanalysis [8]. This publicly available dataset (http://rda.ucar.edu/datasets/ds094.0/) has 37 model atmospheric level altitudes (from surface pressure to 1 mbar) and resolution of 0.5° × 0.5° globally. The adopted dataset spans from March 10, 2011 00:00h UTC to June 10, 2011 00:00h UTC for a total of 14,74 GB of storage space.
Calculations with FLEXPART are serial because the Lagrangian model is strictly linear. To perform the ^{131}I atmospheric transport, 10^7 particles (not necessarily representing real particles, but infinitesimally small air parcels) have been released over time accordingly to the source term description by Katata et al. [5] who provide the release rates of ^{131}I from the Fukushima NPPs from March 11, 2011 20:00h UTC to April 05, 2011 15:00h UTC.
Calculations have been carried out using the Section 3 of the ENEA-CRESCO architecture, equipped with 12-cores processors at 2.4 GHz, each one managing 64 GB of RAM, and therefore able to allocate the >20 GB necessary for managing the large arrays describing the global atmospheric circulations and the dispersion of the tracer particles. In these conditions the resulting run time has been of approximately 50 hours for performing the entire simulation up to June 10, 2011 00:00h UTC.

3. Results

Figure 1 summarizes the simulation results. It illustrates the radioactivity concentration due to ^{131}I released into the atmosphere at specific times and integrated over the total atmospheric column. Immediately after the initial release on March 12, the plume moved eastward reaching the United States west coast on March 16 at 06:00h UTC. The plume trajectory continued eastward reaching the Atlantic Ocean on March 18 and northern Europe on March 20. At the same time the atmospheric circulation brought portions of the plume from Japan into Russian inner regions. The maximum radioactivity concentration was reached in this period nearby Japan and is estimated in about 10 kBq m^{-2}. On March 22 the plume covered the Mediterranean basin, including Italy and the surrounding countries. The maximum estimated radioactivity concentration in Italy is some mBq m^{-2} in the north-east on April 7. In the rest of the country the estimated maximum is about 1 mBq m^{-2}, consistent with local measurements carried out in ENEA Research Centers [9]. In early April the plume extended over the entire northern hemisphere with maximum radioactivity concentration of approximately 1 kBq m^{-2} reaching fractions of mBq m^{-2} in early May due to radioactive decay of ^{131}I and both dry and wet deposition processes.

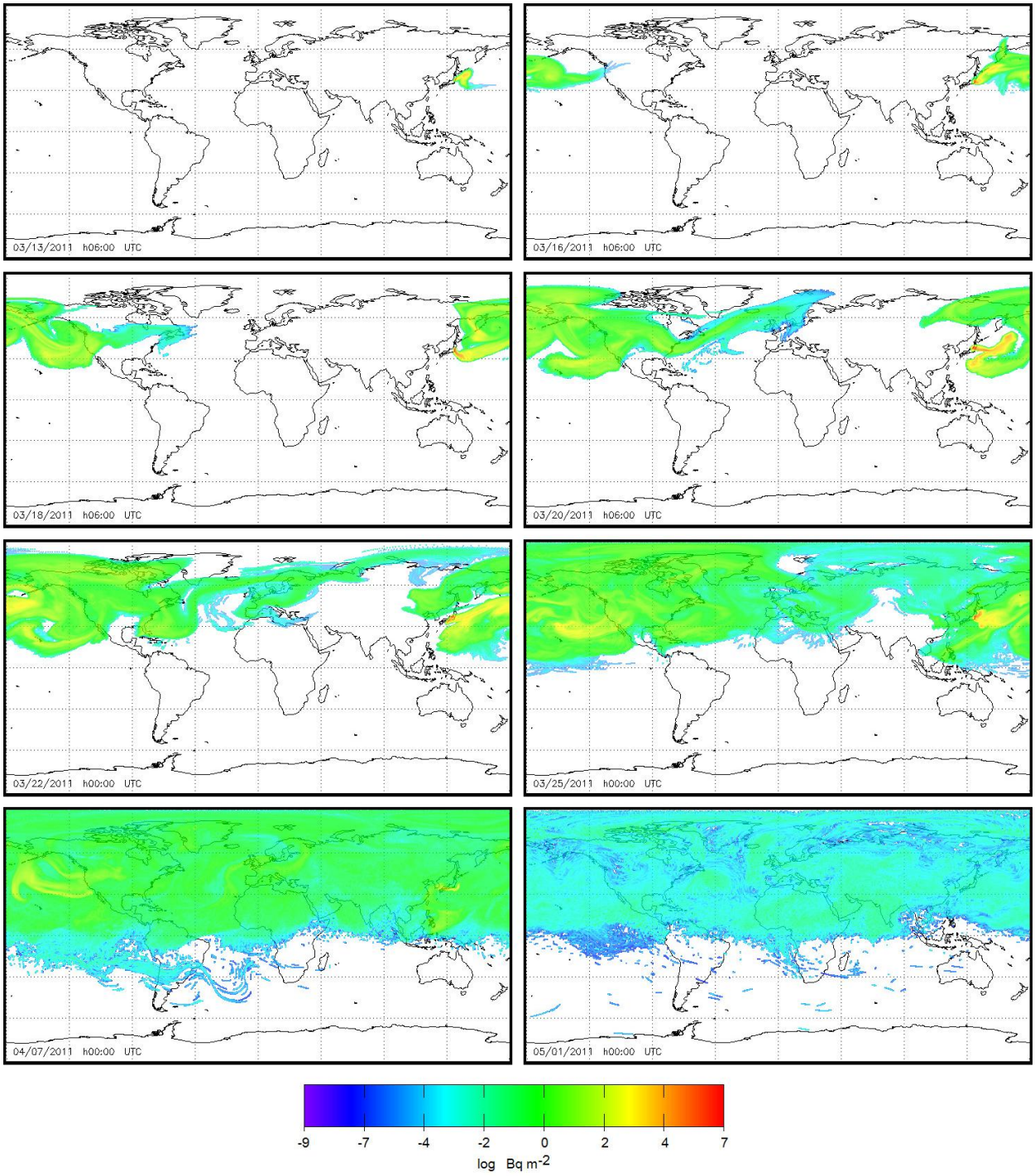

Fig 1. Radioactivity concentration due to ^{131}I released into the atmosphere following the accidental event on March 11, 2011 at the Fukushima NPPs. Different panels illustrate logarithmic concentration integrated over the total atmospheric column at selected times (see text for details). Data visualization is performed using Interactive Data Language (IDL) capabilities of manipulating and displaying large arrays.

The uncertainty associated to the atmospheric dispersion results are mainly due by the following two independent sources: 1) the original uncertainty associated to the quantitative estimation of the source term and 2) the intrinsic uncertainties associated to the Lagrangian model, including those associated to the meteorological data. Based on literature [5] the former can be estimated in a relative value of about 0.5, while the latter is evaluated by carrying 50 classes of particles in the model simulation and determining the concentration separately for each class. These results are then used for evaluating the standard deviation of the mean concentration. This second source of uncertainty can be reduced by increasing the number of particles in the model simulation, yet it increases extending the simulation for a longer time. In this work, the relative value of this uncertainty is comparable with that associated to the source term after 1.5 months by the initial ^{131}I release.

4. Conclusions

A significant accidental event occurred at the Fukushima NPPs after the tsunami struck on March 11 2011. Following the event, volatile radionuclides such as ^{131}I were transported away from the source posing significant concern on the safety of the population and the environment worldwide.
In this work the atmospheric dispersion of ^{131}I is performed by a publicly available and extensively validated Lagrangian model showing that the plume travelled eastward after the initial release reaching the Mediterranean basin on March 22 and covering the entire northern hemisphere by early April with a maximum radioactivity concentration of approximately 1 kBq m^{-2}.
The example reported here illustrates the amount of information that such an approach can provide in case of an accidental event occurring is sensible sites such as NPPs. This amount of information might results pivotal during an emergency response and, before this, in building emergency preparedness and planning mitigation efforts.

5. References

[1] Tokyo Electric Power Company, Inc. *"Fukushima Nuclear Accident Analysis Report"* (2012) TEPCO, Tokyo, Japan.

[2] BURNS, P.C., EWING, R.C., NAVROTSKY, A. *"Nuclear fuel in a Reactor Accident"* Science **335**, (2012) pp. 1184–1188.

[3] HIROSE, K. *"2011 Fukushima Dai-ichi nuclear power plant accident: summary of regional radioactive deposition monitoring results"* (2012) J. Environ. Radioactiv. **111**, pp. 13–17.

[4] CHINO, M., NAKAYAMA, H., NAGAI, H., TERADA, H., KATATA, G., YAMAZAWA, H. *"Preliminary estimation of release amounts of 131I and 137Cs accidentally discharged from Fukushima Daiichi nuclear power plant into atmosphere"* (2011) J. Nucl. Sci. Technol. **48**, pp. 1129–1134.

[5] KATATA, G., OTA, M., TERADA, H., CHINO, M., NAGAI, H. *"Atmospheric discharge and dispersion of radionuclides during the Fukushima Dai-ichi Nuclear Power Plant accident. Part I: Source term estimation and local-scale atmospheric dispersion in early phase of the accident"* (2012) J. Environ. Radioactiv. **109**, pp. 103–113.

[6] STOHL, A., SEIBERT, P., WOTAWA, G., ARNOLD, D., BURKHART, J.F., ECKHARDT, S., TAPIA, C., VARGAS, A., YASUNARI, T.J. *"Xenon-133 and caesium-137 releases into the atmosphere from the Fukushima Dai-ichi nuclear power plant: determination of the source term, atmospheric dispersion, and deposition"* (2012) Atmos. Chem. Phys. **12**, pp. 2313–2343.

[7] STOHL, A., FORSTER, C., FRANK, A., SEIBERT, P., WOTAWA, G. *"Technical Note: The Lagrangian particle dispersion model FLEXPART version 6.2"* (2005) Atmos. Chem. Phys. **5**, pp. 2461–2474.

[8] SAHA, S., MOORTHI, S., PAN, H.L., WU, X., J., W., NADIGA, S., TRIPP, P., et al. *"The NCEP climate forecast system reanalysis"* (2010) Bull. Am. Meteorol. Soc. **91**, pp. 1015–1057.

[9] BARSANTI, M., CONTE, F., DELBONO, I., IURLARO, G., BATTISTI, P., BORTOLUZZI, S., LORENZELLI, R., SALVI, S., ZICARI, S., PAPUCCI, C., DELFANTI, R. *"Environmental radioactivity analyses in Italy following the Fukushima Dai-chi nuclear accident"* (2012) J. Environ. Radioactiv. **114**, pp. 126-130.

MOLECULAR DYNAMICS SIMULATIONS TO STUDY THE STRUCTURAL FEATURES OF A THERMOPHILIC PROTEIN

Anna Marabotti

Laboratory for Bioinformatics, ISA-CNR, Avellino, Italy and Department of Chemistry and Biology, University of Salerno, Fisciano (SA), Italy.
E-mail address: amarabotti@unisa.it

The computational activity described in this report is part of a broader work devoted to the molecular characterization of a maltotriose-binding protein (MalE2) from the thermophilic organism *Thermus thermophilus* [1]. In the complete work, data from molecular dynamics (MD) simulations were combined to data from fluorescence correlation spectroscopy in order to acquire structural information on the pH-induced unfolding of this protein. Data obtained were useful in order to evaluate the structural properties of this protein, for its possible use as biological counterpart of a developing biosensor. It was also interesting to match data obtained with two techniques (computational and experimental) both focused on the study of a single molecule, but with very different timescales (microseconds in the case of fluorescence correlation spectroscopy, nanoseconds in the case of MD simulations).

Introduction

MalE2 is a monomeric sugar-binding protein isolated from a thermophilic organism that shows a very high thermal stability with a melting temperature of 105°C even in the presence of a denaturant such as 2.3 M guanidinium chloride [2]. The three-dimensional structure of MalE2 bound to maltotriose has been solved by X-ray crystallography [3], whereas the structure of the ligand-free protein is not currently available. However, this protein belongs to a well-characterized superfamily of proteins, the ABC proteins, for which structures of the open unliganded form of some representative proteins are available.
In order to study how pH can influence the structural features of this protein, a computational approach was adopted in order to achieve a "molecular portrait" of this macromolecule.

Methods

The structure of the unliganded form of MalE2 has been modelled with an homology modelling approach, using as template the open unliganded form of the maltotriose binding protein from another thermophilic organism, *Thermotoga maritima* (PDB code: 2GHB). In order to take into account information from the X-ray structure of the MalE2 complexed to maltotriose, a strategy already used in the past [4] was applied also in this case. Briefly, the two domains composing the close liganded form of MalE2 from *T. thermophilus* were superposed to the protein from *T. maritima* in order to create a "hybrid" structure in which these domains are oriented as in the open un-liganded form, and the connection between the two domains is made using the structures from *T. maritima.* This "hybrid" structure was then used as template in order to model the complete structure of MalE2, using the program MODELLER 9v7 [5].
Once obtained this model, it was used to perform MD simulations at room temperature simulating three different pH (4.0, 7.0 and 10.0). To do this, a preliminary analysis was performed on the pKa of the charged residues in the protein, using the Web server PROPKA 3.0 [6], and then three different starting systems were created in which the charged groups were protonated according to different pH, using as reference their pKa.

Three MD simulations were then set up for the systems at different pH. The open-source software GROMACS version 4.0.7 [7], was used, running in parallel (MPI) on the CRESCO clusters CRESCO1 and 2. For all the three systems, a 50-ns long simulation was obtained. The whole system (approx. 12700 atoms) was simulated using 32 nodes, obtaining a performance of 15 ns/day (previous benchmarks performed showed that this combination is the best one in terms of scalability of the performances on this system).
At the end of simulations, several analyses were conducted using programs built within GROMACS, and results were visualized and elaborated with the aid of the freely available program Grace (http://plasma-gate.weizmann.ac.il/Grace). Principal component analysis (PCA) [8] was also performed on the trajectories. The covariance matrix was built from the coordinates of Calpha atoms. The results were used to represent the free energy landscape of the systems in different conditions.

Results

Figure 1 shows the picture of the model of MalE2 in open unliganded form. Data about the quality of this model showed that 95.2% of the residues of the model are in the most favored regions of the Ramachandran plot, with respect to 93.7% of the residues of the template, and that no residues are comprised into disallowed regions. The energetic profile of the model shows no peaks of positive energy indicating errors in the structure. Therefore, these data demonstrate the optimal quality of the model.

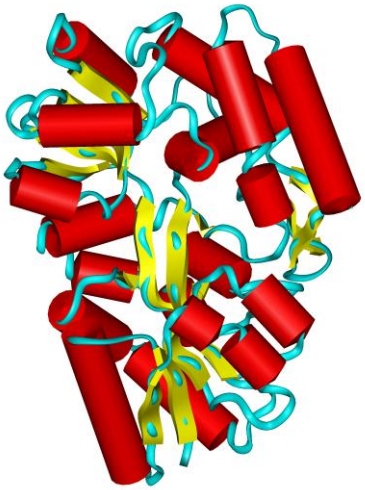

Figure 1: Model of the three-dimensional structure of MalE2 in the open unliganded form. The backbone of the protein is represented as a ribbon, and segments of secondary structures are shown as cylinders (helices) and arrows (strands).

MD simulations at different pH values show that the system reaches the thermodynamic equilibrium after few ns. The diffusion constant of the system was calculated by fitting a straight line through the mean square displacement of atoms from their initial positions, calculated using the program ***g_msd***. The results for the systems at pH 7.0 and 10.0 are in excellent agreement with those obtained by experimental approaches, whereas the data obtained for simulation at pH 4.0 are meaningless considering the standard error, but the absolute value of the result is in line with the experimental data.
A different behavior of the system at pH 4.0 is evident also in the analysis of the root mean square deviation of the protein backbone with respect to the starting structure, indicating that at pH 4.0 the protein is kinetically more unstable than in the other two conditions. In order to highlight this aspect, cluster analysis was made on the trajectories. It was shown that in the simulations at pH 7.0 and 10.0 there is essentially one conformation prevailing along the entire simulation. The analysis of root mean square (RMS) distribution of the structures (Figure 2) shows a regular Gaussian distribution of

the conformation with a narrow peak at 0.2 nm for the structures at pH 7.0, indicating that the conformations are very similar to each other's. At pH 10 the RMS distribution of conformations is still Gaussian, but more enlarged and with some shoulders indicating that distinct subpopulations of conformations during the simulation are detectable. At pH 4, instead, two distinct clusters of conformations are present up to 25 ns of simulation. In the second half of the trajectory, another further cluster is highlighted in the analysis. From these data it appears that at acidic pH, MalE2 shows an enhanced instability of its tertiary structure. Moreover, the impossibility to calculate a meaningful diffusion coefficient for the simulation at pH 4.0 could be due precisely to the coexistence of multiple tertiary conformations of the protein during the simulation. Therefore, even if the timescale of simulation is not sufficient to follow the complete unfolding of the protein, these data can be sufficient to see the early signal of relaxation of the tertiary structure, anticipating the protein unfolding.

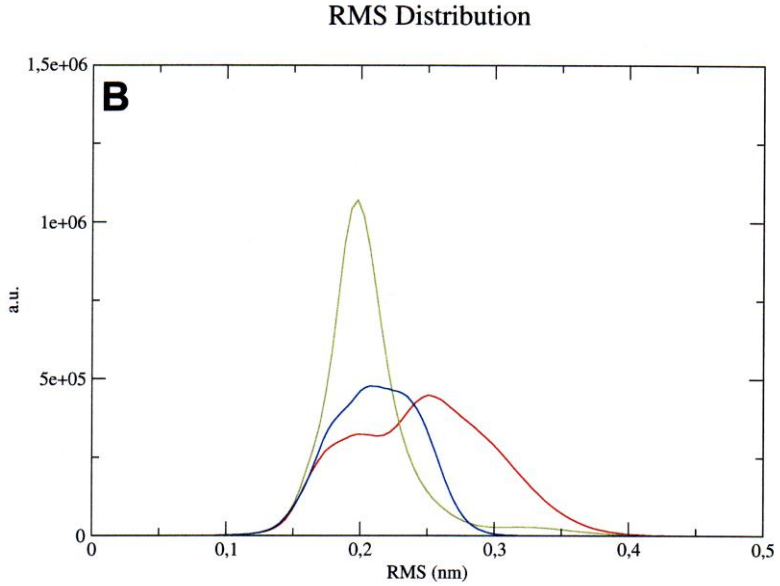

Figure 2: RMS distribution of the structures in the clusters calculated along the three simulation at pH 4.0 (red), pH 7.0 (green) and pH 10.0 (blue).

In order to gain insight into the protein flexibility and to identify large scale collective motions of atoms in MD simulations we performed a PCA on the simulations at three different pH. The results of PCA analysis suggests that the regions of the protein mainly affected by the motions described by the first two eigenvectors are the segments 25–50 and the segments 305–325 for simulations at pH 4.0, and the regions near residue 100 and 170 for simulations at pH 7.0 and pH 10.0. For each simulation at different pH, the results of PCA analysis were used to represent the free energy landscape by projecting the MD simulation on the essential plane defined by the first two eigenvectors (PC1 and PC2). Figure 3 shows the results of this analysis. At pH 7.0 there is a single hollow corresponding to the most probable conformation of this trajectory. On the contrary, at pH 4.0, at least three conformations are present, two of which with a deeper value of probability and with a narrow hollow. At pH 10.0 there are several minima, with two deeper hollows, less narrow than at pH 4.0.

Conclusions

The MD simulations of MalE2 protein at different pH indicate the presence of multiple protein conformations at acidic and basic pH, probably due to the partial unfolding of the MalE2 tertiary structure as a consequence of the induced perturbation of native ionic interactions.
These results were compared to experimental results obtained using the fluorescence correlation spectroscopy technique, and corroborated by circular dichroism, fluorescence emission and light-scattering experiments. From the comparison of experimental and *in silico* results, a protein portrait has been depicted showing that at acidic pH values the protein undergoes a conformational transition towards different molecular forms through the formation of intermediate species. This transition seems to affect mainly the tertiary structure of the protein suggesting the formation of an intermediate state that evolves into a protein unfolded form. At basic pH values, instead, the diffusion coefficient of the protein slightly decreases to the value exhibited at neutral pH values.
In contrast to ensemble methods, which only yield average values for physical and chemical properties and parameters, single-molecule experiments provide information on distributions and time trajectories that would otherwise be hidden by the statistical mean. Using MalE2 as a model, this work demonstrates that new, important insights on the proteins dynamical features can be nicely obtained integrating two different and powerful methodologies, such as fluorescence correlation spectroscopy and MD [1].

Acknowledgements

For the computational part described here, the authors wish to thank dr. Federica Chiappori (ITB-CNR) for fruitful discussions and for providing the tools to create 3D graphs of projections of PCA 1 and 2. We thank ENEA and its HPC team (in particular, Dr. G. Aprea and Dr. S.Podda) for the utilization of ENEA-GRID resources and of the HPC facility CRESCO (http://www.cresco.enea.it), located in Portici (Naples), Italy, for the MD simulations (conv. ISA-ENEA 2008). The project was realized in the frame of CNR Italian Bioinformatics Network.

Figure 3: Projection of the trajectories of MalE2 at pH 4.0 (A), pH 7.0 (B) and pH 10.0 (C) in the essential plane defined by the two first eigenvectors calculated for the simulations. The probability is expressed as relative to the maximum frequency. The color scale (blue-red) defines the most probable conformation.

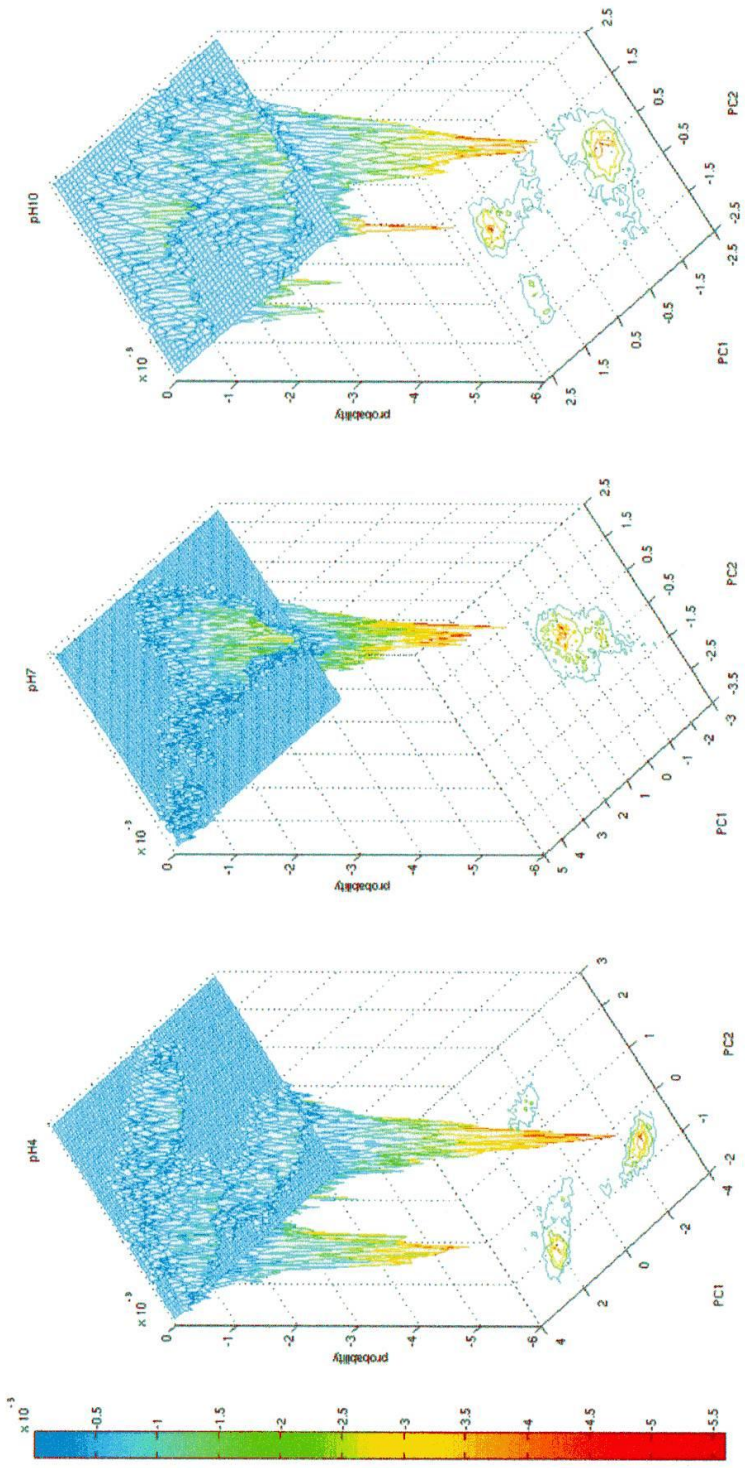

References

[1] VARRIALE A., MARABOTTI A., MEI G., STAIANO M., D'AURIA S. "Correlation spectroscopy and molecular dynamics simulations to study the structural features of proteins" PLoS ONE 8 (2013): e64840.

[2] SILVA Z., SAMPAIO M.M., HENNE A., BOHM A., GUTZAT R., BOOS W., DA COSTA M.S., SANTOS H. *"The high affinity maltose/trehalose ABC transporter in the extremely thermophilic bacterium Thermus thermophilus HB27 also recognizes sucrose and palatinose"* Journal of Bacteriology **187** (2005) pp. 1210–1218.

[3] CUNEO M.J., CHANGELA A., BEESE L.S., HELLINGA H.W. *"Structural adaptations that modulate monosaccharide, disaccharide, and trisaccharide specificities in periplasmic maltose-binding proteins"* Journal of Molecular Biology **389** (2009) pp. 157–166.

[4] SCIRÈ A., MARABOTTI A., STAIANO M., IOZZINO L., LUCHANSKY M.S., DER B.S., DATTELBAUM J.D., TANFANI F., D'AURIA S. *"Amino acid transport in thermophiles: characterization of an arginine-binding protein in Thermotoga maritima. 2. Molecular organization and structural stability"* Molecular Biosystems **6** (2010) pp. 687–698.

[5] SALI A., BLUNDELL T.L. *"Comparative protein modeling by satisfaction of spatial restraints"* Journal of Molecular Biology **234** (1993) pp. 779–815.

[6] OLSSON M.H.M., SØNDERGAARD C.R., ROSTKOWSKI M., JENSEN J.H. *"PROPKA3: Consistent treatment of internal and surface residues in empirical pKa predictions"* Journal of Chemical Theory and Computation **7** (2011) PP. 525–537.

[7] HESS B., KUTZNER C., VAN DER SPOEL D., LINDAHL E. *"GROMACS 4: Algorithms for highly efficient, load-balanced, and scalable molecular simulation"* Journal of Chemical Theory and Computation **4** (2008) pp. 435–447.

[8] AMADEI A., LINSSEN A.B., BERENDSEN H.J. *"Essential dynamics of proteins"* Proteins: Structure, Function and Genetics **17** (1993) pp. 412–425.

Corrosion inhibition of iron in high temperature molten liquid lead by using oxygen injection

Artoto Arkundato[1], Zaki Su'ud[2], Mikrajuddin Abdullah[2], Widayani Sutrisno[2] and Massimo Celino[3]

[1]Physics Department, Jember University, Jl. Kalimantan 37, Jember, Indonesia
[2]Physics Department, Bandung Institute of Technology, Jl. Ganesha 10, Bandung, Indonesia
[3]ENEA, C.R. Casaccia, Via Anguillarese 301, Rome, Italy

Abstract:

For maximum corrosion inhibition of iron (steels) in liquid metal coolant of nuclear reactors, one of the ways is to inject oxygen gases into the coolant. The proper oxygen concentration should be known. However it is not easy to measure this amount because of safety problem and also the cost. One of the excellent methods to overcome this problem is to use a computational method as molecular dynamics method. The molecular dynamics simulation method can be applied to predict the limit value of the proper oxygen concentration of injection. In this research we predicted that the injection within the range of 5.35×10^{-2} wt% - 8.95×10^{-2} wt% (for temperature 750 °C) will reduce the corrosion rate of the iron effectively. We guess that effect of oxygen injection into liquid lead at proper concentration creates a thin oxygen barrier that separates the liquid lead and iron surface from direct interaction.

Keywords: molecular dynamics, liquid metals corrosion, oxygen content, iron oxides

---

1. Introduction

Lead (Pb) metal is one of the most promising coolant material candidates (Zhang and Li, 2008). However, it is well known that the cladding and structural materials are severely corroded if they are exposed to high temperature liquid lead directly. The dissolution of steel components under high temperature liquid lead is very high (Kashezhev et al., 2010; Zhang et al., 2010; Zhang and Li, 2008). Then we need to know a way for inhibiting strong corrosion of liquid lead. One of the techniques to reduce the corrosion is to develop a stable self-healing protective oxide layer on the surface of the structural materials (cladding, pipe, vessel system etc.) to prevent direct dissolution of metal components. This protective layer may be developed by maintaining dissolved oxygen into liquid lead (Bolind, 2009; Rivai and Takahashi, 2010; Zhang et al., 2010; Zhang and Li, 2008). The purpose of the current research is to study the mechanism of corrosion inhibition and to predict the minimum and maximum limit values of oxygen content for development of a continuous stable protective oxide layer for effective corrosion inhibition. We study the corrosion phenomena and inhibition using molecular dynamics method.

2. Theoretical background

2.1 Interatomic potential

To simplify the study we used the Lennard-Jones (LJ) potential (Eq. 1) for simulation:

$$u(r) = k\varepsilon\left[(\sigma/r)^n - (\sigma/r)^m\right] \quad (1)$$

Where σ and ε are the LJ potential parameters. The k coefficient is used to specify the LJ potential function,

$$k = \frac{n}{n-m}\left(\frac{n}{m}\right)^{m/(n-m)} \quad (2)$$

The interaction potential of Fe-Fe and Pb-Pb is supported by potential parameters as reported by Zhen and Davies (1983) based on his experimental data. For O-O interaction we used potential parameter as reported by Lemmon and Jacobsen (2004). To compute the corrosion we used the Arrhenius formula for the diffusion coefficient:

$$D(T) = D_0 \exp(-A/\Re T) \quad (3)$$

To know the structure properties of materials before and after inhibition we calculate the radial distribution function (RDF), $g(r)$ and also observe the stability of the iron structure using the common neighbour analysis (CNA). CNA calculation is performed by OVITO code (Stukowski, 2010). To know the microscopic structure of iron before and after the simulations we plot the coordinate xyz of atoms by using Jmol visualization code (Hanson, 2010).

3. Simulation procedure and details

The study of iron corrosion and its inhibition are described as below procedure:

(I) Moldy MD simulation of oxygen injection into liquid lead to study corrosion inhibition, at temperature 750 °C. Oxygen will be injected with several small different concentrations (wt%). The system is composed by 10745 Fe atoms (bcc structure a = 2.8286 Å) and 40685 Pb atom in liquid phase. The injected oxygen atoms are in different concentration: 0.0583wt%, 0.0771wt%, 0.1152wt%, 0.1552wt%, 0.1938wt% and 0.2307wt%. We used Moldy MD program to do all simulations (Arkundato, 2009; 2010; 2012; 2013; Refson, 2000).

(II) Calculate the MSD, RDF, the diffusion coefficient $D(T)$ and CNA number and observe the microscopic structure of iron.

(III) Analyse what concentration the oxygen will reduce the corrosion rate significantly and efficiently.

4. Results and discussions

4.1 Effect of oxygen injection

The inhibition of iron corrosion in liquid lead was achieved by injecting the oxygen atoms into liquid lead with different small concentration (see Figure 1):

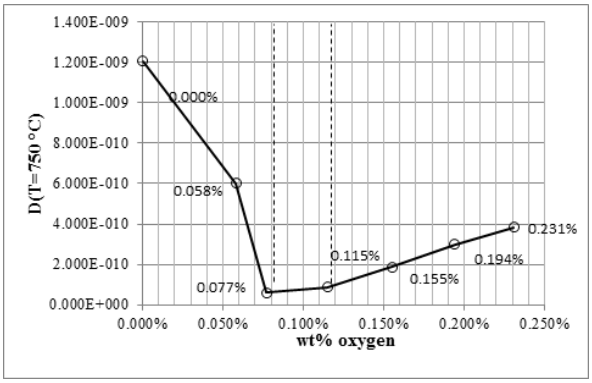

Figure 1.

From that figure we can see that the injection of 0.0771wt% to 0.115wt% will inhibit the iron corrosion rate significantly at the lowest level. At this interval of oxygen concentration the corrosion rate is also stable minimum. Figures 2 show a microstructure of iron during simulations.

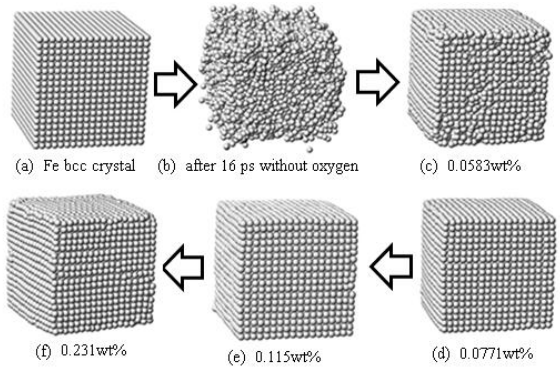

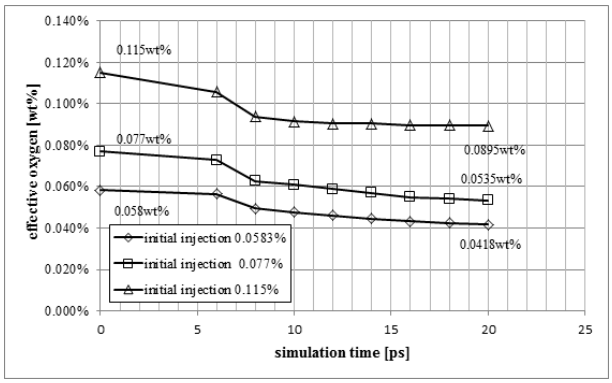

Figure 2.

4.2 Relation between oxygen content and simulation time

The simulation that after 20 ps shows that is not all of oxygen atoms will be used to maintain the maximum corrosion inhibition. We can see for 0.0771wt% of oxygen injection at start of simulation, after 20 ps the iron-lead system only need 0.0535wt% of oxygen for effective corrosion inhibition. For 0.155wt% of oxygen injection at start of simulation, we only need 0.0895wt%.

Acknowledgement

Thanks also to the ENEA CRESCO cloud computing, Rome, Italy, for supporting a part of calculations.

References

Arkundato, A., Su'ud, Z., Mikrajuddin, A., 2010, Corrosion study of Fe in a stagnant liquid Pb by molecular dynamics methods, *AIP Conf. Proc.* 1244 136-144.

Arkundato, A. ,Su'ud, Z., Mikrajuddin, A.,Widayani, S. Massimo, C., 2012, Numerical study: iron corrosion-resistance in lead-bismuth eutectic coolant by molecular dynamics method, *AIP Conf. Proc.* 1454, 65.

Bolind, A. M., 2009, PhD Thesis*, Nuclear Engineering, University of Illinois at Urbana-Champaign, Urbana, Illinois, USA*.

Brodholt, J., Wood, B., 1993, Molecular dynamics simulations of the properties of CO_2-H_2O mixtures at high pressures and temperatures, *American Mineralogist,* 78, 558.

Hanson, R.M., 2010, *Jmol* – a paradigm shift in crystallographic visualization, *J. Appl. Crystallography*, 43(5), 1250-1260, doi:10.1107/S0021889810030256

Kashezhev, A. Z, Ponegev, M. Kh, Sozaev, V. A., Khasanov, A. I, Mozgovo, A. G., 2010, An experimental investigation of the wetting of reactor steels with molten lead and bismuth, *High Temp.*48(5), 756.

Lemmon, E. W., Jacobsen, R. T., 2004, Viscosity and thermal conductivity equations for nitrogen, oxygen, argon, *Inter. J. Thermophysics,* 25(1), 21.

Refson, K., 2000, *Moldy:* A Portable molecular dynamics simulation program for successive and parallel computers, *Comp. Phys. Commun.*. 126(3) 309-328.

Rivai, A. K., and Takahashi, M., 2010, Corrosion characteristics of materials in Pb–Bi under transient temperature conditions, *J. Nucl Mater.,* 398, 139.

Stukowski, A., 2010, *Visualization and analysis of atomistic simulation data with OVITO - the Open Visualization Tool, Simul. Mater.Sci. Eng.* 18.

Zhen, S., Davies, G.J., 1983, L-J n-m potential energy parameters: calculation of the LJ n-m pot energy parameters for metals, *Phys.Stat.Sol*.(a),78, 595.

Shutdown dose rate assessment with the Advanced D1S method: development and applications to ITER TBM Port plug studies

R. Villari, F. Moro, S. Podda
UT FUS-TECN

1. Introduction

The prediction of the shut-down dose rate (SDDR) induced by neutron activation is a major safety task for fusion reactors, as part of planning the operations of intervention and maintenance in order to guarantee the dose limits are not exceeded. More than ten years ago ENEA and the ITER team developed the Direct 1- Step method (D1S) [1,2]. It is based on the use of a modified version of the MCNP5 [3] Monte Carlo code with specially prepared nuclear cross-section data. The D1S is one of the most reliable and validated tools for the three-dimensional calculations of the shutdown dose rates in fusion devices. In this approach the decay gammas of the radioactive nuclides are emitted as prompt and thus, the neutrons and decay gammas are transported in the same single Monte Carlo particle transport simulation. Time correction factors, calculated with FISPACT [4] activation code, are applied to the scored quantities to take into account the build-up and the decay of the radionuclides considered. The "Advanced-D1S" is an improved version developed by ENEA in which new computation capabilities have been introduced, such as the dose rate spatial mesh maps and cooling time dependence [5]. The present paper addresses the recent code developments and applications to ITER [6].

2. Advanced-D1S method

The Advanced D1S method is an improvement of D1S tool [5,6] for the three-dimensional calculation of the shutdown dose rate in fusion devices.

The neutrons generated through fusion reactions interact with the machine components induce the activation reactions and the emitted correspondent decay gammas are transported as prompt in the same run. The decay gammas are emitted according to the reaction (MT number) and each gamma is labeled according to the parent radionuclide.

Special ad hoc prepared libraries are used derived from 'normal' transport libraries. The neutron cross sections of the transport library are replaced with those from the activation library for selected reactions which, in a pre-analysis of the problem, resulted to contribute to the induced activation. Also, the prompt gammas emitted in these reactions have been replaced by decay gammas emitted by the generated radionuclide.

A modified version of MCNP has been implemented. A fictitious delay time in terms of "shakes" is associated to the emitted gamma according to the parent radionuclide in order to distinguish the dose contributions due the different radionuclides. The gamma fluence spectra ($\Phi_\gamma (E)_k$) for each k-radionuclide is calculated in the predefined mesh or cells (FMESH for mesh tally and F4 for standard cell based tally) and multiplied by the proper gamma flux-to-dose conversion coefficients (CC) taken from ICRP74 . In the following description the authors refer generically to dose (D). For the assessment of the personnel exposure the used quantity is the effective dose.

The work-flow of Advanced-D1S is shown in figure 1.

For each k-radionuclide the MCNP results in pSv/n_{source} without any time correction is:

$$D_k\big|_{MCNP} = \int_E CC(E)\cdot\Phi_\gamma(E)_k \qquad (1)$$

where

$CC(E) = \frac{D}{\Phi_\gamma}(E)$: conversion coefficients flux-to-dose in pSv. cm^2/γ;

$\Phi_\gamma(E)_k$ gamma fluence of k-radionuclide in $\gamma/(cm^2\cdot n_{source})$.

The assumption in the MCNP calculation is that both irradiation and decay are instantaneous. Therefore, time correction factors are needed to take into account the production and the decay of each radionuclide dependent on the neutron irradiation history. These factors can be calculated analytically or are derived using an inventory code. In the use of FISPACT for the calculation of the time factors a description of the irradiation scenarios, a generic material (including all parents nuclides of the selected reactions) and a representative neutron flux are needed. Two FISPACT calculations are performed. The time correction factor for the k-nuclide is the ratio between the k-activities at the cooling time t_{cool} (1st FISPACT run) and the total number of k-nuclides produced at the end of a fictitious instantaneous irradiation (T_{irr}=1s), i.e. assuming that all the neutrons are emitted in one second (2nd FISPACT run) multiplied by the total neutron yield. The correction factor for k-radionuclide in s^{-1} is:

$$\tau_k^{-1}(t)\big|_{t_{cool}} = Y_n \frac{A_k(t)\big|_{t_{cool}}}{N_k\big|_{T_{irr}=1s,\,t_{cool}\to 0}} \qquad (2)$$

where:

$A_k(t)\big|_{t_{cool}}$ activity of k-radionuclide at $t=t_{cool}$ in s^{-1}

$N_k\big|_{T_{irr}=1s,\,t_{cool}\to 0}$ number of atoms of k-radionuclide at the end of instantaneous irradiation

$Y_n = \int_0^{Tirr} \frac{dn}{dt'}dt'$ total neutron yield

Except for multi-step reactions and isomeric transitions the correction factor is independent of the neutron spectrum, activation cross section and amount of parent nuclides. It depends only on the irradiation history and this is true if the two FISPACT calculations, real irradiation history and instantaneous, are performed using the same input flux, activation cross-sections and material.
The different contributions to the dose rate multiplied by the proper time correction factor are summed to obtain the total shutdown dose rate.
The shutdown dose rate in μSv/h is:

$$\dot{D}(t)\big|_{tcool} = 3.6x10^{-4} \bullet \sum_k D_k\big|_{MCNP}\cdot\tau_k^{-1}(t) \qquad (3)$$

It is obtained by combing the equations (1) and (2) and the numerical factor $3.6x10^{-4}$ is applied to convert the pSv/s to μSv/h.
In standard D1S version used previously the time correction factors were applied in post-processing or using proper tally multiplier in MCNP input tally card specifications. In Advanced-D1S these factors are used by MCNP and directly applied to the decay gammas. During the Monte Carlo simulation, the time correction factors are read on an external file. These factors are internally applied to each generated gamma according to its parent and multiplied by the corresponding flux-to-dose conversion coefficient to provide directly, as an output result, the shutdown dose rate map in

μSv/h. Full consistency with previous D1S versions have been tested with standard cell based tallies calculations.
The uncertainty on shutdown dose rate calculation is the intrinsic statistical error in coupled neutron-decay gamma transport.
The decay gamma flux and material dose map can be also calculated using proper tally specification. The additional features of Advanced-D1S are the automated time dependence, the possibility to make selective activation and the identification of the dominant nuclides contributing to the dose. Time behaviour, at the moment implemented for standard cell/surface tallies, is obtained by including the decay constant (λ) for each radionuclide contributing to the dose by considering the decay lay. The decay gammas can be emitted from the whole machine but it is also possible to limit the decay gamma generation and transport to particular cells and/or materials with proper specifications in input file. The contribution to the dose from each radionuclide can be provided as well and it permits to identify the dominant nuclides.

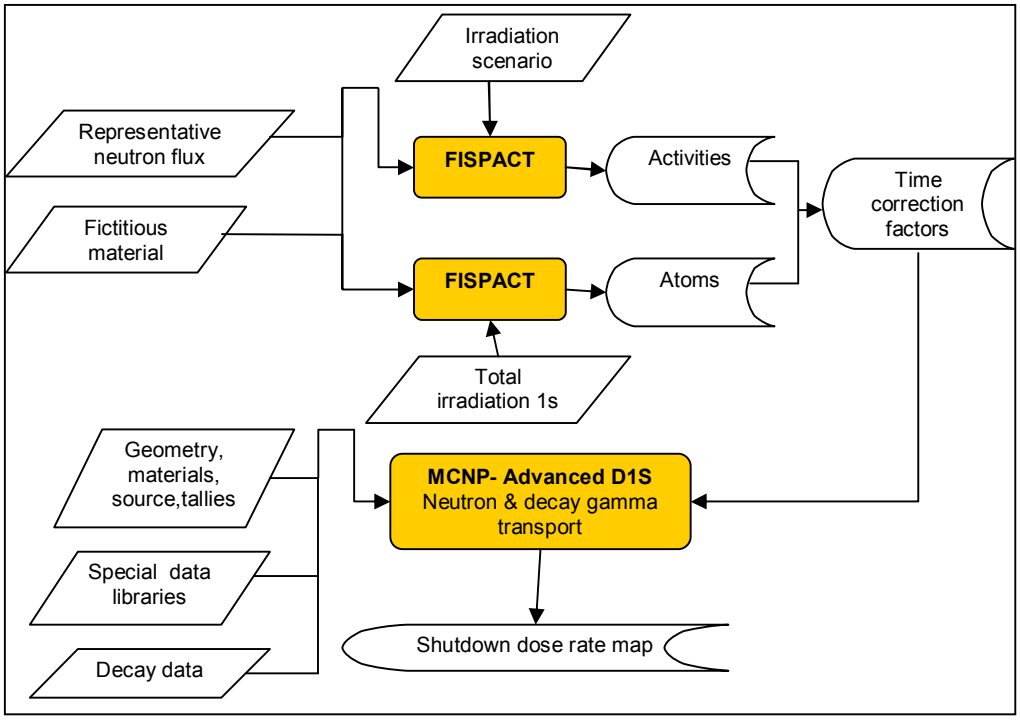

Fig.1. Work flow of the Advanced-D1S approach

3. MCNP5 code on the CRESCO HPC infrastructure

The MCNP5 code, in versions RSICC 1.4 and 1.6 has been compiled on the CRESCO HPC infrastructure in serial and parallel versions. The MPI implementation adopted, among the others provided, is Open MPI. Open MPI is the result of merging effort of different MPI solution and in the opinion of the authors provides the most reliable and supported MPI implementation for any kind of cluster interconnection networks. The MCNP5 compilation and the results, here reported, have been obtained on the CRESCO cluster section 1 and 2, supporting the Open MPI 1.2.8 version. The work of compiling the code on the other sections of the CRESCO cluster adopting newer version of Open MPI (1.4.1, 1.4.2, 1.5.4) is still in progress. The compiler provided by the CRESCO infrastructure includes Intel, Portland and GNU suites. the code has been compiled and tested against all these.

Different patches have been applied to the 'install' and the 'makefile' script and to some routines of the 'src' code directory, aiming to the removal of warnings and in some case of errors preventing the compilation and building of the code. The lack of recast of several variables in C routines of the 'dotcomm' directory, implementing the 'libdotcomm' library, looking after the MPI communication, drives to generation of warnings for 'icc' and 'gcc' compilers, and prevents from building the code using 'pgcc' compiler. These amended MCNP5 versions have been released and are in use of other ENEA departments.

The 'Intel' MCNP5 code compiled version proves an obvious computational superiority compared to the GNU and Portland versions, being Intel the CRESCO cluster processor of sections 1 and 2.

4. Applications to ITER Test Blanket Module port plug studies

Recently Advanced D1S complied on CRESCO HPC has been applied to ITER tokamak port plug studies. The dose rate at 12 days after shutdown has been calculated in maintenance zone of test blanket module (TBM) equatorial port. A detailed 3-D Neutronic model of the TBM port plug with dummy TBMs has been developed and integrated in the last released version of the 40° MCNP ITER reference model (B-lite v-3). The MCNP model is shown in figure 2.

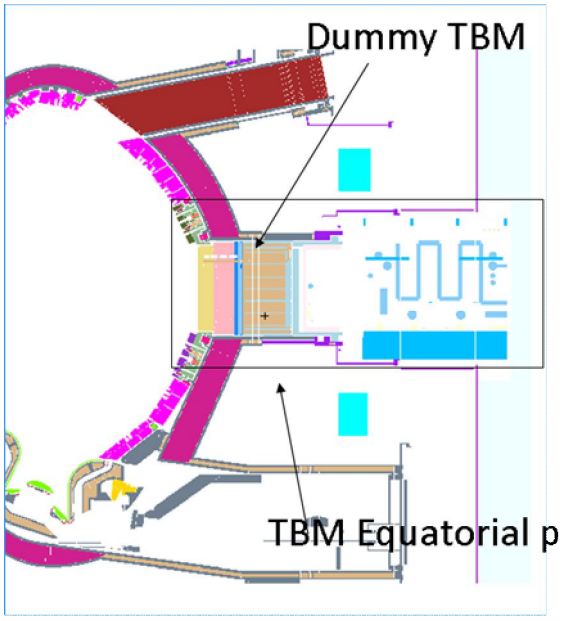

Fig. 2. Poloidal-radial section of B-lite v3 ITER MCNP model with TBM port plug with dummy TBMs.

The TBM frame has a double-dogleg configuration and shims as described in [7,8]. The results of the dose rate calculation in equatorial port at 12 days after shutdown with Advanced-D1S are shown in the figure 3. The materials include relevant impurities and all the ITER components are activated (global model calculation). The SA2 irradiation scenario has been adopted, it is consistent with an average neutron wall load of 0.56 MW/m^2 and a total neutron fluence of 0.3 MWa/m^2 to the first wall. The simulation was carried-out in 24 hours on CRESCO2 using 600 cores and the results refer to 5x10^8 particles. Weigh windows were applied to neutron and gamma to obtain accurate results with a statistical error lower than 10 % in the area of interest. The shutdown dose rate in maintenance area exceeds the ITER design target of 100 μSv/h more than a factor two. Optimization of the design of TBM port plug is in progress as well as shielding studies to reduce the lower port contribution and the activation of port extension and connecting duct.

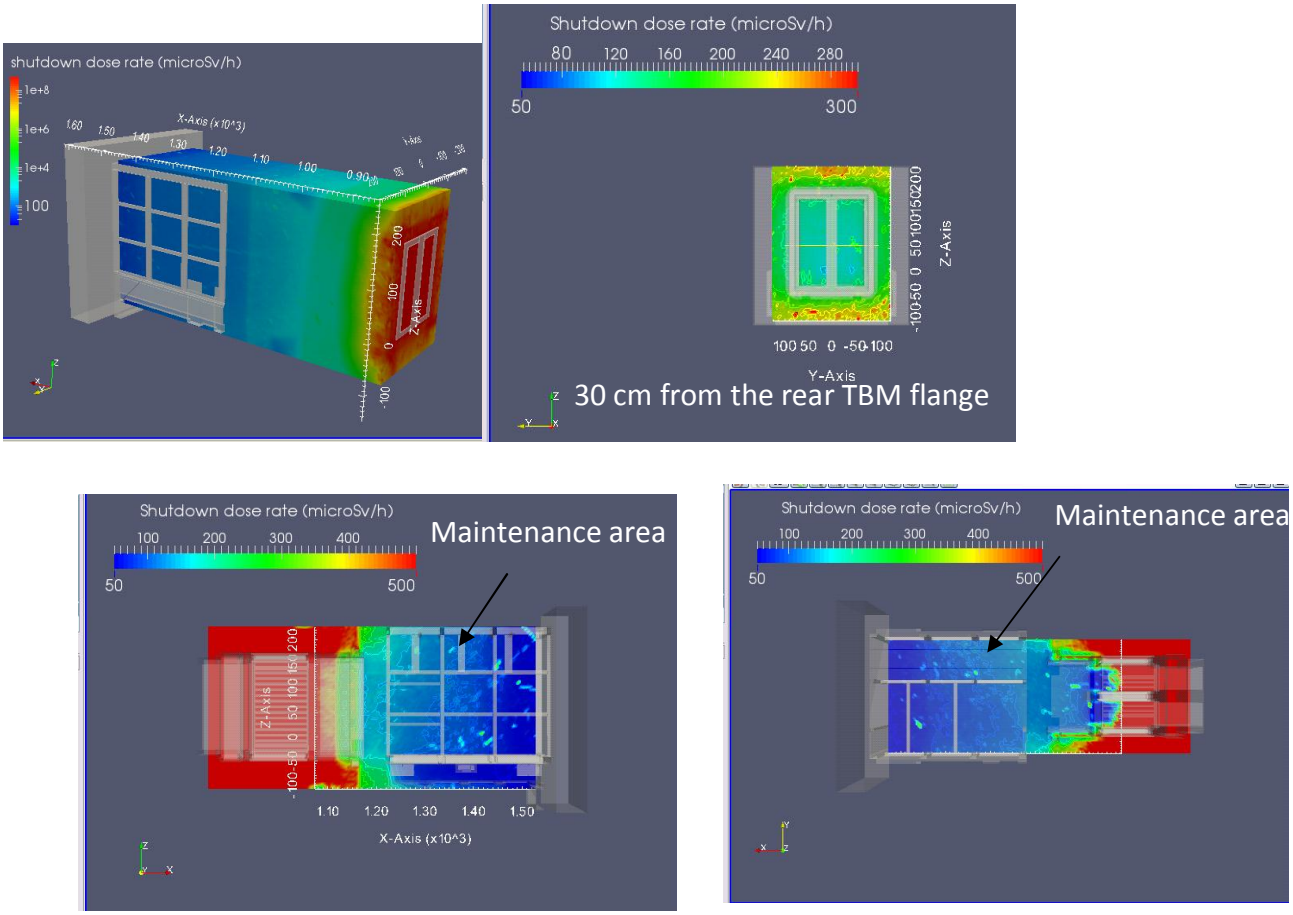

Fig. 3. Shutdown dose rate map at 12 days after shutdown in ITER equatorial TBM port. The dimension of the mesh element was 5x5x5 cm^3. Maps obtained running Advanced D1S on CRESCO_2 using 600 cores for 24h.

5. Limitations and further developments

The coupled neutron-decay gamma transport of Advanced-D1S is an efficient method in providing fast results at different times after shutdown in a single MCNP simulation. The uncertainty in dose rate and decay gamma calculation and identification of contribution from each radionuclide and machine component are intrinsically reliable. Nevertheless it cannot be used for general applications and it shows limitations mainly due to the partial treatment of activation, inadequacy in treating multi-step reactions and inability to simulate situations in which the components have different lifetimes or if they change their positions during irradiation or decay Work in progress is devoted to overcome these limitations by including parameters which control lifetime, through the variation of the correction factors depending on the irradiation conditions of each component. Further efforts are devoted to extend the time evolution capability to mesh tally, to optimize the automatism and the interface between MCNP and FISPACT and in the preparation of the special libraries.

6. Conclusions

The main attractive features of the Advanced D1S methodology in shutdown dose rate predictions are the direct coupling of the decay gamma to neutrons, the time evolution of the dose rate behavior after shutdown and the dose mesh map. The outcomes confirm the essential role of the Advanced-

D1S methodology for a fast and reliable assessment of shutdown dose rates and related statistical uncertainties in present and future fusion devices.

In progress applications of the code for ITER calculations require ~$2x10^6$ hours of CRESCO computing time for 2014.

References

[1] D. Valenza et al., Proposal of shut-down estimation method by Monte Carlo code, Fusion Engineering and Design 55 (2001) 411-418.

[2] L. Petrizzi et al., Improvement and benchmarking of the new shut-down dose estimation method by Monte Carlo code, Proc. of the Monte Carlo 2000 Conf., Lisboa, October 23-26, 2000; Berlin : Springer (2001) 865-870

[3] X5 MONTE CARLO Team, "MCNP—a general Monte Carlo N-Particle transport code: version5 user's guide", LANL report LA-CP-03-0245, October 2005.

[4] R. Forrest, FISPACT-2007 User Manual EASY 2007 Documentation Series UKAEA FUS 534.

[5] R. Villari, et al., Shutdown dose rate benchmark experiment at JET to validate the three-dimensional Advanced-D1S method, Fusion Engineering and Design 87 (2012) 1095-1100.

[6] R. Villari et. al. , Shutdown dose rate assessment with the Advanced D1S method: development, applications and validation, submitted to Fus. Eng. Des.

[7] R. Villari,F. Moro, S. Podda, Neutronic Analysis of ITER TBM PP (CDR), final report, ITER JR5EZH (2013)

[8] B.Y. Kim et al., Status of ITER TBM port plug conceptual design and analyses,submitted to Fus. Eng. Des.

Computational analysis of media effects on model compound MBET-306

C. Guardiani[a] and P. Procacci[a,b]

[a] *Department of Chemistry, University of Florence, Italy*
[b] *Corresponding author:* **piero.procacci@unifi.it**

ABSTRACT

Small-molecule inhibitors of Tumor Necrosis factor alpha Converting Enzyme (TACE) are a promising therapeutic tool for Rheumatoid Arthritis, Multiple Sclerosis and other autoimmune diseases. Here we report on Hamiltonian Replica Exchange Molecular dynamics simulations of a new compound, named MBET-306, that represents the common scaffold of a family of recently discovered tartrate-based TACE inhibitors. In a previous study we suggested the possibility of a two-stage docking mechanism whereby the formation of an intermediate between the drug in a compact conformation and the catalytic Zinc ion, is followed by a structural rearrangement to an extended conformation favored by the local amphiphilic environment. Our simulations in different solvents show that MBET-306, similar to the parental tartrate compounds, responds to a moderately hydrophobic environment with an increase of the fraction of extended conformations, confirming to be a good model compound of tartrate-derived TACE inhibitors. While the experimental characterization of the compound is still underway in our lab, these results already bode well for a systematic use of MBET-306 as a basic building block for the rational design and synthesis of more complex tartrate-derived TACE inhibitors.

INTRODUCTION

Autoimmune diseases comprise more than 50 syndromes including Rheumatoid Arthritis (RA), Multiple Sclerosis (MS) and Lupus Erythematosus [1]. Despite the wide array of affected organs and clinical manifestations, research has highlighted a key role played in most of these diseases by the pro-inflammatory cytokine Tumor Necrosis Factor alpha (TNFa) [2]. TNFa is synthesized as an homotrimeric membrane precursor that is cleaved by the sheddase TNFa Converting Enzyme (TACE) that releases a soluble form (sTNFa) eliciting the auto-immune reaction. In Rheumatoid Arthritis, for example, the soluble TNFa released by activated macrophages interacts with the TNFR1 receptor constitutively expressed on fibroblasts and chondrocytes of the joints activating a signaling pathway that culminates in the expression and secretion of Matrix Metalloproteinases MMP-1 and MMP-13 that hydrolyze the collagen of the joint cartilage severely impairing its function [3]. In Multiple Sclerosis TNFa does not only trigger the neuro-inflammatory reaction [4] but it also inhibit Neuregulin-1 type III, a membrane protein involved in remyelination in the peripheral nervous system thus preventing the repair of the brain lesions induced by MS [5]. The inhibition of TACE enzyme, blocking the release of sTNFa would therefore be extremely beneficial for the treatment of a large number of autoimmune diseases.

The catalytic domain of TACE is characterized by a long binding groove delimited by beta-strand IV and helix C [6]. At the center of the groove lies a catalytic Zinc ion surrounded by two sets of primed and non-primed pockets. Effective inhibitors must displace the catalytic water molecule normally bound to the Zinc ion and they must comprise a group capable of fitting into the S1'-S3' cavity, a deep L-shaped well with hydrophobic walls drilled at the center of the major catalytic groove. As a

consequence, TACE and MMP inhibitors are comprised of two main units [7]: a peptidomimetic backbone designed to recognize the primed pocket, and a Zinc binding group (ZBG). Hydroxamate is a very effective ZBG, but its affinity for Zinc is so high to cause unspecific interactions with MMPs and other metal containing enzymes [8]. This lack of specificity causes severe adverse effects that so far have prevented the clinical application of TACE inhibitors. This is why a number of ZBGs with Zinc affinity lower than that of hydroxamate are currently being tested [9].

A novel promising family of TACE nanomolar inhibitors is represented by bis-amides of L-tartaric acid first developed by Rosner *et al* [10]. These compounds have been recently patented [11] and feature a tartrate core linking a left hand side (LHS) and right hand side (RHS) substituent through amide bonds. The tartrate core acts as a tridentate Zinc chelator in the resolved co-crystals [12,13], while the RHS (R)-1-(4-(1H-pyrazol-1-yl)phenyl)ethanamine group fits into the primed narrow pocket. In a recent computational study [14] we highlighted a correlation between the inhibition constant of these compounds and their compactness in water solution. We explained the correlation by noting that the compact structure of the strong inhibitors optimally exposes the Zinc-binding hydroxyls that may be used to interact with Zinc stabilizing an intermediate. The comparison of the enzyme-bound crystal conformations with the structure of the drugs in bulk solvent suggested that the fate of the intermediate might imply a structural rearrangement of the drug from a compact to an extended conformation. The structural reorganization stage of this two-step docking mechanism is critically favored by the local hydrophobic environment of the TACE active site. Such a low dielectric environment, in fact, enhances the breakdown of the interactions between the RHS and LHS hydrophobic groups making them available for the interaction with the apolar surfaces of TACE pockets.

This promising results prompted our group to synthesize a novel substance, called MBET-306 (shown in Figure 1), featuring a pyrrolidine LHS and ethyl-phenyl RHS moieties that are common to all Dai [12] powerful inhibitors. This design, by preserving all the chemical determinants that impart to the Dai compounds their peculiar conformational behavior in bulk solution, can act as a versatile synthetic precursor for extending the Dai design to other tartrate-based leads by building upon its minimal LHS and RHS moieties. While the experimental characterization through extensive photo-physical measurements is still underway in our lab, we performed a computational study to assess the media effects on the conformational equilibrium of this model compound. The goal of the study is to ascertain whether the stabilization of the extended conformations in a hydrophobic environment that we observed in our previous study also applies to the MBET-306 building block.

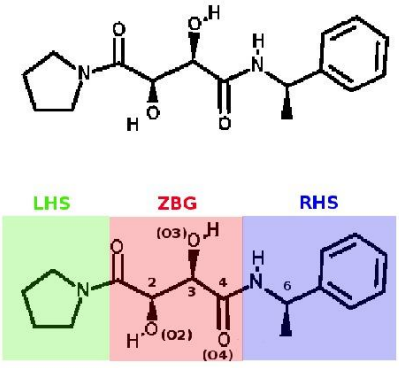

Figure 1. The chemical structure of MBET-306:
2,3-dihydroxy-4-oxo-N-((S)-1-phenylethyl)-4-(pyrrolidin-1-yl)butanamide
The Zinc Binding Group (ZBG) and the Right Hand Side (RHS) and Left Hand Side (LHS) moieties are highlighted in pink, blue and green respectively.

METHOD

The model compound MBET-306 was built using the crystallographic structure of drug-38 (PDB ID: 3O64) designed by Dai *et al* [12] removing the thiazole and pyrazole rings and adding the missing hydrogens with the Molefacture plugin of the VMD program [15]. The structure underwent a geometric optimization with the Gaussian program [16] at the SCF level using the 6-31G* basis set.
Atomic charges were computed using the ESP scheme and then symmetrized to RESP charges using the Antechamber program [17]. The charges computed with this approach were used for the simulations in water and DMSO. A special approach was employed to compute the charges to be used in the chloroform simulation. As will be explained more in detail later on, after the Hamiltonian REMD simulation in DMSO, we performed a clustering analysis of the equilibrium ensemble of the target replica of our compound. The charges of the representatives of the five most populated clusters were computed with the Gaussian program using the Becke-style 3-parameter Density Functional Theory and the 6-311+g(3df,2p) basis set. We then computed a weighted average of the charges of the five structures using the frequencies of the five most populated clusters in DMSO as weights. The resulting charges were used for the simulation in CHCl3.

All Molecular Dynamics simulations were performed with the ORAC suite of programs [18,19] using the General Amber Force Field (GAFF) [20]. The drug was minimized *in vacuo* in 2500 steps of steepest descent followed by 2500 step of conjugate gradient. In the water simulation the compound was solvated with 512 water molecules in a simple cubic box with periodic boundary conditions. For the simulation in DMSO the molecule was surrounded by 125 DMSO molecules while only 64 chloroform molecules were necessary for the simulation in this solvent. The solvated system was equilibrated for *100 ps* in the isothermal-isobaric ensemble at $T=300\ K$ and $p=1\ atm$. The last configuration obtained during the equilibration stage was used as the starting point for Hamiltonian Replica Exchange Molecular Dynamics (REMD) simulations [21] with 8 replicas each simulated for *30 ns*.

In Hamiltonian REM, N replicas of the system are simulated in parallel with different sets of scaling coefficients that act as weights for different additive components of the potential energy. At regular time intervals *N/2* exchanges are attempted among replicas with neighboring sets of coefficients and the exchanges are accepted or rejected according to a Metropolis-like criterion. If the scaling coefficients are appropriately chosen, when the potential energies of the two replicas involved in the exchange are substituted in the expression for the acceptance probability, the less relevant energy terms will cancel out and the acceptance probability will depend on a small subset of degrees of freedom reducing the number of necessary replicas and thus the computational cost of the simulation. In our simulations the torsional and non-bonded potentials of the solute were scaled throughout the replica progression with maximum and minimum scaling factors (1.0, 0.1) corresponding to effective temperatures of 300 K and 3000 K respectively. Exchanges between adjacent replicas were attempted every 100 *fs* with average acceptance probabilities in the range 20-50%. Conformations were saved every 500 *fs* producing a total of 60000 configurations per replica.

The large number of configurations of the equilibrium ensemble of the target replica were analyzed through Quality Threshold clustering [22]. This algorithm requires a distance matrix for all pairs of structures of the population. The structural metrics that we chose was the maximum difference between corresponding pairs of heavy atoms. For each structure in the ensemble the algorithm builds a candidate cluster in such a way that the distance between any two structures of the cluster does not exceed the cutoff distance (that we chose to be *2.0 Å)*. The program then retains only the largest cluster and

removes its structures from the population. The procedure is iterated until all structures of the populations are used.

RESULTS

The compound we are investigating is characterized by the presence of a central core of tartaric acid linking two hydrophobic units at the right and left hand sides. It is therefore appropriate to start our analysis monitoring typical indicators of compactness such as the distance between the centers of mass of the RHS and LHS units (d_{RL}) and the radius of gyration (R_g).

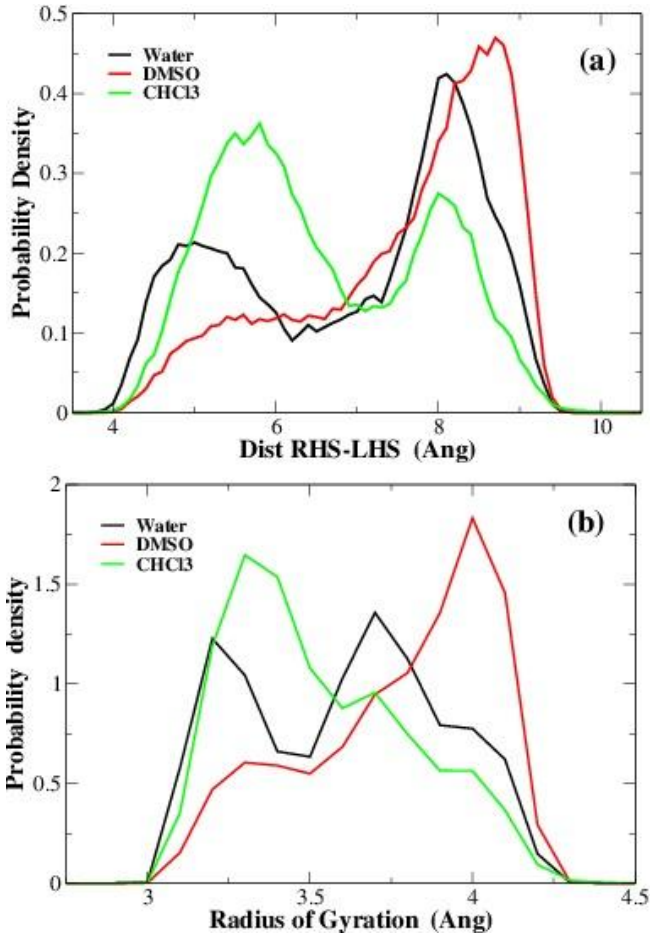

Figure 2. Structural features of the model compound in different solvents.
(a) Probability distribution of the distance between the centers of mass of the RHS and LHS groups.
(b) Probability distribution of the radius of gyration.

In Figure 2 we show the probability distributions of the two indicators in three different solvents of different polarity, namely water, dimethyl-sulfoxide (DMSO) and chloroform (CHCl3). The figure shows that in water the distributions of both indicators are markedly bimodal suggesting the existence of two structural groups comprising compact and extended conformations respectively. In DMSO the peak of compact conformations observed in water reduces to a long tail and the distribution features only a single peak of extended structures. This pattern is the likely consequence of the greater hydrophobicity of DMSO with respect to water. It is noteworthy that in other tartrate drugs we simulated (like drug-1 and drug-38 of Ref [12]) the group of compact conformations comprised almost the entire population.

This was due to the fact that the two apolar units on either side of the tartrate core included two hydrophobic rings and not just one as in the model compound currently under investigation, providing higher structural flexibility and enhancing the hydrophobic effect. When the model compound is simulated in DMSO, the moderate polarity of the solvent relieves the hydrophobic effect allowing the pyrrolidine and phenyl rings to move apart from each other stabilizing a population of entropically favorable, partially bent conformations. Figure 2 also shows that when the model compound is simulated in CHCl3, the distribution of the RHS-LHS distance is again bimodal, but the most populated peak corresponds to compact conformations. This effect is even more pronounced in the case of the radius of gyration whose distribution shows a single high peak of compact structures and then slowly decreases as R_g increases. This is due to the extremely low dielectric constant of chloroform that enhances the interactions between polar groups of the tartaric compound. This did not occur in DMSO where the sulfone group could act as a hydrogen bond acceptor competing with the carbonyl and hydroxyl groups of the tartrate unit. It must therefore be stressed that the compact structures present in water and in CHCl3 are induced and stabilized by different driving forces. In water the driving force is represented by the hydrophobic effect while in CHCl3 there is a dominant enthalpic effect related to electrostatic interactions.

The above patterns can be better clarified through a structural analysis of the equilibrium population of the drug in the target replica using Quality Threshold Clustering. In Figure 3 we show the overlay of the representatives of the most populated clusters of compact and extended conformations of the model compound in the three solvents. The superposition was performed using heavy atoms only.

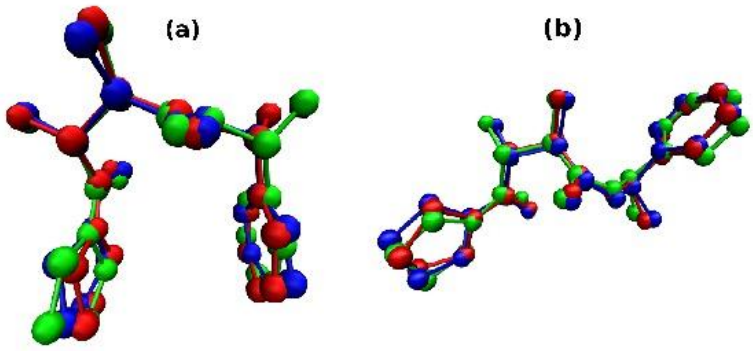

Figure 3. Structural motifs exhibited by the model compound in water (red), DMSO (green) and CHCl3 (blue).
(a) shows the overlay of the representatives of the most populated clusters of compact conformations;
(b) reports the superposition of the centroids of the most populated clusters of extended structures.

Figure 3 shows that the compact and extended motifs are almost identical while the external conditions only shift the equilibrium between the two subpopulations without significantly affecting the structural features. Despite the structural similarity, however, it must be remarked that the compact motif is stabilized by different driving forces in the different solvents. More specifically, in water and DMSO the dominant influence pertains to the hydrophobic effect whereas in CHCl3 the electrostatic interactions represent the driving force. The close proximity of the secondary amide group (N2-H11) to the carboxyl unit involved in the tertiary amide bond (C5=O11) suggests the possibility of a hydrogen bond stabilizing the compact motif in the chloroform environment. In order to provide quantitative support to this working hypothesis it is necessary to: (i) show the existence of the postulated hydrogen bond in the majority of structures of the equilibrium ensemble in CHCl3; (ii) show the existence of a correlation between the presence of the hydrogen bond and the compact structures. Considering that the

strength of a hydrogen bond depends on the proximity of the electronegative atoms involved and on the collinearity of the donor-hydrogen-acceptor triple, we addressed the first issue by computing the potential of mean force (PMF) as a function of the N2-O1 distance and the N2-H11-O1 angle. Figure 4 that shows the contour plot of such PMF, highlights the existence of a main deep minimum of free energy at short N2-O1 distance (about *2.75* Å) and high values of the N2-H11-O1 angle (about 120 degrees), thus providing compelling evidence of the presence of a strong N2-H11-O1 hydrogen bond in a large part of the structures of the equilibrium ensemble. In order to verify the correlation between the hydrogen bond and the compact structures, in Figure 4 we also show the contour plots of the PMF as a function of the RHS-LHS distance and the N2-O1 distance. Also in this case there is a main deep well corresponding to small values of both parameters. This convincingly suggests that the N2-H11-O1 hydrogen bond is indeed the stabilizing agent of compact conformations in CHCl3.

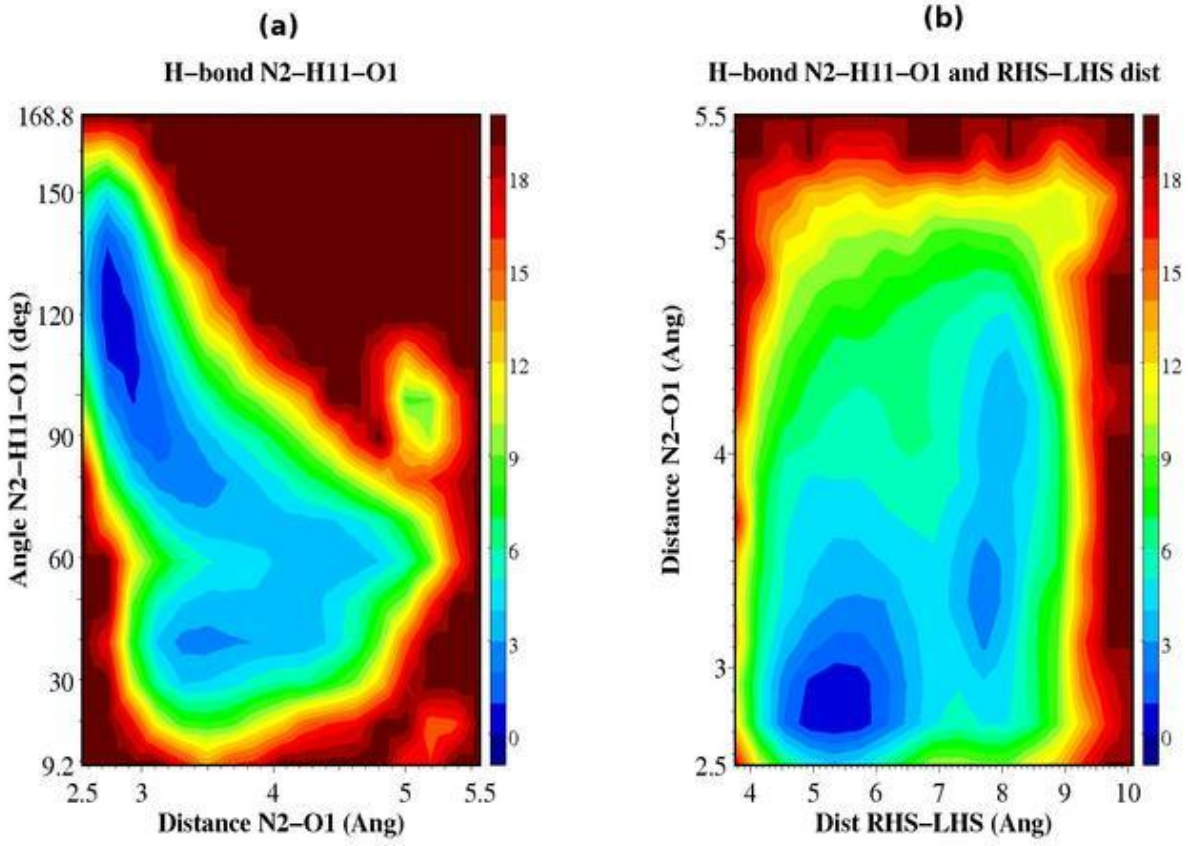

Figure 4. Analysis of N2-H11-O1 hydrogen bond of the model compound MBET-306 in CHCl3.
(a) Contour plots of the PMF of the equilibrium ensemble in CHCl3 as a function of the N2-O1 distance and the N2-H11-O1 angle.
(b) Contour plots of the PMF as a function of the RHS-LHS distance and the N2-O1 distance. Both in (a) and (b) the contour levels are expressed in *kJ/mol*.

CONCLUSIONS

In this study, using extensive generalized ensemble simulations, we characterized the structural impact of the solvent environment on the model compound MBET-306. MBET-306 is based on the bis-amides of L-tartaric acid, recently identified by Dai *et al.* [12] as potent TACE inhibitors. More specifically,

MBET-306 includes the common scaffold of the tartrate-derived TACE inhibitors and can therefore be regarded as a versatile building block for the design and synthesis of more complex tartrate derivatives. In our previous work [14] on a wide panel of TACE inhibitors we suggested the possibility of a two-stage docking mechanism whereby the formation of an intermediate between the drug in a compact conformation and the catalytic Zinc ion, is followed by a structural rearrangement driving the molecule to an extended structure capable of fitting into the binding pockets of the TACE active site. We also verified that a key requirement for such an isomerization to occur is the presence of
a local hydrophobic environment favoring the breakdown of hydrophobic interactions between the aromatic rings of the RHS and LHS groups and the subsequent establishment of new contacts with the hydrophobic surfaces of the primed and non-primed pockets. The sensitivity to a local apolar environment thus appears to be of paramount importance for the TACE inhibition potency of these leads and it is therefore important to ascertain whether this feature is also retained by MBET-306. In order to test this issue, in this work we performed Hamiltonian REMD simulations [21] of MBET-306 in three solvents of different polarity, namely water, DMSO and CHCl3. The simulations showed that while in water the groups of compact and extended conformations are evenly populated, in a moderately hydrophobic solvent like DMSO, there is a significant increase of extended structures. This suggests that MBET-306 has indeed inherited the typical sensitivity to an amphiphilic environment of the parental Dai drugs and can be thus considered a good model for the design of other tartrate TACE inhibitors. On the other hand, the extremely hydrophobic environment of CHCl3 stabilizes intra molecular electrostatic interactions such as hydrogen bonds increasing the population of compact conformations. This suggests that a solvent like CHCl3 often employed in experimental studies, does not realistically reproduce the environment of TACE active site and its use should be discouraged to avoid artifactual results.

LIST OF REFERENCES

[1] PERSIDIS A.
"Autoimmune disease drug discovery"
Nature Biotech. **17** (1999) pp 1038-1039

[2] NEWTON R.C., SOLOMON, K.A., COVINGTON M.B., DECICCO C.P., HALEY P.J., FRIEDMAN S.M., VADDI K.
"Biology of TACE inhibition"
Ann. Rheum. Dis. **60** (2001) pp iii25-iii32

[3] VINCENTI M.P., BRINCKERHOFF C.E.
"Transcriptional regulation of collagenase (MMP-1, MMP-13) genes in arthritis: integration of complex signaling pathways for the recruitment of gene-specific transcription factors"
Arthritis Res. **4** (2002) pp 157-164

[4] GIJBELS K., MASURE S., CARTON H., OPDENAKKER G.
"Gelatinase in the cerebrospinal fluid of patients with multiple sclerosis and other inflammatory and neurological disorders"
J. Neuroimmunol. **44** (1992) pp 29-34

[5] PEREIRA J.A., LEBRUN-JULIEN F., SUTER U.
"Molecular mechanisms regulating myelination in the peripheral nervous system"
Trends Neurosci. **35** (2012) pp 123-134

[6] MASKOS K., FERNANDEZ-CATALAN C., HUBER R., BOURENKOV G.P., BARTUNIK H. ET AL.
"Crystal structure of the catalytic domain of human tumor necrosis factor-alpha-converting enzyme"
Proc. Natl. Acad. Sci. USA **95** (1998) pp 3408-3412

[7] DASGUPTA S., MURUMKAR P.R., GIRIDHAR R., YADAV M.R.
"Current perspective of TACE inhibitors: a review"
Bioorg. Med. Chem. **17** (2009) pp 444-459

[8] TU G.G., XU W.F., Huang H.M., LI S.H.
"Progress in the development of matrix metalloproteinase inhibitors"
Curr. Med. Chem. **15** (2008) pp 1388-1395.

[9] LI N.G., SHI Z.-H., TANG Y.P., LI W., YIN L., DUAN J.A.
"Discovery of Selective Small Molecular TACE Inhibitors for the Treatment of Rheumatoid Arthritis"
Curr. Med. Chem. **19** (2012) pp 2924-2956

[10] ROSNER K.E., GUO Z., ORTH P., SHIPPS G.W. Jr, BELANGER D.B.
"The discovery of novel tartrate-based TNF-alpha converting enzyme (TACE) inhibitors"
Bioorg. Med. Chem. Lett. **20** (2010) pp 1189-1193

[11] DAI C., CHAOYANG
"Compounds for the treatment of inflammatory disorders"
US Patent 8,039,467 (2011)

[12] DAI C., LI D., POPOVICI-MULLER J., ZHAO L., GIRIJAVALLABHAN V.M., ET AL.
"2-(2-Aminothiazol-4-yl)pyrrolidine-based tartrate diamides as potent, selective and orally bioavailable TACE inhibitors"
Bioorg. Med. Chem. Lett. **21** (2011) pp 3172-3176

[13] NIU X., UMLAND S., INGRAM R., BEYER B.M., LIU Y.H., SUN J., LUNDELL D. ORTH P.
"IK682, a tight binding inhibitor of TACE"
Arch. Biochem. Biophys. **451** (2006) pp 43-50

[14] GUARDIANI C., PROCACCI P.
"The conformational landscape of tartrate-based inhibitors of the TACE enzyme as revealed by Hamiltonian Replica Exchange simulation"
Phys. Chem. Chem. Phys. **15** (2013) pp 9186-9196

[15] HUMPHREY W., DALKE A., SCHULTEN K.
"VMD - Visual Molecular Dynamics"
J. Molec. Graphics **14** (1996) pp 33-38

[16] FRISCH M.J., TRUCKS G.W., SCHLEGEL H.B. SCUSERIA G.E., ROBB M.A. ET AL.
Gaussian 09, Revision A.01, 2009

[17] WANG J., WANG W., KOLLMAN P.A. CASE D.A.
"Automatic atom type and bond type perception in molecular mechanical calculations".
Journal of Molecular Graphics and Modelling **25** (2006) pp 247260

[18] PROCACCI P., DARDEN T.A., PACI E., MARCHI M.
"ORAC: a molecular dynamics program to simulate complex molecular systems with realistic electrostatic interacions"
J. Comp. Chem. **18** (1997) pp 1848-1862

[19] MARSILI S., SIGNORINI G.F., CHELLI R., MARCHI M. PROCACCI P.
"ORAC: a molecular dynamics simulation program to explore free energy surfaces in biomolecular systems at the atomistic level"
J. Comp. Chem. **31** (2010) pp 1106-1116

[20] WANG J., WOLF R.M., CALDWELL J.W., KOLLMAN, P.A., CASE D.A.
"Development and testing of a general AMBER force field".
J. Comp. Chem. **25** (2004) pp 1157-1174

[21] FUKUNISHI H., WATANABE O., TAKADA S.
"On the Hamiltonian replica exchange method for efficient sampling of biomolecular systems: application to protein structure prediction"
J. Chem. Phys. **116** (2002) pp 9058-9067

[22] HEYER L.J., KRUGLYAK S. YOOSEPH S.
"Exploring Expression Data: Identification and Analysis of Coexpressed Genes"
Genome Res. **9** (1999) pp 1106-1115.

A high-resolution 46-year atmospheric hindcast for the Mediterranean Basin

G. Sannino, A. Carillo, M. Palma

ENEA –UTMEA-CLIM, via Anguillarese 301, 00123 Rome, Italy
gianmaria.sannino@enea.it

Abstract

In this study we investigate the interannual variability of the Mediterranean Sea over the period 1958-2004 as simulated by an eddy-resolving Ocean General Circulation. The model used is the MITgcm implemented at a horizontal resolution of 1/12º. In the vertical, 72 unevenly spaced Z-levels are used. The model output has been validated through a systematic comparison with most of the available observed data for the period considered. The general surface and intermediate circulation given by the models reproduced reasonable well the main features of the basin-scale circulation. Hydrographic analysis of the model results revealed that the characteristics and distribution of salinity and temperature were in good agreement with observations.

1.Introduction

The present work is performed in the framework of the study of present and future climate for the Euro-Mediterranean area. Different ocean circulation models for the Mediterranean Sea and its sub-basins and a coupled ocean-atmosphere model have been developed at ENEA in the last years. These modeling activities have as main focus the better understanding of both the atmospheric and oceanic climate variability and have been used for the production of scenario simulations.
The development of new versions of these models is ongoing. In particular during the last year a series of simulations have been performed on the CRESCO cluster to setup a new release of the oceanic component. In particular a 46 year long hindcast simulation for the Mediterranean Sea, at the horizontal resolution of 1/12°, has been produced.
The Mediterranean Sea is a semi-enclosed basin in which evaporation exceeds precipitation and river runoff, while heat is lost from the surface. Both mechanisms represent the main driving forces of the Mediterranean thermohaline circulation whose entering upper branch and exiting lower branch are located in the Strait of Gibraltar. Through the Strait an upper flow of fresh and warm Atlantic water spreads in the Mediterranean basin, and a lower flow of colder and saltier Mediterranean water sinks in the North Atlantic, down to a depth of around 1000 m where it becomes neutrally buoyant. The Mediterranean Sea circulation and water masses have been studied for a long time and some schemes of the steady state of its thermohaline circulation have been proposed. The main goal of this work is the assessment of the performances of a numerical model in reproducing the Mediterranean thermohaline circulation. In particular the results obtained from the 46 years of simulation will be discussed in the following paper. Details of the model implementation will be presented in the following paragraph, while model results and discussion will finalize the work.

2.Model description and validation

The model used is a 3D ocean circulation model (MITgcm) developed by Marshall et al. [1,2] at the Massachusetts Institute of Technology. In the present work it has been used in its hydrostatic,

implicit free-surface, partial step topography formulation [3].
At present MITgcm represents the state of the art of the ocean numerical models. It is designed to run on different platforms, from scalar to vectorial. Thanks to a flexible makefile generator, MITgcm can be easily compiled on a huge number of different clusters. MITgcm is wrote in pure Fortran77, so an MPI Fortran compiler is the only requirement. MITgcm is parallelized via MPI through a horizontal domain decomposition technique that is the common practice for atmospheric and ocean models. Our Mediterranean implementation has been run on a CRESCO (section 2). The total number of cpus used during the simulation were 456, even if the maximum number of cpus that can be used (i.e. before the scalability starts to saturate) is 620. The minimum memory per core (GB) obtained running with 456 cpus was 0.85, i.e. a total memory of (0.85*456) 388GB.
The model domain covers the entire Mediterranean Sea and has its boundary conditions in the Atlantic Ocean at 11.28 °W. The model has a horizontal resolution of 1/12º corresponding to 570x264 grid points. In the vertical the model is discretized using 72 unevenly spaced Z-levels going from 1 m at the surface to about 300 m in the deepest part of the basin. The bathymetry is derived from the 10th version of the MERCATOR-LEGOS bathymetry at a resolution of 30"× 30" generated by merging GEBCO-08 database with MEDIMAP bathymetry [4] and Ifremer bathymetry for the Gulf of Lion [5].

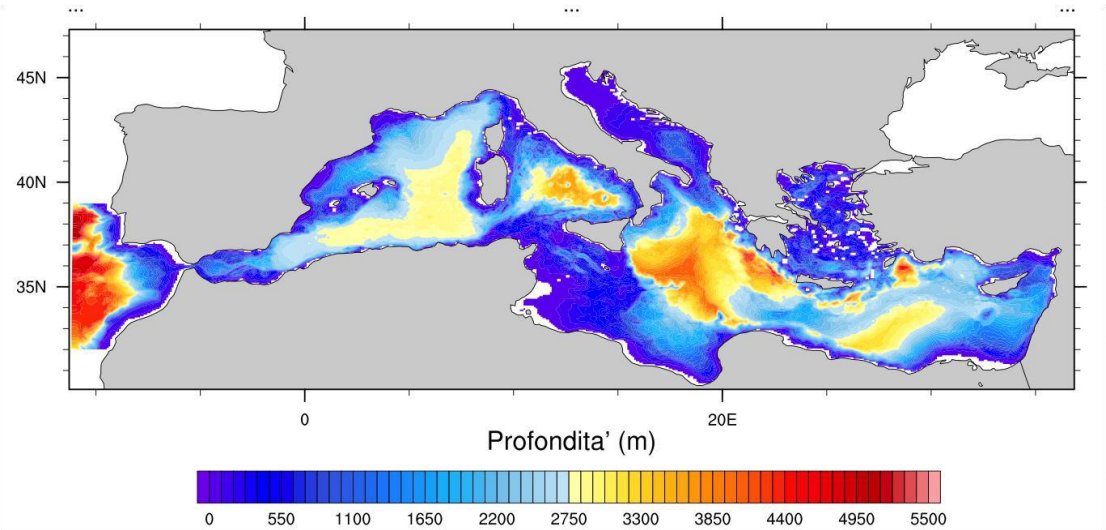

Figure. 1: Model Bathymetry

The simulation covers the period 1958-2004. The model is forced at the surface through six hourly heat and water fluxes derived by a dynamical downscaling of the ERA40 reanalysis performed by ECMWF (European Center for Medium range Weather Forecasting). The simulation is initialized using the MEDATLAS-II monthly climatology data for the month of January. A 3D relaxation of temperature and salinity toward climatological monthly Levitus data [6] is applied at the boundary in the Gulf of Cadiz.

3.Model Results and Discussion

The model output has been validated through a systematic comparison with most of the available observed data for the period considered; in particular an extensive analysis of the main features of the thermohaline circulation (zonal and meridional overturning circulation, deep water formation rate, temperature and salinity fields at surface, intermediate and bottom depths) has been carried out.

In Figures 2 and 3 is shown the evolution of model temperature and salinity compared with that of observational data [7]. Values are averaged horizontally over the main Mediterranean sub-basins and vertically over different layers. From both figures it rises that the general surface and intermediate circulation given by the model reproduce reasonable well the main features of the basin-scale circulation. Hydrographic analysis of the model results revealed that the characteristics and distribution of salinity and temperature were in good agreement with observations. The good agreement found between model temperature, salinity and velocity (not shown) fields toward most of the available observations confirms both the robustness and the effectiveness of the implemented model. A focus has been devoted to verify the ability of the model to represent the deep water formation processes. In Figure 4 the monthly mean mixed layer depth for the entire basin as resulted from the numerical simulation is also shown. Here the main regions recognized as the most productive in terms of deep water formed, i.e. the Gulf of Lion, the Adriatic Sea and the Levantine basin are clearly indicated by the model. Concluding, the analysis performed on the hindcast simulation performed on the CRESCO cluster has shown that the model is able to capture reasonable well the interannual variability of Mediterranean thermohaline circulation for the period 1958-2004. The model is then ready to be included in the next generation of the ENEA coupled climate model.

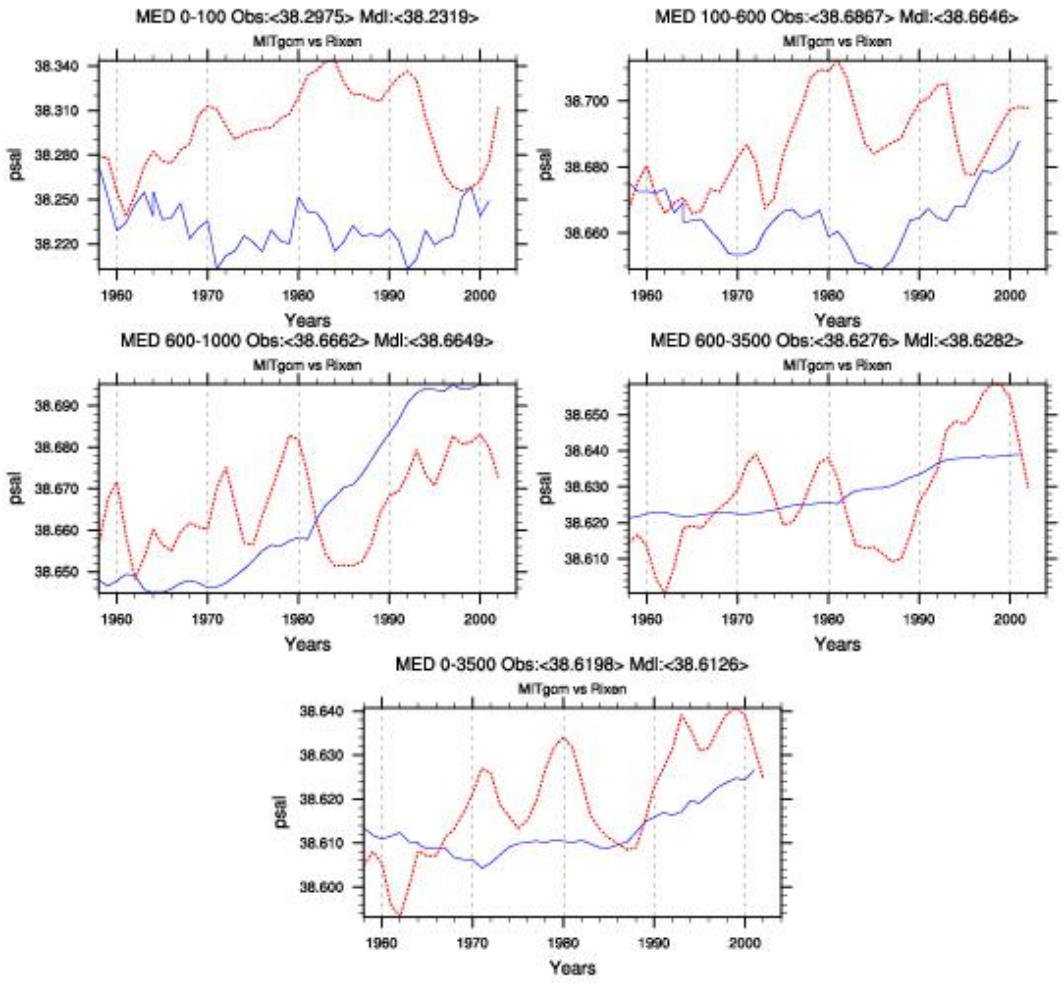

Figure 2: Annual mean salinity in the Mediterranean basin for the simulated 46 years. Model data (solid blue line), MEDATLAS II data (dotted red line).

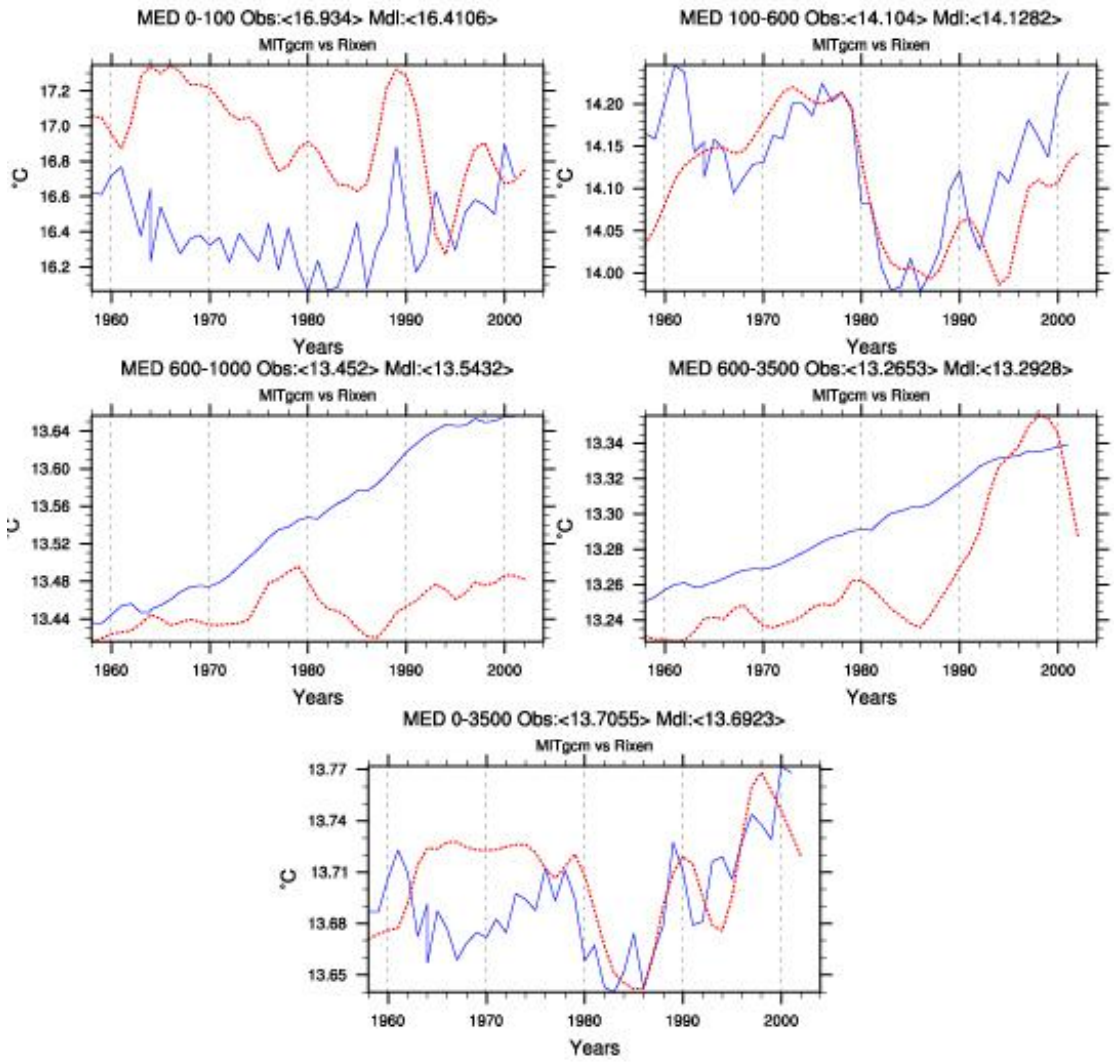

Figure 3: Annual mean temperature in the Mediterranean basin for the simulated 46 years. Model data (solid blue line), MEDATLAS II data (dotted red line).

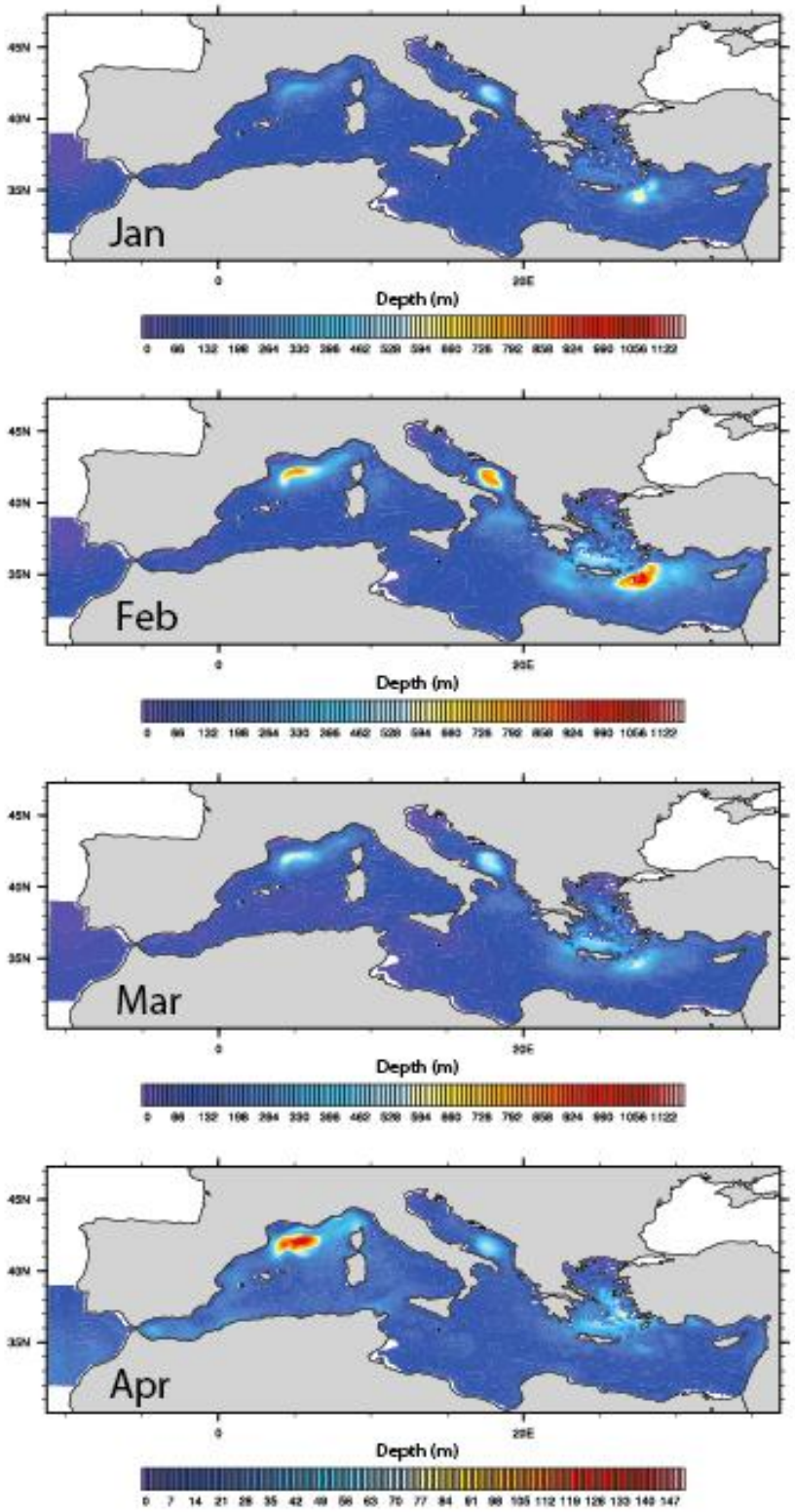

Figure 4: Monthly mean mixed layer depth averaged over the 46years as simulated by the model.

References

[1] MARSHALL J., ADCROFT A., HILL C., PERELMAN L., HEISEY C. "*A finite-volume, incompressible Navier Stokes model for studies of the ocean on parallel computers*". J. Geophys. Res. 102 -C3 (1997) pp. 5753–5766.

[2] MARSHALL J., HILL C., PERELMAN L., ADCROFT A. "*Hydrostatic, quasi-hydrostatic, and nonhydrostatic ocean modeling*". J. Geophys. Res. 102 - C3 (1997) pp. 5733–5752.

[3] ADCROFT A., HILL C., MARSHALL J. "*Representation of topography by shaved cells in a height coordinate ocean model*". Monthly Weather Review 125 9 (1997), pp. 2293–2315.

[4] Medimap Group (2005), Morpho-bathymetry of the Mediterranean Sea, CIESM/Ifremer Edition, 2 maps at 1/2000000.

[5] BERNE S., CARRE D., LOUBRIEU B., MAZE J.P., and NORMAND A. (2004) Le golfe du Lion - Carte morpho-bathymetrique, Ifremer/Conseil Regional du Languedoc-Roussillon Edition.

[6] LEVITUS S. Climatological atlas of the world ocean, (1982) NOAA professional paper 13. U.S. Government Printing Office, Washington, DC.

[7] MEDAR Group (2002) Medatlas/2002 database. Mediterranean and black sea database of temperature salinity and bio-chemical parameters. climatological atlas. IFREMER Edition.

Excitonic effects in low dimensional systems

Viviana Garbuio[(1,2,3)], Claudia Violante[(1,2)], Adriano Mosca Conte[(1,2)], Ihor Kupchak[(4)], Margherita Marsili[(1,5)], Paola Gori[(1,6)] and Olivia Pulci[*(1,2,3)]

[(1)]*European Theoretical Spectroscopy Facility (ETSF)*
[(2)]*Dipartimento di Fisica, Università di Roma "Tor Vergata"*
[(3)]*Mediterranean Institute of Fundamental Physics (MIFP)*
[(4)]*V. Ye. Lashkaryov Institute of Semiconductor Physics of NAS of Ukraine*
[(5)]*Dipartimento di fisica "Galileo Galilei", Università di Padova*
[(6)]*Dipartimento di ingegneria, Università degli studi Roma tre*

Introduction

In this report we briefly review the results that have been obtained in the last year also thanks to the use of the ENEA CRESCO facility. All the works concern the calculation of the electronic and optical properties of materials employing ab-initio theoretical methods based on Density Functional Theory (DFT), Time Dependent Density Functional Theory (TDDFT) and Many Body Perturbation Theory (MBPT).
The report is organized as follows: an overview of the theoretical framework is given, together with a report of the important work of code parallelization, then results are reported. We present the results of two different studies concerning: i) the excited state properties of formamide, both isolated molecule and molecule in water solution; ii) the almost one-dimensional excitons in Si(111)2x1 surface.
While the calculations running on the ENEA CRESCO facility have been mainly carried out by the authors of this report, the complete studies to which we will refer are due to the work of many collaborators, which appear as coauthors in the publications.

Used codes:
Quantum Espresso (www.quantum-espresso.org), EXC (http://etsf.polytechnique.fr/exc/), GW, DP (http://dp-code.org/).

Computational and Theoretical Methods

The theoretical approaches we use are described in our CRESCO report from last year.
Here we just remind that we use DFT for ground state properties [1,2,3], GW for band structure calculations (charged excitations) [4,5,6,7] and the Bethe-Salpeter approach [8] for optical spectra (neutral excitations). The Bethe-Salpeter equation is an important tool to include excitonic effects in the optical properties, in order to obtain a good agreement (quantitative and qualitative) with experiments. To ease the computational applicability, the Bethe-Salpeter equation is rewritten as an eigenvalue problem involving the so-called "excitonic Hamiltonian", whose elements can be calculated starting from DFT wavefunctions, GW quasiparticle energies and the screened Coulomb interaction.
We work on a MBPT code to better parallelize it and therefore to make it more efficient and useful for the study of more complex physical systems. This code computes both the screening function and the self-energy corrections.

* Corresponding author, olivia.pulci@roma2.infn.it

The main program flow is very roughly shown in the schema of **Figure 1**. In general, the task is to compute a very large H matrix, whose size is N_mxN_m for the set of N_q parameters (points). Each matrix element H_{ij} is computed as a sum of N_k values of some function R. Having the number of MPI processes, the program splits them into equal groups ("pools") in such a way that each pool is computing the H matrix for the part of data points. In the picture, all the processes are split into two pools and each of them computes $N_q/2$ parameters (i.e. we parallelize the loop "DO 1").
The size of H matrix may be very large and in some cases the program may exceed the size of available memory. To avoid such a problem, this matrix is distributed over group of processes ("k-pool"). In **Figure 2**, this k-pool is a 4x4 processes group, so each process computes small block of H matrix of approximately Nm/4xNm/4 size. Hence, here we parallelize the loop "DO 3". Finally, splitting the pool into many k-pools, we can parallelize the loop "DO 2". In **Figure 2,** pool 0 is split into 3 k-pools: Kp00, Kp01 and Kp02, so each process computes only approximately Nk/3 values of R function. Since the block of H matrix and auxiliary variables on each MPI process may allocate all memory on the computing node, in some cases it is not possible to use more than 1 MPI process per node, though there are many cores available for computing. In order not to waste processor time, OpenMP kind of parallelization is used to compute the value of R function and/or matrix elements Hij. At the end of the program, all equivalent blocks of H matrix from different k-pools are summed at the single k-pool (Kp00 for Pool 0 or Kp10 for Pool 1) and after final processing of computed data, program is terminated.

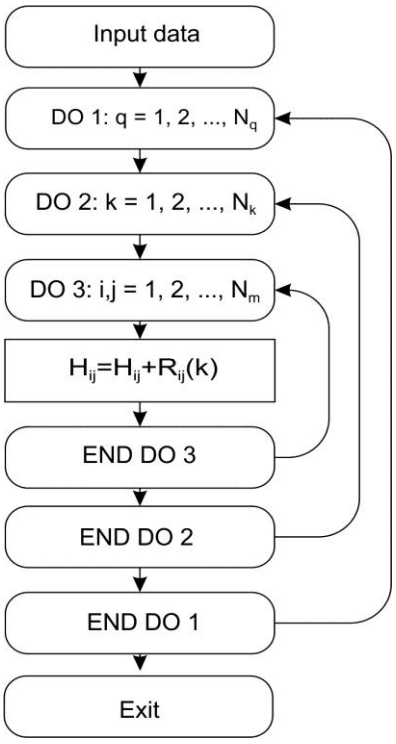

***Figure 1**:MBPT code flow chart*

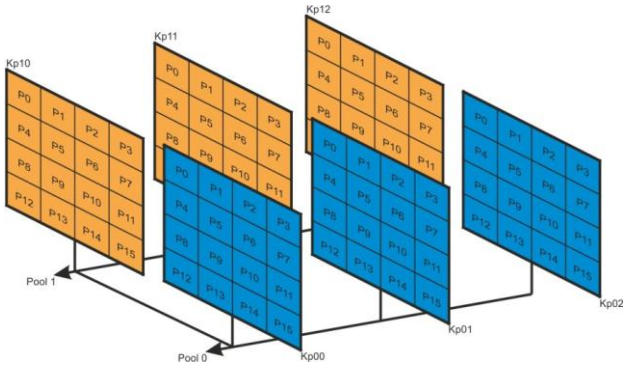

***Figure 2**:graphic representation of k-pools*

RESULTS:

Formamide in water solution

We perform ab-initio quantum calculation of the optical properties of formamide in vapor phase and in water solution. We employ TDDFT for the isolated molecule and MBPT methods for the system in solution. In order to take into account the liquid disorder we average over several molecular dynamics snapshots.

We find that the excited state properties of the gas-phase formamide are strongly modified by the presence of the water solvent: both the geometry of the molecule is distorted and the electronic and optical properties are severely modified. In detail, the presence of the water solvent greatly modifies the formamide properties: the molecule is not planar anymore, with a dihedral angle changing from 179.3 degrees to 160.7 degrees, the electronic gap is reduced, and the optical absorption spectrum is redshifted of about 0.8 eV in the main intense peak. This peak in the spectrum of the solution is due to a strongly bound exciton, with a binding energy of 2.5 eV.
The excitonic wavefunction related to this structure, shown in **Figure 3**, is delocalized both over formamide and water molecules. We find that this important interaction among the formamide and the water molecules forces to use fully quantum methods for the calculation of the excited state properties of this system and less computer demanding approaches such as TDLDA, effective medium theory and QM/MM methodologies (with the quantum region limited to the formamide molecule only) cannot be applied to this system [9].

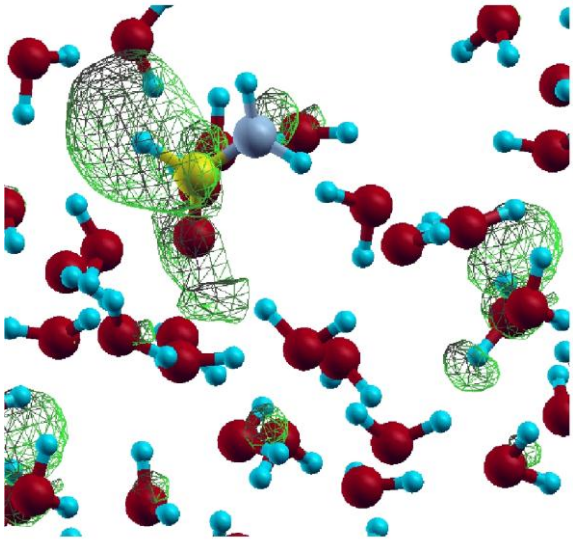

Figure 3*: stick and ball image of formamide in water solution.*
Also the excitonic wavefunction is shown.

Isomers of the Si(111)2x1 surface

The Si(111)2x1 surface has been widely investigated [10] and its structure is well known to consist of Pandey chains, with the addition of a small tilting (buckling) of the topmost atoms. Two possible isomers of the surface can be distinguished in relation to the conventional sign of the buckling. These two structures, called Si(111)2x1 positive buckling (pb) and negative buckling (nb), coexist in high n-doping conditions [11], while at room temperature and low doping only the pb isomer is observed in experiments.
Despite their slight difference in the geometry, we find that these two isomers are characterized by deep differences in the electronic and optical properties [12].
In particular, we have calculated Reflectance Anisotropy Spectra (RAS), including the excitonic effects. The solution of the Bethe-Salpeter equation puts in evidence the quasi-one-dimensional character of the lowest energy surface exciton responsible for the RAS main peak for both isomers; this exciton is very localized along the direction perpendicular to the Pandey chains and its probability distribution is extended over 80 Å along the chains for the positive buckling and even more for the negative buckling (see **Figure 4**), whose exciton is thus more delocalized along the chain.

Comparing electronic gaps (0.44 eV for nb and 0.77 eV for pb) and optical gaps (0.31 eV for nb 0.45 eV for pb), we find a larger binding energy for the positive buckling isomer (0.32 eV) with respect to the negative buckling (0.13 eV), in agreement with the larger excitonic radius of the nb structure.
The importance of the differences between the optical gaps and the surface excitons of the two isomers, highlighted previously, is connected to the possibility to exploit them to further investigate the coexistence of the two configurations at different temperatures and levels of doping, comparing experimental RAS spectra of Si(111)2x1 to theoretical results.

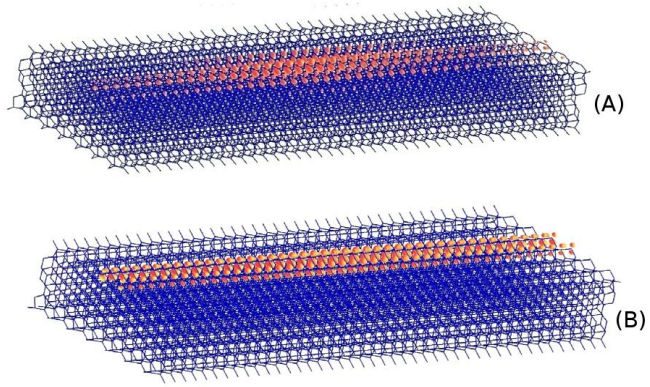

Figure 4*: excitonic wavefunction of Si(111)2x1 positive buckling (A) and negative buckling (B).*

Bibliography

[1] P. Hohenberg and W. Kohn, "*Inhomogeneous Electron Gas"*, Phys. Rev. B **136**, 864 (1964).
[2] R. M. Dreizler and E. K. U. Gross, "*Density Functional Theory",* (Springer-Verlag, Heidelberg, 1990); R. O. Jones and O. Gunnarsson, *"The density functional formalism, its applications and prospects",* Rev. Mod. Phys. **61**, 689 (1989).
[3] W. Kohn and L. J. Sham, *"Self-Consistent Equations Including Exchange and Correlation Effects",* Phys. Rev. A **140**, 1113 (1965).
[4] L. Fetter and J. D. Walecka, *"Quantum Theory of Many Body Systems",* (McGraw-Hill, New York, 1981).
[5] L. Hedin, *"New Method for Calculating the One-Particle Green's Function with Application to the Electron-Gas Problem",* Phys. Rev. A **139**, 796 (1965); R. D. Mattuck, "*A Guide to Feynman Diagrams in the Many Body Problem",* (McGraw-Hill, New York, 1976).
[6] L. Hedin and B. J. Lundquist, in: Solid State Physics, Vol. **23**, edited by H. Ehrenreich, F. Seitz, and D. Turnbull (Academic Press, New York, 1969), p. 1.
[7] F. Aryasetiawan and O. Gunnarsson, *"The GW method",* Rep. Prog. Phys. **61**, 237 (1998); L. Johsson and J. W. Wilkins, *"Quasiparticle Calculations in Solid",* Solid State Phys. **54**, 1–218 (2000).
[8] G. Onida, L. Reining and A. Rubio, *"Electronic excitations: density-functional versus many-body Green's-function approaches"*, Rev. Mod. Phys. **74**, 601 (2002).
[9] Garbuio, M. Cascella, R. Del Sole, M. Marsili and O. Pulci, "*Excited state properties of formamide in water solution: An ab initio study",* J. Chem. Phys. **137**, 164317 (2012).
[10] see for example M. Rohlfing and S. G. Louie, *"Excitons and Optical Spectrum of the Si(111)-(2x1) Surface",* Phys. Rev. Lett. **83**, 856 (1999) and ref. therein.
[11] G. Bussetti, B. Bonanni, S. Cirilli, A. Violante, M. Russo, C. Goletti, P. Chiaradia, O. Pulci, M. Palummo, R. Del Sole, P. Gargiani, M. G. Betti, C. Mariani, R. M. Feenstra, G. Meyer and K. H. Rieder, *"Coexistence of Negatively and Positively Buckled Isomers on n+-Doped Si(111)-2x1",* Phys. Rev. Lett. **106**, 067601-1 (2011).
[12] C. Violante, A. Mosca Conte, F. Bechstedt and O. Pulci, *"Geometric, electronic, and optical properties of the Si(111)2×1 surface: Positive and negative buckling "*, Phys. Rev. B **86**, 245313 (2012).

Shear-band formation in $Cu_{64}Zr_{36}$ metallic glass under uniaxial compression

J. Zemp[1], M. Celino[2], J. F. Löffler[1], B. Schönfeld[1]

[1]Laboratory of Metal Physics and Technology, Department of Materials, ETH Zurich, 8093 Zürich, Switzerland. [2]ENEA, C. R. Casaccia, Via Anguillarese 301, 00123, Rome, Italy

*Corresponding Author: Jérôme Zemp
E-mail: jerome.zemp@mat.ethz.ch. Tel.: +41 (0)44 633 61 71

Abstract
In a previous study $Cu_{64}Zr_{36}$ metallic glass was simulated by Molecular Dynamics. A larger sample, which is a prerequisite to study shear-band formation in metallic glasses, was now built using replicas of a small sample. An annealing step at sufficiently high temperature is needed to get rid of any periodicity introduced by the replicas. Shear bands are formed under uniaxial compression and visualized using the atomic local shear strain. In the early stages of yielding several shear bands are observed, while one shear band dominates at larger plastic deformation.

Introduction

Metallic glasses offer a unique combination of mechanical, electrical and magnetic properties. Currently, limited sample size and low ductility present major drawbacks. Knowledge of the atomic structure is of great importance to set up structure-property relationships, analogous to crystalline metals. By carefully selecting composition and processing techniques, metallic glasses with a broad range of properties might be achievable.
The absence of long-range translational order in metallic glasses is crucial for their mechanical properties. Plastic deformation is usually limited to compression, while brittle fracture occurs in tension. In crystalline alloys plasticity is carried by dislocations, whereas in metallic glasses plastic deformation is localized in so-called shear bands, with a thickness of the order of some tens of nanometers. The structural processes leading to the formation of shear bands are of great interest for the design of new metallic glasses with improved mechanical properties.
Experimental methods have their limitations in tracking the formation and dynamics of shear bands due to the size and the timescale of the phenomenon. Molecular Dynamics (MD) simulations, however, offer a way towards a conceptual understanding of shear-band formation. Previously, an amorphous $Cu_{64}Zr_{36}$ sample containing 11664 atoms was simulated. Following this work, a larger sample was produced to study the formation of shear bands under uniaxial compression.

Methods

The LAMMPS simulation package [1] is used for the MD simulations. Interatomic forces are calculated from the potential developed by Mendelev et al. [2]. The exact procedure to obtain the sample that is used as a starting configuration is described in the CRESCO annual report 2011 [3]. All simulations were carried out on the portici cluster using 32-512 processors depending on computational costs. For the observation of shear-banding in MD simulations a rather large sample (> 1 million atoms) is needed. Otherwise the sample box could be smaller than the typical shear-band size, which will result in a homogenous deformation process. However, the simulation of such a large sample by quenching from the melt is very costly in terms of computation time. Thus, a large box with 1’399’680 atoms and 11.4 nm × 28.5 nm × 68.4 nm in size is built by stacking together

2×5×12 replicas of the small sample. This is followed by an annealing step at 1000 K for 2 ns to get rid of any periodicity that was introduced due to employing replicas. After annealing the sample was cooled again to 50 K at a rate of 0.1 K ps^{-1}. Uniaxial deformation along the long axis (z-axis) is then applied using a constant strain rate of 10^7 s^{-1}. According to Shimizu et al. [4], the local atomic shear strain is calculated which compares the current configuration to a reference configuration and quantifies the structural changes in the neighborhood of any atom. Visualization is realized using the open-source software OVITO [5].

Results and Discussion

The need for annealing the sample after construction is seen in Figure 1. Using the common-neighbor-analysis [6] feature of OVITO, a periodic pattern is observed for the common-neighbor-analysis index of icosahedron-like atomic clusters.

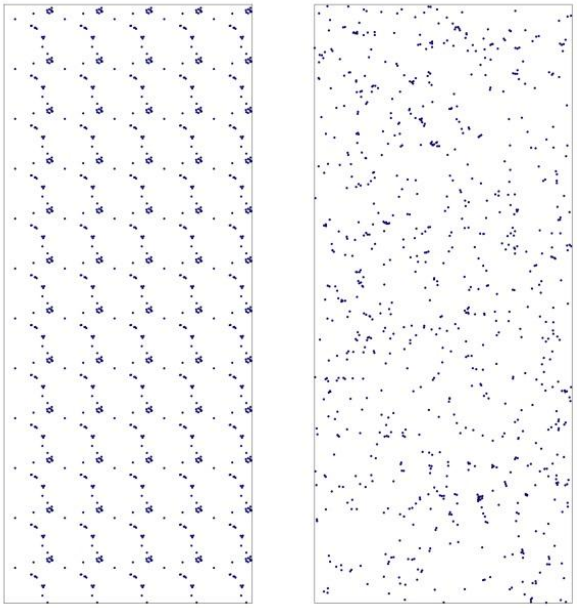

Figure 1: Icosahedron-like coordinated atoms within a slice of 10 nm thickness as determined by the common-neighbor-analysis feature of OVITO. A periodic pattern is observed in the non-annealed sample (left), while the annealed sample (right) does not show any periodicity.

No such pattern is observed when looking at the annealed sample. However, the annealing might not only remove the undesired features but also change the general structure of the glass. To check if any significant changes occurred during annealing, the radial distribution function was compared before and after annealing (not shown). The differences are small and thus considered acceptable, whereas any periodicity is believed to introduce unwanted artifacts in the subsequent mechanical testing.

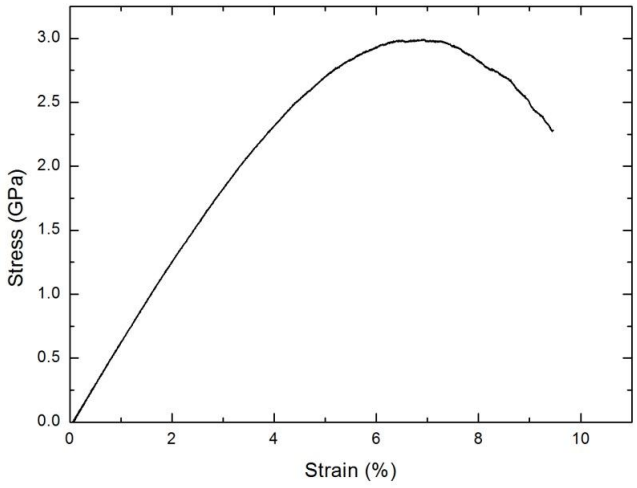

Figure 2: Stress-strain curve for uniaxial loading along the z-axis with a strain rate of 10^7 s^{-1}. A deviation from ideal linear

elastic behavior is observed starting at approximately 3% strain.

In Figure 2 the stress-strain curve for a constant strain rate of 10^7 s^{-1} is plotted. The yield strength is around 3.0 GPa (Ritter et al. [7] ~4.6 GPa, Cao et al. [8] ~3.7 GPa) and the Young's modulus around 68 GPa (Ritter et al. [7] ~87 GPa, Cao et al. [8] ~70 GPa). The reasons for the difference between the present values and those in the literature can be versatile: (i) The strain rate used for the literature data is 4 times larger, which results in a larger yield strength; (ii) different heat treatments of the samples may lead to a different topological short-range order, e.g., the amount of Cu-centered icosahedra can be different, which has an influence on the mechanical properties of Cu-Zr metallic glasses [9]; (iii) Cao et al. [8] used a different potential. Consequently, it is not possible to directly transfer MD simulation results to reality. Yet, MD simulations are the only tool to directly follow atomic movements during mechanical deformation.

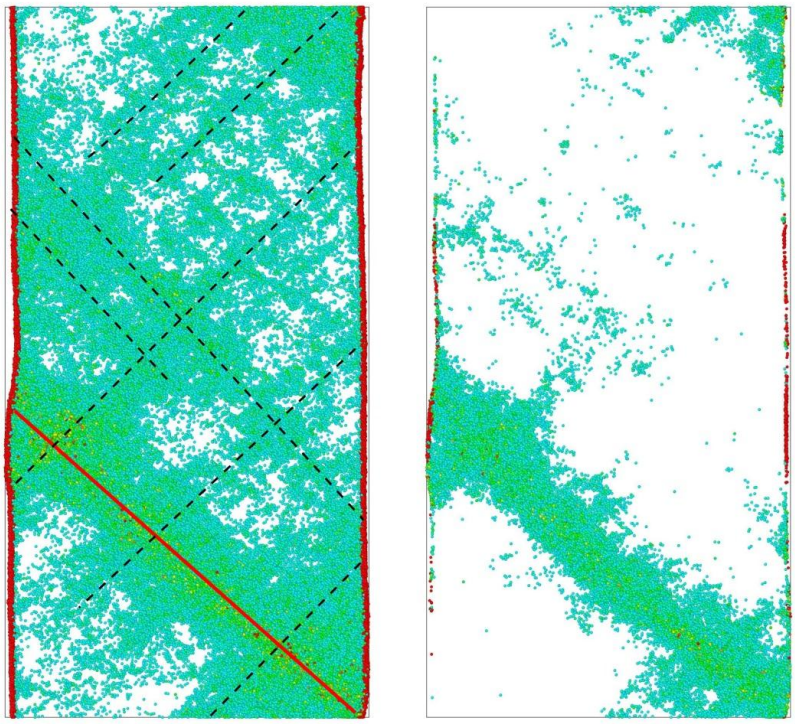

Figure 3: Atomic local shear strain after 9.4% strain. Only atoms with a strain > 0.2 are shown. Red corresponds to a high and blue to a low local strain. Considering the total macroscopic strain (left), extended regions are affected by the deformation. However, deformation only occurring between 8.4% and 9.4% strain is highly localized into one shear band (right).

Plastic deformation in metallic glasses is localized in shear bands, which is shown in Figure 3. The atoms are colored according to the local atomic shear strain with a coloring gradient from blue to red for increasing strain values. One dominant (red solid line) and several minor (black dashed lines) shear bands are observed, with angles between 40° and 45° with respect to the load axis. A strain accumulation is seen at the intersection points of different shear bands. The local strain accumulated between 8.4% and 9.4% macroscopic strain (right snapshot in Figure 3) shows a heterogeneous strain distribution. This is a result of the weakening of the structure within the shear band due to the destruction of stable local structural motifs [8]. In other words, the deformation is initially carried by several shear bands, while in the plastic regime only a single shear band dominates.

Conclusions

Using replicas of a previously simulated $Cu_{64}Zr_{36}$ metallic glass sample, a large sample was constructed to perform a uniaxial compression experiment. After an annealing step at 1000 K for 2 ns, no artificially introduced periodicity could be observed anymore. Shear-banding was visualized

by calculating the atomic local shear strain. During early stages of yielding several shear bands can be identified, whereas a single shear band dominates when the sample is further compressed.

References

[1] PLIMPTON S. *"Fast Parallel Algorithms for Short-Range Molecular Dynamics"* J. Comp. Phys. **117** (1995) pp. 1-19.

[2] MENDELEV M.I., KRAMER M. J., et al. *"Development of suitable interatomic potentials for simulation of liquid and amorphous Cu–Zr alloys"* Phil. Mag. **89** (2009) pp. 967-987.

[3] ZEMP J., CELINO M., SCHÖNFELD B., LÖFFLER J.F., *"Molecular Dynamics simulations of $Cu_{64}Zr_{36}$ metallic glasses"* Cresco Progress Report 2011, ISBN 978-88-8286-268-8.

[4] SHIMIZU F., OGATA S., et al. *"Theory of shear banding in metallic glasses and molecular dynamics calculations"* Mater. Trans. **48** (2007) pp. 2923-2927.

[5] STUKOWSKI A. *"Visualization and analysis of atomistic simulation data with OVITO - the Open Visualization Tool"* Modelling Simul. Mater. Sci. Eng. **18** (2010) 015012. (Software available on www.ovito.org)

[6] HONEYCUTT J. D., ANDERSEN H. C. *"Molecular dynamics study of melting and freezing of small Lennard-Jones clusters"* J. Phys. Chem. **91** (1987) pp. 4950-4963**.**

[7] RITTER Y., SOPU D., et al. *"Structure, stability and mechanical properties of internal interfaces in $Cu_{64}Zr_{36}$ nanoglasses studied by MD simulations"* Acta Mater. **59** (2011) pp. 6588-6593.

[8] CAO A. J., CHENG Y. Q., et al. *"Structural processes that initiate shear localization in metallic glass"* Acta Mater. **57** (2009) pp. 5146-5155.

[9] CHENG Y. Q., SHENG H. W., MA E. *"Relationship between structure, dynamics, and mechanical properties in metallic glass-forming alloys"* Phys. Rev. B **78** (2008) 014207.

Combustion Activities and Performance Analysis of the HeaRT Code

F.R. Picchia, E. Giacomazzi, D. Cecere, N. Arcidiacono
UTTEI-COMSO, Casaccia Research Center, ENEA – Rome, ITALY

Corresponding Author: Franca Rita Picchia, rita.picchia@enea.it

Abstract

This article briefly summarizes combustion activities (year 2012) done by the numerical simulation group of the Sustainable Combustion Processes Laboratory by means of the in-house code HeaRT. More space is given to performance analysis of HeaRT on the CRESCO platforms and on the Blue Gene Shaheen platform located at KAUST (King Abdullha University of Science and Technology), Center for Deep Computing Research (CDCR). Tests on Shaheen were done within a Development Project approved by KAUST in preparation of an Executive Project aimed at simulating a whole premixed combustor exhibiting thermo-acoustic instabilities.

HeaRT Combustion Activities

In 2012 most of the activities related to the HeaRT code were devoted to its development, and in particular to optimization, generalization for geometrical topologies management, complex geometry treatment, robustness of numerical integration spatial schemes, physical modelling. In this section, the HeaRT code is described along with these improvement activities.

HeaRT deals with three-dimensional cilindrical and cartesian multi-block computational domains using structured grids. It is based on the Large Eddy Simulation approach, and it can simulate unsteady turbulent flows, reactive or not, at low and high Mach numbers. It implements a fully compressible formulation also at low Mach numbers to capture unsteady features related to pressure oscillations, such as thermo-acoustic instabilities. The code can manage complex geometries by means of the Immersed Volume Method developed by the authors. This technique was validated in laminar and turbulent flows, without and with chemical reactions [1-3]. HeaRT can also simulate multi-phase flows by means of an eulerian – eulerian mesoscopic approach; this model was validated against nonreactive turbulent flow data [4] and coal devolatilization tests [5].

The compressible equations are written in conservative form and solved within a staggered formulation to improve dispersive properties of spatial numerical schemes. In particular, the code implements a finite-difference spatial integration and a third-order Runge-Kutta integration in time. Different spatial schemes are implemented, ranging from a second-order central scheme, to a third-order upwind-biased scheme (AUSM), and to a fifth-third order WENO scheme for supersonic flows. In particular, the implementation of the AUSM scheme in convective terms of momentum transport equations has enhanced the numerical stability in premixed flame calculation. Since June 2013 the authors have also been developing and implementing a staggered sixth-order compact scheme to achieve more accurate solutions. A finite-volume second-order accurate scheme is adopted for dispersed phases in multi-phase flows. A finite-volume approach is also used in computational cells cutting complex geometries within the Immersed Volume Method. Explicit Gaussian filtering of momentum variables has been implemented to damp unphysical wiggles. Non-reflecting Navier-Stokes-Characteristic-Boundary-Conditions are implemented at open boundaries in their extended form to take into account the effect of variable transport properties and local heat release. A synthetic turbulence generator is adopted to produce turbulence at flow inlets.

Diffusive transports include Fourier law and species enthalpy transport due to species diffusion in the heat flux, and differential diffusion according to Hirschfelder and Curtiss law in the mass diffusion flux. Radiant transfer of energy can also be considered by means of the M1 diffusive model. Molecular properties are accurately estimated by means of the kinetic theory. They are tabulated apart from diffusion binary coefficients. Wilke's, Mathur's, Hirschfelder and Curtiss' mixing laws are used to estimate mixture viscosity, conductivity and diffusion coefficients.
Different sub-grid models are implemented: the Dynamic Smagorinsky model, the subgrid kinetic energy equation, the Fractal Model, a flamelet-progress variable approach. CHEMKIN format is adopted for detailed chemical kinetic schemes.
The HeaRT code is equipped with a set of pre- and post-processing programs: programs to generate/regenerate the fluid-dynamic field on differently discretized meshes, some programs for statistical calculations, a program to convert the output fields into files readable by TecPlot, and finally a program (PRE-DEC) to pre-generate the sub-optimal domain decomposition varying the number of the computational cores. The latter has been developed to choose 'a priori' the number of processes that fits better for the specific case under simulation.
HeaRT is implemented in FORTRAN95 and its parallelism is based on Domain Decomposition and Message Passing paradigm. The latter decision was taken to make the code nearly 'machine independent' over the ENEA computational GRID that hosts different kind of HPC platform(cluster of single- or multi-core machines, SMP machines and so on). A Domain Decomposition approach and MPI (Message Passing Interface) are used for the parallel implementation of the HeaRT code. In this approach, the three-dimensional computational domain, defined by a multi-block orthogonal structured grid, is partitioned into a number of sub-domains by means of a partitioning process based on a genetic algorithm. The "fitness function" implemented into the genetic algorithm aims at balancing the computational cost of the involved processors and at minimizing the amount of data to be communicated across the processors boundaries.

The HPC Platform Shaheen

Shaheen, installed at KAUST (King Abdullha University of Science and Technology) Center for Deep Computing Research (CDCR), has been built in partnership with IBM. It is a 16-rack IBM Blue Gene/P system capable of performing at a processing power of 220 Tflops. Each node of Shaheen is equipped with four 32-bit, 850 Mhz PowerPC 450 cores and 4GB DDR memory. In aggregate, Shaheen has 65,536 compute cores and 64TB of memory.
Shaheen, debuted at #14 on the TOP500 list during June 2009 and moved to #126 in November 2012. It has been designed with a view to environment protection, so Shaheen ranked #9 on the TOP Green500 list (the list of the most Energy efficient supercomputers in the world) in November 2009, providing 378.77 MegaFlops per Watt consumed, but it moved to #167 in November 2012. However Shaheen remains one of the most powerful supercomputers in the Middle East and KAUST plans to turn its facility into a Petascale system in the future, and then to ExaFlop size (one million trillion calculations per second).
Blue Gene/P jobs execute on blocks of nodes with specific size and shape requirements. On Shaheen, the valid block sizes (in nodes) are: 64, 128, 256, 512, 1024, 1536, 2048, 3072, 4096, 4608, 6144, 8192, 9216, 12288, 16384. It can operate in one of three modes to support either a pure MPI program or a hybrid model of MPI and OpenMP: Virtual Node Mode (VN), Dual Node Mode (DUAL), SMP node mode (SMP). In this work the VN mode was selected to run one process for each core as in the CRESCO clusters.

Performance Analysis

The test case chosen for the present performance analysis is a laboratory-scale slot burner experimentally investigated by Filatyev et al. at the Department of Mechanical Engineering of the Purdue University(USA), and also numerically simulated via a Direct Numerical Simulation approach by John B. Bell [6], at the Center for Computational Science and Engineering of the Lawrence Berkeley National Laboratory. This test case has been chosen because a slot Bunsen flame represents one of the major categories of turbulent premixed combustion. This test case was also chosen to validate a new turbulent combustion model developed by the authors of this report.

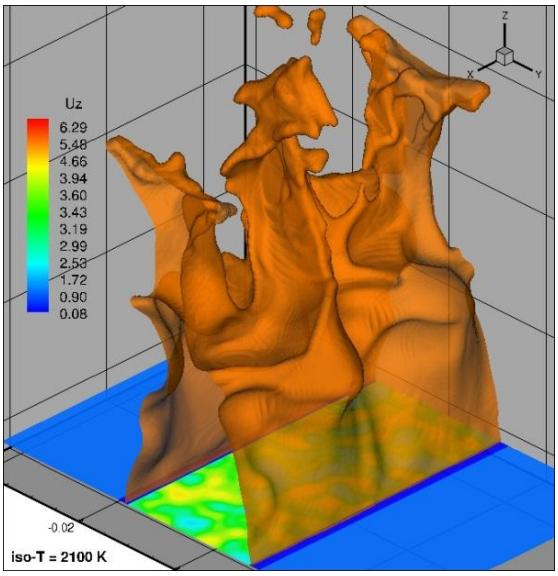

Fig. 1. Instantaneous iso-temperature surface of the test case used for performance analysis. The instantaneous turbulent flow velocity distribution at the central inlet is also shown.

The slot burner consists of three rectangular burners: a central burner and two side burners with the three flow exits separated by two 2 mm sidewalls; each of them has a cross-section of 2.5 cm x 5.0 cm and a length of 20 cm and is fed with a stoichiometric mixture of methane and air. The central burner is used to create the Bunsen flame, while the side burners contain flat flames to produce hot products at the same velocity of the products of the Bunsen flame; this strategy avoids shear layers, and unwanted turbulence, that could be originated at the boundaries when the products meet the room air. The computational domain is 7.5 cm x 5.0 cm x 10 cm and begins at the burner exit.

The performances of the HeaRT code were evaluated varying the number of computational nodes on three different parallel machines (CRESCO2, CRESCO3, Shaheen), and using two meshes with different spatial resolution. The coarser mesh, here called SMALL, has 5100500 (250x202x101) cells and the finer mesh, here called BIG, has 47752416 (534x432X207) cells. The analysis is based on common metrics used to compare serial and parallel algorithms: speed-up, efficiency (defined as the speed-up divided by the number p of processors/cores), wall time. The speed-up is defined as the ratio between the time required by a serial algorithm to solve a specific problem and the time required by a parallelized version of the same algorithm to solve the same problem by using more than one processor/core. In this analysis, a serial version of the HeaRT code in not available to provide a reference serial time. Furthermore, since one single compute core has not a sufficient amount of memory to run the test case (on neither of the platforms), the time required by the lowest running number of cores is chosen as reference time to estimate the speedup and parallel efficiency, in particular, 16 cores for SMALL the case and 128 cores for the BIG one. A linear speed-up or ideal speed-up is obtained when speed-up=p with an efficiency=1, but this cannot happen mainly for a couple of reasons: first, effective load balancing is difficult to achieve, especially with complex three-dimensional geometries; second, besides the effects due to the h/w and s/w architecture of target machine there is a non-linear overhead due to the inter-cores and inter-nodes communications.

So the larger is the number of processors/cores, the more the relative speed-up moves away from its ideal trend. The wall-time here used is defined as the time spent by the processor/core with highest load of calculation to execute an integration time-step. In these tests, Shaheen was operated in the Virtual Node Mode (VN) to run one process for each core as in the CRESCO clusters.
The analysis proved that HeaRT performs well in terms of Speed-Up and Efficiency, as shown in Fig. 2. The best performances are achieved on Shaheen. CRESCO3 gives similar results.

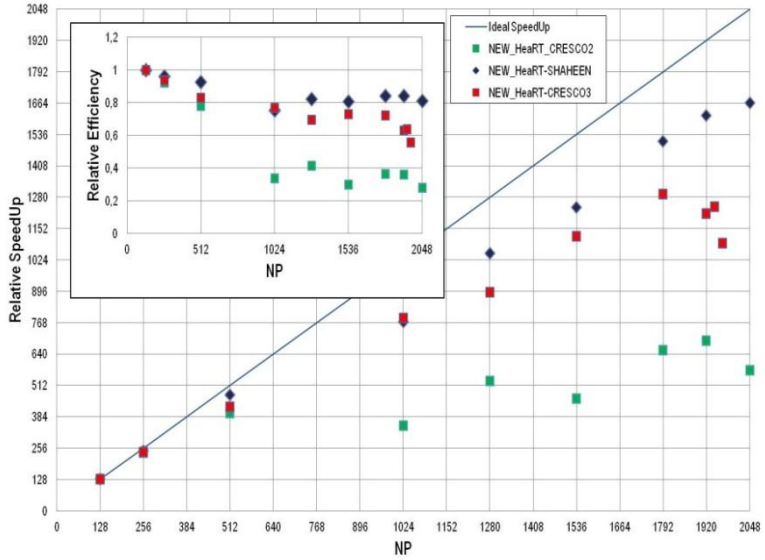

Fig. 2. Comparison of Speed-Up and Efficiency for the BIG test case on CRESCO2, CRESCO3 and Shaheen.

CRESCO 2 performs well up to 512 cores; performances become poor for a larger number of cores because processors of different family and frequency are mixed. It is observed that for CRESCO3 the last three domain decompositions chosen above 1920 cores are characterized by higher parallelization costs (estimated by the fitness function of the genetic decomposition algorithm) that justify the decrease of the performance. As shown in Fig. 3 on Shaheen instead the Speed-Up slope continues to be positive by increasing the number of cores.

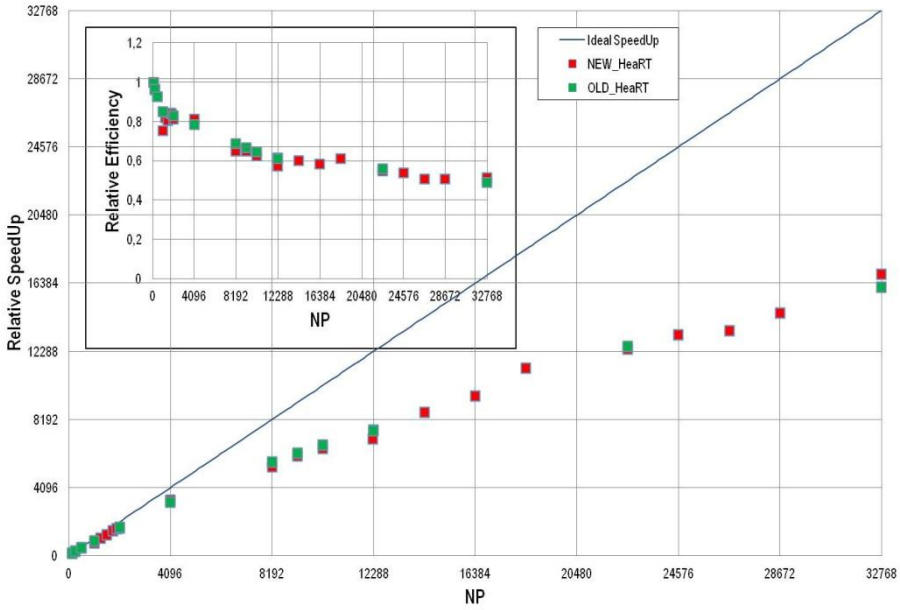

Fig. 3. Speed-Up and Efficiency of the BIG test case on Shaheen.

Apart from the Speed-Up and Efficiency trends, what is more important for the time-to-solution is the Wall-Time per time-step. Since, each node of Shaheen is equipped with four 32-bit, 850 MHz PowerPC 450 cores, while the CRESCO cluster is equipped with 64-bit, XEON and AMD 2.4 GHz

cores, a reduced wall time performance is expected for Shaheen, as shown in Fig. 4. In fact, the ratio between the Wall-Times of Shaheen and CRESCO3 ranges from 3.5 at 128 cores to 2.7 at 1920 cores; the ratio between the Wall-Times of Shaheen and CRESCO2 ranges from 6.1 at 128 cores to 2.6 at 1920. The difference between the Wall-Times of CRESCO2 and CRESCO3 decrease by increasing the number of cores.

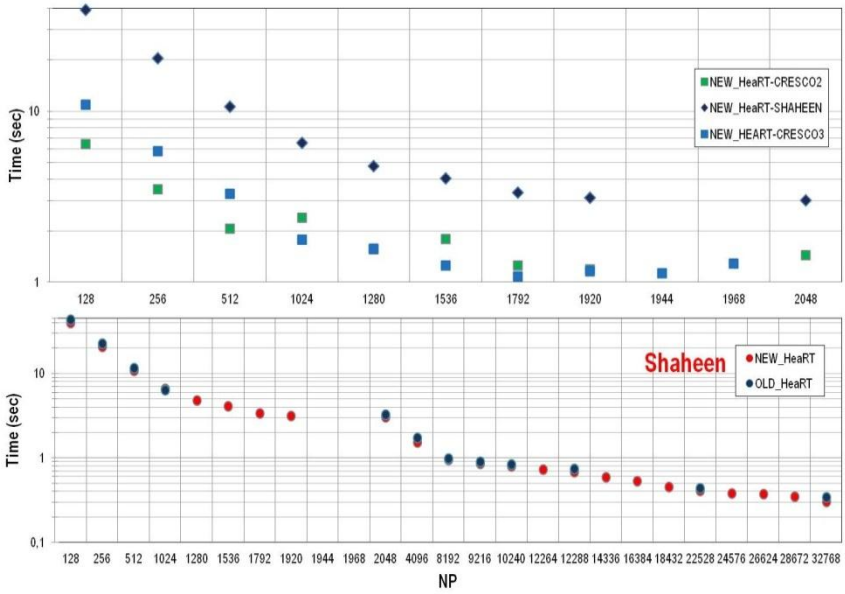

Fig. 4. Wall-Time comparison for the BIG test case on CRESCO2, CRESCO3 and Shaheen (above).
Wall-Time comparison for the BIG test case between two different versions of the HeaRT code on Shaheen (bottom).

This difference is likely due to the sharing of a floating point unit each two cores on CRESCO3. Despite the lower frequency clock of Shaheen's processors the Wall-Time per time-step keeps decreasing upon increasing the number of cores, thus resulting into a lower time-to-solution.

References

[1] CECERE D., E. GIACOMAZZIE. *"An Immersed Volume Method for Large Eddy Simulation of Compressible Flows"*, submitted to Computer Methods in Applied Mechanics and Engineering, Elsevier, on 27 May 2013.
[2] CECERE D., GIACOMAZZI E., PICCHIA F.R., ARCIDIACONO N., DONATO F. "*An Immersed Volume Method for Complex Geometries Treatment in Compressible Reactive Fluids",* XXXV Meeting of the Italian Section of the Combustion Institute, Milano, Italy, 10-13 October 2012.
[3] CECERE D., GIACOMAZZI E., PICCHIA F.R., ARCIDIACONO N., DONATO F. "*An Immersed Volume Method for for Large Eddy Simulation of Compressible Flows"*,7th Turbulence, Heat and Mass Transfer (THMT12), Begell House, Inc., Palermo, Italy, 24-27 September, 2012.
[4] DONATO F., GIACOMAZZI E., CECERE D., PICCHIA F.R., ARCIDIACONO N., FAVINI B., BRUNO C. "*Large Eddy Simulation of Particle Laden Flows"*, XXXIV Event of the Italian Section of the Combustion Institute, Rome, Italy, 24-26 October 2011.
[5] DONATO F., ROSSI G., FAVINI B., GIACOMAZZI E., CECERE D., PICCHIA F.R., ARCIDIACONO N. *"LES Simulation of a Devolatilization Experiment on the IPFR Facility",* XXXV Meeting of the Italian Section of the Combustion Institute, Milano, Italy, 10-13 October 2012.
[6] BELL J.B., DAY M.S., GRCAR J.F., LIJEWSKY M.J., DRISCOLL J.F., FILATYEV S.A. *"Numerical simulation of a laboratory-scale turbulent slot flame"*, Proceedings of the Combustion Institute 31:1299-1307, 2007.

PARTICLE SIMULATION OF ALFVEN MODE DYNAMICS IN NUCLEAR FUSION DEVICES

Sergio Briguglio[1], Giuliana Fogaccia[1], Gregorio Vlad[1] and Xin Wang[2]

[1]ENEA, CR Frascati, via Enrico Fermi 45, 00044 Frascati, Rome, Italy
sergio.briguglio@enea.it, giuliana.fogaccia@enea.it, gregorio.vlad@enea.it
[2]IFTS, Zhejiang University, Hangzhou 310027, China, wangxinnku@zju.edu.cn

Introduction

The realization of a nuclear fusion reactor based on magnetic confinement requires that a gas mixture of deuterium and tritium is heated up to temperatures of the same order of the temperatures reached in the centre of stars. In such conditions, many fusion reactions take place between nuclei of deuterium and nuclei of tritium, each yielding an alpha particle (that is, a nucleus of helium) and a neutron. Both these particles are produced with a large kinetic energy. The neutron is captured by a blanket surrounding the reaction chamber, where it deposits its energy. The alpha particles, electrically charged, should be confined in the reaction chamber by the magnetic field, in order to thermalize inside the deuterium-tritium plasma. When the plasma heating due to alpha particles exceeds a certain threshold, the external heating can be suppressed and the so called ignition condition is reached: the burning plasma is able to self-sustain. In order to reach such condition, it is of crucial importance that alpha particles are well confined inside the plasma; that is, their outward transport has to be low enough. As a matter of fact, alpha particles are produced with kinetic energies of order of few MeV, corresponding to velocities of the same order of the Alfvén velocity (the propagation speed of an electromagnetic field perturbation in magnetically confined plasmas). It is then easy that alpha particles interact with such perturbations (called Alfvén waves) in a resonant way: with an almost constant wave-particle phase relationship. Resonant alpha particles can then transfer energy to Alfvén waves in a very efficient way, inducing the wave amplitude to grow. In turn, the wave electromagnetic field can affect resonant particle orbits, enhancing their transport and degrading their confinement. The investigation of the interactions between alpha particles and Alfvén waves is then very relevant to predict the possibility of a certain magnetic confinement device to attain ignition conditions.

One of the most suited approaches for this type of investigations is represented by particle simulation. It consists in imitating the behaviour of the physical system by a large set of *numerical* particles, each being representative of all the physical particles belonging to a little portion of the phase space. At each time step, the electromagnetic fields are computed on the basis of suited momenta of the particle distribution (like density or current) and particles are *pushed* by the fields just computed. In principle, each of the particle species contained in the plasma (deuterium and tritium ions, electrons, alpha particles) can be represented by a corresponding numerical particle population. In practice, however, it can be worth reserving the particle representation to alpha particles, while describing the bulk plasma species by a *fluid* representation (a set of equations evolving a limited number of momenta of their distribution function). This mixed approach is called a *hybrid magnetohydrodynamic-particle* approach. Such approach, as well as the full-particle one, is also suited to study the behaviour of present day devices (still far from the ignition conditions), where the

Alfvén waves can interact with other species of fast particles (different from alpha ones); namely, the high-energy particles produced by additional heating methods (neutral beam injection or microwave heating).

Computational details

The ENEA-Frascati theory group has developed, in the last twenty years, a hybrid magnetohydrodynamic-particle simulation code, called HMGC [1]. It solves fluid MHD (magnetohydrodynamic) equations for the bulk plasma, closed by a term related to one or more particle species, computed by particle-simulation methods. The code has proved to be one of the most advanced of the same class in the world, and has been applied both to the interpretation of experimental observations in present day tokamaks and the prediction of next generation ones (in particular, ITER). Moreover, it has been widely used to get a deeper comprehension of saturation mechanisms of Alfvén waves and the effect these waves produce on fast ion transport, for suited numerical experiments. The main limitation of HMGC is that it can only describe systems with magnetic surfaces characterized by circular meridian section. As more general systems have proved to be more suited to reach high-confinement regimes, a second hybrid code has been developed, able to describe general-shape magnetic surfaces and named HYMAGYC.

Both codes have been parallelized for distributed-shared memory architectures, with the distributed-memory level managed by the message-passing library MPI and the shared-memory level by the high-level parallel programming environment OpenMP.

The resources needed for hybrid MHD-particle simulations depend on the typical wavelengths of the electromagnetic perturbations described. ITER oriented simulations should be able to include waves with toroidal numbers (the number of full wavelengths contained along the major circumference of the torus) of order 30. In order to get a detailed description of the plasma behavior, such number would correspond to memory resources approximately equal to 2000 GBytes. On the other hand, the need of maintaining the elapsed time for a significant simulation under the limit of 100 hours, would require a very large architecture of not less than 10000-20000 processors. When running the code on the CRESCO architecture, less ambitious cases have then been investigated, with toroidal numbers less than 10 and computational requirements one order of magnitude smaller than the ITER-oriented ones. Typical jobs require order 500 processors for 24 hours of elapsed time.

Both HMGC and HYMAGYC are written in Fortran90 and can be compiled using pgi and ifort compilers.

The MPI library is used by the HMGC code. HYMAGYC, on turn, requires MPI, BLAS and LAPACK libraries. FFTW3 and HIGZ (CERN public libraries) are required by several sources to post process the output results of both codes.

Results

HMGC has been used, during 2012, to investigate two different issues: the evolution of the so called *electron fishbone mode* [2] and the saturation mechanism of *Toroidal Alfvén Eigenmodes* (TAEs). The electron fishbone mode is an electromagnetic perturbation driven unstable (that is, caused to grow in amplitude) by high energy electrons produced, e.g., by the electron cyclotron heating and/or Lower Hybrid heating/current drive. It has been observed in several present day tokamaks, included the Frascati Tokamak Upgrade (FTU). It is characterized by bursting behaviour, with each burst

accompanied by significant mode frequency variation and radial redistribution of energetic electrons. HMGC simulations have shown that modes of this type can effectively be driven unstable by the resonant interaction with a fast-electron population, with frequency and radial localization (see Fig. 1) compatible with those observed in experiments. They have also shown that mode-particle interactions enhance the outward resonant particle radial transport, while the mode frequency is continuously adjusted to prolong the resonant interaction with the displaced particles (see Fig. 2). This shows that the fast electron radial redistribution and the frequency chirping are strictly related phenomena.

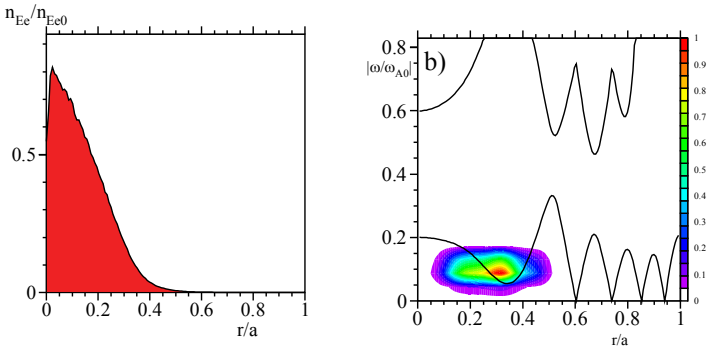

Fig. 1. Normalized energetic electron density profile during linear phase (left); power spectrum of the perturbed electrostatic potential (right) for an electron fishbone simulation.

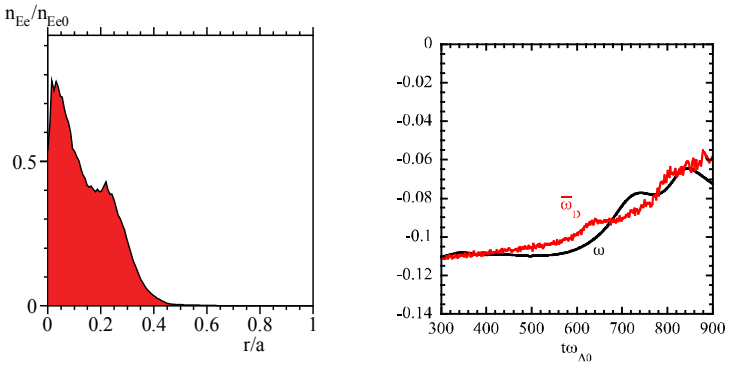

Fig. 2. Normalized energetic electron density profile after nonlinear saturation (left); frequency chirping of the electron fishbone mode (right, black curve) compared with the average characteristic frequency of the resonant energetic particles (right, red curve).

The saturation of TAEs has been studied by looking at the behavior of resonant particles in the coordinate space (Θ,P_ϕ), where Θ is the wave phase seen by the energetic particle, and P_ϕ the toroidal component of the energetic particle momentum. Resonance condition corresponds to constant Θ. The quantity P_ϕ is, for any particle, a constant of its unperturbed motion. In the presence of a fluctuating field, particle orbits are displaced in P_ϕ. For particles far from the resonance condition the effect of this perturbation is negligible (they continue to be non resonant). On the opposite, for resonant or quasi-resonant particles, the radial displacement causes the loss of the resonance conditions; such particles start to drift in Θ. [Eventually, this phase drift causes the effect of the field on particle P_ϕ motion to invert its sign. The resulting orbit in (Θ,P_ϕ) space is approximately a closed one (see Fig. 3)]. Eventually, this phase drift causes a P_ϕ drift such that the resulting orbits in the (Θ,P_ϕ) space is approximately a closed one. Such closed orbits (see Fig. 3), that involve more particles the larger is the mode amplitude, give rise to mixing of high density and low density portions of the resonantparticle populations. Correspondingly, the density profile is locally flattened, with strong decreasing of the power transfer from particles to the mode.

Power transfer survives aside the flattened region, where the density gradient is still large (see Fig. 4). As the flattened region, whose width increases with mode amplitude, covers the whole region where the resonant power transfer can take place, saturation occurs.

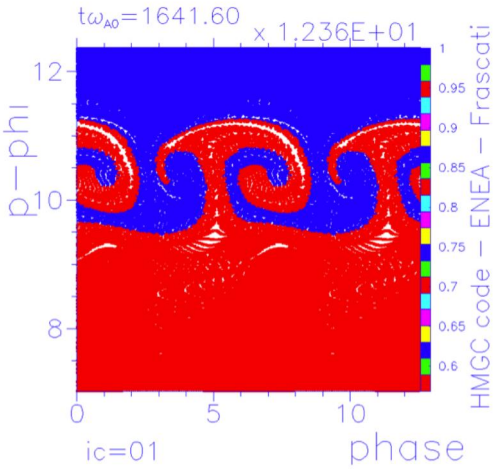

Fig. 3. Energetic particle orbits in the phase space coordinates (Θ,P_ϕ).

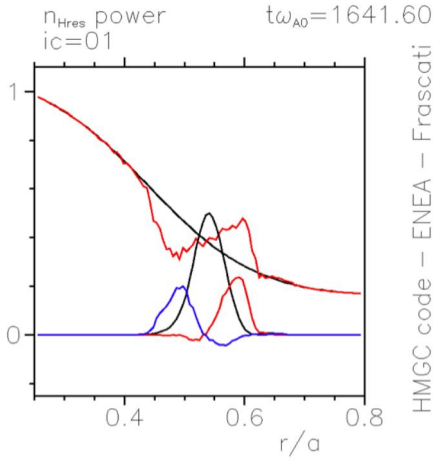

Fig. 4. Energetic particle density profile during linear phase (black upper curve) and at saturation (red upper curve). Wave-particle power exchange profile during linear phase (black lower curve) and at saturation (red and blue lower curves).

The more general code, HYMAGYC, is actually under validation. Results of simulations performed by such code and HMGC have been compared. In particular, the benchmark case has been performed for a simulation with toroidal number n=2, in the presence of a Maxwellian energetic ion population. Similar phenomenology is shown by two codes. At low energetic particles equilibrium density, a mode at the upper Alfvén continuum is driven unstable, while, at higher density values, the most unstable mode lays in the lower Alfvén continuum. For low values of energetic particle density, the frequencies and growth rates of the upper continuum unstable mode are similar between HYMAGYC and HMGC; for higher values of energetic particle density, a larger discrepancy both in frequency and growth rate is observed for the lower continuum unstable mode (see Fig. 5).

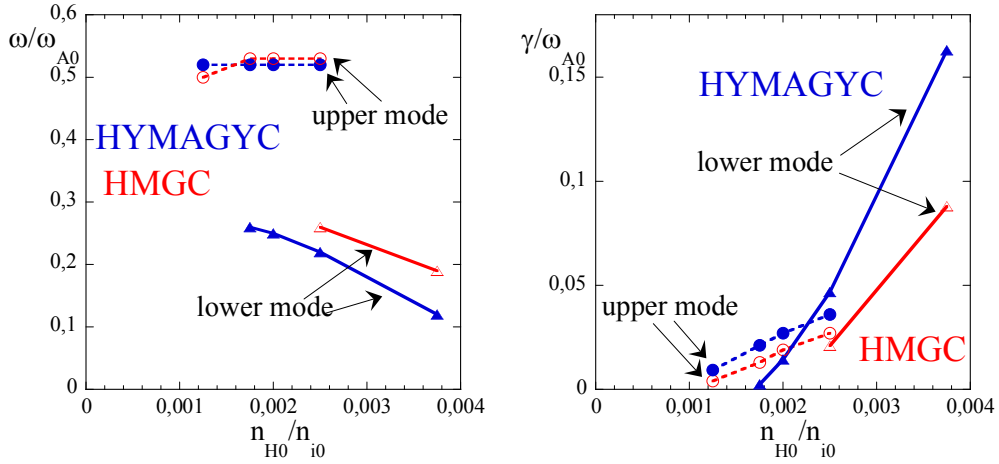

Fig. 5. Comparison between HMGC and HYMAGYC codes: normalized frequency (left) and growth rate (right) vs. normalized energetic particle density.

Conclusions

Predicting the behavior of plasmas close to ignition condition with respect, in particular, to the confinement of fast ions produced by fusion reactions and/or additional heating methods require a strong simulation effort. Hybrid magnetohydrodynamic-particle simulations performed by the numerical tools developed in Frascati have enlightened several relevant aspects of the dynamics of Alfvén modes and their interaction with fast ions. The CRESCO computational architecture has revealed precious for obtaining these results. ITER-relevant simulations will require at least one order of magnitude increase in the computational resource size.

Acknowledgements

The authors are indebted to Fulvio Zonca and Liu Chen for many valuable suggestions and discussions.

References

[1] BRIGUGLIO S., VLAD G., ZONCA F.,KAR C. "*Hybrid magnetohydrodynamic-gyrokinetic simulation of toroidal Alfvén modes*" Phys. Plasmas **2** (1995) pp. 3711-3723

[2] VLAD G., S. BRIGUGLIO S., FOGACCIA G., ZONCA F., DI TROIA C., FUSCO V., WANG X. "*Electron fishbone simulations in FTU-like equilibria using XHMGC*" In Fusion Energy 2012, Vienna, 2012. International Atomic Energy Agency. Paper 77-TH/P6-03. Proceedings of the 24th International Conference on Fusion Energy, San Diego, USA, 8-13/10 2011.

AB-INITIO CALCULATIONS OF Nb_3Sn SUPERCONDUCTING PROPERTIES UNDER APPLIED MECHANICAL STRAIN

G. De Marzi and L. Morici
ENEA UTFUS-COND C. R. Frascati
Corresponding author: demarzi@enea.it

ABSTRACT

Using calculations from first principles based on the density functional theory, we have studied the strain sensitivity of superconducting Nb_3Sn. The Nb_3Sn lattice cell was deformed in the same way as observed experimentally on multi-filamentary, technological wires subject to loads applied along their axes. The phonon dispersion curves and electronic band structures along different high-symmetry directions in the Brillouin zone were calculated, at different levels of applied strain ε, both on the compressive and the tensile side. Starting from the calculated averaged phonon frequencies and electron-phonon coupling, the superconducting characteristic critical temperature of the material T_c, has been calculated by means of the Allen-Dynes modification of the McMillan formula. As a result, the characteristic bell-shaped T_c *vs*. ε curve, with a maximum at zero intrinsic strain, and with a slight asymmetry between the tensile and compressive sides, has been obtained. These first-principle calculations thus show that the strain sensitivity of Nb_3Sn has a microscopic and intrinsic origin, originating from shifts in the Nb_3Sn critical surface. In addition, our computations show that variations of superconducting properties of this compound are correlated to stress-induced changes in both the phononic and electronic properties.

Finally, the strain function describing the strain sensitivity of Nb_3Sn has been extracted from the computed $T_c(\varepsilon)$ curve, and compared to experimental data from multi-filamentary, composite wires. Both curves show the expected bell-shaped behavior, but the strain sensitivity of the wire is enhanced with respect to the theoretical predictions of the bulk, perfectly binary and stoichiometric Nb_3Sn. Understanding the origin of this difference might open potential pathways towards the improvement of the strain tolerance in such systems.

INTRODUCTION

In this paper, we present a computational study on the intermetallic compound Nb_3Sn, a superconducting material currently used in accelerator magnets and nuclear fusion research. The A15 phase Nb_3Sn compound [1] is currently being used in a variety of large-scale scientific projects employing high-field superconducting magnets (above 10 T) [2], including ITER (the International Thermonuclear Experimental Reactor) [3], the 1 GHz NMR project [4], and the CERN LHC Luminosity Upgrade [5].

In these high-field magnets, the mechanical loads during cooldown (due to different thermal contractions) and operation (due to Lorentz forces) can be very large, and since the superconducting properties of Nb_3Sn strongly depend on strain [6], an overall performance degradation can take place.

Therefore, for a magnet's sound design it is of fundamental importance to have knowledge of the behavior of the superconducting parameters (namely the critical temperature T_c, the upper critical field B_{c2}, and the critical current I_c) as a function of the strain ε.

Of particular interest is the uniaxial stress (either in tension or compression), acting along the axial direction of the composite, multi-filamentary wires used in such systems: in a Cable-in-Conduit Conductor (CICC) [7], for example, the Nb_3Sn wires are inserted into stainless steel conduits, and compressive stresses due to the different thermal contraction coefficients of the different materials become important [8].

Within the framework of the Unified Scaling Law [9], many authors [10, 11] have proposed modified scaling equations which take into account the uniaxial strain dependence through the so-called strain function, $s(\varepsilon)$, but few attempts have been made [10, 12] to obtain a scaling law based on microscopic parameters. To this purpose, a very first step would be to accurately determine the electronic band structures, the phonon dispersion curves and the electron-phonon coupling terms, and study their evolution as a function of the applied strain. To this aim, the knowledge of the Nb_3Sn lattice cell deformation when a multifilamentary wire is subject to different stress components is of basic importance. Recent high resolution X-ray diffraction experiments on mechanically loaded samples [13] have shown in detail how the Nb_3Sn lattice cell deforms in the axial and the transverse directions; in particular, it was observed that the stress is completely transferred from the macroscopic level to the individual grains within the composite structure, so that a macroscopic uniaxial load directly corresponds to a stretching of the Nb_3Sn lattice cell along the same direction, with the cell contracting in the transverse direction of an amount corresponding to a Poisson's ratio ν equal to 0.38.

The structural and electronic properties of Nb_3Sn have been theoretically studied by several groups [14], whereas the full phonon dispersion relations have been calculated by means of a tight-binding method [15] and - more recently - by an *ab-initio* pseudopotential approach [16]. In particular, the calculations by Tütüncü *et al*. give evidence of a strong interaction between the electronic states near the Fermi level and several phonon modes (longitudinal acoustic phonons and a group of optical phonon modes with average frequency of 4.5 THz) along the [111] direction.

However, to the best of our knowledge no systematic *ab-initio* investigations have been made on studying the evolution of the band structure, phonon dispersion curves and superconducting parameters (electron-phonon mass enhancement parameter, λ, and T_c) as a function of an applied uniaxial strain. In the present work, this issue has been addressed by employing the plane-wave pseudopotential method, the density-functional theory, and a linear-response technique [17], and by using the results by Tütüncü *et al*. for the undistorted cell as a starting baseline for our calculations.

REQUIRED COMPUTATIONAL RESOURCES

Computations have been carried out by way of the ENEA-CRESCO computational facility. We analyzed a superconducting material starting from its microscopic characteristics and, in order to achieve meaningful results, we realized since the beginning of our project design that our problem needed to be solved in the framework of quantum mechanics. As is well known, quantum systems may be studied in various representations, one among the others being the Kohn-Sham density functional theory. The Kohn-Sham approach has the advantage of being the only one affordable for ab-initio computations on complex quantum systems, but is usually resource intensive and the computational load depends sensibly on the specimen complexity. The intrinsic symmetries of the analyzed sample under study play a significant role, but it is rarely compatible with conventional computational systems, if not for exceptionally elementary case studies. The system of our interest, namely the Nb_3Sn superconductor, strongly benefited from the material cubic-like cell symmetry for computational savings, but a clock wall time of 77 years of the CRESCO powerful parallel computational system was required in any case

to achieve our results. We initially submitted our jobs to the CRESCO-Portici parallel queues, subsequently migrating to the CRESCO-Frascati system as soon as a PFS machine has been made available from Frascati ENEA Centre. A disk quota of 1 TB was attributed to our account in order to carry out our simulations, and the standard ab-initio Quantum-Espresso-4.3.2 open source code has been installed and used; initially at Portici, lastly at Frascati. The Quantum espresso code may be freely downloaded from http://www.quantum-espresso.org/ as source code. It can be installed by way of CRESCO fortran 95 outfit compiler, takes speed advantages from BLAS, LAPACK and FFT installed libraries and MPI parallelization.

DETAILS OF COMPUTATION

We used density functional theory and density-functional perturbation theory [17] as implemented in the Quantum-ESPRESSO software distribution, within the local-density approximation [18], a plane-wave expansion up to 40 Ry for the kinetic energy cutoff and ultrasoft pseudopotentials for Nb and Sn.

The Brillouin zone has been sampled on a 8 X 8 Monkhorst-Pack (MP) mesh, corresponding to 126 special **k**-points within the irreducible part of the Brillouin zone (IBZ). We have also considered more dense grids 16 X 16 X 16 but the results did not change considerably.

Lattice dynamical calculations have been performed within the framework of the self-consistent density functional perturbation theory (DFPT), in which the dynamical matrices are calculated by sampling the IBZ with 8 independent **q**-points in the tetragonal phase. Dynamical matrices at any wave vectors can be Fourier deconvolved on this mesh, and the phonon dispersion curves along arbitrary symmetry directions can be easily obtained. In order to check the accuracy of the Fourier interpolation, we compared the results of this procedure with direct calculations on selected **q**-points not present in the grid.

A denser grid of **k**-points (24 X 24 X 24 MP divisions) has been used in order to determine the electron-phonon interaction parameter λ, calculated as the Brillouin-zone average of the mode-resolved coupling strengths $\lambda_{\boldsymbol{q},j}$:

$$\lambda = \sum_{\boldsymbol{q},j} W(\boldsymbol{q}) \lambda_{\boldsymbol{q},j} \quad (1)$$

where j indicates a phonon polarization branch, and W(**q**) are the weights associated with the phonon wavevectors **q**, normalized to 1 in the first Brillouin zone.

The lattice parameter of the cubic cell is set to 5.29 Å [19]. For an uniaxial stress along the z-direction (σ_z) and under the assumption that the system is transversally isotropic, the strain state can be expressed as:

$$\varepsilon_x = \varepsilon_y = -\nu\frac{\sigma_z}{E};\ \varepsilon_z = \frac{\sigma_z}{E} \quad (2)$$

which reflects the variation of the lattice parameters of the tetragonally distorted cell.

In Eq. (2), ν is the Poisson's ratio whereas E represents the Young's modulus. In our computations, ν has been set to the value measured in composite wires (ν = 0.4 [13]), and the distortions have been calculated in the strain range ±1.0 %, in steps of 0.2 %.

RESULTS

The Nb_3Sn cubic phase belongs to the ($P\frac{4_2}{m}\bar{3}\frac{2}{n}$) space group and the O_h^3 point-group symmetries, as shown in Fig. 1a. The Sn atoms are situated on a bcc matrix whereas the faces of the cube are occupied by Nb atoms which form three sets of orthogonal chains along the principal axes. When a uniaxial strain is applied along the c-direction, the lattice is tetragonally distorted, with the Nb-chains in the [001] direction differing from those in the [100] and [010] directions, as shown in Fig. 1b. The distorted structure has a reduced symmetry D_{4h}^9 ($P\frac{4_2}{m}\frac{2}{m}\frac{2}{c}$).

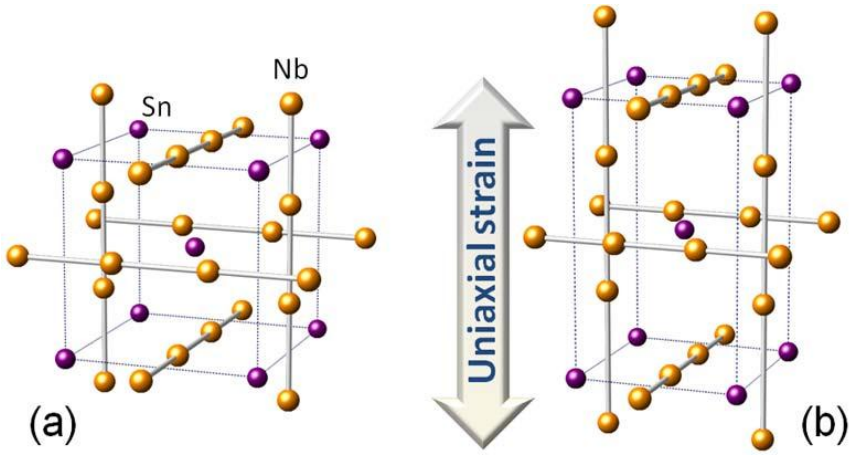

Fig. 1 The arrangement of atoms in the cubic (a) and tetragonal (b) phase of A15 Nb_3Sn. The Nb atoms in the 2e sites form chains along the [001] direction, whereas those in the *4k* sites are in chains along the [100] and [010] directions. To make the distortion clear, in (b), the cell is stretched to the abnormal value of $\varepsilon = 40\%$, whereas the Poisson's ratio ν is set to 0.4.

Starting from the cubic cell, a uniaxial strain has been applied to the cell along the *c*-direction, according to Eq. (2). As a result, the deviatoric components of the strain lowered the system's point group symmetries: most of the phonon degeneracies have been removed and a change in both the electronic and phonon dispersion bands have been induced.

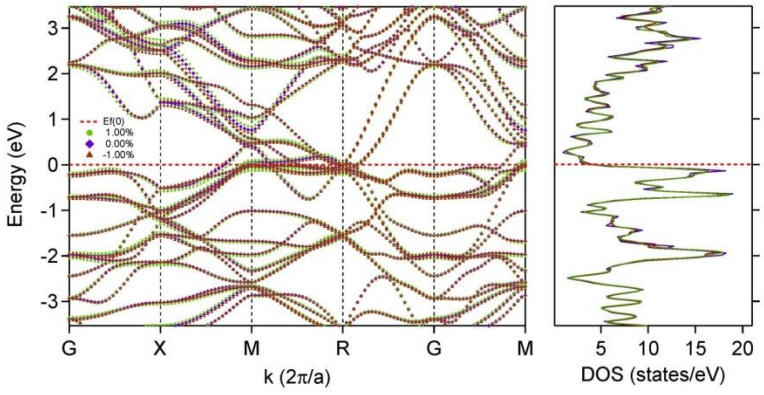

Fig. 2 The electronic band structure and density of states for Nb_3Sn calculated for three representative strain states: +1.0 % (•), zero applied strain (♦), and -1.0 % (▲). The Fermi level is set to 0 eV.

The calculated electronic structure along many high-symmetry directions of the simple-cubic Brillouin zone are displayed in Fig. 2 for three representative values of the applied strain (zero, 1.0 % and -1.0 %). The energy bands of the cubic crystal are shown as diamonds, whereas the circles and the triangles represents the 1.0 % and -1.0 % strain states, respectively. Indeed, the tetragonal deformation does not affect the electronic structure in a severe way: the energy bands of the distorted and undistorted cell are almost unchanged, and there is no evident splitting of the cubic bands at the Fermi level, E_F. The

electronic DOS is also not drastically affected by the tetragonal distortion. In Fig. 2, the Fermi level is marked by a dashed horizontal line and is set to 0 eV. It is interesting to notice that E_F falls close to a sharp peak in the electronic DOS [14], with a value for the density of states of the order of 20 states/eV. This peak is generated by several nearly dispersionless bands crossing the Fermi level in the Γ-M, Γ-R, and M-R directions and deriving from the *4d* states of Nb atoms [16].

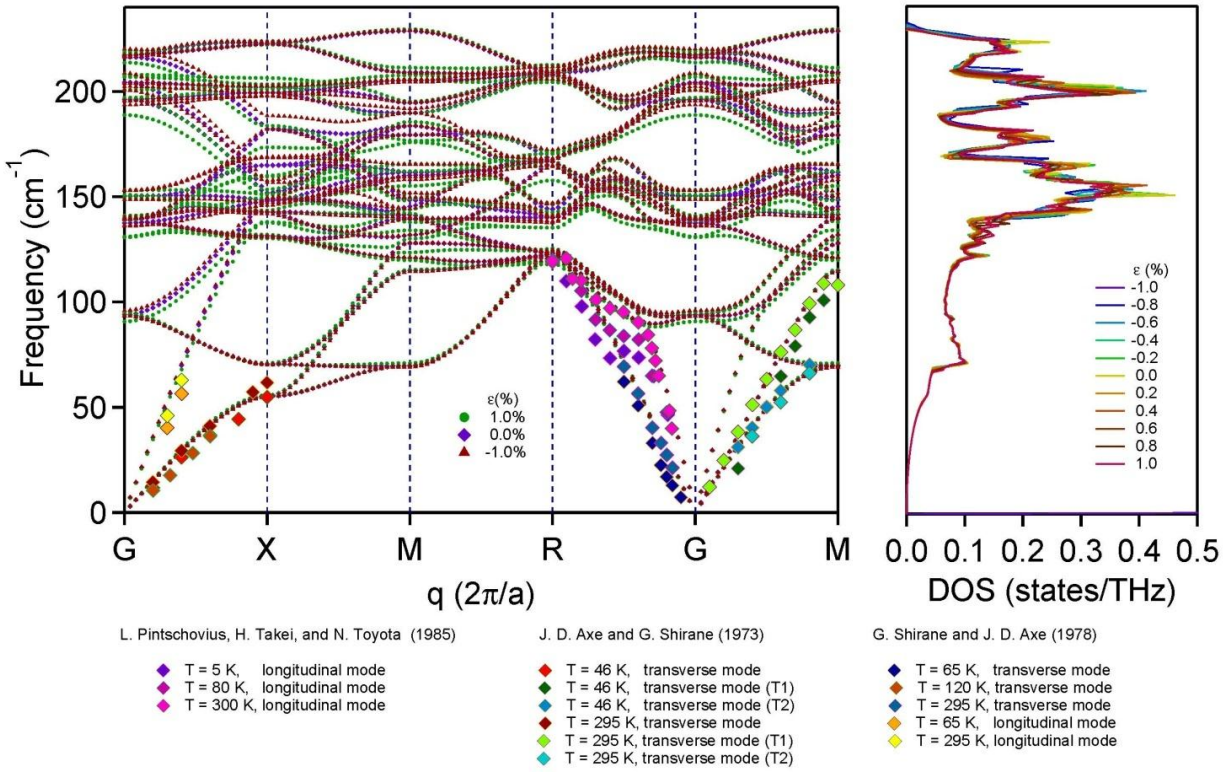

Fig.3 (a) Phonon dispersion curves of Nb_3Sn at three different strain states: +1.0 % (•), zero applied strain (♦), and -1.0 % (▲); (b) phonon DOS at each calculated strain. For completeness, experimental curves are also reported.

The electronic band structures (Fig. 2) and phonon dispersion curves (Fig. 3) along different high–symmetry directions in the Brillouin zone have been calculated at different levels of applied strain ε, both on the compressive and the tensile side. Starting from the calculated averaged phonon frequencies and electron–phonon coupling, the superconducting characteristic critical temperature of the material, T_c, has been calculated by means of the Allen–Dynes modification of the McMillan formula:

$$T_c = \frac{\hbar\omega_{ln}}{1.20} e^{-\frac{1.04(1+\lambda)}{\lambda-\mu^*(1+0.62\lambda)}} \quad (3)$$

where μ^* is the effective Coulomb-repulsion parameter which describes the interaction beetween electrons, and ω_{ln} is a weighted logaritmically averaged phonon frequency, defined as:

$$\omega_{ln} = e^{\frac{2}{\lambda}\int_0^{+\infty}\frac{d\omega}{\omega}\alpha^2(\omega)F(\omega)\ln(\omega)} \quad (4)$$

where $\alpha^2(\omega)F(\omega)$ is the Eliashberg spectral function. We assumed a negligible strain dependence of μ^* compared to the other parameters, and frozen it as a constant in our computations [10].

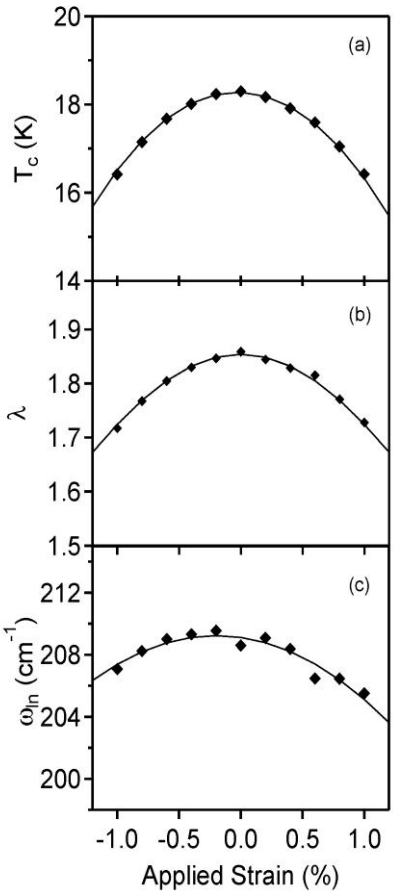

Fig.4 The behavior of: (a) the superconducting critical temperature, T_c; (b) the *el-ph* coupling constant, λ; and (c) the logarithmically averaged phonon frequency ω_{ln} as a function of an applied uniaxial strain. Lines are guide for eye.

As it can be clearly seen in Fig. 4, the characteristic bell–shaped T_c *vs.* ε curve, with a maximum at zero intrinsic strain and with a slight asymmetry between the tensile and compressive sides, has been obtained. These first–principle calculations thus show that the strain sensitivity of Nb_3Sn has a microscopic and intrinsic origin, originating from shifts in the Nb_3Sn critical surface. In addition, our computations show that variations of superconducting properties of this compound are correlated to stress–induced changes in both the phononic and electronic properties.

Our calculations also show that $N(E_F)$ is influenced by strain. This quantity is related to the *el-ph* coupling constant and to the averaged phonon frequency trhough the following expression [21]:

$$N(E_F) = \frac{M\omega_{RMS}^2\lambda}{\langle I^2\rangle} \qquad (5)$$

in which $\langle I^2\rangle$ is the average over the Fermi surface of the *el-ph* matrix element squared, ω_{RMS} is a weighted RMS phonon frequency and M is the average ionic mass. By further assuming that the strain sensitivity of the normalized averaged frequencies ω_{RMS} and ω_{ln} are the same [20] and that $\langle I^2\rangle$ does not depend on any applied strain, it follows that $N(E_F,\varepsilon) \propto \lambda\omega_{ln}^2$. The strain dependence of $N(E_F)$, calculated either directly or through Eq. 5 are consistent with one another, as can be clearly seen in Fig. 5. Results of Figs. 4-5 thus provide evidence that the strain is affecting both the phononic and the electronic properties in the same way.

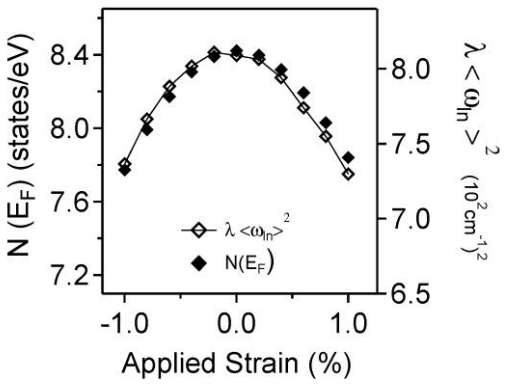

Fig.5 Density of states at Fermi level, $N(E_F)$, calculated as a function of strain. The curve is overlapped to the product function $\lambda \cdot \omega_{ln}^2$, which in good approximation should be proportional to N(EF) [21].

Finally, the strain function describing the strain sensitivity of Nb_3Sn has been extracted from the computed T_c curve, and compared to experimental data from multi–filamentary wires (Fig. 6).

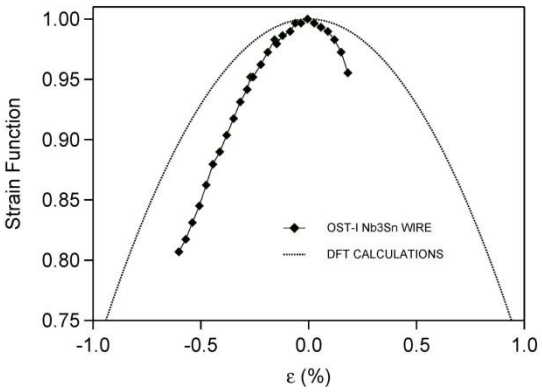

Fig.6 Direct comparison between the theoretical (dashed line) and experimental (line and markers) strain function [22]. The theoretical $s(\varepsilon)$ correctly reproduces a bell shape, the mismatch being attributed to those extrinsic effects generally observed in technological wires.

Both curves show the expected bell–shaped behaviour, but the wire strain sensitivity is enhanced as to the bulk theoretical predictions which are perfectly binary and stoichiometric Nb3Sn. Understanding the origin of this difference might open potential pathways towards improvements in the strain tolerance of such systems.

References

[1] B. T. Matthias, Phys. Rev. **92**, 874 (1953).
[2] T. Miyazaki, T. Hase, and T. Miyatake, *Handbook of Superconducting Materials* (Bristol: IOP Publishing, 2003), pp. 639-72.
[3] A. Vostner, and E. Salpietro, Supercond. Sci. Technol. **19**, S90 (2006); N. Mitchell, A. Devred, P. Libeyre, B. Lim, F. Savary, and the ITER Magnet Division, IEEE Trans. Appl. Supercond. **22**, 4200809 (2012); A. Devred, I. Backbier, D. Bessette, G. Bevillard, M. Gardner, M. Jewell, N. Mitchell, I. Pong, and A. Vostner, IEEE Trans. Appl. Supercond. **22**, 4804909 (2012).
[4] H. Wada, and T. Kiyoshi, IEEE Trans. Appl. Supercond. **12**, 715 (2002).
[5] L. Bottura, G. de Rijk, L. Rossi, and E. Todesco, IEEE Trans. Appl. Supercond. **22**, 4002008 (2012).
[6] G. Rupp, J. Appl. Phys. **48**, 3858 (1977); J. Ekin, IEEE Trans. Magn. **15**, 197 (1979); B. ten Haken, Ph.D Thesis, Technical Unicersity of Twente, Enschede, The Netherlands (1994); J. Ekin, J. Appl. Phys. **62**, 4829 (1987).
[7] M. O. Hoenig, A. G. Montgomery, and S. J. Waldman, IEEE Trans. Magn. **15**, 792 (1979); P. Bruzzone, IEEE Trans. Appl. Supercond. **16**, 839 (2006); M. Spadoni, IEEE Trans. Magn. **30**, 1699 (1994).
[8] A. Nijhuis, and Y. Ilyin, Supercond. Sci. Technol. **19**, 945 (2006); N. Mitchell, Supercond. Sci. Technol. **18**, S396 (2005).
[9] J. Ekin, Cryogenics **20**, 611 (1980).
[10] D. M. Taylor, and D. P. Hampshire, Supercond. Sci. Technol. **18**, S241 (2005); S. Oh, and K. Kim, J. Appl. Phys. **99**, 0330909 (2006).
[11] A. Godeke, B. ten Katen, H. H. J. ten Kate, and D. C. Larbalestier, Supercond. Sci. Technol. **19**, R100 (2006); D. Arbelaez, A. Godeke, and S. Prestemon, Supercond. Sci. Technol. **22**, 025005 (2009); W. D. Markievicz, Cryogenics **46**, 864 (2006).
[12]W. D. Markievicz, Cryogenics **44**, 767 (2004).
[13] L. Muzzi, V. Corato, A. della Corte, G. De Marzi, T. Spina, J. Daniels, M. D. Michiel, F. Buta, G. Mondonico, B. Seeber, R. Flükiger, and C. Senatore, Supercond. Sci. Technol. **25**, 054006 (2012).
[14] B. Sadigh, and V. Ozoliņš, Phys. Rev. **B 57**, 2793 (1998); Z. W. Lu, and B. M. Klein, Phys. Rev. Lett. **79**, 1361 (1997); L. F. Mattheiss, and W. Weber, Phys. Rev. **B 25**, 2248 (1982); B. M. Klein, L. L. Boyer, D. A. Papaconstantopoulos, and L. F. Mattheiss, Phys. Rev **B 18**, 6411 (1978); G. Arbman, and T. Jarlborg, Solid. State Commun. **26**, 857 (1978).
[15] W. Weber, Physica B+C **126**, 217 (1984); W. Weber, *Electronic Structure of Complex Systems* (Plenum Press, New York, 1984), vol. 113, p. 345.
[16] H. M. Tütüncü, G. P. Srivastava, S. Bağcı, and S. Duman, Phys. Rev. **B 74**, 212506 (2006).
[17] S. Baroni, P. Giannozzi, and A. Testa, Phys. Rev. Lett. **58**, 1861 (1987); S. Baroni, S. deGironcoli, A .Dal Corso, and P. Giannozzi, Rev. Mod. Phys. **73**, 515 (2001).
[18] N. Troullier, and J. L. Martins, Phys. Rev. **B 43**, 1993 (1991),
[19] R. G. Maier, Z. Naturforsch. Teil **A 24**, 1023 (1969); V. Guritanu, W. Goldacker, F. Bouquet, Y. Wang, R. Lortz, G. Goll, and a. Junod, Phys. Rev. **B 70**, 184526 (2004).
[20] K. C. Lim, J. D. Thompson, and G. W. Webb, Phys. Rev. **B 27**, 2781 (1983).
[21] W. L. McMillan, Phys. Rev. **167**, 331 (1968).
[22] G. De Marzi, V. Corato, L. Muzzi, A. della Corte, G. Mondonico, B. Seeber, and C. Senatore, Supercond. Sci. Technol. **25**, 025015 (2012).

Use of Monte Carlo in State-of-the-Art PWR Design: Continuing Analysis of the Impact of the Heavy Reflector of a Typical Large Size GEN III+ Reactor Design on some Safety Features: Completion of the Ex-Core Detector Calculations and Examination of the Impact on Flux Tilt. Development and Testing of New Algorithms within Monte Carlo Eigenvalue Calculations employing the Source-Iteration Method

K.W. Burn
ENEA, C.R. Frascati
Via E. Fermi 45, 00040 Frascati – IT
e-mail: kennethwilliam.burn@enea.it

Summary

This report covers work carried out over the period Sept. 2011 – Aug. 2012 and is in two parts. The first part deals with safety issues related to the thick steel reflector of a typical large size GEN III+ reactor design. Concerning the impact of the steel reflector on the signal in the ex-core detectors, issues left open from the previous year's work (moving the ^{252}Cf primary source assemblies from their outer core positions one assembly position inwards towards the core centre; generation of results for the Sb-Be secondary source assemblies) are addressed. All the results for the ex-core detectors were summarized in a paper at the TopSafe-2012 meeting in April, 2012 [3].

In current operating plants with large cores, flux tilt can be a problem. Although it may be due to a variety of factors and may also involve positive feedback effects, one possible contributory cause that may be simply modelled is a variation in the coolant density. It is known that relatively small azimuthal variations in the coolant density in the external assemblies can induce a proportionately high power asymmetry throughout the core (especially at low power) with a conventional baffle-water configuration as reflector. To understand what impact the thick steel reflector has on this effect, results have been generated with a 2-dimensional model of the reactor core at HZP and at 30% NP.

The second part deals with the development of new algorithms to reduce the variance in eigenvalue calculations with the source-iteration approach. As a first step a "superhistory" approach has been introduced into MCNP5. An adjustment of the ν-value to ensure a supply of children at each normalization in the case that k_{eff} differs appreciably from unity has not yet been inserted. Following this, the development will be articulated in two steps – firstly a search for the trade-off between an optimum population within each cycle (or superhistory) and at the next normalization point (i.e. end of superhistory); secondly a search for the trade-off between cycle size and number of normalization points.

1. Use of Monte Carlo in State-of-the-Art PWR Design: Continuing Analysis of the Impact of the Heavy Reflector of a Typical Large Size GEN III+ Reactor Design on some Safety Features: Completion of the Ex-Core Detector Calculations and Examination of the Impacton Flux Ti

1.1 Introduction

The work has been performed within the framework of an agreement between ENEA and IRSN (**I**nstitut de **R**adioprotection et de **S**ûreté **N**ucléaire). The particular area of the activity deals with safety issues concerning the thick steel reflector of a typical large size GEN III+ reactor design and in particular the differences caused by this reflector compared with current PWR designs. The work is a continuation of [1]. It has been published in [2].

1.2 Completing the Activity on Ex-Core Detectors

Left over from the previous year's activity were an evaluation of the change in signal in the ex-core detectors when the primary source assemblies are moved one assembly position towards the core centre and an analysis of the signal in the ex-core detectors from the secondary source assemblies.
Moving the ^{252}Cf primary source assemblies from their outer position, one assembly position towards the core centre reduces the signal in the ex-core detectors by approximately one order of magnitude when fissions are turned off. This becomes a factor of roughly 2 when fissions are included. These results hold both for the heavy steel reflector and the conventional one (baffle + water).
As far as the Sb-Be secondary sources are concerned, firstly the ^{123}Sb(n,γ) rate in each of the 16 secondary source pins in each of the 3 secondary source assemblies in 4 axial segments was evaluated under conditions of criticality, then the neutron source was formed assuming it to be proportional to the amount of ^{124}Sb ($T_{1/2}$ = 60.2 d) present, then, under conditions of 0.95 criticality, these neutrons were transported outside the core, through the reflector to the detector. Excluding fissions, the signal in the ex-core detectors with the steel reflector is around 3 orders of magnitude higher than with the water reflector. (These signals are completely negligible compared with when fission is switched on.) Including fissions, the ratio of the signal in the ex-core detectors with conventional reflector and with steel reflector varies between 4.1 and 3.7, depending on which detector is considered. All the results for the ex-core detectors were presented to the TopSafe-2012 meeting at Helsinki in April, 2012 [3].

1.3 Flux Tilt

The flux tilt may be due to a variety of factors and also involve positive feedback effects. One possible contributing cause that can be modelled relatively simply is a variation in the coolant density. Thus the coolant water density in the outer assemblies of opposite core quadrants was changed slightly – see Fig. 1 where an increase in the water density in the SE quadrant is shown with a corresponding decrease in the NW quadrant. The tilt is then defined by the increase in power in the whole SE quadrant compared with the mean and the decrease in power in the NW quadrant compared with the mean (see Fig. 2). (Note that the increase and decrease are not necessarily the same.)
In these calculations a 2-dimensional model of the reactor core was employed. This was for reasons of simplicity, speed and ease of comparison with deterministic approaches. However it should be borne in mind that 3-D effects, due for example to the axial variation in the temperature field of the core, exist and are important in current models that represent flux tilt.

1.4 Concluding Remarks

The activity dealing with the effect of the heavy steel reflector on the ex-core neutron detectors has been concluded. That concerning the effect of the heavy steel reflector on the phenomenon of flux tilt is still under-way.

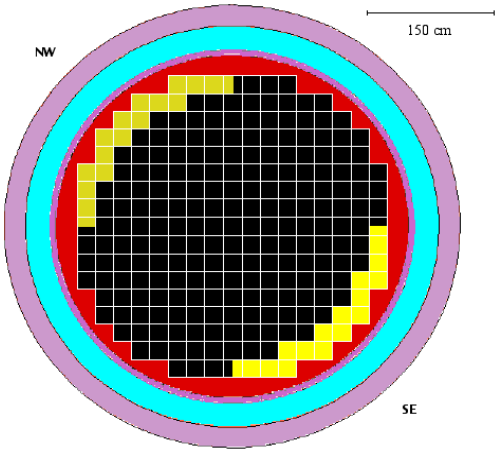

Fig. 1: Assemblies defining the change in water density that may induce the tilt

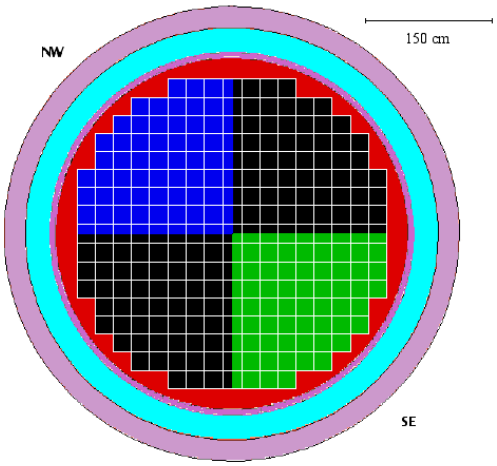

Fig. 2: Assemblies defining the flux tilt

2. Development of Monte Carlo Algorithms for Eigenvalue Calculations

2.1 Introduction

For many years optimization of fixed source Monte Carlo radiation transport calculations has been under development at ENEA [4]. Recently the focus has been redirected from fixed source to eigenvalue calculations employing the source iteration approach.
At first sight the developments at ENEA, named "DSA" (Direct Statistical Approach to Variance Reduction Optimization), look to be well suited to deal with the source iteration approach as:

a) They explicitly take into account correlations between progeny coming from the same progenitor, be the event an artificial bifurcation (*viz.* splitting) or a natural bifurcation [e.g. (n,xn), fission].

b) They search for the optimum trade-off between greater splitting that decreases the second moment and increases time (and thereby allows less source particle histories to be run in a given time) and greater Russian roulette that increases the second moment and decreases time (and thereby allows more source particle histories to be run in a given time).

In the source iteration method, correlations between fission daughters contribute to underestimating the standard error, which is calculated under the assumption that fission generations are independent. Furthermore the balance between the number of fission neutrons per generation and the total number of generations is decided empirically. Both these issues look susceptible to an approach such as the DSA. Furthermore the question of calculating a neutronic/photonic response in a spatially limited domain in a source-iteration calculation remains an unsolved problem.

2.2 Discussion of Approach

Initially an attempt was made to treat the source-iteration problem as a fixed source problem by firstly assuming that the fundamental mode of fission sites has been reached and secondly sampling fission chains starting from this source, normalizing the result from each source history by both the length of the fission chain. Unfortunately calculating responses in this way gives a first moment that tends to decrease dramatically as the number of cycles increases. This is because more successful fission neutrons tend to make longer fission chains, and because of the normalization by the length of each fission chain, tend to count less than less successful fission neutrons with shorter fission chains (due to absorption, leakage, etc.).
An approach nearer the source-iteration algorithm looked to be indicated. As a first step the number of fission site renormalizations was reduced from "at every fission generation" to "at every L fission generations", i.e. the "superhistory" approach.

2.3 Superhistories

Reducing the number of fission site renormalizations was first proposed in [5] to reduce the bias in the estimated variance. Here it is employed instead as a first step in an approach to improve variance reduction.
The DSA is not a stand-alone code but employs the well-known general-purpose radiation transport code, MCNP [6], as a vehicle. Thus any code is distributed as a "patch" to MCNP that could also be modified to patch another code.
As a first step, a superhistory patch has been inserted into MCNP5 (ver. 1.4). An adjustment of the ν-value to ensure a supply of children at each normalization in the case that k_{eff} differs appreciably from unity, as made in [5], has not yet been inserted.

2.4 Current State of Project (as at near end 2012)

The superhistory patch has been tested and runs. The current version of the DSA patch for fixed source problems was updated between 2010 and 2011 to be compatible with MCNP5 (ver. 1.3) and in particular to run with MPI. Currently the DSA patch is being updated to MCNP5 (ver. 1.4). (An important advantage of ver. 1.4 over ver. 1.3 is the presence of the Shannon entropy diagnostics.) It will then be combined with the superhistory patch and further developed to calculate spatially limited neutronic responses in reactor cores (e.g. in-core neutron detectors) and neutron detector responses near fissile storage arrays.

The development will be articulated in two steps – firstly a search for the trade-off between an optimum population within each cycle (or superhistory) and at the next normalization point (i.e. end of superhistory); secondly a search for the trade-off between cycle size and number of normalization points.

3. Hardware and Software employed in these activities

As far as software is concerned, for the first part of the activity, a patched version of MCNP5 (ver. 1.3) was employed. The patch involved substantial modifications to the original code (the patch was approximately 20500 lines long compared with the original code length of just under 80000). Instead for the second part of the activity, the superhistory patch is currently just 500 lines. (However subsequent to this work it has been integrated with a modified DSA patch for k_{eff} problems and reached more than 22000 lines.) Furthermore a separate stand-alone code is also required that is built around the IMSL version 1.0 library.

Parallelism was exploited as much as possible. A local parallel version of MCNP was used [7] that is built on MPI for IBM AIX POE. The parallelism was maintained in the DSA-patched version. However the stand-alone code built around IMSL is scalar.

The sp.5-x (x = 2,3,4,5,6,7,8,10,13) IBM AIX clusters at ENEA, Frascati were employed. There are 16 nodes available on all these machines apart from sp5-2 (14) and sp5-13 (64). The longest runs took a week-end, although typical long runs took less time and ran overnight (12-15 h). An interesting aspect is that, whilst normal Monte Carlo employs a limited (and constant) number of output quantities, the DSA requires large output arrays, with a hierarchical structure. The work of combining such arrays generated on different nodes is certainly non-negligible and means that there is an appreciably less than linear gain with an increase in the number of nodes.

References

1. K.W. Burn "Analysis of the Impact of the Heavy Reflector of a Typical Large Size GEN III+ Reactor Design on the Ex-Core Detector Signals with Monte Carlo Techniques (Employing MCNP-5)", PAR2010-ENEA-LD2-010 (2011)
2. K. W. Burn, "Continuing Analysis with Monte Carlo Techniques of the Impact of the Heavy Reflector of a Typical Large Size GEN III+ Reactor Design on some Safety Features: Completion of the Ex-Core Detector Calculations from PAR2010 and Examination of the Impact on the Phenomenon of Flux Tilt", ENEA NNFISS-LP2-084 (2012)
3. K.W. Burn, G. Bruna, B. Normand "Impact of the Heavy Steel Reflector of a Current Large PWR Design on some Safety Features", presented at TopSafe-2012, Helsinki, 2012
4. K.W. Burn "Optimizing Monte Carlo to Multiple Responses: the Direct Statistical Approach, 10 Years On", *Nucl. Technol.* **175**, 138 (2011)
5. R.J. Brissenden, A.R. Garlick "Biases in the Estimation of K_{eff} and Its Error by Monte Carlo Methods", *Ann. Nucl. Energy* **13-2**, 63 (1986)
6. X-5 Monte Carlo Team "MCNP – A General Monte Carlo N-Particle Transport Code, Version 5", LA-UR-03-1987 (2003)
7. S. Podda, private communication

LES SIMULATION OF A DEVOLATILIZATION EXPERIMENT ON THE IPFR FACILITY

F. Donato*, G. Rossi, B. Favini**, E. Giacomazzi*, D. Cecere***
F.R. Picchia*, N.M.S. Arcidiacono*

Corresponding author: filippo.donato@enea.it
* ENEA-UTTEI/COMSO Via Anguillarese 301, 00123 Roma
** DIMA, "Sapienza" University, Via Eudossiana 18, 00184 Roma

Introduction

Oxy-combustion of pulverized coal has raised some interest from industrial players in the energy production field, as a promising technique to meet future emission requirements. The present work is part of a larger activity aimed at developing and validating a Large Eddy Simulation (LES) solver applicable to the study of this kind of burners, even in MILD conditions.
In the present work, after briefly recalling the models implemented in the HeaRT code, the Isothermal Plug Flow Reactor (IPFR) facility, owned by the International Flame Research Foundation (IFRF), is described. Finally the results of the validation of the HeaRT code against the data from a devolatilization test performed on this facility are presented.

Mathematical and numerical model

The version of the HeaRT code used in the present work solves both the continuous and the dispersed phase in an Eulerian frame. The model thus belongs to the Eulerian-Eulerian class of solvers for multiphase flows. The code has been provided in the past years with modules for the simulation of the radiation field, heterogeneous reactions and coal thermal degradation. The equations adopted for the continuous and the dispersed phase as well as the adopted model to treat the advected condensed scalars (used to model tar evolution), the radiation heat transfer and coal chemical kinetics have been described in previous publications [1, 2, 3]. The numerical procedure is also described in [2, 3].

The IPFR facility

In the present section the results obtained by simulating a devolatilization experiment performed on the IPFR facility at IFRF in Livorno (Italy) are described. With reference to Figure 1 the combustion chamber is composed by a modular drop tube with inner diameter D_1 = 0.15 m and total length L_1 = 4.5 m. The tube is equipped with probe accesses at several sections for both coal feeding and sampling. A natural gas fired burner is present at the top of the facility and the exhaust gases coming from this burner are used to set up the desired experimental conditions inside the drop tube. The possibility to dilute such exhaust gases with Nitrogen is also foreseen in order to have greater flexibility. At the bottom of the combustion chamber a quenching system and a system for coal residuals and ashes collection are present. The residence time can be varied by changing the access for the coal feeding probe. Further information about the facility or the experimental procedure can be found in [4].

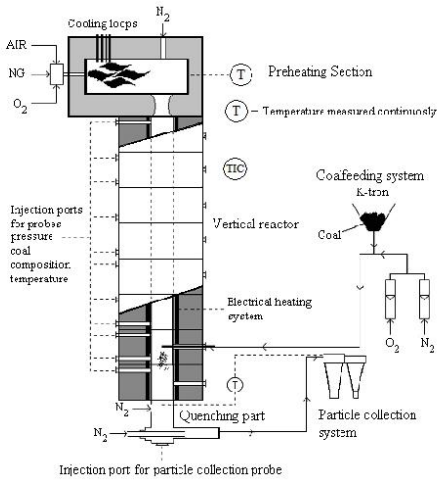

Figure 1. Scheme and characteristics of the IPFR facility (Taken from ref. [7])

Numerical setup

In the configuration adopted for the simulated test the coal injection is located at the tube axis through a hole with diameter D_{inj} = 0.0085 m. The proximate and ultimate analysis for the tested coal are reported in Table 1.

The simulated domain extends to Z_{max} = 3.05 m. A detail of the adopted grid for the first 0.2 m in axial direction is reported in Figure 2. The cells with the smallest dimensions are at the top center of the domain, where the coal injection takes place. The smallest cell size in the axial direction is Δz_{min} = 0.001 m while in radial direction is Δr_{min}= 0.000425 m. The radial discretization is independent from the axial position while the grid is stretched in the axial direction and the maximum cell dimension reaches Δz_{max}= 0.019 m at the outlet section. The tangent direction has been discretized using 16 planes with constant distribution, while 48 cells have been used in the radial direction and 500 in the axial direction. The grid is therefore composed by 384000 cells.

Proximate analysis (as fired- %w/w)				**Ultimate analysis (as fired- %w/w)**			
Moisture	Volatiles	Ash	Fixed carbon	C	H	N	S
3.39	25.26	15.32	56.04	69.56	4.54	1.64	0.57

Table 1. Proximate and ultimate analysis for the tested coal

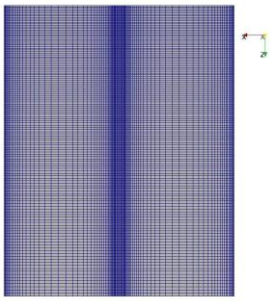

Figure 2. Adopted grid for the first part of the domain (0.2 m in axial direction)

The imposed boundary conditions for the gas phase are adiabatic viscous walls at r = R_{max} = 0.075 m while at the outlet section (z = Z_{max}) a characteristic equations treatment [5] is imposed, with asymptotic pressure equal to 1 atm. For the dispersed phase an upwind outlet is imposed at both walls and at the outlet section. The inlet section at z = Z_{min} is divided into 3 regions: the coal injection, the injector wall and the exhaust gas inlet. The coal injection is positioned for 0 m < r < 0.00425 m. Here coal and N2 as carrier gas enter the domain with mass flow rates W_{coal}= $3.05556 \cdot 10^{-5}$

kg/s and W_{inj} N2 = 5.80093•10^{-4} kg/s and imposed temperatures T_{coal} = 298.15 K and T_{N2}^{inj}= 293 K. In order to simulate the expansion cone at the injection, a radial mean component has been added to the carrier gas velocity which presents a linear dependence from the radial coordinate. This component is zero at the axis and equal to the axial component for r = 0.0425 m. The dispersed phase is here injected with volumetric fraction α_{inj} = 4.316•10^{-4} and axial velocity $u_{p,z}$ = 1 m/s. The experiment has been run with particle diameter d_p at the injection in the range [38 : 90] μm. The adopted model has been chosen to be monodispersed for computational time constraints, although the HeaRT code is able to deal with different classes of particles with different initial dimensions. The particle number density at the inlet n_p^{inj} has been imposed in order to have a particle dimension of d_p^{inj} = 70 μm. The radial velocity has been imposed following the law $u_{p,r}$ = 12.83 s^{-1} • r. The exhaust gases enter the inlet with the following composition in terms of mass fraction: Y_{CO2}= 0.104292, Y_{H2O}=0.0853841, Y_{O2} = 0.00824372 and Y_{N2} = 0.80208018. The temperature is given by the nominal set point T_{eg}^{ann} = 1373 K while the total mass flow rate is W_{eg}^{ann} = 1.26103•10^{-2} kg/s. The dispersed phase enters from this section with volumetric fraction α_{eg}^{ann} = 10^{-12} which is just a numerical approximation to zero. The injector wall ranges from r = 0.00425 m to r = 0.0063561 m. In this interval the temperature and chemical species values are linearly interpolated between the values imposed at the coal injection and at the exhaust gas inlet in order to enhance the stability of the radiation field solver. Null pressure gradient is imposed on the entire inlet and null gradient is also imposed on all the radiative variables on the entire domain boundary.

The initial conditions are set equal to the variable values at the exhaust gas inlet with the exception of the velocity of both phases which is set to zero.

The simulations have been performed on the CRESCO2 cluster installed in the ENEA Research Center in Portici. The adopted compiler is the Intel Fortran and the parallelization implementation used is the open-mpi-1.2.8. The simulation has been performed using 64 cores with a typical computing time for each timestep of 0.11 s. The simulated time is 0.47 s. Each instantaneous field needs approximately 180 MB of disk space and the overall disk space used on the fast access hard drives in Portici was 33 GB.

Results

In Figure 3 an instantaneous field of the gas temperature T and of the momentum module ρu are presented for the first 0.4 m of the domain in axial direction. It can be seen how the cold jet enters the chamber till z = 0.3 m and even further. This feature of the flow has a strong influence on the coal conversion since the gas temperature influences the particle heating up. The jet momentum reaches the equilibrium with the outer flow approximately at the same distance from the inlet.

In Figure 4 instantaneous distributions of the CO mass fraction and of the dispersed phase volume fraction are reported. It can be seen how the released CO concentrates around the zones with the higher particle concentration.

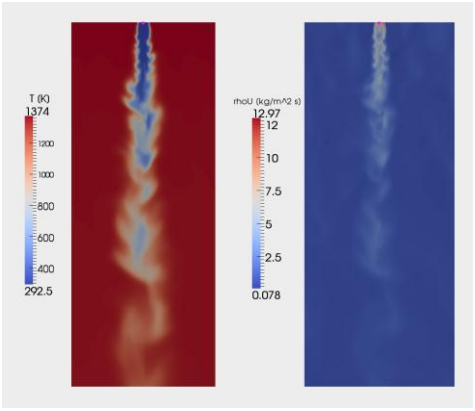

Figure 3. Gas phase temperature (left) and momentum module (right) instantaneous distribution.

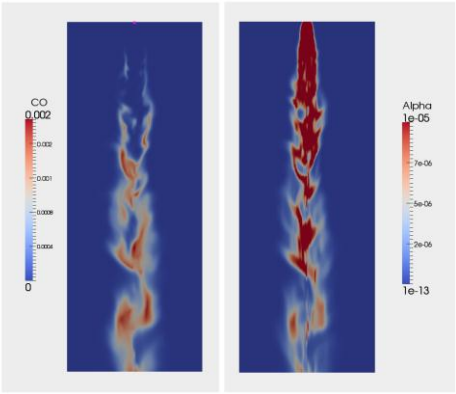

Figure 4. CO mass fraction (left) and dispersed phase volume fraction (right) instantaneous distribution.

Finally in Figure 5 the numerical and experimental data on coal conversion are compared, at least for two sampling points. It can be seen how the numerical data are well within the uncertainty range of the measures.

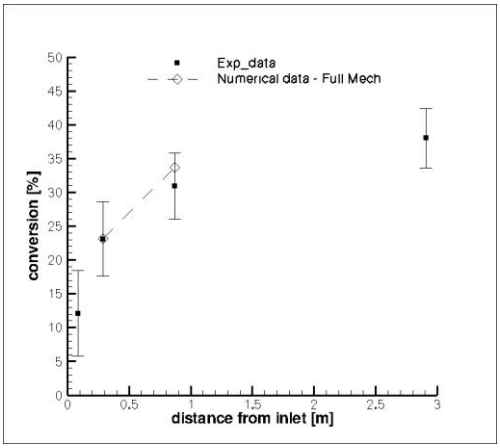

Figure 5. Comparison between experimental and numerical data on coal conversion

Conclusions

In the present work the validation of the HeaRT code against an IPFR devolatilization experiment is presented. The implementation of the POLIMI devolatilization model [6] in the HeaRT code has proved its capability in well reproducing coal conversion experimental data. It should be also noted that in order for the validation to be successful, the coupling of a radiation field solver with the dispersed phase model was necessary.

References

[1] F. DONATO, G. ROSSI, B. FAVINI, E. GIACOMAZZI, D. CECERE, F.R. PICCHIA, N.M.S. ARCIDIACONO. "*Les simulation of a devolatilization experiment on the IPFR facility*". Proceedings of the XXXV Meeting of the Italian Section of the Combustion Institute. Milan, October 10-12, 2012

[2] F. DONATO. "*Numerical modelling of two-phase reacting flows*". Phd thesis in Energetics, XXII cycle, Dept. of Electric Engineering, Univ. Sapienza, Rome, 2009.

[3] F. DONATO, G. CALCHETTI, A. DI NARDO, B. FAVINI. "*Simulazione di un combustore con tecnologia ISOTHERM*". ENEA internal report COMSO/2011/007EL, Casaccia Research Center, Via Anguillarese 301, 00123 - Santa Maria di Galeria (Rome), 2011.

[4] E. BIAGINI, L. BIASCI, M. MARCUCCI. "*Description of the isothermal plug flow reactor and the experimental procedures for combustion studies on solid fuels*". IFRF research report IFRF Doc No G03/y/03, Livorno (ITALY), 2011.

[5] J.C. SUTHERLAND, C.A. KENNEDY. "Improved boundary conditions for viscous reacting compressible flows". *J. Comp. Phys.*, **101**:502-524, 2003.

[6] S. SOMMARIVA, T. MAFFEI, G. MIGLIAVACCA, T. FARAVELLI, E. RANZI. *"A predictive multi-step kinetic model of coal devolatilization"*. Fuel, **89**:318, 2010.

USAGE STATISTICS OF CRESCO IN 2012

F. Palombi, F. Ambrosino, G. Aprea, T. Bastianelli, F. Beone, G. Bracco, M. Caporicci, M. Chinnici, A. Colavincenzo, A. Cucurullo, P. Dangelo, A. Dellacasa, M. Derosa, A. Funel, G. Furini, D. Giammattei, G. Giannini, S. Giusepponi, R. Guadagni, G. Guarnieri, A. Italiano, A. Mariano, G. Mencuccini, C. Mercuri, S. Migliori, P. Ornelli, S. Pecoraro, A. Perozziello, A. Petricca, D. Piccinelli, S. Pierattini, S. Podda, F. Poggi, G. Ponti, A. Quintiliani, A. Rocchi, C. Scio, F. Simoni

ENEA – Unità Tecnica Sviluppo Sistemi per l'Informatica e l'ICT (UTICT)

Abstract

In 2012 the ENEA Linux Clusters ran numerical simulations for an integrated time of about 20 million CPU hours, equivalent to 2260 years. Computational activities covered several research sectors, ranging across Material Science, Computational Fluid Dynamics, Biophysics, Climate Research and Nuclear Fusion. In this report, we review the software and hardware features of the CRESCO systems and discuss some usage statistics.

1. Introduction

Since 2008, CRESCO - an acronym for Computational RESearch centre on Complex systems - supports all numerical activities performed at ENEA, the Italian Agency for New Technologies, Energy and Sustainable Economic Development. Thanks to a family of four powerful Linux Clusters, CRESCO has allowed the agency to step forward in the big arena of High Performance Computing (HPC) and take a major position at a national level. The Center was originally based on two main clusters, CRESCO1 and CRESCO2, installed at the ENEA site of Portici, and some secondary ones, namely CRESCOF, CRESCOC and CRESCOB, installed respectively at the ENEA sites of Frascati, Casaccia and Brindisi. All the machines are still on-service after several years of full activity. Although in June 2013 a third big machine, named CRESCO3, became operative and in March 2014 a newer and bigger one, numbered CRESCO4, will be inaugurated, this report concerns the computational activities specifically performed in 2012, when CRESCO1 and CRESCO2 were the main operating clusters. For the reader convenience, we review below their hardware specs:

CRESCO1: 42 fat nodes IBM x3850-M2, with 4 Xeon Quad-Core Tigerton E7330 processors (2.4GHz,1066MHz,6MB L2), 32GB RAM (12 extra-fat nodes with 64 GB RAM), for a total number of 672 cores;

CRESCO2: 256 blades IBM HS21, with 8 dual Xeon Quad-Core Clovertown E5345 processors (2.33GHz, 1333MHz, 8MB L2), 16 GB RAM, for a total number of 2048 cores; 56 blades IBM HS21, with 2 Xeon Quad-Core Nehalem E5530 (2.33GHz, 8MB L3), 16GB RAM, for a total number of 448 cores; 28 blades IBM HS21, with 2 Xeon Quad-Core Westmere E5620 (2.4GHz, 8MB L3), 16 GB RAM, for a total number of 224 cores.

Both machines are interconnected via an IB network (4XDDR), based on a set of switches: 1 CISCO SFS7024 IB switch with 288 ports, 1 CICSCO SFS 7012 switch with 144 ports and 5 CISCO SFS7000 switches with 24 ports for a total of 120 ports.

The two clusters are embedded into a grid infrastructure known as ENEA-GRID. This provides access to the computational resources as a single virtual system. A detailed description of the ENEA-GRID components can be found in ref. [1], while a discussion of how CRESCO1 and CRESCO2 are integrated into the ENEA-GRID environment is given in ref. [2]. Ref. [3] provides a detailed analysis of the usage statistics in 2009.

2. Statistical analysis of user activities

The numerical simulations performed on CRESCO1/2 in 2012 as well as the studies presented in this report can be grouped into 6 major areas:

- Material Science (13 contributions)
- Computational Fluid Dynamics (5 contributions)
- Biophysics (4 contributions)
- Climate Research (4 contributions)
- Nuclear Physics (3 contributions)
- Information & Technologies (1 contribution)

The distribution of the contributions per research sector testifies a preeminence of numerical studies in Material Science. In order to quantify the relative proportions between the above areas in terms of CPU time, we made use of JobRama, an in-house application aimed at monitoring usage data, as they are produced by the Platform LSF™ [4]. JobRama has been developed in the framework of CRESCO and is now available to all users: every ENEA-GRID member can employ it as a tool to monitor the status of all available computational resources at any given time. On the administrator side, it gives the possibility to compute aggregate accounting data. JobRama can be reached on-line at

https://jobrama.enea.it.

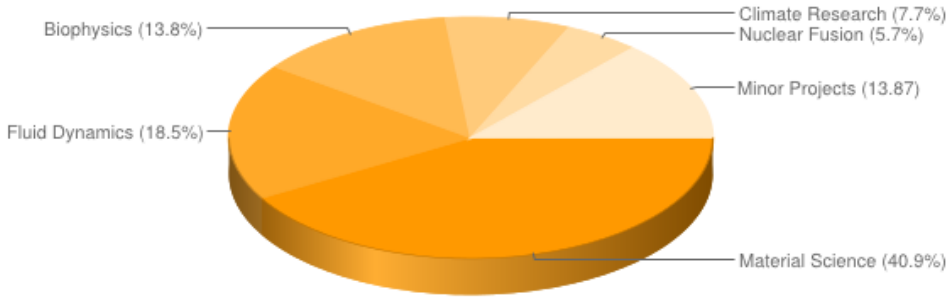

Fig. 1: distribution of CRESCO computational resources per area in 2012

The analysis performed on JobRama assumes the time interval 01.01.2012 – 31.12.2012 as the reference period, for which a total Wall Clock Time (WCT) W0 = 19,818,624.0 h = 2262.4 years has been measured on CRESCO1 and CRESCO2. For each contribution to the present report, we

considered all author names and for each of them we examined all the corresponding ENEA-GRID accounts (for historical reasons, some users have more than a single one): using JobRama we computed the overall WCT associated to each account and the average number of cores used by the account owner. Users authoring several contributions have been counted only once. Results of the analysis are reported in Tab. 1 and depicted in Fig. 1.

Research Area	***WCT (hours)***	***WCT (years)***	***Fraction of WCT := WCT/W0***
Material Science	8.105e+6	925.22	0.409
Fluid Dynamics	3.577e+6	408.33	0.181
Biophysics	2.740e+6	312.78	0.138
Climate Research	1.523e+6	173.86	0.077
Nuclear Physics	1.120e+6	127.85	0.057

Table 1: Distribution of CRESCO computational resources in 2012

Upon summing the numbers contained in the rightmost column of Tab. 1, we obtain a usage fraction of 83%, which measures the representativeness of the present report with respect to the total usage of the two clusters. The remaining WCT has been spent in minor projects, which partly belong to the above areas and partly to other less representative ones.

The overall number of users with WCT > 0.001 years was 81 in 2012. In Fig. 2, we report a plot of their WCT measured in hours vs. a progressive identification number obtained by sorting the users according to decreasing WCTs. As in previous years, we roughly observe a power-like distribution of the WCT, with the first 10 users (representing 12% of the total number) collecting about 75% of the total WCT and a long tail of users gently employing the remaining computational resources.

3. Simulation Codes

In Tab. 2, we report the complete list of the simulation codes used on CRESCO in 2012 grouped according to research areas. The list has been obtained from an analysis of the contributions to the present report. For the reader convenience, we give below a description of each software package.

Research Area	***Codes***
Material Science	Simulation: MOLDY, LAMMPS, Quantum ESPRESSO, EXC, GW, DP, CPMD, DLPOLY Visualization: OVITO, JMOL
Fluid Dynamics	Simulation: HeaRT (ENEA), ANSYS-FLUENT, OpenFOAM
Biophysics	Simulation: ORAC, MODELLER, GROMACS, AMBER Analysis: WHAM
Atmospheric Modelling	Simulation: MITgmc, FLEXPART, RegCM4, RAMS, FARM
Nuclear Physics and Technology	Simulation: FISPACT, MCNP5, HMGC (ENEA), HYMAGIC (ENEA)

Table 2: Simulation codes used on CRESCO in 2012

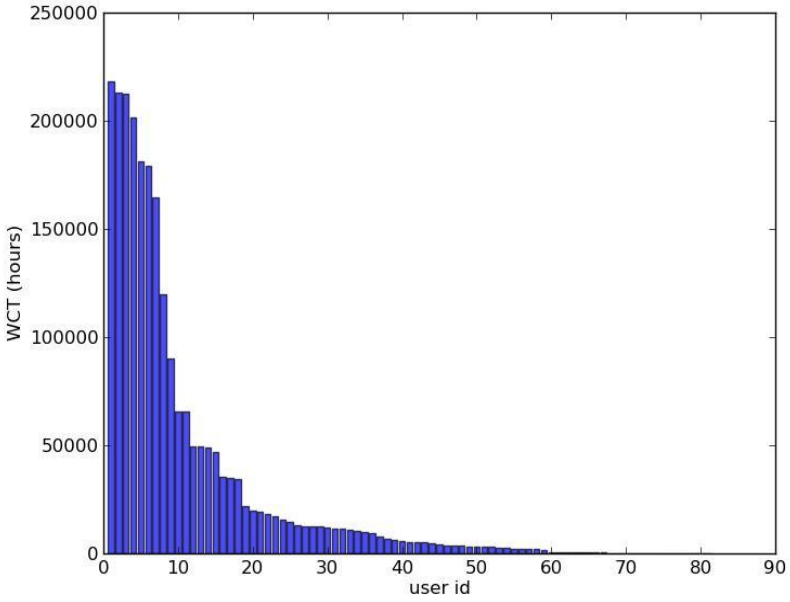

Fig. 2: WCT of CRESCO users in 2012 measured in hours vs. user id's.

3.1 Codes used for Material Science simulations

- **MOLDY**

Website: *https://code.google.com/p/moldy/*

Programming language: Fortran90

Software licence: GNU GPL v2

Description: MOLDY is a parallelized OpenMP short-ranged molecular dynamics program, first written at Harwell Laboratory in the 1980s. The program is rewritten in a modular fashion to allow for easy user modification, in particular the implementation of new inter-atomic potentials. Using Link Cells and Neighbor Lists, the code fully exploits the short range of the potentials, and the slow diffusion expected for solid systems. The code allows for a wide variety of boundary conditions, including constant pressure, temperature and strain rate. It also incorporates molecular statics via the conjugate gradients minimization of the enthalpy. The code will enable simulation of millions of atoms using short range potentials. Currently modules for Embedded Atom, Finnis-Sinclair, Lennard Jones and Morse potentials exist. In addition, the "magnetic" potential formalism of Ackland and Wallenius is available for separate compilation. Alloys containing a number of elements can be simulated, subject only to the available potentials.

- **LAMMPS**

Website: *http://lammps.sandia.gov/*

Programming language: Current version is C++, Older versions are Fortran77/90

Software license: GNU GPL

Description: LAMMPS is a classical molecular dynamics code, and an acronym for Large-scale Atomic/Molecular Massively Parallel Simulator. LAMMPS has potentials for soft materials

(biomolecules, polymers) and solid-state materials (metals, semiconductors) and coarse-grained or mesoscopic systems. It can be used to model atoms or, more generically, as a parallel particle simulator at the atomic, meso, or continuum scale. LAMMPS runs on single processors or in parallel using message-passing techniques and a spatial-decomposition of the simulation domain. The code is designed to be easy to modify or extend with new functionality.

- **Quantum ESPRESSO**

Website: *http://www.quantum-espresso.org/*

Programming language: C and Fortran95

Software license: GNU GPL v2

Description: Quantum ESPRESSO is an integrated suite of Open-Source computer codes for electronic-structure calculations and materials modeling at the nanoscale. It is based on density-functional theory, plane waves, and pseudo-potentials.

- **EXC**

Website: *http://etsf.polytechnique.fr/exc/*

Programming language: Fortran 90, with some insertion of C (parser, utilities) and perl scripts for tests

Software license: GNU GPL v2

Description: EXC is an exciton code working in reciprocal space, frequency domain, and using plane waves basis. Its purpose is to calculate, ab-initio, the dielectric and optical properties, like absorption, reflectivity, refraction index, electron and X-ray energy loss, for a large variety of systems, ranging from bulk systems, surfaces, to clusters or atoms (using the super-cell method), by solving the Bethe-Salpeter equation.

- **DP**

Website: *http://dp-code.org/*

Programming language: Fortran90 and C

Software license: In the Academic and Public Research World, DP is distributed under the terms of the Scientific Software Open Source Academic For Free License. To commercial parties DP is distributed under other Licenses, to be negotiated from case to case.

Description: DP is a code for Linear Response Time-Dependent Density-Functional Theory (LR-TDDFT) in Frequency Reciprocal (k-ω) space on a Plane Waves (PW) basis set. Some quantities (the Kohn-Sham polarizability and the exchange correlation kernel) are calculated in Real (r) space. The code aims at performing simulations of Dielectric and Optical Spectroscopy (Optical Absorption, Reflectivity, Refraction Indices, EELS, IXSS, CIXS, ...).

- **CPMD**

Website: *http://www.cpmd.org/*

Programming language: Fortran77

Software license: *CPMD license*

Description: The CPMD code is a parallelized plane wave/pseudo-potential implementation of Density Functional Theory, particularly designed for ab-initio molecular dynamics.

- **DL_POLY**

Website: *http://www.stfc.ac.uk/cse/25526.aspx*

Programming language: Fortran90

Software license: DL_POLY_4 is supplied to individuals under an academic license, which is free of cost to academic scientists pursuing scientific research of a non-commercial nature. Commercial organizations must acquire the package.

Description: DL_POLY is a general purpose classical molecular dynamics (MD) simulation software, providing scalable performance from a single processor workstation to a high performance parallel computer.

- **OVITO**

Website: *http://www.ovito.org/*

Programming language: C++

Software license: GNU GPL

Description: OVITO is a freely available visualization software, covering both the analysis and the visualization of large-scale atomistic datasets produced by molecular dynamics/statics and Monte-Carlo simulation codes. The name OVITO is an acronym for Open Visualization Tool, emphasizing that this software has been designed with flexibility and extensibility in mind.

- **JMOL**

Website: *http://jmol.sourceforge.net/*

Programming language: JAVA

Software license: GNU Lesser GPL

Description: Jmol is a free, open source molecule viewer for students, educators, and researchers in chemistry and biochemistry. It is cross-platform, running on Windows, Mac OS X, and Linux/Unix systems. The JmolApplet is a web browser applet that can be integrated into web pages. The Jmol application is a standalone Java application that runs on the desktop. The JmolViewer is a development tool kit that can be integrated into other Java applications.

3.2 Codes used for Computational Fluid Dynamics simulations

- **ANSYS-FLUENT**

Website:
http://www.ansys.com/Products/Simulation+Technology/Fluid+Dynamics/Fluid+Dynamics+Products/ANSYS+Fluent

Programming language:

Software license:

Description: ANSYS Fluent is a commercial code to model flow, turbulence, heat transfer, and reactions for industrial applications ranging from air flow over an aircraft wing to combustion in a furnace, from bubble columns to oil platforms, from blood flow to semiconductor manufacturing, and from clean room design to wastewater treatment plants.

- **OpenFOAM**

Website: *http://www.openfoam.com/*

Programming language: C++

Software license: GNU GPL

Description: OpenFOAM is a free software which allows to perform simulations of complex fluid flows involving chemical reactions, turbulence and heat transfer, to solid dynamics and electromagnetics. It includes tools for meshing, notably *snappyHexMesh*, a parallelised mesher for complex CAD geometries, and for pre- and post-processing.

- **HeaRT** (developed at ENEA)

Programming language: Fortran95

Software license: the package can be obtained with restrictions upon request to the authors

Description: HeaRT (Heat Release and Turbulence) is a fully compressible, reactive, unsteady, flow solver that implements an original LES subgrid scale model, named Fractal Model.

3.3 Codes used for Biophysics simulations

- **ORAC**

Website: *http://www.chim.unifi.it/orac/*

Programming language: Fortran 90

Software license: GNU GPL

Description: ORAC is a suite to simulate at the atomistic level complex biosystems. It includes multiple time steps integration, Smooth Particle Mesh Ewald method, constant pressure and constant temperature simulations. It also implements the most advanced techniques for enhanced sampling in atomistic systems including replica exchange with solute tempering, metadynamics on multidimensional reaction coordinates subspaces, and potential of mean force reconstruction along arbitrary reaction paths using non equilibrium molecular dynamics techniques.

- **MODELLER**

Website: *http://salilab.org/modeller/9v7/release.html*

Programming language: Fortran90

- **Software license:** MODELLER is free for academic use. To obtain an academic license key, the user must complete a license agreement. A license key is then sent by e-mail.

Description: MODELLER is used for homology or comparative modeling of protein three-dimensional structures. The user provides an alignment of a sequence to be modeled with known related structures and MODELLER automatically calculates a model containing all non-hydrogen atoms. MODELLER implements comparative protein structure modeling by satisfaction of spatial restraints, and can perform many additional tasks, including de novo modeling of loops in protein structures, optimization of various models of protein structure with respect to a flexibly defined objective function, multiple alignment of protein sequences and/or structures, clustering, searching of sequence databases, comparison of protein structures, etc.

- **GROMACS**

Website: *http://www.gromacs.org/*

Programming language: C++

Software license: GNU GPL

Description: GROMACS is a versatile package to perform molecular dynamics, i.e. simulate the Newtonian equations of motion for systems with hundreds to millions of particles. It is primarily designed for biochemical molecules like proteins, lipids and nucleic acids that have a lot of complicated bonded interactions, but since GROMACS is extremely fast at calculating the non-bonded interactions (that usually dominate simulations) many groups are also using it for research on non-biological systems, e.g. polymers.

- **AMBER**

Website: *http://ambermd.org/*

Programming language: C, C++ and Fortran90

Software license: GNU GPL

Description: AMBER refers to two things: a set of molecular mechanical *force fields* for the simulation of biomolecules (which are in the public domain, and are used in a variety of simulation programs); and a *package of molecular simulation programs* which includes source code and demos. The suite consists of about 50 programs.

- **WHAM**

Website: *http://membrane.urmc.rochester.edu/content/wham*

Programming language: ANSI C

Software license: GPL and BSD

Description: WHAM is a fast, memory efficient implementation of the Weighted Histogram Analysis Method.

3.4 Codes used for Atmospheric Modelling

- **MITgmc**

Website: *http://mitgcm.org/*

Programming language: Fortran77

Software license: The code is freely downloadable and apparently under no license. As a courtesy, the authors ask to send an e-mail upon downloading to keep track of the users.

Description: The MITgcm (MIT General Circulation Model) is a numerical model designed for study of the atmosphere, ocean, and climate. Its non-hydrostatic formulation enables it to simulate fluid phenomena over a wide range of scales; its adjoint capability enables it to be applied to parameter and state estimation problems. By employing fluid isomorphisms, one hydrodynamical kernel can be used to simulate flow in both the atmosphere and ocean.

- **FLEXPART**

Website: *http://transport.nilu.no/flexpart*

Programming language: Fortran90

Software license: GPL v3

Description: FLEXPART is a particle dispersion model. FLEXPART can be driven with meteorological input data from a variety of global and regional models, most commonly from the ECMWF.

- **REGCM4**

Website: *http://www.ictp.it/research/esp/models/regcm4.aspx*

Programming language: Fortran90

Software license: GNU GPL

Description: RegCM4 is package for regional climate modeling. It includes land surface, planetary boundary layer, and air–sea flux schemes, a mixed convection and tropical band configuration, radiative transfer and boundary layer schemes. The model can be interactively coupled to a 1D lake model, a simplified aerosol scheme (including organic carbon, black carbon, SO4, dust, and sea spray), and a gas phase chemistry module (CBM-Z)

- **RAMS**

Website: *http://rams.atmos.colostate.edu/rams-description.html*

Programming language: Fortran90

Software license: GNU GPL

Description: RAMS, the Regional Atmospheric Modeling System, is a highly versatile numerical code for simulating and forecasting meteorological phenomena, and for depicting the results. Its major components are: an atmospheric model which performs the actual simulations, a data analysis package which prepares initial data for the atmospheric model from observed meteorological data and a post-processing model visualization and analysis package which interfaces atmospheric model output with a variety of visualization software utilities.

- **FARM**

Website: *http://www.aria-net.it/*

Programming language: Fortran90

Software license: software developed by ENEA and ARIANET

Description: FARM, the flexible air quality regional model, is a three-dimensional Eulerian grid model with K-type turbulence closure, which accounts for the transport, chemical reactions and ground deposition of atmospheric pollutants.

3.5 Codes used for Nuclear Physics and Technology

- **FISPACT**

Website: *http://www.ccfe.ac.uk/EASY.aspx*

Programming language: Fortran95

Software license: The program is obtained upon request to the RSICC of the Oak Ridge National Laboratory

Description: The European Activation SYstem (EASY), developed and maintained at Culham Centre for Fusion Energy, is an international standard for simulation of activation, transmutation processes caused by nuclear reactions and decay. It integrates information from data files and collaborators around the world into a single user-friendly package, which is invaluable for nuclear researchers and has wider applications for industry; nuclear fission and fusion, accelerator physics, isotope production, stockpile and fuel cycle stewardship, materials characterization, life and storage cycle management. The FISPACT code allows to embed many more features in terms of energy range; up to GeV; incident particles, alpha, gamma, proton, deuteron, neutron; and neutron physics, self-shielding effects, temperature dependence and covariance so as to really cover all application needs: transport, shielding, inventory, medical, astrophysics.

- **MCNP5**

Website: *https://mcnp.lanl.gov/*

Programming language: C and Fortran90

Software license: MCNP5 is a trademark of Los Alamos National Security, LLC, Los Alamos National Laboratory. The program is obtained upon request to the RSICC of the Oak Ridge National Laboratory.

Description: MCNP is a general-purpose Monte Carlo N-Particle code that can be used for neutron, photon, electron, or coupled neutron/photon/electron transport. Specific areas of

application include, but are not limited to, radiation protection and dosimetry, radiation shielding, radiography, medical physics, nuclear criticality safety, Detector Design and analysis, nuclear oil well logging, Accelerator target design, Fission and fusion reactor design, decontamination and decommissioning. The code treats an arbitrary three-dimensional configuration of materials in geometric cells bounded by first- and second-degree surfaces and fourth-degree elliptical tori.

- **HMGC and HYMAGYC (developed at ENEA)**

Website: *http://www.afs.enea.it/vlad/Papers/Userguide-HMGC.pdf*

Programming language: Fortran90

Software license: the packages are distributed only upon request to the authors in the framework of scientific collaborations

Description: HMGC is a hybrid magneto-hydro-dynamic particle simulation code developed at ENEA, which allows to solve fluid MHD equations for bulk plasma. The main limitation of HMGC is that it can only describe systems with magnetic surfaces characterized by circular meridian section. HYMAGYC, also developed at ENEA, allows to describe more general-shape surfaces.

3.6 Distribution of the computational resources per simulation code

In Fig. 3 we report a plot of the distribution of the computational resources per simulation code. The distribution has been indirectly reconstructed by linking the WCT of the contributors to the software packages they declare to use in their contributions. The reader should notice that the presence of authors using several software packages makes it difficult to perform the reconstruction precisely, as it is impossible for the CRESCO administrators to distinguish how WCTs split between different simulation codes. For such cases, we have equally partitioned the WCT of the authors over the various codes they used. From the plot, we observe that the most used software packages are respectively Quantum-ESPRESSO, HeaRT, CPMD, AMBER and MITgmc.

3.7 Distribution of the computational resources per technical unit

Research activities at ENEA are performed within technical units focused on specific topics. In Fig. 4 we report a plot of the distribution of the computational resources per ENEA technical unit, with the various acronyms reading

UTTEI	Advanced Technologies for Energy and Industry
UTRINN	Renewable Energy Sources
UTMEA	Energy and Environmental Modelling
UTTMAT	Material Technologies
UTFISSM	Methods for Reactor Safety and Fuel Cycle
UTFUS	Nuclear Fusion

Table 3: Acronyms of the ENEA technical units involved in simulations on CRESCO in 2012

It should be observed that external (non-ENEA) users are always linked to a contact person working at ENEA and thus their WCT can be certainly referred to the technical unit of the contact person. We observe that the distribution is well balanced between various technical units, with the largest

contributions being provided by UTTMAT, UTICT and UTTEI.

3.8 Usage of CRESCO by external institutions

In Fig. 5, we report a plot of the distribution of the computational resources per external institutions. All in all, the total WCT produced by non-ENEA users amounts to 648 years, corresponding to 29% of the total WCT produced in 2012. The largest contributions come from the universities of Florence, Rome 'La Sapienza" and Rome 'Tor Vergata'. It is important to notice that very often external users submitted jobs from their respective accounts, yet in some cases it occurred that contact persons working at ENEA took care of the simulations in the framework of collaborations with the external institution and thus jobs were submitted from internal accounts. For this reason, the plot is only roughly indicative of the impact of collaborations between ENEA and external institutions on the usage of CRESCO.

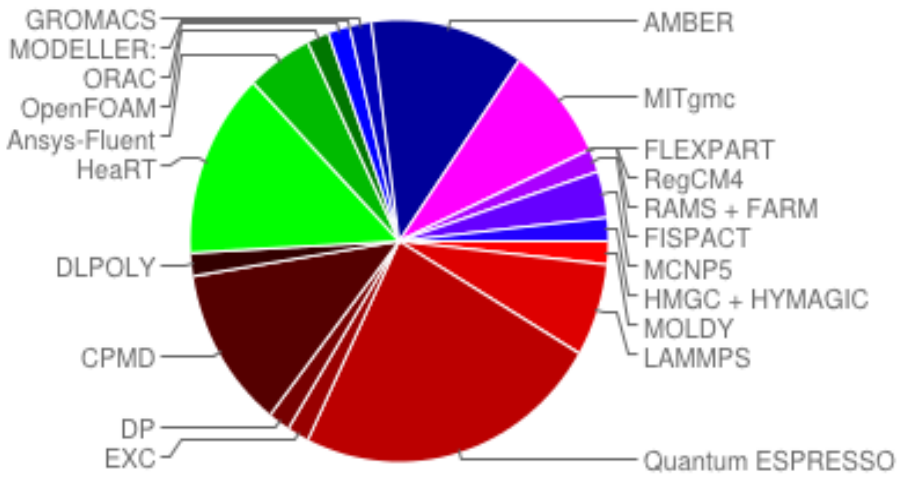

Fig. 3: Approximate distribution of CRESCO computational resource in 2012 per simulation code

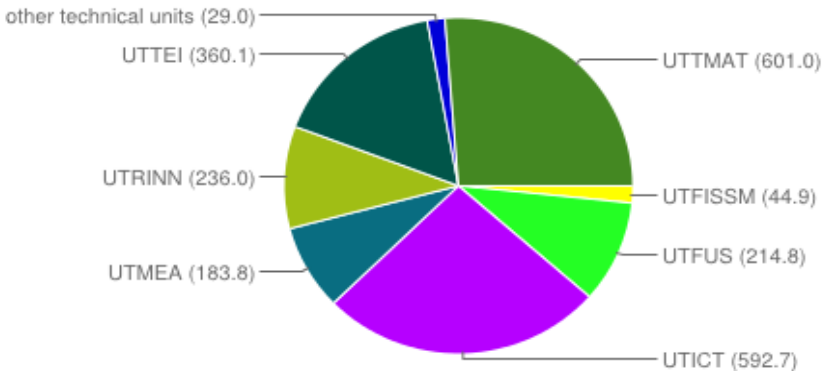

Fig. 4: WCT in years per ENEA technical unit. The total WCT amounts to 2262 years

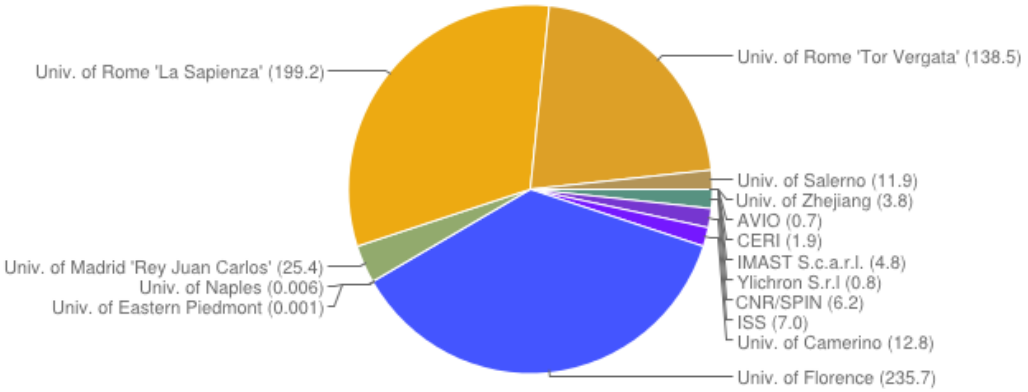

Fig. 5: WCT in years per external institution. The total WCT amounts to 648 years.

Conclusions

We have reported some statistics concerning the usage of CRESCO in 2012. Figures, compatible with those measured in previous years, provide evidence of the strategical importance of the High-Performance-Computing services offered by UTICT-HPC for ENEA and the academic/industrial institutions ENEA collaborates with. The very high usage rate of the machines operating in 2012 suggests that the forthcoming entry into service of the new Linux clusters CRESCO3 and CRESCO4 will be welcomed with enthusiasm by the scientific community.

Bibliography

[1] High Performance Computing on CRESCO Infrastructure: research activities and results 2010-2011. ISBN: 978-88-8286-268-8 (2012).
http://utict.enea.it/it/rapporti-tecnici/high-performance-computing-on-cresco-infrastructure-research-activities-and-results-2010-2011/view

[2] High Performance Computing on CRESCO Infrastructure: research activities and results 2009-2010. ISBN: 978-88-8286-242-8 (2011).
http://utict.enea.it/it/rapporti-tecnici/high-performance-computing-on-cresco-infrastructure-research-activities-and-results-2009-2010/at_download/file

[3] Calcolo ad alte prestazioni sul sistema CRESCO: contributi degli utenti 2008-2009 (2010).
http://utict.enea.it/it/rapporti-tecnici/calcolo-ad-alte-prestazioni-sul-sistema-cresco-contributi-degli-utenti-2008-2009/at_download/file.

[4] A. Abbas, *Grid Computing,* Charles River Media. pp. 110–117. ISBN: 1-58450-276-2 (2004).

Published by ENEA

Central Relations Unit, Communication Service

Lungotevere Thaon di Revel, 76 – 00196 Rome

www.enea.it

Scientific Editor: *Filippo Palombi* (ENEA, UTICT-HCP, Frascati Research Centre)

Graphic composition and cover: *Delinda Piccinelli* (ENEA, UTICT-PRA, Frascati Research Centre)

Published on-line in May 2014